

# 2017 Utah Winter Fine Particulate Study Final Report



**Submitted to the Utah Division of Air Quality (UDAQ)  
March 16, 2018**

Munkhbayar Baasandorj  
Steven Brown  
Sebastian Hoch  
Erik Crosman  
Russell Long  
Phillip Silva  
Logan Mitchell  
Ian Hammond  
Randal Martin  
Ryan Bares  
John Lin  
John Sohl  
Jeff Page

University of Utah  
NOAA ESRL  
University of Utah  
University of Utah  
EPA ORD  
USDA  
University of Utah  
Utah State University  
Utah State University  
University of Utah  
University of Utah  
Weber State University  
Weber State University

Stuart McKeen	NOAA ESRL
Christopher Pennell	UDAQ
Alessandro Franchin	NOAA ESRL
Ann Middlebrook	NOAA ESRL
Ross Petersen	University of Utah
Gannet Hallar	University of Utah
Dorothy Fibiger	NOAA ESRL
Caroline Womack	NOAA ESRL
Erin McDuffie	NOAA ESRL
Alexander Moravek	University of Toronto
Jennifer Murphy	University of Toronto
Amy Hrdina	University of Toronto
Joel Thornton	University of Washington
Lexie Goldberger	University of Washington
Ben Lee	University of Washington
Theran Riedel	EPA ORD
Andrew Whitehill	EPA ORD
Kerry Kelly	University of Utah
Jaron Hansen	BYU
Delbert Eatough	BYU



## Table of Contents

<b>1</b>	<b>INTRODUCTION</b>	<b>1</b>
1.1	CHEMICAL CHARACTERISTICS OF PM <sub>2.5</sub>	3
1.2	METEOROLOGY OF PCAPS AND EXCHANGE PROCESSES	5
1.3	OVERVIEW OF 2016-17 WINTER	6
1.4	SCIENTIFIC QUESTIONS AND STUDY GOALS	13
<b>2</b>	<b>METHODS</b>	<b>15</b>
2.1	TWIN OTTER MEASUREMENTS	15
2.1.1	INSTRUMENT PAYLOAD	15
2.1.2	TWIN OTTER FLIGHT STRATEGY	19
2.2	BALLOON OBSERVATIONS	21
2.3	NEWS HELICOPTER OBSERVATIONS	23
2.4	GROUND SITE NETWORK	24
2.4.1	CACHE VALLEY SITES	25
2.4.2	SALT LAKE VALLEY SITES	31
2.4.3	METEOROLOGICAL OBSERVATIONS IN THE SLV	34
2.4.4	TRAX OBSERVATIONS	40
2.4.5	UTAH VALLEY SITE	41
2.4.6	PASSIVE AMMONIA NETWORK	42
2.5	MODEL SUPPORT AND APPLICATIONS	45
<b>3</b>	<b>OBSERVATIONS OF AEROSOLS AND TRACE GASES</b>	<b>47</b>
3.1	AEROSOL COMPOSITION AND SIZE DISTRIBUTIONS	47
3.1.1	COMPARISON AMONG THE MAJOR BASINS	47
3.1.2	VERTICAL AEROSOL DISTRIBUTIONS	58
3.1.3	SUMMARY AND CONCLUSIONS	63
3.2	OXIDIZED NITROGEN AND OZONE	64
3.3	AMMONIA	77
3.3.1	PASSIVE NH <sub>3</sub> SAMPLER NETWORK MEASUREMENTS	77
3.3.2	GROUND BASED REAL TIME NH <sub>3</sub> MEASUREMENTS	81
3.3.3	AIRCRAFT NH <sub>3</sub> MEASUREMENTS	85
3.4	HALOGENS	91
3.5	GREENHOUSE GASES	102
3.6	VOLATILE ORGANIC COMPOUNDS	104
<b>4</b>	<b>LIMITING AND EXCESS REAGENTS FOR AMMONIUM NITRATE</b>	<b>110</b>
4.1	METHOD #1 - MOLAR RATIOS OF OXIDIZED TO REDUCED NITROGEN	110

4.1.1	TWIN OTTER OBSERVATIONS	111
4.1.2	GROUND SITE OBSERVATIONS	114
<b>4.2</b>	<b>METHOD #2 - THERMODYNAMIC MODELING</b>	<b>116</b>
4.2.1	RESULTS FROM ALL REGIONS (ALL TWIN OTTER DATA)	117
4.2.2	SALT LAKE VALLEY	120
4.2.3	CACHE VALLEY	122
4.2.4	UTAH VALLEY	124
<b>4.3</b>	<b>SUMMARY, FUTURE ANALYSES AND OUTSTANDING QUESTIONS</b>	<b>126</b>
<b>5</b>	<b>EXCHANGE PROCESSES</b>	<b>128</b>
<b>5.1</b>	<b>DOWN-CANYON FLOWS</b>	<b>129</b>
<b>5.2</b>	<b>DAYTIME SIDEWALL VENTILATION - 29 JANUARY 2017</b>	<b>131</b>
<b>5.3</b>	<b>LAKE BREEZE CIRCULATION - 30 JANUARY 2017</b>	<b>132</b>
<b>5.4</b>	<b>SYNOPTICALLY-FORCED LAKE EXCHANGE</b>	<b>133</b>
<b>5.5</b>	<b>INTER-BASIN EXCHANGE</b>	<b>134</b>
<b>6</b>	<b>EMISSIONS</b>	<b>137</b>
<b>6.1</b>	<b>AMMONIA EMISSIONS</b>	<b>137</b>
<b>6.2</b>	<b>RESIDENTIAL WOOD COMBUSTION</b>	<b>140</b>
<b>7</b>	<b>MODELS OF NORTHERN UTAH WINTER AIR QUALITY</b>	<b>142</b>
<b>7.1</b>	<b>UTAH REGULATORY MODELING PROGRESS</b>	<b>143</b>
7.1.1	EFFECT OF AMMONIA INJECTION ON MODEL PERFORMANCE	144
7.1.2	EFFECT OF METEOROLOGICAL MODELING ON MODEL PERFORMANCE	145
<b>7.2</b>	<b>WRF/CHEM MODELING FOR UWFPS-2017</b>	<b>147</b>
7.2.1	WRF/CHEM CONFIGURATION	148
7.2.2	EMISSIONS	150
7.2.3	UNCERTAINTIES RELATED TO METEOROLOGY	150
7.2.4	UNCERTAINTIES RELATED TO EMISSIONS AND PHOTOCHEMISTRY	152
7.2.5	COMPARING WITH COLUMN INTEGRATED DATA FROM TWIN OTTER MISSED APPROACHES	155
<b>7.3</b>	<b>UNIVERSITY OF UTAH TRAJECTORY INFORMATION</b>	<b>156</b>
<b>8</b>	<b>IMPLICATIONS CONTROL STRATEGY DEVELOPMENT</b>	<b>158</b>
<b>8.1</b>	<b>LIMITING REAGENT IN AMMONIUM NITRATE FORMATION</b>	<b>158</b>
<b>8.2</b>	<b>EMISSIONS OF NH<sub>3</sub> AND NO<sub>x</sub></b>	<b>159</b>
<b>8.3</b>	<b>RESIDENTIAL WOOD COMBUSTION</b>	<b>161</b>
<b>9</b>	<b>RECOMMENDATIONS FOR FURTHER RESEARCH</b>	<b>163</b>
<b>10</b>	<b>REFERENCES</b>	<b>169</b>

## List of Figures

- Figure 1.1 Map of Utah (left) with area of detail (right) showing the three major valleys subject to wintertime particulate matter pollution. The Cache Valley in the north spans northern Utah and southern Idaho and is primarily rural, while the Salt Lake and Utah Valleys to the south include the major urban areas of Salt Lake City and Provo..... 1
- Figure 1.2 Map of the three federal Daily PM<sub>2.5</sub> nonattainment areas in Utah. The Salt Lake (blue) and Utah (green) nonattainment areas have recently been designated as “serious”..... 2
- Figure 1.3 Potential temperature at the base and top of the Salt Lake City Basin from radiosonde observations by the National Weather Service (top), and the Valley Heat Deficit (VHD, black) and the smoothed observations of PM<sub>2.5</sub> pollutant concentrations (red) from the UDAQ Hawthorne (HW) site. Data covers the main observational period of the experiment, from 15 December 2016 through 20 February 2017. Note that the horizontal dashed line marks the NAAQS for PM<sub>2.5</sub> and the horizontal red-black dashed line marks the VHD threshold value of 4.04 MJ m<sup>-3</sup> and a PM<sub>2.5</sub> concentration of 17.5 µg m<sup>-3</sup>. ..... 7
- Figure 1.4 Daily average PM<sub>2.5</sub> mass loadings for representative sites in each of the three valleys indicated in Figure 1.1 during the 2016 - 2017 winter (December 1 2016 - February 28, 2017). Grey shaded regions indicate the times during which the Twin Otter research flights occurred. Bars across the top indicate the pollution episodes in Table 1.1..... 8
- Figure 1.5 Time-height cross sections of ceilometer backscatter profile and contours of isentropes at the Landfill Site (LFL) in the Salt Lake Basin for three of the pollution episodes in early 2017. Isentropes are from KSLC radiosonde dataset. Note that some intermittent power outages occurred at the site. .... 10
- Figure 1.6 Time series of PM<sub>2.5</sub>, PM<sub>10</sub>, NO<sub>x</sub>, O<sub>3</sub>, RH and T for representative sites in each of the three valleys during the UWFPS (January 15 - February 15, 2017)..... 12
- Figure 2.1 Instrument layout inside the Twin Otter showing the location of the scientific instruments and the location of the seats for the flight scientist and a second scientist (jump seat)..... 18
- Figure 2.2 Left: Photograph of the scientific instrument payload inside of the aircraft (photograph taken from the rear of the aircraft, facing forward). Right: Indication of the locations of sample inlets. The AMS + UHSAS shared a custom aerosol inlet on the right side of the aircraft, while the I<sup>2</sup> ToF CIMS sampled from a custom gas phase inlet on the left side. Both NO<sub>x</sub>CaRD and the QC-TDLAS instruments sampled through upward facing inlets mounted on the top of the aircraft. .... 18
- Figure 2.3 Example Twin Otter flight patterns. Flight tracks are from January 18, 2017, and are color coded by altitude above sea level as the legend shows. Blue circles indicate locations of airfields throughout the region where the Twin Otter executed missed approaches. The

left panel shows the north flight plan that covered the north metro areas along the east side of the Great Salt Lake, the Cache and Bear River Valleys, Great Salt Lake and the Tooele Valley. The right panel shows the south flight plan that covered the southern end of Great Salt Lake, and the Salt Lake and Utah Valleys. Bottom panels show aircraft altitude (left axes = km, right axes = feet) against elapsed flight time, with locations of missed approaches corresponding to the airfields in the upper panels..... 20

Figure 2.4 The tethered balloon platform carried an ozonesonde on every flight with other payloads alternating between flights. The launch point was collocated with the Utah Division of Air Quality Ogden O2 ground station to provide a calibration reference. The winch raised and lowered the balloon from ground to 500 feet (150 m) high, then back down. Each flight lasted approximately 6 minutes. .... 23

Figure 2.5 The KSL-TV helicopter with inlet location shown (top, A) and instrument box (bottom, B). .... 24

Figure 2.6 Map showing the locations of the ground-based observation sites and the tethered-balloon deployment. .... 25

Figure 2.7 Map (UTM grid, 100 m elevation contours) of the northern part of the Salt Lake Valley showing the locations of meteorological observation sites. Blue dots mark sites with multiple meteorological sensors and/or profilers, as described in Table 2.7. Red dots mark automatic temperature data loggers deployed along an elevation transect between ~1300 m and 2150 m ASL. The thick elevation contour approximately shows the coastline of the Great Salt Lake. .... 35

Figure 2.8 The TRAX Red, Green, and Blue train lines in the SLV. The University of Utah greenhouse gas monitoring network (blue triangles), University of Utah air quality research sites (yellow squares), and the UDAQ’s HW site (cyan star) are also shown. The population density is superimposed in brown shading, and the inset shows the location of the SLV as a red box in the western U.S. .... 40

Figure 2.9 Display of the components of the Ogawa Model 3300 passive sampler. Sampler components are: 1) a porous end cap, 2) a stainless steel screen, 3) a sampling pad, 4) a retainer ring, and 5) a base with hollowed ends [55]..... 43

Figure 2.10 Passive ammonia sampler as deployed at the rural Lewiston (Cache Valley) sample location – without (left) and with the wind/precipitation cap (right)..... 43

Figure 2.11 Passive ammonia sampler locations in the Cache Valley (left) and along the Wasatch Front (right). .... 44

Figure 2.12 4-km (left) and 12-km (right) domains used in the WRF-Chem simulations for the UWFSP-2017 study. Diurnally averaged NO<sub>x</sub> emissions from the NEI-2011 emissions inventory (January, weekday) are also shown. The red box in the 4-km domain demarks the limits used in a diagnostic analysis of the study period..... 46

- Figure 3.1 Example of Twin Otter flight tracks during PCAP events (left and center) and during a non-PCAP event (right). Size and color of the data points are proportional to the total mass of non-refractory  $PM_{10}$  measured by the aerosol mass spectrometer (AMS)..... 48
- Figure 3.2 Mass fractions of the non-refractory components of the sub-micron aerosol mass measured with the aerosol mass spectrometer (AMS) on the NOAA Twin Otter. At the top panel are shown pie charts of the average mass fractions for the PCAP (pollution) Episode #5, Episode #6 (Table 1.1), and for data measured during clear conditions. In the lower panes are the data as function of point number. Aerosol nitrate is blue, ammonium is orange, sulfate is red, chloride is pink, and organic material is green..... 49
- Figure 3.3 Mass fractions as a function of non-refractory, total sub-micron aerosol mass measured with the aerosol mass spectrometer (AMS) on the NOAA Twin Otter. The panel in the upper left corner contains all the data (R1) taken during the UWFPS. In the other panels, the data shown are selected by location. The mass fraction corresponding to ammonium nitrate is shown in blue and calculated as the sum of the nitrate ion ( $NO_3^-$ ) and the associated ammonium ion ( $NH_4^+$ ). The organic mass fraction is green, the sulfate mass fraction is red and the chloride mass fraction is light pink. .... 50
- Figure 3.4 Left: Comparison between the total mass measured with the AMS (y-axis) and the total aerosol volume measured with the UHSAS (x-axis). The data are colored by date and time. Right: AMS measured  $NH_4^+(p)$  versus calculated amount of  $NH_4^+(p)$  required to neutralize all measured anions. The data are colored by ammonium nitrate mass fraction. The black line is a linear fit through the data. .... 51
- Figure 3.5 Time series showing increased  $PM_{2.5}$  concentrations during PCAPs and the correlation between  $PM_{2.5}$  versus ( $NO_y-NO_x$ ) in Logan, Utah during the UWFPS study period.  $PM_{2.5}$  is expressed in units of  $\mu g m^{-3}$  on the left y-axis and  $NO_y-NO_x$  is expressed in units of ppbv on the right y-axis..... 52
- Figure 3.6 Left panel: comparison between the submicron aerosol mass measured by the EPA aerosol mass spectrometer and the  $PM_{2.5}$  mass, measured using a Teledyne T640 by the EPA at the L4 site in Logan. In color is the date at which the measurements were carried out going from 14 January 2017 (blue) to 14 February 2017 (red). Right panel: chemical composition of the non-refractory mass of submicron aerosol particles measured by the EPA aerosol mass spectrometer at the Logan L4 site. In blue is the nitrate mass fraction, in orange is the ammonium mass fraction, in green is the organic mass fraction, in red is the sulfate mass fraction, and in pink is the chloride mass fraction..... 53
- Figure 3.7 AMS measured  $NH_4^+(p)$  versus amount of  $NH_4^+(p)$  required to neutralize all measured anions. Color indicates the date between 14 January and 14 February 2017. Linear fit is shown in relation to the 1:1 line. .... 54
- Figure 3.8 Left: Average particle composition of  $PM_{2.5}$  measured at UU site by AIM-IC for 13-17 February 2017 period. Total  $PM_{2.5}$  mass was measured by TEOM and matches well the features seen by the AIM-IC, which only resolves the soluble inorganic components. All mass loadings are reported in  $\mu g$  per standard cubic meter of air. Right: Total  $\mu$ equivalents of

anions ( $\text{Cl}^-$ ,  $\text{NO}_2^-$ ,  $\text{NO}_3^-$ , and  $\text{SO}_4^{2-}$ ) and cations ( $\text{Na}^+$ ,  $\text{K}^+$ ,  $\text{NH}_4^+$ ,  $\text{Mg}^{2+}$ , and  $\text{Ca}^{2+}$ ) measured by the AIM-IC during 13-21 February 2017. The 1:1 ratio is shown in the dashed line. Markers are colored by total measured  $\text{PM}_{2.5}$  mass (not including water). ..... 55

Figure 3.9 Mass concentrations of sodium ( $\text{Na}^+$ ), calcium ( $\text{Ca}^{2+}$ ), and magnesium ( $\text{Mg}^{2+}$ ) in  $\text{PM}_{2.5}$  measured at UU site by AIM-IC for 25 January-5 February 2017 period. All mass loadings are reported in  $\mu\text{g}$  per standard cubic meter of air. .... 55

Figure 3.10 Particle size distributions as a concentration matrix, with the x-axis representing time in MST, the y-axis representing the particle size in nm and the colors represent the concentration normalized by size bin ( $\text{dN}/\text{dLogDp}$ ) in number  $\text{cm}^{-3}$ . The data in the figure are from the SMPS and APS instruments at the WBB at UU from 26 January 2017 to 5 February 2017. .... 56

Figure 3.11 Example of different spatial patterns of  $\text{PM}_{2.5}$  in the SLV during a PCAP event in February 2016 (panels A-C). Panel D shows the relationship between TRAX observations and the DAQ HW site in February 2016. .... 57

Figure 3.12 Examples of air draining out of the canyons surrounding the SLV with lower concentrations of  $\text{PM}_{2.5}$  during a PCAP event in December 2016, indicated by the lower concentrations in the white circles. .... 57

Figure 3.13 Example of a partial mix-out (yellow shaded region in the left panel) on 19 January 2017. During the short period of time when  $\text{PM}_{2.5}$  was lower, the spatial pattern observed by TRAX shows higher  $\text{PM}_{2.5}$  at the northern part of the Green TRAX line near the SLC airport and lower values elsewhere. The vertical profile indicates moderate winds above the boundary layer that may have scoured the top of the PCAP (right panel). .... 58

Figure 3.14 Vertical profiles of AMS data (revision R1) obtained from the NOAA Twin Otter aircraft during takeoffs and landings at the SLC airport and selected missed approaches to other airfields in the region. On the x-axes are plotted concentrations of the aerosol nitrate in blue, ammonium in orange, sulfate in red, organic compounds in green, chloride in pink, and the aerosol total mass in grey. On the y-axes is plotted the altitude above sea level. The thick black lines are averages of the concentrations over 20 m steps, the thinner black lines show the variability (one standard deviation) of the averages. .... 59

Figure 3.15 Vertical profiles measured using the aerosol mass spectrometer (AMS) on the NOAA Twin Otter (revision R1). On the x-axes are plotted concentrations of the total aerosol mass. On the y-axes is plotted the altitude above sea level. The thick black lines are averages of the concentrations over 100 m steps, the horizontal bars show the variability in the data (one standard deviation). In the left panel are shown data collected during takeoff and landings at the Salt Lake City Airport, in the center are data from missed approaches at the Logan airport in the Cache Valley, and on the right are data from missed approaches at the Provo airport in Utah Valley. .... 60

Figure 3.16 The top row is typical of data taken outside of a pollution event (28 January 2017) by the balloon borne Met One GT-526 particle counter. The bottom row is typical of data obtained on the morning of the first day (31 January 2017) of the strongest pollution event

that was measured. The particle diameter range for the first column is 0.3 $\mu\text{m}$ -10 $\mu\text{m}$ , the second column is 1.0 $\mu\text{m}$ -10 $\mu\text{m}$ , and the third column is 5.0 $\mu\text{m}$ -10 $\mu\text{m}$ . The blue upward pointing triangles are during ascent, and the red downward pointing triangles are during descent..... 61

Figure 3.17 Vertical profile of PM<sub>2.5</sub> data ( $\mu\text{g m}^{-3}$ ) collected in the SLV from KSL-TV helicopter and potential temperature (K, red line) from nearest 0000 UTC rawinsonde observations at the Salt Lake City Airport for helicopter flight periods (left) at 1830-2015 UTC (11:30 am - 1:15 pm MST) on 18 January 2017 and (right) at 2145-2240 UTC (2:45 pm - 3:40 pm MST) on 3 February 2017..... 62

Figure 3.18 Time traces of NO<sub>2</sub>, NO, O<sub>3</sub>, and O<sub>x</sub> measured at the respective ground sites in the three valleys during the main UWFPS intensive window. Other UDAQ ground sites in the area (not shown here) also monitor these species continuously. .... 66

Figure 3.19 Averaged diurnal profiles of NO<sub>2</sub>, NO, O<sub>3</sub>, and O<sub>x</sub> for the six ground sites from 12/01/2016 - 2/28/2017. Solid lines are diurnal profiles consisting of data taken during pollution episodes, and dashed lines consist of data taken during non-pollution events. The yellow shading indicated daytime hours..... 68

Figure 3.20 A typical Twin Otter flight track, colored and sized by NO<sub>2</sub> (left) and O<sub>3</sub> (right), during a pollution episode (upper) and non-pollution (lower) event..... 69

Figure 3.21 A portion of the flight tracks from Figure 3.20 zoomed in on the Salt Lake City region, colored and sized by NO<sub>2</sub> (left) or O<sub>3</sub> (right), during a pollution episode (upper) or non-pollution (lower) event, with a typical TRAX trip overlaid in outlined circles, with the same coloring. Major interstates are shown in blue lines..... 70

Figure 3.22 Time traces of NO<sub>2</sub>, NO, and O<sub>3</sub> for three representative ground sites are shown in solid line, with averaged values from the Twin Otter and TRAX shown in circles and triangles, respectively, when each vehicle passed nearby the ground site. Similar plots can be made for other UWFPS and UDAQ sites, such as in Figure 3.24 and Figure 3.25. .... 71

Figure 3.23 Comparison of ozone measurements on the Twin Otter and on the ground. In the left panel, all Twin Otter flyovers at all ground sites are plotted. In the right panel, only daytime flyovers are plotted. .... 72

Figure 3.24 NO<sub>2</sub> concentrations on two days in January, as measured at the Logan ground site (grey line), and by the Pandora column in Logan (solid circles). .... 73

Figure 3.25 A typical ozonesonde (left) with 13 ascents and descents in the morning hours as the CBL starts to develop. By averaging only the data at the surface, indicated by the large circles, the ozonesonde data can be directly compared to O<sub>3</sub> measurements at a nearby UDAQ monitoring site (right). In the right panel, surface level O<sub>3</sub> time traces from both the ozonesonde (red circles) and Twin Otter missed approaches in Ogden (blue circles) are overlaid on the ground site (black line). .... 74

Figure 3.26 Averaged vertical profiles of NO<sub>2</sub>, NO, total NO<sub>y</sub>, summed NO<sub>y</sub>, and O<sub>3</sub> during sustained ascents and descents in the SLV, on four flights spanning the extent of the major pollution event in late January. .... 75

Figure 3.27 Averaged vertical profiles for three major basin in northern Utah. Vertical profiles of NO<sub>2</sub>, NO, summed NO<sub>y</sub> and O<sub>3</sub> for the entire UWFPS campaign are separately averaged for pollution episodes (solid lines) and non-pollution events (dashed lines). .... 75

Figure 3.28 Modeled 24-hr averaged NO<sub>x</sub> emissions with 1.3 km resolution from the SMOKE model for February 1, 2017 are shown on the left. The center and right panels contain sample Twin Otter flight tracks colored by the observed NO<sub>x</sub> concentration..... 76

Figure 3.29 Cache Valley ambient NH<sub>3</sub> as measured by the passive sampler network during the 2017 UWFPS. .... 77

Figure 3.30 Wasatch ambient NH<sub>3</sub> as measured by the passive sampler network during the 2017 UWFPS. .... 77

Figure 3.31 Contour plots of the average ambient NH<sub>3</sub> for Cache Valley and the Wasatch Front during the 2017 UWFPS..... 79

Figure 3.32 Indoor air NH<sub>3</sub> during the 2017 UWFPS..... 81

Figure 3.33 Cache Valley ambient NH<sub>3</sub>, particulate-bound NH<sub>4</sub>, and PM<sub>2.5</sub> as measured at the Logan EPA trailer location during the 2017 UWFPS..... 82

Figure 3.34 Ammonia time series at SM as measured by low-cost solid-state NH<sub>3</sub> sensor. .... 83

Figure 3.35 Observed NH<sub>3</sub>(g), NH<sub>4</sub><sup>+</sup>(p), calculated total NH<sub>x</sub> in the SLV during Jan 25 to Feb 21. Particle loading and ambient concentration are given in ppbv. .... 84

Figure 3.36 Time series of HNO<sub>3</sub>(g), NH<sub>3</sub>(g) and NO<sub>3</sub><sup>-</sup>(p) and NH<sub>4</sub><sup>+</sup>(p) during episode #7 captured during UWFPS. Particle loading and ambient concentration are given in ppbv..... 84

Figure 3.37 Frequency distributions of NH<sub>3</sub> and NH<sub>4</sub><sup>+</sup>-aerosol mixing ratios measured from the Twin Otter airplane for different regions under PCAP and non-PCAP conditions..... 85

Figure 3.38 Ammonia mixing ratios measured from the Twin Otter airplane for the North flight pattern. Only data from the lowest steady flight level is shown. .... 88

Figure 3.39 Ammonia mixing ratios measured from the Twin Otter airplane for the South flight pattern. Only data from the lowest steady flight level is shown. .... 88

Figure 3.40 Ammonia mixing ratios during missed approaches at different airports in the region. .... 89

Figure 3.41 Comparison of NH<sub>3</sub> mixing ratios between Twin Otter measurements and the Logan ground site as a) time series and b) direct comparison of the respective time periods. Twin Otter data shown represents the missed approaches at Logan airport, located approximately 3 km NW of the Logan ground site. Mean values (blue dots, with standard deviations) are the average NH<sub>3</sub> mixing ratios between 1 km before and 1 km after the start and end of the

runway. Maximum values (red diamonds) were observed directly above the runway and are most representative for the NH <sub>3</sub> mixing ratios at ground level.....	90
Figure 3.42 Comparison of NH <sub>3</sub> mixing ratios between Twin Otter measurements and the UU ground site as a) time series and b) direct comparison of the respective time periods. Mean values (blue dots, with standard deviations) are the average NH <sub>3</sub> mixing ratios within a horizontal 1 km x 1 km grid around the ground site. Corresponding NH <sub>3</sub> mixing ratios from the ground site (black dots) represent the mean concentration during the 1 hour sampling interval.....	90
Figure 3.43 Top panel: spatial distribution of Cl <sub>2</sub> mixing ratios obtained on 22 Twin Otter flights. The color scale is proportional to mixing ratio, but saturates at 0.3 ppb to make the distribution visible over the entire domain. See text for details on Cl <sub>2</sub> mixing ratios near the U.S. Magnesium facility. Bottom panel: example time series of several halogen species and SO <sub>2</sub> from an afternoon intercept of the plume from U.S. Magnesium facility. ....	93
Figure 3.44 Spatial distribution of HCl during the UWFPS campaign aboard the Twin Otter. The color scale saturates at 8 ppb, the thickness of the lines is directly proportional to mixing ratio. ....	94
Figure 3.45 Spatial distribution of SO <sub>2</sub> as measured by the I <sup>+</sup> ToF CIMS on Twin Otter during UWFPS. Individual point sources associated with power generation and other industries are clearly observable. The relatively small enhancement mean the U.S. Magnesium facility can be useful for constraining halogen emissions. ....	95
Figure 3.46 Chlorine concentration in the Utah Valley. There are two places that show consistent spikes in chlorine across multiple flights through the Utah Valley. In the map, the blue outline is Utah Lake and the arrows correspond to the arrows in the time series. The second increase in chlorine, which is not marked with an arrow is directly below the third on the map. While these sources are much smaller than U.S. Magnesium, they appear to be consistent sources of chlorine in the Utah Valley and may affect the chemistry. ....	96
Figure 3.47 Ozone depletion event observed on 16 January. Graph shows data from near U.S. Magnesium plant with observed dihalogen mixing ratios (Cl <sub>2</sub> , BrCl) and halogen oxides (BrO, ClO) well above background. O <sub>x</sub> (O <sub>3</sub> + NO <sub>2</sub> ) shows an inverse relationship with the halogen oxides. This episode was the lowest observed O <sub>x</sub> during the campaign, but there were many other observations of O <sub>x</sub> being depleted when halogen oxides were high.....	97
Figure 3.48 Map of flight from 16 January. The flight track is colored by O <sub>3</sub> mixing ratio. The lowest observed O <sub>3</sub> was in proximity to the U.S. Magnesium plant. The expanded portion of the map shows the area included in the time series in Figure 3.47.....	97
Figure 3.49 Spatial distribution of ClNO <sub>2</sub> measured by the CIMS on 22 Twin Otter flights during the UWFPS campaign. The color scale saturates at 1 ppb. ....	98
Figure 3.50 ClNO <sub>2</sub> (top) and Cl <sub>2</sub> (bottom) mixing ratios measured by I <sup>+</sup> ToF CIMS at the Logan (Cache Valley) ground site during the UWFPS 2017 campaign.....	99

Figure 3.51 CINO<sub>2</sub> and Cl<sub>2</sub> mixing ratios from the Logan ground site measurements during a stagnation event with the highest sustain mixing ratios of CINO<sub>2</sub>. The Cl<sub>2</sub> was usually much lower and more episodic than the CINO<sub>2</sub> though during this event a unique period occurred with Cl<sub>2</sub> greater than CINO<sub>2</sub> for several hours. The cause of this change in Cl<sub>2</sub>:CINO<sub>2</sub> is not yet known. .... 100

Figure 3.52 Comparison of CINO<sub>2</sub> at the Logan ground site and from Twin Otter missed approaches at the Logan-Cache airport. The ground site shows, generally, higher CINO<sub>2</sub> than measured aloft by the Twin Otter. Work is ongoing to determine if this variation in measurement is real or instrumental differences. .... 101

Figure 3.53 Comparison of Cl<sub>2</sub> at the Logan ground site and from Twin Otter missed approaches at the Logan-Cache airport. The Twin Otter CIMS routinely shows Cl<sub>2</sub> at or below the detection limit in this area, while the CIMS based at the Logan ground site indicates Cl<sub>2</sub> mixing ratios up to 10 pptv. .... 101

Figure 3.54 Comparison of N<sub>2</sub>O<sub>5</sub> at the Logan ground site and from Twin Otter missed approaches at the Logan-Cache airport. N<sub>2</sub>O<sub>5</sub> observed from the Twin Otter showed higher mixing ratios than observations from the ground site. This is consistent with past observations. At the surface, NO + NO<sub>3</sub> is a more important NO<sub>3</sub> pathway and there is increased loss of N<sub>2</sub>O<sub>5</sub> due to deposition and higher relative humidity. .... 102

Figure 3.55 Map of the Utah Urban CO<sub>2</sub> Network (UUCON) measurement sites along the Wasatch front (Blue triangles) and TRAX lines (Red and Green) indicating light rail based mobile GHG measurements. .... 103

Figure 3.56 CO<sub>2</sub> and PM<sub>2.5</sub> measured at the EPA Logan trailer during the 2017 UWFPS. The black line shows CO<sub>2</sub> ppm (left axis) and the blue line shows PM<sub>2.5</sub> (right axis). .... 104

Figure 3.57 CH<sub>4</sub> and PM<sub>2.5</sub> measured at the EPA Logan trailer during the 2017 UWFPS. The gold line shows CH<sub>4</sub> ppm (left axis) and the blue line shows PM<sub>2.5</sub> (right axis). .... 104

Figure 3.58 Time series of hourly averaged VOCs measured at UU along with PM<sub>2.5</sub> and CO during UWFPS. .... 106

Figure 3.59 Diurnal trends of key VOCs, PM<sub>2.5</sub>, O<sub>3</sub>, CH<sub>4</sub> and CO measured at UU during polluted and clean conditions. .... 107

Figure 3.60 Weekly trends of key VOCs and NO<sub>x</sub> at UU. .... 108

Figure 3.61 Diurnal trends of the ratios of HCHO, CH<sub>3</sub>CHO, HCOOH and CH<sub>3</sub>COOH versus CO. .... 109

Figure 4.1 UWFPS flight track with Salt Lake City “Box Pattern” shown in red. .... 111

Figure 4.2 Time Series of Nitrogen Ratio from Salt Lake City. Each point represents the average ratio for a single “box-pattern” shown in Figure 4.1. Yellow/Gray shading indicates day/night as defined by SZA ≥ 90°. Time period of pollution episodes events are shown by gray boxes. Color scale shows the average altitude above sea level (meters ASL) of each box. .... 112

Figure 4.3 UWFPS Flight track with level, 30-second average intervals shown in red. .... 112

Figure 4.4 Time Series of Nitrogen Ratio from Cache Valley. Individual points represent 30-second averages over constant altitudes. Yellow/Gray shading indicates day/night as defined by  $SZA \geq 90^\circ$ . Time period of pollution episodes are shown by gray boxes. Color scale shows the average altitude above sea level (meters ASL)..... 113

Figure 4.5 UWFPS Flight track with level, 30-second average intervals shown in red..... 113

Figure 4.6 Time Series of Nitrogen Ratio from Utah Valley. Individual points represent 30-second averages over constant altitudes. Yellow/Gray shading indicates day/night as defined by  $SZA \geq 90^\circ$ . Time period of pollution episodes are shown by gray boxes. Color scale shows the average altitude above sea level (meters ASL)..... 114

Figure 4.7 Ratio of Oxidized to Reduced Nitrogen for pollution episode #7 and clear (after 18 Feb.) periods in mid-February. Yellow/Gray shading indicates day/night as defined by  $SZA \geq 90^\circ$ . Markers are colored by the total measured  $PM_{2.5}$  aerosol mass (not including water). ..... 115

Figure 4.8 Time series of Nitrogen Ratio at the Logan Ground Site. Black dots represent 5-minute averages. Yellow/Gray shading indicates day/night as defined by  $SZA \geq 90^\circ$ . Time period of pollution episodes are shown by gray boxes. .... 116

Figure 4.9 Comparison between measurements (x-axis) and model results (y-axis) of the phase partitioning of ammonium (yellow), nitrates (blue) and chloride (pink). All Twin Otter data are shown. The leftmost column shows the total  $NH_x$ , nitrate, and chloride (gas+aerosol) and constitutes the input of the model. The central and rightmost columns show the gas and aerosol phase predicted by the model using measured temperature and relative humidity. .... 118

Figure 4.10 Comparison between original model results (from Figure 4.9, here on the x-axis) and the simulation case where the input of total nitrate is divided by 2 (y-axis). All Twin Otter data are shown. The leftmost column shows the concentrations of total  $NH_x$ , nitrate, and chloride (gas+aerosol). The central and rightmost columns show, respectively, the gas and aerosol phase predicted by the model for the new conditions using measured temperature and relative humidity. .... 119

Figure 4.11 Same as Figure 4.10, except the input of total  $NH_x$  is divided by 2..... 120

Figure 4.12 Comparison between original model results (from Figure 4.9, here on the x-axis) and the case where the input of total nitrate is divided by 2 (y-axis), for Salt Lake Valley only. The leftmost column shows the total  $NH_x$ , nitrate, and chloride (gas+aerosol). The central and rightmost columns show the gas and aerosol phase predicted by the model for the new conditions using measured temperature and relative humidity..... 121

Figure 4.13 Same as Figure 4.12, except the input of total  $NH_x$  is divided by 2..... 122

Figure 4.14 Comparison between original model results (from Figure 4.9, here on the x-axis) and the case where the input of total nitrate is divided by 2 (y-axis), for Cache Valley only. The leftmost column shows the total  $NH_x$ , nitrate, and chloride (gas+aerosol).The central and

rightmost columns show the gas and aerosol phase predicted by the model for the new conditions using measured temperature and relative humidity.....	123
Figure 4.15 Same as Figure 4.14, except the input of total $\text{NH}_x$ is divided by 2.....	124
Figure 4.16 Comparison between original model results (from Figure 4.9, here on the x-axis) and the case where the input of total nitrate is divided by 2 (y-axis), for Utah Valley only. The leftmost column shows the total $\text{NH}_x$ , nitrate, and chloride (gas+aerosol). The central and rightmost columns show the gas and aerosol phase predicted by the model for the new conditions using measured temperature and relative humidity.....	125
Figure 4.17 Same as Figure 4.16, except the input of total $\text{NH}_x$ is divided by 2.....	126
Figure 5.1 Schematic Illustration of diurnal exchange processes affecting the evolution of a PCAP in the SLV.....	128
Figure 5.2 Time series of wind speeds, wind direction, $\text{PM}_{2.5}$ and ozone concentrations collected at four selected sites near the mouths of tributary canyons (PAR, RB), the valley sidewall (UU) and the basin floor (HW) during the onset of a particulate pollution episode. ....	130
Figure 5.3 Illustration of basin sidewall ventilation on 29 January 2017. A schematic of the process is shown in the top left panel. Vertical (red) and pseudo-vertical temperature profiles (black) are shown for 1700 MST in the top right. The evolution of the convective boundary layer is shown in the lidar backscatter (bottom). The recirculation of sidewall-ejected aerosols at ~2050 m ASL reaches HW shortly after 1400 MST. ....	131
Figure 5.4 Analysis of the surface wind field and surface $\text{PM}_{2.5}$ concentrations during the 30 January 2017 lake breeze event. The last panel shows a smoothed vertical profile of $\text{PM}_{2.5}$ concentrations from observations on a local news helicopter taken in the northern part of the basin. ....	133
Figure 5.5 Analysis of the surface wind field and surface $\text{PM}_{2.5}$ concentrations during the 3 February 2017 lake “recharge” event. The last panel shows a photograph of the shallow tongue of polluted air “recharging” the basin.....	134
Figure 5.6 Wind speed ( $\text{m s}^{-1}$ ) and wind direction at the Point of the Mountain Utah Department of Transportation weather station between 16-21 January 2017 (top) and 26 January- 2 February 2017 (bottom).....	135
Figure 5.7 Analysis of HRRR-STILT backward trajectories (left panel), Mesowest surface wind speeds (middle panel, barb and red value, in $\text{ms}^{-1}$ ) and $\text{NH}_3$ concentrations from the NOAA Twin Otter during the afternoon of 17 January 2017. The red circled region indicates the region of southerly inter-basin from the Utah Valley into the SLV and the associated high $\text{NH}_3$ concentrations ( $\text{NH}_3$ figure courtesy Alex Moravek and Jennifer Murphy).....	136
Figure 5.8 (a) analysis of HRRR-STILT backward trajectories, (b) Mesowest surface wind speeds (barb and red value, in $\text{m s}^{-1}$ ), and (c) TRAX $\text{PM}_{2.5}$ concentrations during mid-morning hours on 31 January 2017.....	136

Figure 6.1 2014 NEI NH<sub>3</sub> emissions totals (tons/day) for several Northern Utah counties. Emission totals have been temporally processed to reflect a typical winter weekday. .... 137

Figure 6.2 24-hour average of 2014 NEI NH<sub>3</sub> emission rates (moles/hr) allocated across a 1.33 km Northern Utah modeling domain. Emission rates reflect a typical winter weekday in February. The left panel shows emissions at the surface and the right panel shows the sum of all emissions from all the layers above the surface. Shown are the total emission rates (large map) and the contributions from different emission sectors (small maps). .... 138

Figure 6.3 Scatterplots of NH<sub>x</sub> vs other gas phase compounds (NO<sub>x</sub>, CO<sub>2</sub>, CO and CH<sub>4</sub>) measured at the UU ground site. .... 139

Figure 6.4 Scatterplots of NH<sub>x</sub> vs other gas phase compounds (CO<sub>2</sub> and CH<sub>4</sub>) measured at the Logan ground site. .... 139

Figure 7.1 (Left panel) Gridded 1.33 km NH<sub>3</sub> emissions prior to ammonia injection. (Right panel) Gridded NH<sub>3</sub> emissions after NH<sub>3</sub> injection. County borders shown by thin black lines. The large red feature (right panel) in the northern region of the modeling domain implies much more NH<sub>3</sub> was injected into Cache County. .... 143

Figure 7.2 (Left panel) Measured PM<sub>2.5</sub> aerosol species ( $\mu\text{g m}^{-3}$ ), for January 7, 2011, an example pollution day, at HW. (Right panel) Modeled PM<sub>2.5</sub> aerosol species. .... 144

Figure 7.3 (Top) Observed potential temperature (K) and RH (90% threshold, dashed blue line). (Bottom) Modeled potential temperature (K) and cloud water mixing ratio ( $0.1 \text{ g kg}^{-1}$  threshold, dashed blue line). Presence of clouds and large NH<sub>3</sub>(g) emissions could lead to increased oxidation of SO<sub>2</sub>(g) to SO<sub>4</sub><sup>2-</sup>(p). .... 145

Figure 7.4 Modeled concentrations of 24-hour PM<sub>2.5</sub> ( $\mu\text{g m}^{-3}$ ) at the 1.33 km grid cell collocated with UDAQ's HW monitor (red). Observations of 24-hour PM<sub>2.5</sub> from UDAQ's HW monitor (black). Red dashed line shows NAAQS ( $35 \mu\text{g m}^{-3}$ ). The period simulated is January 1, 2011 to January 10, 2011. .... 145

Figure 7.5 (Top) Observed temperature at HW compared to (bottom) modeled temperature for January 1 – January 8, 2011 (UTC). Red boxes highlight the near-surface vertical temperature structure for January 4 and January 5. Differences between simulated and observed temperature gradients are likely due to mid-level clouds observed, but absent in the WRF simulation. .... 146

Figure 7.6 Modeled 24-hour PM<sub>2.5</sub> performance at HW before increasing vertical diffusion rates in the model (red). Observations of 24-hour PM<sub>2.5</sub> from UDAQ's HW monitor (black). Modeled PM<sub>2.5</sub> on January 3 is particularly high due to the incorrect simulation of clouds in WRF. 147

Figure 7.7 (a) Heat Deficit at KSLC from observations and 3 model cases. (b) Column sum of total oxidized nitrogen over the Wasatch Box from the WRF/Chem simulations for 3 model cases described in the text. .... 152

Figure 7.8 Column Nitrate versus column NO<sub>x</sub> from Twin Otter missed approaches and landings from observations and a representative model simulation. Integrals are over altitudes < 1 km

AGL. The simple theory assumes nitrate is formed by a first-order loss of NO<sub>x</sub>, both nitrate and NO<sub>x</sub> are removed by a first-order meteorological process, and initial conditions are from the measurement with highest column NO<sub>x</sub>. ..... 156

Figure 7.9 An example of footprint graphics provided for the aircraft data of 1/26/17, available on the University of Utah website. .... 157

Figure 8.1 NH<sub>3</sub> and NO<sub>x</sub> emissions in Northern Utah counties retrieved from the UDAQ inventory. Shown are the total emissions per county for a day in February and the ratio of NO<sub>x</sub>/NH<sub>3</sub> emissions. .... 160

Figure 8.2 Ratio of NO<sub>x</sub>/NH<sub>3</sub> emissions retrieved from the UDAQ inventory for a day in February. Considering that only about 5-30 % of NO<sub>x</sub> are oxidized to nitrate, the orange colored areas (NO<sub>x</sub>/NH<sub>3</sub> ratio ~ 10) indicate regions where NH<sub>4</sub>NO<sub>3</sub> formation might be NH<sub>3</sub> limited assuming that local emissions represent the reagent limitation in a given area. .... 160

## List of Tables

Table 1.1 Pollution episodes observed during the 2016-2017 winter .....	8
Table 1.2 Snow depth in inches every three days in the three valleys during January 15th - February 15th (source cocorahs.org).....	9
Table 2.1 NOAA Twin Otter Instrumentation.....	17
Table 2.2 NOAA Twin Otter flights during UWFPS .....	21
Table 2.3 EPA/USU Analyzers/Samplers Operated during UWFPS at Logan, UT .....	25
Table 2.4 UDAQ/USDA Analyzers/Samplers Operated during UWFPS at SM.....	29
Table 2.5 Samplers operated during UWFPS at UU .....	31
Table 2.6 EPA and UDAQ Analyzers/Samplers Operated during UWFPS at HW .....	33
Table 2.7 The main meteorological observational sites in the SLV during UWFPS.....	35
Table 2.8 Locations and elevation of Hobo® automatic temperature dataloggers deployed along an elevation transect in the northeastern Salt Lake City Basin during UWFPS .....	38
Table 2.9 UDAQ, EPA and BYU Analyzers/Samplers Operated during UWFPS at LN .....	41
Table 2.10 Latitude and longitude of passive sampling network sites. ....	44
Table 3.1 A summary of NO <sub>2</sub> , NO, O <sub>3</sub> , and NO <sub>y</sub> measurements during the UWFPS campaign. ....	65
Table 3.2 Average ambient NH <sub>3</sub> (plus/minus 95% CI).....	80
Table 7.1 WRF/Chem settings used in the base configuration for UWFPS-2017 simulations. ....	148
Table 7.2 NEI-2011 Emissions (January weekday) for select Utah counties. Units are short tons per day, NO <sub>x</sub> as NO <sub>2</sub> .....	150
Table 7.3 Percentage increase in NO <sub>3</sub> <sup>-</sup> (p) + HNO <sub>3</sub> due to model perturbation (upper limits) ...	155

# Executive Summary

The air basins along Utah's Wasatch Range, a region with 2.4 million residents (2010 Census), experience some of the most severe fine particulate matter (particulate matter with aerodynamic diameter less than 2.5 micron, PM<sub>2.5</sub>) air pollution in the United States. High levels of PM<sub>2.5</sub> degrade visibility and are a significant public health concern associated with increased incidence of respiratory illness such as aggravation of asthma and premature mortality. PM<sub>2.5</sub> pollution episodes in northern Utah are closely related to the passing of high pressure ridges that favor the formation of persistent cold air pools (PCAPs) in Utah's topographic basins. During these multi-day episodes, vertical mixing is suppressed and pollutants emitted or formed near the surface accumulate in a shallow region known as the atmospheric boundary layer. In the Salt Lake valley, the depth of this boundary layer is 300 - 800 meters (1000 - 2500 feet). Boundary layer depths in other nearby regions, such as the Cache Valley, are typically somewhat shallower. Pollutant accumulation and subsequent atmospheric chemistry leads to elevated levels of primary and secondary pollutants including PM<sub>2.5</sub>.

In the Salt Lake Valley, the National Ambient Air Quality Standard (NAAQS) for 24-h PM<sub>2.5</sub> of 35 µg m<sup>-3</sup> is exceeded during 6 multi-day PCAP events comprising 18 days in an average winter, with large inter-annual variability in the duration and frequency of PCAP episodes. The US EPA declared three regions in northern Utah, home to approximately 80% of Utah's population, as non-attainment areas (NAA) for 24-h PM<sub>2.5</sub> in 2009: Salt Lake City (which includes Davis, and parts of Weber, Box Elder, and Tooele Counties), Provo, and Logan with adjacent Franklin County, Idaho. The Salt Lake City and Provo NAAs have since been re-classified as "serious", requiring more stringent regulations to reduce PM<sub>2.5</sub>. Despite the severity of these pollution episodes, uncertainties remain in the chemical and meteorological processes governing the formation of PM<sub>2.5</sub> and improved scientific understanding is needed for the development of effective control strategies.

The principal component of PM<sub>2.5</sub> during winter air pollution events is ammonium nitrate (NH<sub>4</sub>NO<sub>3</sub>), which is formed in the atmosphere via reversible reactions of ammonia (NH<sub>3</sub>) and nitric acid (HNO<sub>3</sub>). Ammonia is directly emitted from both agricultural sources, such as animal husbandry, and combustion sources, such as vehicle emissions or residential wood combustion. Nitric acid, by contrast, is a secondary pollutant that forms from chemical reactions of nitrogen oxides (NO<sub>x</sub> = NO + NO<sub>2</sub>). The latter are primary pollutants associated with combustion sources, such as vehicle emissions, power generation and industrial activity. Particulate ammonium nitrate therefore results from a complex interaction of meteorology, emissions sources and atmospheric chemistry.

## Methodology

The wintertime chemistry that leads to ammonium nitrate is thought to be altitude dependent, with more rapid chemistry occurring in the upper parts of the polluted boundary layer compared to the surface level. Previous studies have been limited to surface-based measurements, and therefore have not been able to fully characterize the rates and governing factors behind winter  $PM_{2.5}$  formation. The 2017 Utah Winter Fine Particulate Study (UWFPS), one of the most comprehensive studies in this region to date, was conducted to address major questions with respect to ammonium nitrate aerosol formation in the stable, polluted boundary layers associated with the valleys of northern Utah. As part of this study, a National Oceanic and Atmospheric Administration's (NOAA) light aircraft, the Twin Otter, flew a suite of scientific instrumentation over the three major valleys of northern Utah, including Cache, Salt Lake, and Utah valleys, from January 15 to February 15, 2017. These flights surveyed the chemical conditions responsible for the formation of fine particulate pollution and probed the horizontal and vertical distributions of the most important trace gases and aerosols.

The use of a heavily instrumented light aircraft is a new approach to the study of air pollution in winter boundary layers. It is possible in part due to recent technological advances that allow for detailed atmospheric chemical measurements with instruments that are light enough to be deployed on small aircraft, which in turn can fly within the required, low altitude range. Application of this approach will improve understanding of winter air pollution in northern Utah and potentially other regions of the United States in the future.

In addition to the aircraft flights, a wide suite of trace gas, particulate and meteorological observations were made at multiple sites located in Cache, Salt Lake, and Utah Valley to augment the aircraft data and provided continuous measurements during both clean and polluted conditions. Detailed meteorological observations were carried out to monitor the formation, persistence and decay of cold-air pools. Besides nocturnal clean air injection through tributary canyons, exchange of air between different basins, as well as air to/from the Great Salt Lake (synoptically forced or as lake breeze) and from above the cold air pools, are additional important meteorological processes that lead to transport and mixing of pollutants from different locations and altitudes that were characterized during UWFPS.

## Results

Seven multi-day pollution episodes with elevated  $PM_{2.5}$  were observed during 2016 – 2017 winter. Two dominating episodes with multiple NAAQS exceedances occurred during the UWFPS period, providing an opportunity to study the chemical and meteorological conditions during and outside pollution episodes in different environments and examine the temporal, spatial, and vertical variability of chemical conditions. The Twin Otter executed 23 successful research flights across

13 flight days, capturing moderate to severe pollution events and clean periods. Despite the heterogeneity of the sources, the chemical composition of  $PM_{2.5}$  was quite uniform in all the basins. Consistent with previous ground-based studies,  $PM_{2.5}$  mass was dominated by ammonium nitrate during high pollution events, with an average contribution based on aircraft data of 75%. Other components of  $PM_{2.5}$  that are common in other urban areas, such as organic species (composed of carbon, oxygen and hydrogen) and sulfate (composed of sulfur and oxygen) made up the remaining mass (<20% and <5% on average). The average vertical profile in the Salt Lake Valley shows an increase of aerosol mass loading with altitude with a maximum at ~350 m (1200 feet) above ground level (AGL) and low values above 700 m (2300 feet). In contrast, the vertical distribution of aerosol mass loadings in Utah and Cache Valleys show shallower mixing depth with a maximum near the surface in Utah Valley and a relatively uniform aerosol distribution within the first ~300 m (1000 feet) above ground level (AGL) in Cache Valley.

Nitrogen oxide ( $NO_x$ ) levels show a clear spatial gradient across the northern Utah domain, with higher levels in more populated urban areas closer to the local sources and lower in rural areas such as the Cache Valley. The observed spatial patterns are broadly consistent with those in the emissions inventory used by the Utah Division of Air Quality (DAQ) for air pollution modeling. As a pollution episode progresses,  $NO_x$  and ammonium nitrate increase in the three valleys. Ozone, an oxidant that is typically associated with summertime air pollution, is lower during winter pollution episodes in the Wasatch region, an effect that is generally characteristic of urban winter air pollution. The influence of the daily cycle of the mixing within the boundary layer is evident in the observed temporal changes and the vertical distribution of the trace gases and  $PM_{2.5}$ . The highest  $NO_x$  and lowest ozone are often found near the surface at night as the  $NO_x$  pollutants are emitted and trapped within a near surface layer that is much shallower than the boundary layer. Nighttime reactions of the concentrated  $NO_x$  emissions tend to reduce ambient ozone levels. The shallow nighttime surface layer mixes during the day with the boundary layer due to the effect of sunlight heating the surface, but the boundary layer depth remains relatively constant, with little mixing of pollution to elevations above the cold air pool. These characteristics are manifested in the Twin Otter observations. Aircraft and surface level measurements of  $NO_x$  and ozone show clear deviations at night due to the lack of mixing at that time of day, but the same observations agree reasonably well during daylight hours when mixing of surface level and air aloft is more efficient. As the aircraft sampled the vertical structure within and above the boundary layer, a sharp distinction between the polluted air (higher  $NO_x$  and  $PM_{2.5}$ , lower ozone) trapped in the valley and the air above the basin was also seen at all times of day.

## Findings

### 1. Limiting Reagents in Ammonium Nitrate Formation

One of the key questions with respect to ammonium nitrate is attribution of the limiting reagent (i.e., primary ammonia or secondary nitrate) within the three basins. The Twin Otter payload was designed to sample the gas and particulate phase chemical composition of the air and provided

spatially resolved data of the relative amounts of gases and particles across the region and as a function of height above ground. The ground-based observations at Logan in Cache Valley, and at the University of Utah site in the Salt Lake Valley, provided continuous observations of the ammonium nitrate system at fixed locations. Using the combined results, two types of analyses were performed to address the question of the limiting reagent.

The first method examines the ratio of the observed total nitrate to total reduced nitrogen. Twin Otter measurements in the three major air basins (Cache, Utah and eastern Salt Lake Valleys) indicate that across northern Utah, total secondary nitrate, expressed as the sum of both gas and particulate phases, is present in lower concentrations than total primary reduced nitrogen (derived from ammonia), again expressed as the sum of both gas and particulate phases. Thus, secondary nitrate appears to limit the process of ammonium nitrate formation, suggesting that controls leading to reductions in secondary nitrate would be effective at reducing  $PM_{2.5}$ . However, the extent to which the system is nitrate limited varies from valley to valley and as a function of time and altitude. Of the three major valleys, the Cache Valley was most clearly in the nitrate limited regime although the nitrate limitation may be more severe at the surface than aloft. Both Salt Lake and Utah Valleys are predominantly nitrate limited, but may also have periods of reduced nitrogen limitation later in a pollution episode if the PCAP persists longer. It is possible that as pollution episodes proceed, the system evolves from a more nitrate to a less nitrate limited regime. Of the three major valleys, the Salt Lake Valley is the least nitrate limited during pollution episodes and is often within the ammonium limited regime later in the episodes. This may suggest that the system in Utah Valley and particularly the one in the Salt Lake Valley is close to the equivalence point between nitrate limited and ammonium limited regimes, and reductions in either reagent (nitrate and/or ammonia) may be effective in leading to reductions in ammonium nitrate aerosol. Validation of this result, including a quantitative analysis of the associated uncertainties, will require further analysis of UWFPS data.

A second method for determining limiting reagents relies on modeling of the thermodynamics of gas and aerosol phase nitrate and reduced nitrogen. The model is then used to determine the response of total  $PM_{2.5}$  to an arbitrary, fixed reduction in either component. Results of this approach may be more definitive than the simpler comparison of total concentrations outlined in the preceding paragraph, but will require further analysis to reach robust conclusions regarding the most effective control strategies.

## **2. Emissions**

During UWFPS, high time resolution real-time ammonia measurements were conducted aboard the Twin Otter and in Logan in the Cache Valley. However, continuous ammonia measurements were limited along the Wasatch Front. The observed ammonia concentrations are typically much higher in the Cache Valley air basin compared to the Wasatch Front, but also more variable, showing significant enhancements near agricultural sources. Similarly, ammonia in Utah valley shows more variability with lower mixing ratios above Utah Lake and larger regions of isolated

higher concentrations near Spanish Fork and Lindon. Ammonia levels in the Salt Lake Valley are on average lower than in Utah Valley. The observed high spatial variability of ammonia is in disagreement with the current inventory, which shows comparable  $\text{NH}_3$  emissions in the inventories for Cache, Utah and Salt Lake Counties, indicating a potential misrepresentation of the spatial distribution of ammonia sources in the inventory. Since the Wasatch Front appears to be less nitrate limited, better characterization of  $\text{NH}_3$  sources in this region will be critical. Multiple independent observations indicate the importance of inter-basin exchange processes that can potentially transport ammonia from Utah Valley to Salt Lake Valley. If the transport of ammonia is a significant contributor to the ambient ammonia in the Salt Lake Valley, a reduction of ammonia in Utah Valley prior to the passages of high pressure systems could potentially reduce  $\text{PM}_{2.5}$  in the Salt Lake and Utah Valleys during pollution episodes. More work is needed to characterize the ammonia sources and determine the contribution of transport processes on ambient ammonia.

As noted above, the observed distributions of nitrogen oxides, the precursors to secondary nitrate, are similar to those found in the emissions inventories and are concentrated near the largest urban areas in the region. Therefore, although the current analysis of the UWFPS data does not provide a quantitative assessment of the accuracy of nitrogen oxide emission inventories, observations suggest no qualitative disagreement with distribution of these emissions as represented by the inventory.

### **3. Residential Wood Combustion**

Past ground-based work has shown varying contributions of wood smoke emissions to  $\text{PM}_{2.5}$  in the study region. The major emissions from wood smoke include carbon containing compounds that are thought to contribute mainly to the organic component of  $\text{PM}_{2.5}$ , which as noted above contributed less than 20% to the final particulate mass in the aircraft observations during high pollution episodes. This figure represents a preliminary, upper limit to the contribution of wood combustion to regional fine particulate mass as other sources such as vehicular emissions can also contribute to organic aerosol. The actual contribution of residential wood combustion to total  $\text{PM}_{2.5}$  is uncertain and near the surface it will vary spatially depending on the specific location and time of the day. Hence, the potential importance of spatial and vertical variability needs to be considered while interpreting surface site observations for determining the residential wood combustion contribution to total  $\text{PM}_{2.5}$  in a basin.

### **Future Research**

Although UWFPS was the most comprehensive study of its kind and used a novel methodology for the study of winter air pollution, significant further research will be required to make best use of the data and to reach more definitive findings regarding the sources and processes leading to winter fine particulate matter in northern Utah and elsewhere. Continuing analysis of UWFPS

2017 data, and field studies that build on UWFPS 2017 in the future, should ideally include, but not necessarily be limited to, the following.

- Chemical mechanisms for ammonium nitrate and oxidants. The next phase of UWFPS analysis will focus on the atmospheric chemical processes that lead to ammonium nitrate, and the time of day and altitude range in which they are most prevalent, to improve models of ammonium nitrate formation.
- Quantification of key meteorological processes. Data from UWFPS will aid in determining the role of processes such as exchange of air between different valleys in northern Utah, exchange with the Great Salt Lake, and exchange between the polluted boundary layer air and the clear air aloft.
- Variation of nitrate limitations during pollution episode evolution. A finding from UWFPS is that the system is limited by secondary nitrate early in pollution episodes, but that this limitation becomes less severe with time. The finding has important implications for control strategies and should be more carefully examined during further analysis.
- Improve understanding of chlorine chemistry. UWFPS has provided the first measurements of reactive chlorine compounds in Utah. This is an important current research topic and one that may be especially important in Utah given its proximity to the Great Salt Lake. Future analysis and measurements should focus on these cycles.
- Uncertainties in ammonia sources. Emissions inventories, their spatial distributions, and the contributions of inter-basin exchange of ammonia are important, unresolved issues that will require further analysis and measurement. Determination of the relative contribution of vehicular and agricultural sources of ammonia is an important issue that will require further examination using UWFPS data and potentially additional measurements in the future.
- Uncertainties in wood smoke contributions to fine particulate mass. Measurements during UWFPS can partially, but not fully, quantify this particulate matter source. Future studies that include more comprehensive measurements and spatial distribution of carbon containing gas and aerosol phase species are required.
- Better characterization of volatile organic compounds (VOCs). Measurements during UWFPS targeted the major components of ammonium nitrate aerosol. However, VOCs play important roles in the chemical processes that lead to ammonium nitrate and are themselves important tracers of emission sources. Future measurements should also incorporate state of the art measurements of these compounds.
- Uncertainties in meteorological modeling. Limitations imposed by local topography, Salt Lake water temperature specification, land-use characterization including snow and urban effects, parameterized boundary layer physics, model grid resolution, and current computational constraints can all prevent adequate simulations of cold-pool development and evolution. Ongoing meteorological research will make use of UWFPS and future observations to better constrain these processes so that regulatory models best represent the evolution of pollution episodes in northern Utah. Fully-coupled meteorological and chemical models at high spatial resolution are needed to determine the contributions of various meteorological processes on PCAP chemistry.

# 1 Introduction

The air basins along Utah's Wasatch Range (Figure 1.1), a region with 2.4 million residents (2010 Census), experience some of the most severe particulate matter (PM) air pollution in the United States. Although there is considerable inter-annual variability in the number, severity and duration of pollution events, analysis of historical data shows that the region exceeds the National Ambient Air Quality Standard (NAAQS,  $35 \mu\text{g m}^{-3}$ , 24 hours) for particulate matter with aerodynamic diameter smaller than  $2.5 \mu\text{m}$  ( $\text{PM}_{2.5}$ ) on average 18 days out of the year [1]. The majority of exceedance days occur in December, January and early February during a period when passages of high pressure systems lead to stably stratified valley atmospheres, or persistent cold air pools (PCAPs), that trap urban emissions within a shallow boundary layer [1]. Particulate matter exceedances in northern Utah are similar to those seen in urban mountain valleys across the western United States, but Salt Lake City is by far the largest urban area subject to these air quality issues in the intermountain west, and it experiences the highest PM concentrations [2]. Particulate matter accumulates at rates of  $6\text{-}10 \mu\text{g m}^{-3} \text{ day}^{-1}$  during PCAP events to reach maximum daily average concentrations of  $70\text{-}80 \mu\text{g m}^{-3}$  [1, 3] in the Salt Lake City area, and up to  $132.5 \mu\text{g m}^{-3}$  in Logan, UT [4]. Hourly  $\text{PM}_{2.5}$  at Logan has been reported as high as  $182 \mu\text{g m}^{-3}$  in January of 2004 [4].

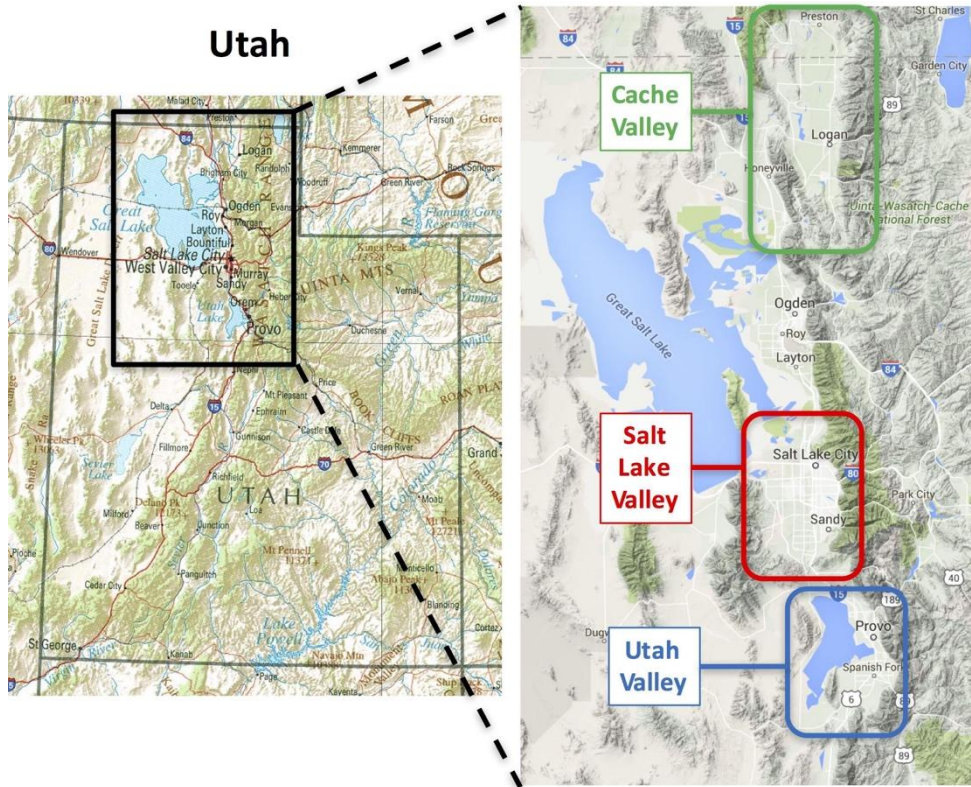


Figure 1.1 Map of Utah (left) with area of detail (right) showing the three major valleys subject to wintertime particulate matter pollution. The Cache Valley in the north spans northern Utah and southern Idaho and is primarily rural, while the Salt Lake and Utah Valleys to the south include the major urban areas of Salt Lake City and Provo.

High PM<sub>2.5</sub> mass loadings in northern Utah are a significant public health concern. They have been specifically associated with adverse health effects in the region, including a 42% higher rate of emergency room visits for asthma during the latter stages of air pollution events [5] and a 4.5% increase in the risk for acute ischemic coronary events per 10 µg m<sup>-3</sup> particulate concentration [6]. The US EPA declared three regions, including part or all of 7 counties in northern Utah, as non-attainment areas (NAA) in 2009 [7] as shown in Figure 1.2. Two nonattainment regions are located along Utah's Wasatch Front (Salt Lake City Utah NAA, Provo Utah NAA), where 80% of Utah's population lives, while one region (Logan Utah-Idaho NAA) consists of the Cache Valley in the northernmost part of the state. Because of recent failures to bring these areas back into attainment with the standard, the two NAAs along the Wasatch Front have been re-designated in December 2016 as "serious" NAA, a designation more critical than "moderate". Under the Federal Clean Air Act, The State of Utah is mandated to demonstrate attainment of the federal standard at a future date, normally five years out from a present-day "base" year. The state is also required to develop more stringent regulations to reduce PM<sub>2.5</sub>. The demonstration of federal attainment is determined by using regional air quality modeling. Current uncertainty in the scientific understanding of these pollution episodes propagates directly into air quality models and limits the model's usefulness for assessing emission control strategies. Hence, detailed measurements of the atmospheric composition and meteorological conditions are essential to improve the scientific understanding of these events and provide constraints on the air quality models.

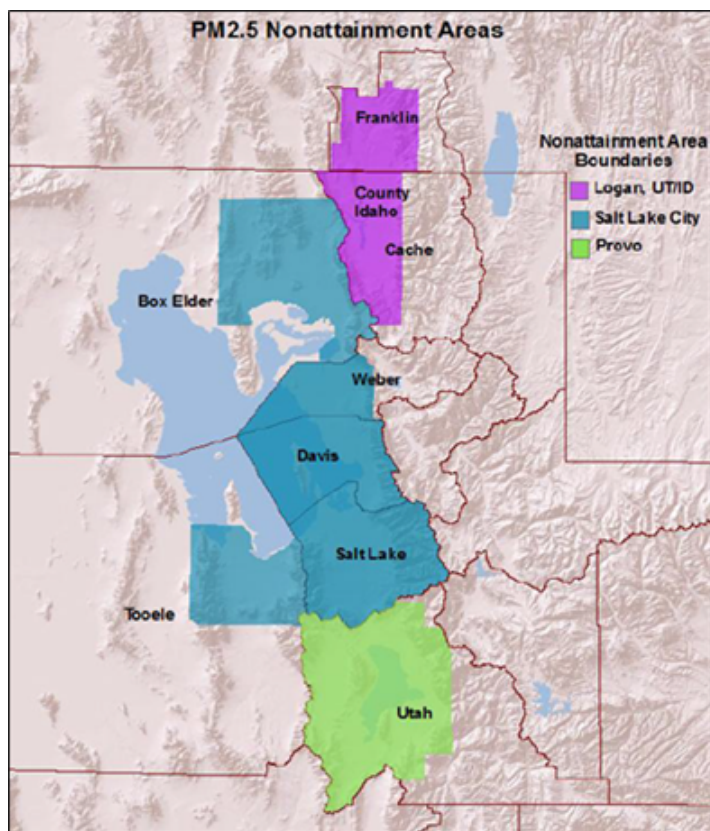


Figure 1.2 Map of the three federal Daily PM<sub>2.5</sub> nonattainment areas in Utah. The Salt Lake (blue) and Utah (green) nonattainment areas have recently been designated as "serious".

## 1.1 Chemical Characteristics of PM<sub>2.5</sub>

The chemical composition of PM<sub>2.5</sub> in northern Utah, and the mechanisms by which it forms, have received less attention than in other regions of the U.S. despite the severity of the problem in Utah. Chemically speciated PM<sub>2.5</sub> measurements come from EPA and UDAQ monitoring sites in the Cache, Salt Lake and Utah Valleys [1, 3, 8-11]. Much of the database is based on 24-hour filter measurements, but is augmented by intensive operating periods in different years that produce data at hourly time resolution for major primary trace gases, inorganic acids and bases, inorganic PM<sub>2.5</sub> ions, and organic matter.

The principal component of PM<sub>2.5</sub> during winter air pollution events is ammonium nitrate, which is responsible for up to 70% of PM<sub>2.5</sub> mass during PCAPs and 40% outside of PCAPs [10]. Ammonium chloride may also contribute up to 15% of PM<sub>2.5</sub> mass during periods of high concentrations, although the source of the aerosol chloride is unclear [9]. Nearly all studies within the last 20 years find sulfate to be a minor contributor to PM<sub>2.5</sub> during PCAPs [1, 3, 8-14]. The contribution of organics is more difficult to estimate. Residential wood combustion (RWC) is in general thought to be an important source of organic aerosol during wintertime in a number of western mountain basins [2]. Several studies in the Salt Lake City area have inferred organic mass from the difference between total mass and the sum of all inorganic ions (e.g., [10]). Other studies have determined organic mass from filter samples and a total organic carbon measurement following IMPROVE protocols [2]. Most studies find a dominant contribution from ammonium nitrate during PCAP events, although some suggest a substantial contribution from organic carbon.

Because ammonium nitrate is generally the single largest component of PM<sub>2.5</sub> mass, it is subject to the greatest scrutiny with respect to its sources and potential control strategies. There are several important research questions with respect to ammonium nitrate production within polluted winter boundary layers. The first is the limiting reagent within any given region. Most studies that have considered the balance between reduced nitrogen (the sum of gas phase ammonia, NH<sub>3</sub>(g), and particulate ammonium, NH<sub>4</sub><sup>+</sup>(p)) and oxidized nitrogen (the sum of gas phase nitric acid, HNO<sub>3</sub>(g), and particulate nitrate, NO<sub>3</sub><sup>-</sup>(p)) suggest that oxidized nitrogen is the limiting reagent. Measurement of total inorganic ions in PM<sub>2.5</sub> suggests that NH<sub>4</sub><sup>+</sup> is balanced by the sum of sulfate and nitrate, providing evidence for excess NH<sub>3</sub> since a cation deficit would be expected in the NH<sub>3</sub> limited case [9]. Surface level data from a site in the center of Salt Lake City also suggested a slight excess of reduced nitrogen, although oxidized and reduced nitrogen are nearly equal [10]. As discussed further below, attribution of the limiting reagent in the ammonium nitrate equilibrium may be a complicated question, since there may be considerable horizontal and vertical variation in the distribution of each reagent that has not been adequately probed from surface level measurements.

A second question is the role of residual layer, atmospheric chemistry and transport in determining surface level PM<sub>2.5</sub> levels. Diurnal cycles of aerosol mass at surface level typically exhibit a rise during morning hours, somewhat prior to maximum photochemical activity. This time dependence

is consistent with overnight production of aerosol in the residual layer, followed by mixing from the residual layer to the surface during morning breakup of the nocturnal boundary layer as indicated by observations in the SLV of Baasandorj *et al.* [15]. Long term monitoring in Salt Lake City suggests that primary pollutants, such as CO and NO<sub>x</sub>, undergo characteristic weekday-weekend cycles seen in other locations, but that PM<sub>2.5</sub> does not have a strong weekday-weekend cycle [1]. This observation is consistent with a PM<sub>2.5</sub> reservoir buildup that lags primary NO<sub>x</sub> emissions. Together, these observations indicate that the composition of and transport within the residual layer is important to understanding the mechanism for winter PM<sub>2.5</sub> formation in northern Utah. Residual layer chemistry and transport has been identified as a factor in the buildup of ammonium nitrate aerosol in other regions, such as California's San Joaquin Valley [16-21].

A third question is the source of oxidants that convert NO<sub>x</sub> emissions to soluble nitrate and the rate at which this oxidation occurs. Because NO<sub>x</sub> is primarily emitted as nitric oxide (NO), two molecules of oxidant are required to convert NO<sub>x</sub> to HNO<sub>3</sub> by daytime photochemical reactions, R1 and R2 below.



Alternatively, 1.5 molecules of oxidant are required to convert NO to soluble nitrate via nighttime processes, with N<sub>2</sub>O<sub>5</sub> as the intermediate.



Sources of oxidants include background ozone or photochemical reactions of VOC and NO<sub>x</sub> that produce oxidants including OH and O<sub>3</sub>. If entrainment of background O<sub>3</sub> is the major source, then the oxidant limitation depends on the dynamics of the PCAP and the mixing efficiency with background O<sub>3</sub> from the free troposphere. If photochemistry is the major oxidant source, then its response to both VOC and NO<sub>x</sub> emissions becomes important, as is the case for summertime urban boundary layers. Oxidant sources may also be influenced by the interaction between the reactive nitrogen and aerosol chloride. Nighttime NO<sub>x</sub> oxidation occurs simultaneously with activation of photolabile halogen in the form of nitryl chloride (ClNO<sub>2</sub>) in regions rich in aerosol chloride [22, 23].



The recent analysis from Salt Lake City showing several μg m<sup>-3</sup> attributable to ammonium chloride aerosol, accounting for 15% of PM<sub>2.5</sub> mass, suggests that this chemistry may be particularly active in that region. If so, the atmospheric chemistry of winter PM<sub>2.5</sub> in northern Utah may be complex,

with a nighttime residual layer component and a daytime photochemical component due to atomic chlorine. Baasandorj *et al.* [15] recently suggested that the nighttime processes in the upper part of PCAPs and subsequent daytime transport of PM<sub>2.5</sub> rich air down to the surface play an important role contributing to the near surface PM<sub>2.5</sub> enhancements during these pollution episodes.

## 1.2 Meteorology of PCAPs and Exchange Processes

The Salt Lake Valley (SLV) and other Utah basins experience persistent cold-air pool (PCAP) episodes under high-pressure synoptic conditions during the wintertime [1, 24]. Under the stable atmospheric PCAP conditions, vertical mixing is inhibited and particulate pollutants accumulate and affect the population along the Wasatch Front. A major field study funded by the National Science Foundation, the Persistent Cold-Air Pool Study (PCAPS), was conducted in the SLV in 2010-2011. The goals of PCAPS were to improve understanding of the meteorological formation, maintenance, and decay of cold-air pools [24]. PCAPS data and subsequent scientific analysis resulted in improved understanding of PCAP boundary-layer structure and climatology of wintertime particulate pollution in the SLV [3, 25-28], improved understanding of the interactions between synoptic weather systems and PCAP events [29, 30], and improved numerical simulations of PCAP episodes [31-33]. The following meteorological ingredients, of which only some may be present during any given PCAP, have been found to play an important role in the lifecycle of PCAPs [24]:

### 1. PCAP formation and maintenance mechanisms:

- Cold-air emplacement in the Great Salt Lake Basin below mountaintop level from a cold low pressure system prior to PCAP onset;
- High pressure and associated subsidence temperature inversion (capping layer) that initially forms above mountaintop and descends over time;
- Snow cover leading to a higher surface albedo, decreasing the absorption of incoming solar radiation at the surface. Deep snow cover further reduces the ground heat flux, allowing for more rapid nocturnal near-surface cooling.
- Calm, clear nights that promote efficient nocturnal radiative cooling and near-surface radiative temperature inversions.
- Cold air from over the Great Salt Lake returning to engulf the SLV following partial pollution mix-out events after the passage of weak weather systems;
- Persistent stratus cloud decks that limit incoming solar radiation and redistribute radiative cooling from the surface to cloud top.

### 2. PCAP decay mechanisms:

- Synoptic westerly and southwesterly flows that slowly erode the PCAP from the top down;
- Modification of PCAP through absorption of solar radiation at the land surface;
- Cooling aloft associated with approaching storm system;
- Rapid increase in winds and decrease in temperature associated with a strong cold front (results in complete removal of PCAP in 1-2 hours).

The intensity of PCAPs is often described through the use of valley heat deficit [1] (Section 2.4.3). While the various meteorological ingredients associated with PCAPs are well-known, the relative importance of these various factors varies from PCAP episode to episode and is difficult to quantify with limited meteorological observations during non-field study periods. In addition, the relationship and complex interactions between meteorology, flow patterns within the PCAP, and the chemistry remains a major unanswered scientific question [15].

Meteorological transport and mixing processes such as horizontal and vertical advection are inhibited due to the overall stable stratification within PCAPs. Nevertheless, thermally driven flows such as downvalley and downslope, and upvalley and upslope flows [34] can be triggered by thermal contrasts within and amongst the basins and surrounding topography affected by PCAPs. Further, the thermal inertia of the Great Salt Lake results in lake breeze circulations [24, 25], while inter-basin air mass exchanges, forced by either horizontal gradients in temperature between the Utah and Salt Lake Valleys or by regional pressure gradients, are commonly observed.

The cold-air pool exchange processes resulting from diurnal mountain wind systems, inter-basin exchange, and lake breeze circulations are often weaker under PCAP than under non-PCAP conditions. Nevertheless, they are expected to influence pollutant and precursor concentrations and thus to modify chemical processes within PCAPs.

A meteorological experiment, funded by NSF (Grant # AGS-1723337) and the Utah DAQ, was conducted in January and February 2017 to allow the characterization of *Cold-Air Pool Exchange Processes* and PCAP evolution and to complement the chemical observation of UWFPS.

### **1.3 Overview of 2016-17 Winter**

Here we explore the key meteorological and chemical variables during the 2016-2017 winter and give a brief overview of the meteorological and chemical evolution of two primary PCAP episodes sampled by the NOAA Twin Otter research flights. Figure 1.3 explores the relationship between the Valley Heat Deficit (VHD) and  $PM_{2.5}$  in the SLV and helps identify 7 pollution episodes with elevated  $PM_{2.5}$ , while Figure 1.4 and Figure 1.5 compare the levels of  $PM_{2.5}$  and other species measured in three valleys. The valley heat deficit (VHD) is a measurement of the amount of energy that would be needed to bring a valley or basin atmosphere to a neutral stratification (Section 2.4.3). The upper panel of Figure 1.3 shows the time series of potential temperatures at the valley floor (~1300 m MSL) and at the mean top height of the Salt Lake City Basin, ~2200 m MSL, derived from radiosonde observations by the National Weather Service from the Salt Lake City Airport. The difference between the two curves indicates the bulk stability of the valley atmosphere. When the two curves meet, the atmosphere is referred to as neutral for dry adiabatic processes and there is no resistance to vertical mixing. The further the two curves deviate, the higher is the stability and the harder it is to mix pollutants emitted at the surface. These time series further illustrate that the strong wintertime cold pool episodes are often caused by warm air

advection aloft rather than through enhanced cooling near the surface. The bottom panel of Figure 1.3 shows the VHD together with smoothed  $PM_{2.5}$  mass loadings (red curve). The good correlation between VHD and  $PM_{2.5}$  becomes evident, and has previously been reported by Whiteman *et al.* [1].

Persistent cold air pools or PCAPs in the SLV can be defined as periods when the VHD exceeds a threshold value of  $4.04 \text{ MJ m}^{-3}$  for at least three consecutive 12-hourly atmospheric soundings [1]. This VHD threshold value corresponds to  $PM_{2.5}$  concentrations of  $17.5 \mu\text{g m}^{-3}$ , which is half of the NAAQS for  $PM_{2.5}$ . After a VHD value of  $4.04 \text{ MJ m}^{-3}$  is reached, pollution concentrations tend to increase monotonically at a rate of approximately  $10 \mu\text{g m}^{-3} \text{ day}^{-1}$  [1].

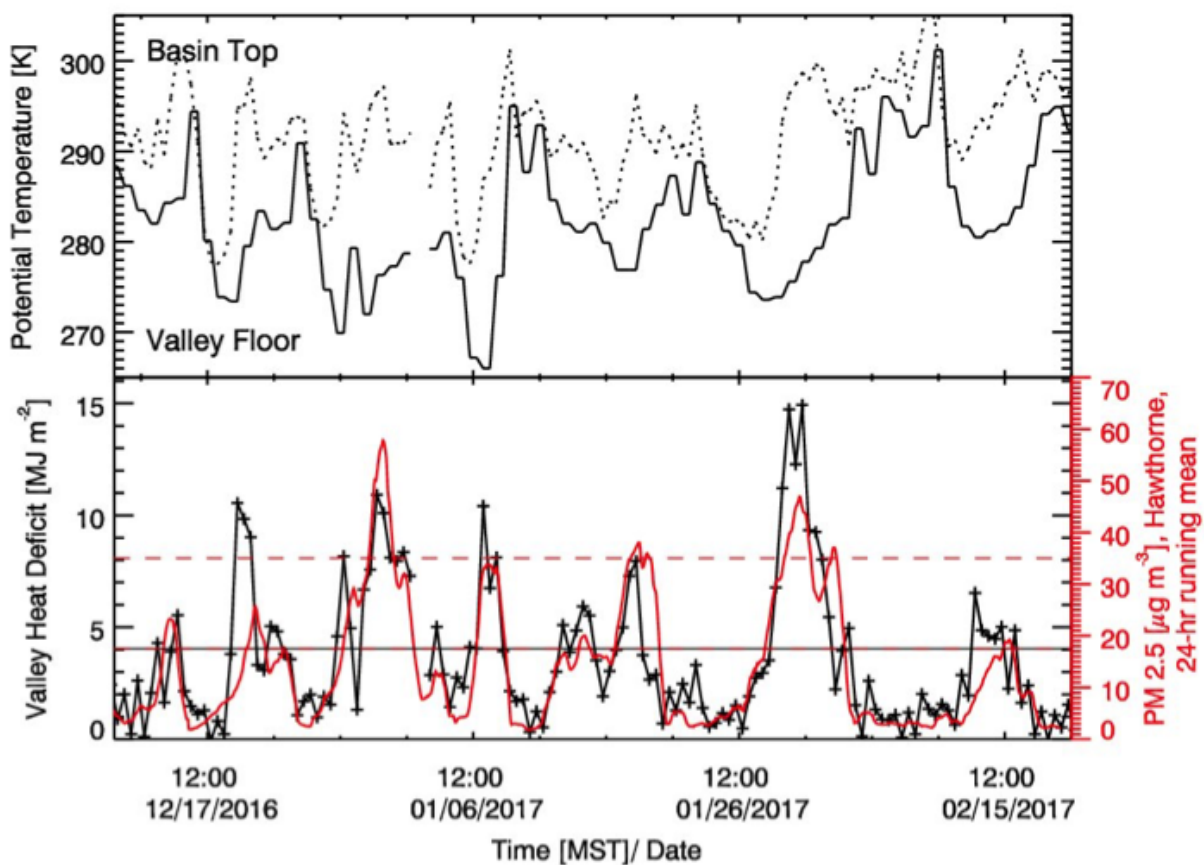


Figure 1.3 Potential temperature at the base and top of the Salt Lake City Basin from radiosonde observations by the National Weather Service (top), and the Valley Heat Deficit (VHD, black) and the smoothed observations of  $PM_{2.5}$  pollutant concentrations (red) from the UDAQ Hawthorne (HW) site. Data covers the main observational period of the experiment, from 15 December 2016 through 20 February 2017. Note that the horizontal dashed line marks the NAAQS for  $PM_{2.5}$  and the horizontal red-black dashed line marks the VHD threshold value of  $4.04 \text{ MJ m}^{-3}$  and a  $PM_{2.5}$  concentration of  $17.5 \mu\text{g m}^{-3}$ .

Seven multi-day pollution episodes with elevated  $PM_{2.5}$ , associated with stagnant conditions, were observed during the 2016-2017 winter (Table 1.1). Three of these episodes (13 - 15 December

2016, 18 - 24 December 2016, 13 - 18 February 2017) were brief with observed  $PM_{2.5}$  levels remaining below the NAAQS. There were four major pollution episodes (27 December 2016- 2 January 2017, 6 - 9 January 2017, 13 - 20 January 2017, 27 January - 4 February 2017) when  $PM_{2.5}$  levels built up to exceed the NAAQS, leading to a total of 7, 8, and 3 exceedances in Logan, Salt Lake City and Provo-NAAAs, which encompass most of Cache, Salt Lake, and Utah valleys, respectively (Figure 1.4). Figure 1.4 shows a time series of  $PM_{2.5}$  at representative sites, and shows the periods when the Twin Otter was operating in the region.

Table 1.1 Pollution episodes observed during the 2016-2017 winter

#	Dates	Intensity
1	13 - 15 December 2016	Moderate
2	18 - 24 December 2016	Moderate
3	27 December 2016 - 2 January 2017	Severe
4	6 - 9 January 2017	Severe
5	13 - 20 January 2017	Severe
6	27 January - 4 February 2017	Most persistent and severe
7	13 - 18 February 2017	Moderate

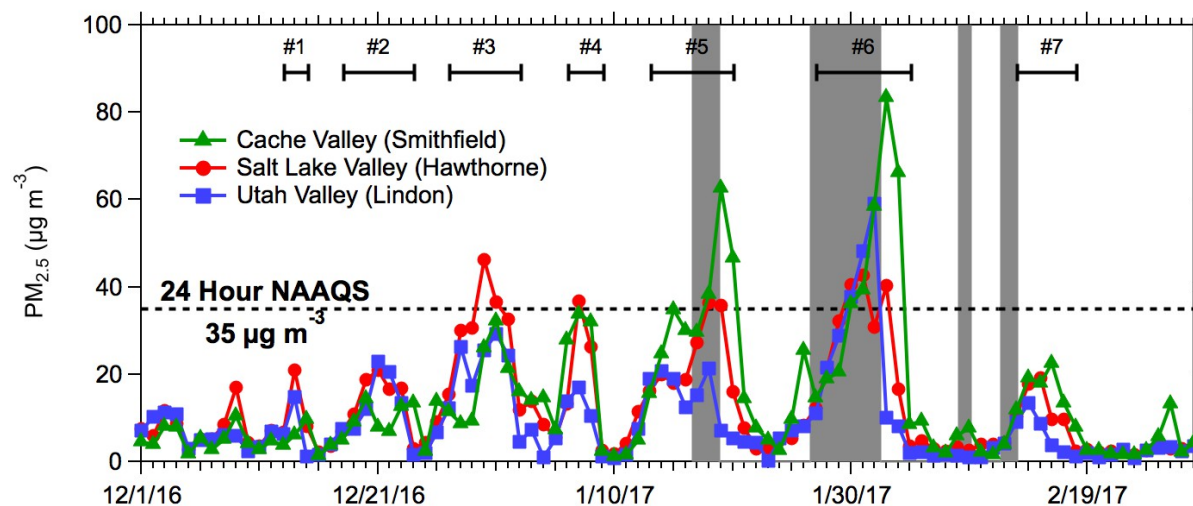


Figure 1.4 Daily average  $PM_{2.5}$  mass loadings for representative sites in each of the three valleys indicated in Figure 1.1 during the 2016 - 2017 winter (December 1 2016 - February 28, 2017). Grey shaded regions indicate the times during which the Twin Otter research flights occurred. Bars across the top indicate the pollution episodes in Table 1.1

January and February 2017 were characterized by above-average precipitation in northern Utah associated with several active storm track periods during these months (5.0 cm observed in January versus normal of 3.2 cm, 4.3 cm in February versus normal of 3.2 cm). These active storm tracks resulted in less frequent PCAP conditions than is climatologically observed.

However, the two dominating episodes during the 2016-17 winter occurred during the UWFPS period when the NOAA Twin Otter was deployed in Utah: 13 - 20 January 2017, 27 January - 4 February 2017 as shown in Figure 1.4. Temperatures were below normal in January associated with the active storm track (mean January temperature of 27.15 F versus normal of 29.75 F). In February, warm storms and periods of high pressure without snow cover resulted in higher temperatures than average (39.95 F versus normal of 34.2 F).

Snow cover is an important variable in PCAP occurrence and strength (Table 1.2). The Cache Valley saw the deepest and most persistent snow cover during the January-February 2017 period.

*Table 1.2 Snow depth in inches every three days in the three valleys during January 15th - February 15th (source cocorahs.org)*

Date	Salt Lake Valley	Utah Valley	Cache Valley
Jan 15th	0-1"	0	7-9"
Jan 18th	0	0	6-8"
Jan 21st	4-10"	2-4"	10-12"
Jan 24th	4-8"	2-4"	21-27"
Jan 27th	3-8"	2-4"	19-24"
Jan 30th	3-7"	NA	18-22"
Feb 2nd	1-5"	1-3"	18-20"
Feb 5th	0"	0"	11-15"
Feb 8th	0"	0"	6-12"
Feb 11th	0-1"	0"	3-8"
Feb 14th	0"	0"	1-3"

Meteorological summaries of the two primary episodes of the UWFPS study in the SLV are given below:

- 13 January – 21 January 2017. The pollution layer observed in this PCAP was between 400 – 800 m deep, which is significantly deeper than the typical mean depth of ~400 m for PCAPs in the SLV [28] (Figure 1.5). The factors contributing to the ‘non-classical’ behavior of this PCAP were a lack of snow cover, the relatively weak subsidence inversion with a reduced capping stability, thick clouds and associated vertical mixing below the cloud base during more than half of the episode. Wind speeds aloft remained light during this episode until strong southwesterly flow ahead of two strong storm system resulted in top-down erosion of the CAP beginning on 19 January.

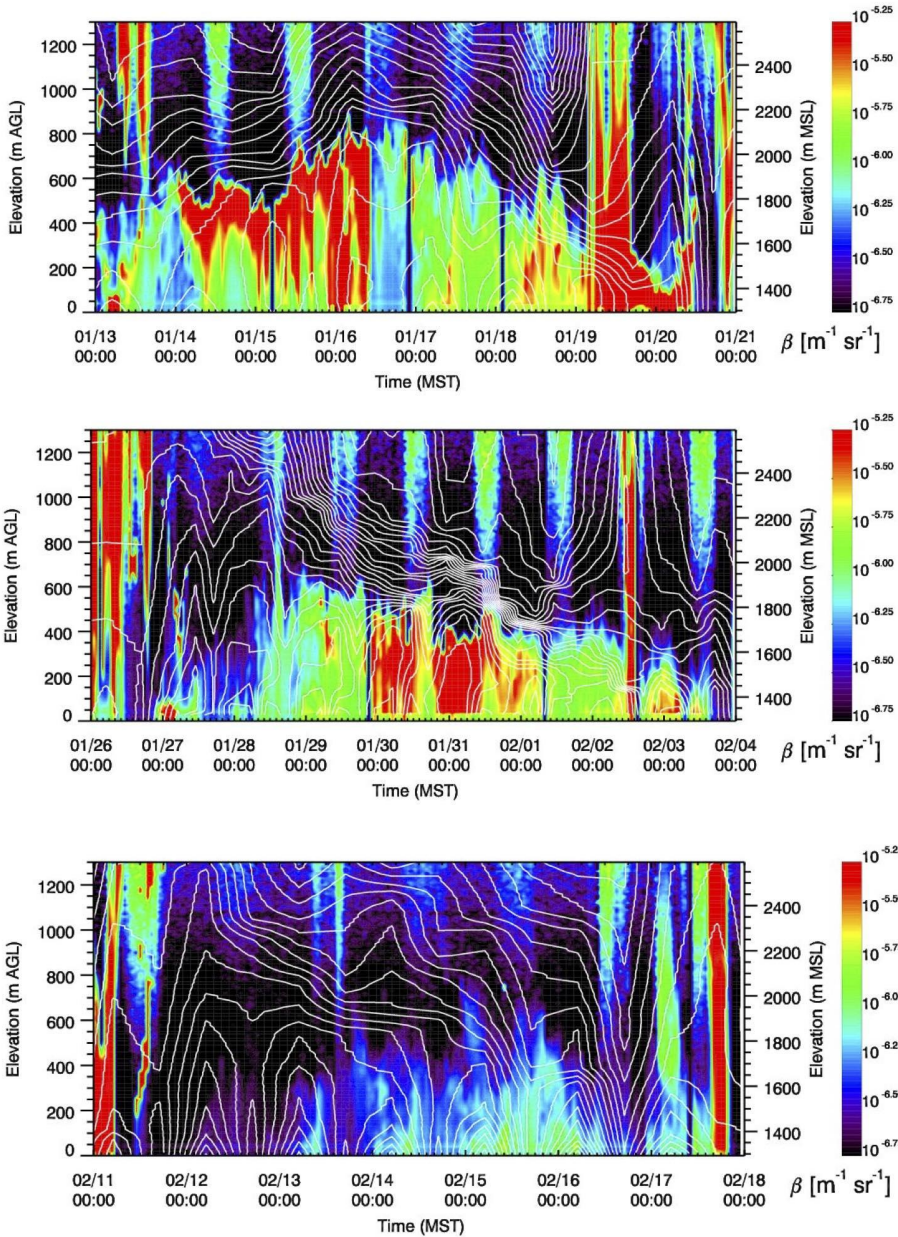


Figure 1.5 Time-height cross sections of ceilometer backscatter profile and contours of isentropes at the Landfill Site (LFL) in the Salt Lake Basin for three of the pollution episodes in early 2017. Isentropes are from KSLC radiosonde dataset. Note that some intermittent power outages occurred at the site.

- 26 January – 3 February 2017. This episode was a classic PCAP, with an onset marked by cold air left in place by a storm system and several inches of fresh snow on the ground, followed by a large high pressure ridge over the Western USA. A subsidence inversion associated with the high pressure system descended from ~1200 m AGL on 27 January

to near 400 m AGL by 1 February. This capping layer confined the pollution layer below the base of the descending stable layer, as illustrated by ceilometer backscatter (Figure 1.5). A period of low clouds developed in the Great Salt Lake Basin and SLV in the middle of the episode (30 Jan – 1 February), decreasing nighttime stability and increasing sub-cloud turbulent mixing. Winds above the stable layer at 700 hPa were generally light from 27 January – 30 January, but increased above  $10 \text{ m s}^{-1}$  from the 31<sup>st</sup> January until the end of the episode, eroding the polluted stable layer in the SLV to only 100-200 m by the 3<sup>rd</sup> of February. The end of the episode was further complicated by air mass exchanges with the Great Salt Lake (Section 5).

Figure 1.6 provides an overview of the chemical conditions for Logan (L4) and Smithfield (SM) in the Cache Valley, Hawthorne (HW) and University of Utah (UU) in the SLV, North Provo (NP) and Lindon (LN) located in Utah Valley during UWFPS (See methods section for site description).

As shown,  $\text{PM}_{2.5}$ ,  $\text{PM}_{10}$ , and  $\text{NO}_x$  are enhanced at all measurement sites during the pollution episodes. Although the pollution typically starts building around same time in the three valleys, the end dates can vary due to the meteorological processes leading to a well-mixed atmosphere and the differences in the topographic sheltering of the three basins. Typically, the valley cold pools are first eroded in Utah Valley, followed by a mix-out in the SLV, while the pollution episodes tend to persist the longest in Cache Valley. A consistent pattern was observed during the two major episodes of UWFPS. The pollution episodes were persistent and most severe in the Cache Valley where a steady, continuous buildup and the highest  $\text{PM}_{2.5}$  with 24-h values reaching up to  $80 \mu\text{g m}^{-3}$  were observed. Similarly,  $\text{PM}_{2.5}$  in the Utah Valley built up steadily reaching up to 24-h value of  $60 \mu\text{g m}^{-3}$  until the mix-out that occurred first in the Utah Valley. In contrast,  $\text{PM}_{2.5}$  in the SLV reached a plateau with a 24-h value of approximately  $45 \mu\text{g m}^{-3}$  after a steady increase over first four days of the 27 January - 4 February 2017 episode. This pattern appears to be quite common and seen in the long-lasting episodes of the past [15].  $\text{PM}_{2.5}$  and  $\text{PM}_{10}$  are well correlated with  $\text{PM}_{2.5}$  constituting  $\sim 70 - 85\%$  of  $\text{PM}_{10}$  during pollution episodes.

$\text{NO}_x$  levels as high as 200 ppbv are observed in urban Utah and Salt Lake Valleys. They appear to be lower in the more rural Cache Valley as indicated by SM measurements, but values as high as 150 ppb are seen in Logan at the end of the 27 January - 4 February 2017 episode. As expected,  $\text{O}_3$  is lower and often depleted at night at more urban sites (Logan in Cache, sites in the Salt Lake and Utah valleys) during pollution episodes. Peak  $\text{O}_3$  during the day is 40 - 50 ppb outside the pollution episodes, consistent with the wintertime background  $\text{O}_3$  in Utah [35], but it decreases to values as low as 10 - 20 ppb later in the pollution episodes. Compared to Logan, higher  $\text{O}_3$  is observed at the more rural SM site. Similarly,  $\text{O}_3$  is higher at UU, a site on the valley sidewall, than that at HW, a site located in the urban corridor of the SLV. These observations indicate spatial, temporal and vertical variability of chemical conditions that exist within each valley and among the three valleys.

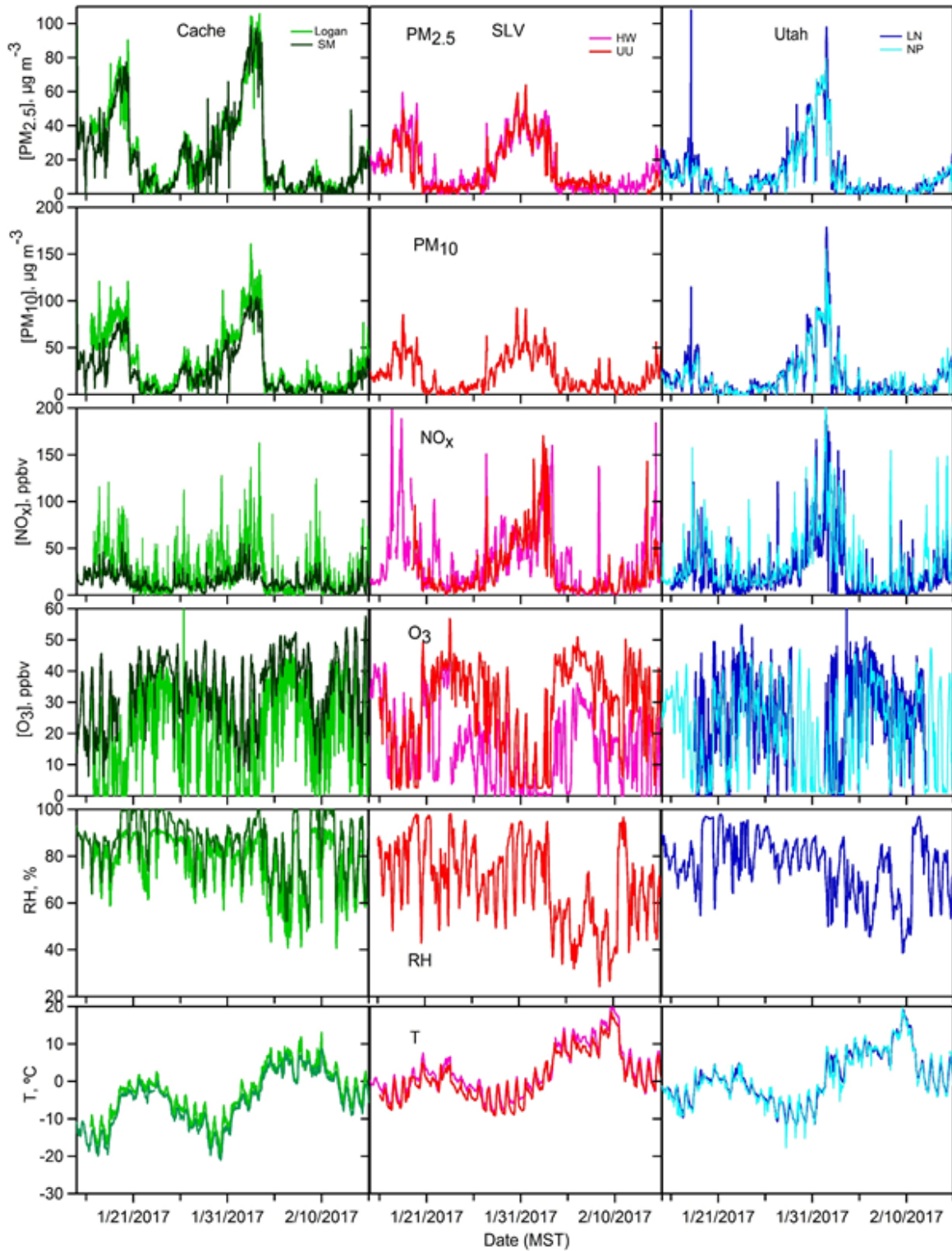


Figure 1.6 Time series of  $PM_{2.5}$ ,  $PM_{10}$ ,  $NO_x$ ,  $O_3$ , RH and T for representative sites in each of the three valleys during the UWFPS (January 15 - February 15, 2017).

## 1.4 Scientific Questions and Study Goals

The 2017 Utah Winter Fine Particulate Study (UWFPS) was designed to address major questions with respect to ammonium nitrate aerosol formation in the stable, polluted boundary layers associated with the valleys of northern Utah. The study design was based on the use of a light aircraft, the NOAA Twin Otter, to probe the horizontal and vertical distribution of trace gases and aerosols important to ammonium nitrate. Ground based measurements within the different valleys augmented the aircraft data and provided continuous measurements during both clean and polluted conditions. Major scientific goals and questions are outlined below.

*Question 1.* What is the spatial distribution, both vertically and horizontally, of key trace gases and aerosols related to PM formation? What are the limiting and excess reagents in ammonium nitrate formation, and what are the key source regions? What are the limiting and excess reagents in oxidant and nitric acid formation? Do these limitations and / or sources vary significantly across the region?

Emissions within the three major valleys of the Wasatch Front are expected to be heterogeneous, with the largest urban emissions in the SLV and the largest agricultural emissions in the Cache Valley. Aircraft flights across all 3 valleys at different times of day characterize the spatial distribution of  $\text{NH}_3$ ,  $\text{HNO}_3$  and  $\text{NO}_x$ , together with intermediates in  $\text{NO}_x$  oxidation. Aircraft measurements at different times of day characterize transport of trace gases and aerosols, to assess the efficiency of residual layer transport in the distribution of pollutants and / or inter-valley coupling.

*Question 2.* How do these distributions and the associated chemistry vary as a function of time of day? What are the most important chemical mechanisms for ammonium nitrate aerosol?

Morning, afternoon and night flights characterize the chemical and meteorological evolution of boundary layer breakup, re-establishment, and overnight residual layer chemistry and transport. Rates of chemical reactions may vary with altitude and time of day. Vertical profiles probe this chemical composition and boundary layer structure.

*Question 3.* What is the role of the Great Salt Lake and Utah Lake, both chemically and meteorologically, in regional air quality? Are they significant sources of aerosol chloride that interacts with nitrogen oxide chemistry? Do they play a role in transport and /or storage of polluted air masses?

Flights over the region's lakes at various altitude characterize the transport of pollutants and chemical composition at different altitudes.

*Question 4.* Are there significant aerosol sources other than ammonium nitrate? What is the role of, for example, residential wood combustion as a source for organic aerosol?

Aircraft based aerosol composition data provides new detail to the measurement of organic aerosol composition to the northern Utah valleys. Iodide CIMS measurements provide organic and nitrogen containing compounds characteristic of residential wood combustion.

*Question 5.* What are the key emission sectors for aerosol precursors? What is the role of agricultural, industrial, urban, home heating, and natural emissions?

Aircraft measurements can be compared to emissions inventories developed by UDAQ to assess the emission sources responsible for PM<sub>2.5</sub>. This comparison will benefit from local 3-D air quality modeling capabilities of investigators in Utah, at the EPA and at NOAA.

The remainder of this report is structured as follows. Section 2 provides the details of the methods employed for respective measurements and models. Sections 3-7 explore observations of aerosols and trace gases, limiting and excess reagents for ammonium nitrate, exchange processes, and emissions in detail by combining the aircraft and available ground-based observations to answer the key questions outlined above. Section 8 discusses the policy implications of the major findings of this study. Finally, Section 9 concludes the report by summarizing the unanswered questions and requirements for future air quality studies in the region.

## 2 Methods

### 2.1 Twin Otter Measurements

The NOAA Twin Otter aircraft carried a scientific instrument payload that was designed to characterize sources and chemistry related to ammonium nitrate aerosol formation. The flight plans were further designed to encompass all of the major air basins in northern Utah that experience high winter PM<sub>2.5</sub> pollution and to provide horizontal and vertical distributions of the most important trace gases and aerosols. This section will first describe the scientific instruments and then the flight strategy.

#### 2.1.1 Instrument Payload

Table 2.1 shows the Twin Otter atmospheric chemistry instruments. Figure 2.1A shows the layout of the instrumentation in the aircraft, and Figure 2.1B shows the instrumentation inside the aircraft and the positioning of inlets outside of the aircraft.

Aerosol was sampled using the perpendicular near-isokinetic inlet described and characterized in Perring *et al.* [36] that was modified to accommodate a 3 liter per minute (LPM) total inlet flow and the lower cruise speed of the Twin Otter. The sample air was split between the AMS and the UHSAS instruments, described below.

The Aerosol mass spectrometer (AMS, Aerodyne Research) measures the chemical composition of the non-refractory mass of sub-micron aerosol particles. The working principle of the AMS is to 1) focus ambient aerosols with an aerodynamic lens 2) evaporate the aerosol particles by heating them at 600°C 3) analyze the evaporated molecules with an electron-impact ionization mass spectrometer. When the mass spectra are recorded as a function of time only the AMS is used in MS mode. Additionally, with any AMS it is also possible to measure mass spectra as a function of particle size (pTOF mode). The size information is retrieved by measuring the aerosol time of flight from a chopper, located after the aerodynamic lens, to the mass spectrometer [37-39]. A pressure-controlled inlet was used to maintain a constant mass flow rate into the instrument as the aircraft changed altitude [40]. The NOAA AMS deployed on the Twin Otter aircraft is also equipped with a light scattering (LS) module that provides a more accurate size information in the range 200-1000 nm and on the collection efficiency [41]. The average limit of detection for NO<sub>3</sub><sup>-</sup>, NH<sub>4</sub><sup>+</sup>, Org, SO<sub>4</sub><sup>-2</sup>, Cl<sup>-</sup> and for the total aerosol mass were 0.04, 0.09, 0.33, 0.03, 0.07, 0.38 μg m<sup>-3</sup> respectively. The uncertainty on the concentrations is estimated to be 20% [42]. The TO-AMS was operated in MS mode (6 seconds, 4 open+2 closed) and pTOF mode (4 seconds) in 27 sub-cycles of 10 seconds total. We measured in LS mode for 30 seconds every 4.5 minutes. The aircraft AMS measurements are reported in units per standard cubic meter of air (sm<sup>-3</sup>), where standard conditions are 273 K and 1 atm.

The Ultra High Sensitivity Aerosol Spectrometer (UHSAS) is an optical-scattering based aerosol spectrometer to measure aerosol size distributions. The aerosol particles enter the instrument and scatter the light produced by a solid-state laser (1054 nm, 1 kW cm<sup>-2</sup>). Mirrors capable of collecting light over a large solid angle (22°–158°) direct the scattered light to two different photodiodes. An avalanche photodiode (APD) for detecting the smallest particles and a low-gain PIN photodiode for detecting particles in the upper size range. The signals generated by the scattered light are used for particle sizing, since the amount of light scattered correlates strongly with particle size [43]. The data during the UWFPS were collected every 3 s and they were corrected for coincidence and for changes in the UHSAS inlet flow [44].

The University of Washington's high-resolution iodide time-of-flight chemical ionization mass spectrometer (I<sup>-</sup> ToF CIMS) is capable of online, fast-time response measurements of a suite of reactive inorganic gaseous halogen (Cl<sub>2</sub>, Br<sub>2</sub>, ClNO<sub>2</sub>, etc.) and nitrogen oxide (N<sub>2</sub>O<sub>5</sub>, HNO<sub>3</sub>, HONO, etc.) species. The spectral resolution and simultaneous acquisition across a wide mass-to-charge range provide molecular composition information of individual species and their isotopologues, all clustered with the iodide reagent ion. The major components of the I<sup>-</sup> ToF CIMS were as first described by Lee *et al.* [45] with upgrades implemented to improve in-flight calibration and sampling protocol Lee *et al.* [46].

The NOAA custom-built, nitrogen oxide cavity ring down spectrometer (NOxCARD) measured nitrogen oxides (NO, NO<sub>2</sub>) total reactive nitrogen (NO<sub>y</sub>) and ozone (O<sub>3</sub>) with 1 second time resolution. The instrument measures NO<sub>2</sub> by optical absorption at 405 nm, and quantitatively converts NO and O<sub>3</sub> into NO<sub>2</sub> by reaction with excess O<sub>3</sub> or NO, respectively, in two separate channels [47, 48]. A fourth channel converts NO<sub>y</sub> to NO and NO<sub>2</sub> by thermal dissociation in a quartz inlet at 650 °C and subsequently converts NO to NO<sub>2</sub> in excess O<sub>3</sub> [49]. The measurement precision is 50 pptv or better, but zero uncertainty can be as large as 0.2 ppbv.

A continuous wave Quantum Cascade Tunable Infrared Laser Differential Absorption Spectrometer (QC-TLDAS, Aerodyne Research Inc.) measured ammonia (NH<sub>3</sub>) [50]. Prior to installation, the instrument was optimized for a lower total weight. Ambient air was aspirated at a flow rate of 4 LPM through a multi pass absorption cell (0.5 L, 76 effective path length) and NH<sub>3</sub> absorption was detected at 965.3 cm<sup>-1</sup> during the experiment. Particulate matter was filtered by a PFA (Teflon) impactor and an additional bypass flow rate of 16 LPM was introduced to purge the 0.5 m long inlet line. The precision of the instrument at 1 Hz sample frequency during the UWFPS campaign was significantly degraded from its usual performance due to difficulties with the laser source. Precision achieved during UWFPS was 150 ppt (1σ). The limit of detection (3σ) was 450 ppt at the 1 Hz sample frequency and 90 ppt for a 30 s averaging interval.

A commercial met probe (Avantech) measured meteorological parameters (T, P, RH, winds) GPS location and aircraft parameters (heading, pitch, roll, etc). Wind data were compromised for some flights, making only partial coverage available.

The total scientific instrument payload was approximately 1500 lbs., including support equipment (gas cylinders, pumps, etc.) and inlets, as Table 2.1 shows. The allowable payload was defined by target aircraft endurance (see further below under flight planning) of 3 hours per flight, determined by the amount of fuel at takeoff, and the requirement for two pilots and two scientific operators.

Table 2.1 NOAA Twin Otter Instrumentation

Instrument	Species Measured	Institution	Power (kVA)	Weight (lbs.)	Precision	Accuracy	Ref
AMS <sup>a</sup>	Aerosol composition	NOAA	1.1	560	<0.4 $\mu\text{g m}^{-3}$	20%	[51]
UHSAS <sup>b</sup>	Aerosol size distributions	University of Toronto	0.1	50			[44]
I <sup>-</sup> ToF CIMS <sup>c</sup>	HONO, HNO <sub>3</sub> , N <sub>2</sub> O <sub>5</sub> , ClNO <sub>2</sub> , Halogens	University of Washington	1.7	380	1-15 pptv	30%	[45]
NO <sub>x</sub> CaRD <sup>d</sup>	NO, NO <sub>2</sub> , NO <sub>y</sub> , O <sub>3</sub>	NOAA	0.5	280	50 pptv	NO, NO <sub>2</sub> , O <sub>3</sub> 5%, NO <sub>y</sub> 12%	[49]
QC-TDLAS <sup>e</sup>	NH <sub>3</sub>	University of Toronto	1.0	230	150 pptv		[50]
Met Probe	T,P Winds, GPS,	NOAA	0.3	20			
Total			4.7	1520			
Twin otter capacity			~ 7	1500			

<sup>a</sup> Aerosol mass spectrometer

<sup>b</sup> Ultra high sensitivity aerosol spectrometer

<sup>c</sup> Iodide ion time of flight chemical ionization mass spectrometer

<sup>d</sup> Nitrogen oxide cavity ring down spectrometer

<sup>e</sup> Quantum cascade tunable diode laser absorption spectrometer

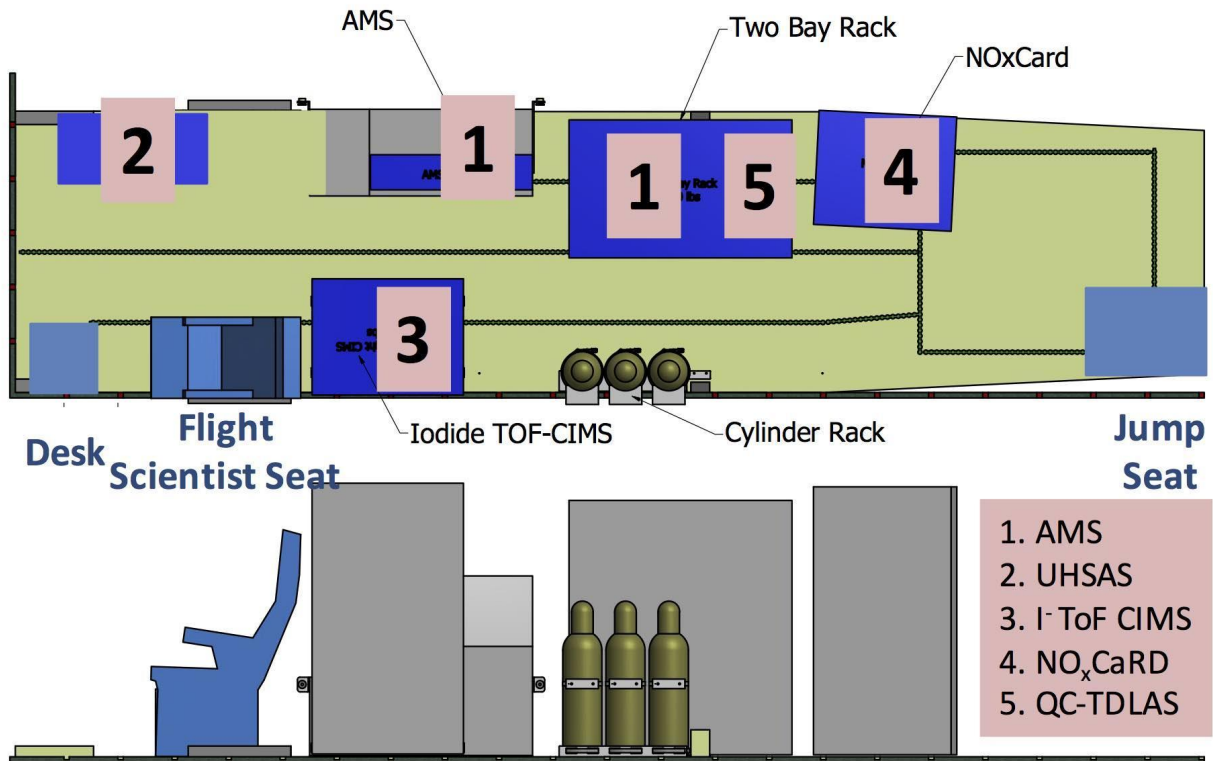


Figure 2.1 Instrument layout inside the Twin Otter showing the location of the scientific instruments and the location of the seats for the flight scientist and a second scientist (jump seat).

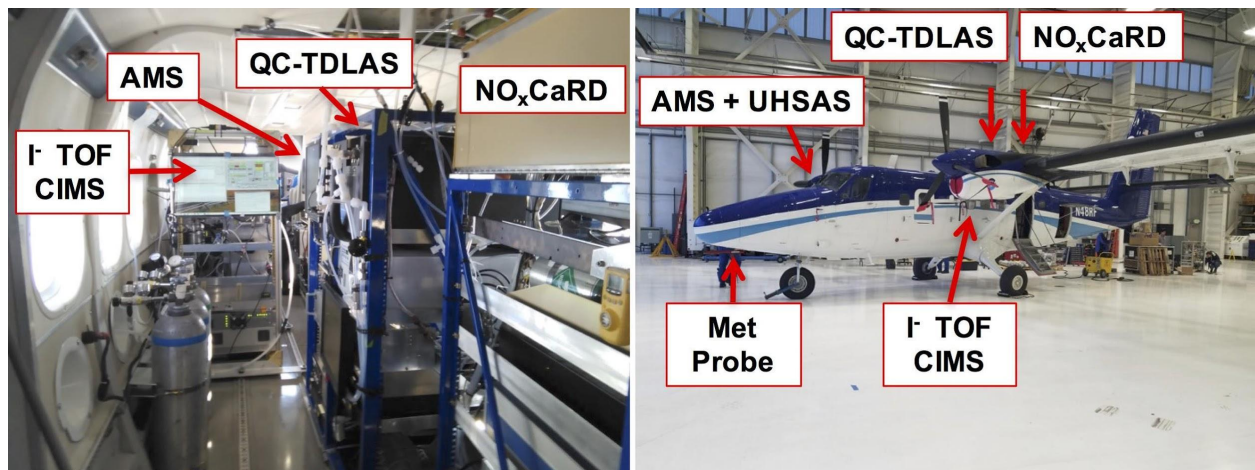


Figure 2.2 Left: Photograph of the scientific instrument payload inside of the aircraft (photograph taken from the rear of the aircraft, facing forward). Right: Indication of the locations of sample inlets. The AMS + UHSAS shared a custom aerosol inlet on the right side of the aircraft, while the I ToF CIMS sampled from a custom gas phase inlet on the left side. Both NO<sub>x</sub>CaRD and the QC-TDLAS instruments sampled through upward facing inlets mounted on the top of the aircraft.

### 2.1.2 Twin Otter Flight Strategy

The Twin Otter was based at TAC air at the Salt Lake City international airport (KSLC). The flight strategy consisted of two flight plans, generally executed sequentially, to achieve coverage of the major air basins in northern Utah, as Figure 2.3 shows. The two flight plans were each 2.5 - 3 hours in duration. Landing, refueling and taking off typically required one hour in between the two flights. Thus, a flight day with full coverage of both flights was approximately 6 - 7 hours in total duration. The two plans were not always flown in the same order or at the same time of day, as Table 2.2 shows. Variation in takeoff time was intended to characterize photochemistry, nighttime chemistry and the morning periods when both boundary layer structure and photochemistry are in transition. As the table shows, however, most of the flights during polluted periods took place in afternoon and evening. This was a logistical constraint imposed by fog that precluded flights during morning hours during severely polluted conditions (e.g., January 30), and due to the loss of flight hours at the conclusion of the second PCAP because of a bird strike on February 1. The bird strike required an approximately 1-week maintenance period for repairs, during which time conditions changed from polluted to clean. Weather conditions also required deviations from the nominal flight plans on some days, especially in the case where a low cloud ceiling prevented ascending to the maximum altitude (12,500 ft / 3.8 km for the unpressurized cabin without oxygen) for the Twin Otter. On flight days with lower ceilings, the Twin Otter sampled the same air space at low altitude but did not profile to higher altitude.

The Twin Otter sampled through an altitude range from ground level at Salt Lake International Airport (1288 m / 4225 ft above sea level, ASL) through 3800 m / 12,500 ft. ASL. Most of the level cruising legs were at altitudes near 300 m / 1000 ft. above ground level (AGL) in order to sample within the relatively shallow boundary layers in the major valleys during PCAPs. The flight patterns took advantage of airfields throughout the region to execute missed approaches that brought the aircraft near ground level, often within 10 m of the runways. Figure 2.3 shows the location of these airfields and plots of aircraft altitude vs. elapsed time. The maximum operational altitude of 3800 m was defined by safety of operation without oxygen in the unpressurized cabin. Spiral ascents on each flight plan took the aircraft to this altitude. These spirals occurred on the north flight plan over the Wasatch Mountains between Brigham City and Logan and over the Oquirrh Mountains between Bolidner (Tooele Valley) and Salt Lake. The south flight plan included one spiral ascent over the Traverse Mountains between the SLV and Provo. This altitude sampled the free troposphere under all conditions and helped to define the strength of meteorological inversions as well as the levels of background ozone above the valleys.

The Twin Otter executed 23 successful research flights across 13 flight days, capturing moderate to severe pollution events and one clean period. With the exception of one flight for which the ammonia instrument was unavailable due to an issue with its laser, all instruments reported data for all 23 flights.

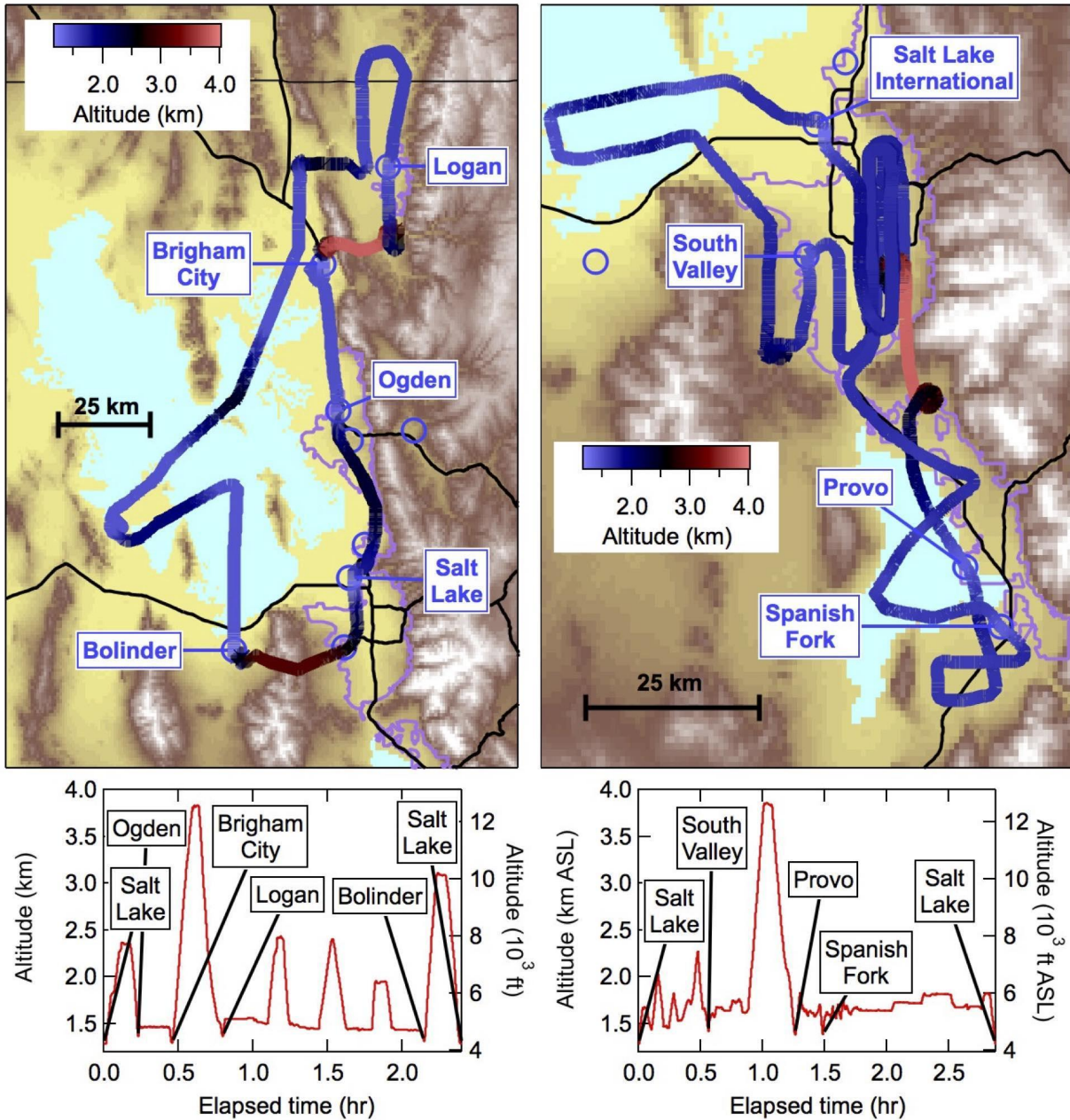


Figure 2.3 Example Twin Otter flight patterns. Flight tracks are from January 18, 2017, and are color coded by altitude above sea level as the legend shows. Blue circles indicate locations of airfields throughout the region where the Twin Otter executed missed approaches. The left panel shows the north flight plan that covered the north metro areas along the east side of the Great Salt Lake, the Cache and Bear River Valleys, Great Salt Lake and the Tooele Valley. The right panel shows the south flight plan that covered the southern end of Great Salt Lake, and the Salt Lake and Utah Valleys. Bottom panels show aircraft altitude (left axes = km, right axes = feet) against elapsed flight time, with locations of missed approaches corresponding to the airfields in the upper panels.

Table 2.2 NOAA Twin Otter flights during UWFPS

Date	Flight #	Takeoff (MST)	Duration (hours)	Flight Plan	Time of Day	Conditions/ episode number	Notes
Jan 16	1	14:34	2.6	North	Afternoon	#5	
Jan 17	2	14:15	2.6	South	Afternoon	#5	
	3	18:06	2.7	North	Evening	#5	
Jan 18	4	13:54	2.4	North	Afternoon	#5	
	5	17:39	2.9	South	Evening	#5	
Jan 26	6	14:34	2.7	North	Afternoon	Mod. Polluted	
	7	18:19	2.3	South	Evening	Mod. Polluted	Low ceiling
Jan 27	8	11:00	3.1	South	Midday	#6	
	9	15:03	2.7	North	Afternoon	#6	
Jan 28	10	17:37	2.8	North	Evening	#6	
	11	21:17	3.3	South	Night	#6	
Jan 30	12	07:30	1.2	South	Morning	#6	Fog
	13	11:36	3.1	North	Midday	#6	
Jan 31	14	11:56	3.1	South	Midday	#6	
	15	15:57	1.6	North	Afternoon	#6	
Feb 1	16	11:19	0.9	North	Midday	# 6	Bird strike
Feb 8	17	02:10	2.7	North	Night	Clean	Low ceiling
	18	05:56	2.9	South	Morning	Clean	Low ceiling
Feb 9	19	00:30	2.5	South	Night	Clean	Low ceiling
Feb 11	20	16:56	2.6	North	Evening	Mod. Polluted	
	21	20:32	2.9	South	Night	Mod. Polluted	
Feb 12	22	19:15	2.2	North	Evening	Mod. Polluted	
	23	22:39	2.5	South	Night	Mod. Polluted	

## 2.2 Balloon Observations

Weber State University's tethered balloon system was used to measure an air column from ground level to 500 feet (150 m) above ground. Balloon flight operations were located approximately halfway between Logan and Salt Lake City near UDAQ's Ogden station (Figure 2.6) and 1.25 miles (2.02 km) from the end of the runway used by the NOAA Twin Otter when making missed approaches at the Ogden airport (Figure 2.3). Each flight lasted approximately six minutes including a two minute pause at the high point. A total of 114 flights were completed during 14 operational periods. The operational periods were selected to sample the air at sunrise, mid-afternoon, and sunset. Because the afternoon data showed no strong altitude dependence and the sunset data had no obvious patterns, resources were concentrated mostly on the sunrise operational periods.

The primary target was ozone, as such the balloon hoisted an electrochemical cell (ECC) ozonesonde, EN-SCI model 2ZV7-ECC, attached to an iMet model 1-RSB radiosonde on every flight. Ozone concentrations were calculated from the raw data using the NOAA SkySonde client software. Each flight carried a second payload that was either a Met One GT-526 particle counter, a prototype of a custom-made device we call the AtmoSniffer, or a set of cameras.

The GT-526 is a six-channel nephelometer measuring particle size from 0.3 $\mu\text{m}$  to 10 $\mu\text{m}$ . The channel counts are cumulative, thus the first channel contains counts of all particles from 0.3 $\mu\text{m}$  through 10 $\mu\text{m}$ , the second channel is 0.5 $\mu\text{m}$  through 10 $\mu\text{m}$ , the third channel is 0.7 $\mu\text{m}$  - 10 $\mu\text{m}$ , etc. The remaining channels do the same starting at 1.0 $\mu\text{m}$ , 2.0 $\mu\text{m}$ , and 5.0 $\mu\text{m}$ , respectively. Two identical GT-526 units were used. One unit was only for flight and one unit was gently handled to ensure that it maintained calibration. Each day the two units were operated next to each other for a few minutes to verify that they were in reasonable agreement. As a further check on the data the particle counts were compared to the UDAQ O<sub>2</sub> PM<sub>2.5</sub> data. Exact comparisons are not possible as the particle size ranges are different and the units and method of measurement are different. However, the trends were consistent between the GT-526 counts (near ground level) and the reported mass densities from the UDAQ O<sub>2</sub> instrumentation. The evidence indicates that the flight unit (whose data are reported here) maintained its calibration during the UWFPS study period.

The AtmoSniffer is a prototype instrument that we are developing as a lightweight device that can be flown under balloons or drones. It includes multiple measurements including PM, O<sub>3</sub>, NH<sub>3</sub>, NO<sub>2</sub>, CO, and SO<sub>2</sub>. Due to the prototype status of the AtmoSniffer, these values are considered uncalibrated. There was also an issue with sensor warm-up time that was being investigated. The result is that the AtmoSniffer data will only be provisional and can only be used for general trends at this point.

The cameras varied between flights both in model and orientation. The goal was to measure transparency of the atmosphere by looking at high-contrast targets. No data will be reported from this effort as a method of calibration has yet to be developed.

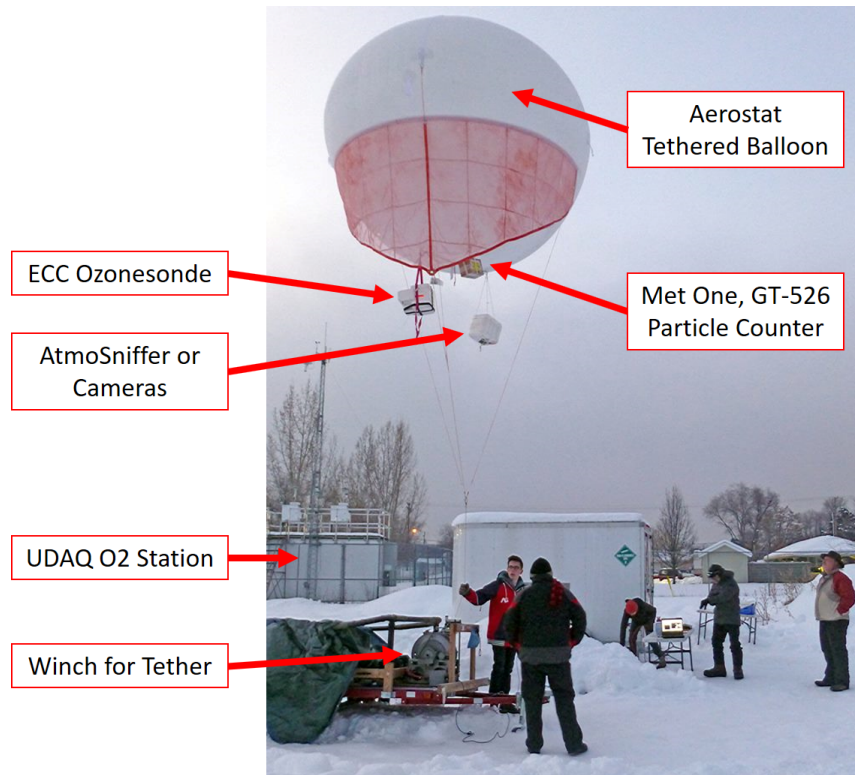


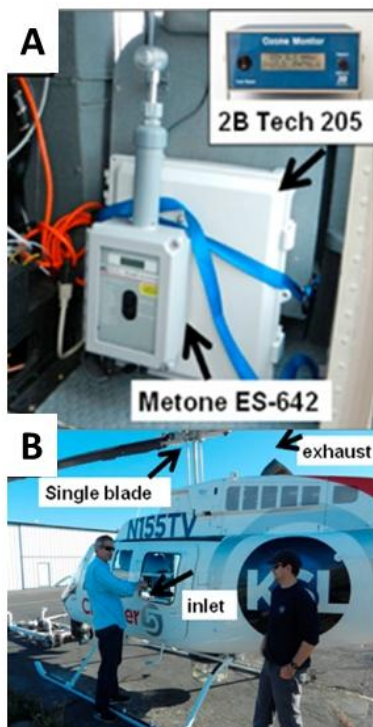
Figure 2.4 The tethered balloon platform carried an ozonesonde on every flight with other payloads alternating between flights. The launch point was collocated with the Utah Division of Air Quality Ogden O<sub>2</sub> ground station to provide a calibration reference. The winch raised and lowered the balloon from ground to 500 feet (150 m) high, then back down. Each flight lasted approximately 6 minutes.

## 2.3 News Helicopter Observations

The UU research group has partnered with KSL-TV and installed particulate and ozone pollution monitoring instruments on the KSL Chopper [52]. This measurement project began in June 2015 and is ongoing. The helicopter was outfitted with air quality instruments beginning in June 2015 (Figure 2.5). The goal of the helicopter air quality monitoring is to provide near real-time mapping of large horizontal and vertical gradients in pollution for government forecasters and the public. The following instruments were installed on the helicopter:

- **PM<sub>2.5</sub>**: ES-642 dust monitor with PM<sub>2.5</sub> cyclone from Met One Instruments Inc. measures particulate concentration using laser nephelometer (precision: 3 µg/m<sup>3</sup>, uncertainty: 8% of NIOSH 0600).
- **O<sub>3</sub>**: Model 205 Dual Beam Ozone Monitor (O<sub>3</sub>) from 2B Technologies (precision: 2% uncertainty: 2%). It uses UV absorption at 254 nm and this method is approved by EPA as a Federal Equivalent Method (FEM).
- **Atmospheric pressure**: Campbell Scientific 106 Barometer (pressure) (precision: 0.03 hPa, uncertainty: 0.3–1.5 hPa).

- **Data logging:** Campbell Scientific CR1000 data logger.
- **GPS:** Garmin GPS18X-5HZ 010-00321-37 GPS Receiver.



The CR1000 datalogger collects samples from the ES-642 (PM<sub>2.5</sub>), 2B 205 (O<sub>3</sub>), CS 106 barometer, and the Garmin GPS18X-5HZ every 2 s, and then averages and logs observations every 10 s. A Sierra Wireless Airlink Raven XT cellular modem is used to transmit 10-s data observations to the University of Utah Center for High Performance Computing every 5 min. The on-board pressure sensor is also utilized to restrict cellular communications when the helicopter flies at higher altitudes. The transmitted data is then processed for near-real time display at the following website:

<http://meso2.chpc.utah.edu/aq/>

Data download page at: [http://meso2.chpc.utah.edu/gslso3s/cgi-bin/mobile\\_data.cgi](http://meso2.chpc.utah.edu/gslso3s/cgi-bin/mobile_data.cgi)

Plot archive at <http://meso2.chpc.utah.edu/aq/cgi-bin/map.cgi>

*Figure 2.5 The KSL-TV helicopter with inlet location shown (top, A) and instrument box (bottom, B).*

## 2.4 Ground Site Network

As part UWFPS, a wide suite of trace gas, particulate and meteorological observations were made at five sites located in Cache, Salt Lake, and Utah Valley (Figure 2.6). Sections below describe the ground site network in detail and Table 2.3 - Table 2.10 provide a summary of measurements made in each valley.

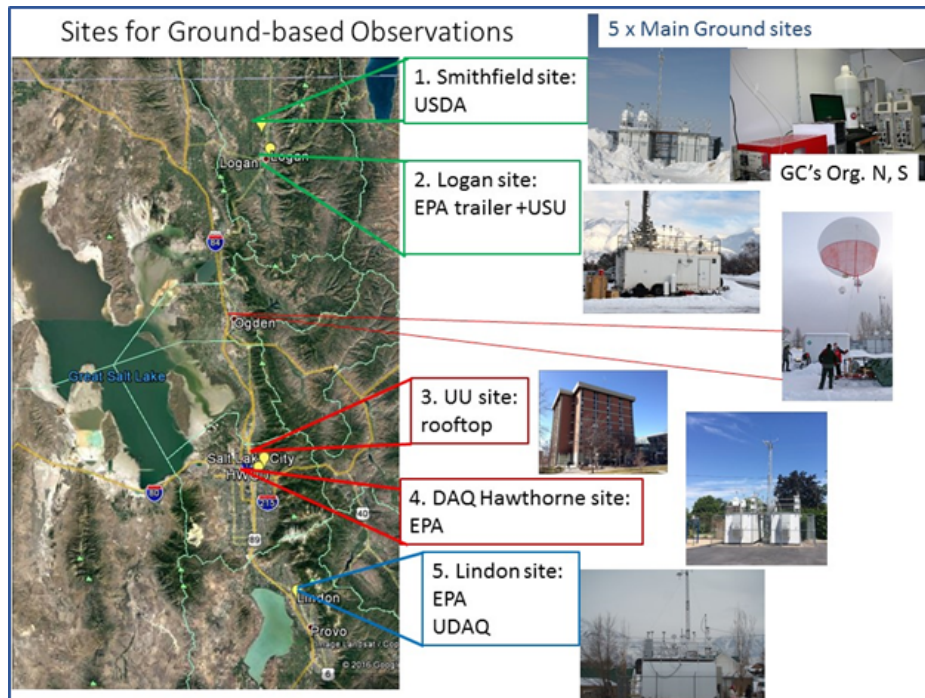


Figure 2.6 Map showing the locations of the ground-based observation sites and the tethered-balloon deployment.

## 2.4.1 Cache Valley Sites

### Logan (L4) site

EPA and Utah State University (USU) measurements in the Cache Valley during UWFPS were conducted at a temporary sampling station located on the Utah State University campus in Logan, UT (41°45'31.95"N, 111°48'54.44"W). EPA analyzers and samplers operated during UWFPS are listed in Table 2.3 along with the analyzer/sampler operation principle designation information (EPA Federal Reference or Equivalent Method number).

Table 2.3 EPA/USU Analyzers/Samplers Operated during UWFPS at Logan, UT

Manufacturer and Model	Operation Principle	FRM/FEM Designation No.
<b>Trace Gas</b>		
2B Technologies Model 211 (Ozone)	UV Photometric	EQOA-0514-215
Teledyne API T500U (NO <sub>2</sub> )	Cavity Attenuated Phase Shift (CAPS) Spectroscopy	EQNA-0514-212

Teledyne API T200U (NO, NO <sub>2</sub> , NO <sub>x</sub> )	Chemiluminescence	RFNA-1194-099
Teledyne API T200U NO <sub>y</sub> (NO, NO <sub>y</sub> )	Chemiluminescence	NA
Aerodyne CIMS	Chemical Ionization (I <sup>-</sup> ) Mass Spectrometry (CIMS)	NA
Picarro G2508 CRDS (NH <sub>3</sub> , CH <sub>4</sub> , CO <sub>2</sub> )	Cavity Ringdown Spectroscopy	NA
<b>Particulate Matter</b>		
Teledyne API T640 (continuous PM mass)	Broadband spectroscopy using 90° white-light scattering	EQPM-0516-236
Aerodyne TOF-AMS (continuous NR-PM <sub>1</sub> composition)	Time-of-Flight Aerosol Mass Spectrometry (TOF-AMS)	NA
Tisch PM <sub>2.5</sub> High Volume Air Sampler (PM <sub>2.5</sub> composition)	24-hr filter-based sample	NA
<b>Remote Sensing/Meteorology</b>		
Vaisala WXT520 Weather Transmitter (WS, WD, T, RH, BP, Prec.) <sup>1</sup>	Various	NA
Vaisala CL 51 Ceilometer (MLH) <sup>2</sup>	Aerosol backscatter LIDAR	NA
Campbell Scientific CS135 Ceilometer (MLH) <sup>2</sup>	Aerosol backscatter LIDAR	NA
Pandora (NO <sub>2</sub> and O <sub>3</sub> columns)	Sun photometer	NA
<b>Volatile Organic Compounds</b>		
Summa Canisters	12-hr samples (2 per day) GC-FID analysis	NA

<sup>1</sup> WS-wind speed, WD-wind direction, T-temperature, RH-relative humidity, BP-barometric pressure, Prec.-precipitation)

<sup>2</sup> MLH-mixing layer height

Most analyzers were housed within the temperature-controlled shelter during the sampling campaign except for the Tisch High Volume PM samplers, which were located immediately adjacent to the shelter at ground level. Instruments were calibrated according to manufacturers' operation manuals and in accordance with FRM requirements listed in 40 CFR part 50, Appendix F and D. During the UWFPS campaign, nightly automated zero and span checks were performed to monitor the validity of the calibration and control for drifts or variations in the span and/or zero response. Both the calibration gas concentrations and the nightly zero and span gas concentrations were delivered using a NIST-traceable and programmable dynamic dilution calibration system (Teledyne API Model T700U). Constituents were delivered to the system from EPA protocol ( $\pm 2\%$  accuracy) reference gas standards and/or the T700U enclosed ozone generator (with NIST traceable photometer).  $\text{NO}_2$  was generated by the gas phase titration (GPT) of the NO span gas with ozone. Dilution air that had been scrubbed of all contaminants (zero air via a Teledyne T701H zero air generator) was delivered to the mixing system to meet test gas dilution needs. During UWFPS, a glass inlet with sampling height located approximately 5 m above ground level (AGL) and a subsequent sampling manifold were shared by all instruments. Particulate filters were used on the inlets of all trace gas analyzers to prevent the sampling of particulates. Particle filters were changed weekly. The Teledyne API T200U  $\text{NO}_y$  analyzer was operated without a particle filter to allow sampling of particulate nitrate, a key component of  $\text{NO}_y$ . One-minute averaged data generated by the analyzers were collected and logged using a field deployable data acquisition system (Envidas Ultimate). All analyzers were operated according to their designation (FRM and FEM analyzers) and/or manufacturer provided operator's manual. Calibration data and nightly zero and span data were excluded from the final data set.

Oxidized gas-phase chemical species were monitored using an iodide-adduct high-resolution time-of-flight chemical ionization mass spectrometer ( $\text{I}^-$  ToF CIMS, Aerodyne Research Inc.) run in negative ion mode. The CIMS was housed within a temperature-controlled enclosure and sampled ambient air directly at  $\sim 2$  L/min from the same glass sampling manifold as the criteria pollutant instruments. Reported mixing ratios of the analyte gases were averaged up to 1-minute from 6-second data which is available if higher time-resolution is needed. Signals for unreported gas-phase compounds of potential interest can also be evaluated upon request to confirm the presence of such compounds in ambient air.

Ambient ammonia ( $\text{NH}_3$ ), methane ( $\text{CH}_4$ ), and carbon dioxide ( $\text{CO}_2$ ) were monitored at the Logan EPA trailer location using a Picarro Model G2508 cavity ring-down spectrometer. Data were collected on a nominal 5-second sampling rate, and averaged up to one-minute sample periods. The system collected concentration data from Jan. 17 to Feb. 14, 2017. Ambient air was pulled through the same glass manifold as the trace gas species and was transferred to the instrument via an insulated, heated-traced ( $40^\circ\text{C}$ ),  $\frac{1}{4}$ " TFE tube. The instrument was calibrated/verified pre- and post-deployment using commercially-purchased standard gases and zero air. Additionally, for the  $\text{NH}_3$  calibrations, and prior to introduction to the sample inlet, the zero air was passed through a citric acid coated column to assure an effective  $\text{NH}_3$  zero.

Continuous PM mass measurements were made using the Teledyne T640 mass analyzer. The T640 employs broadband spectroscopy using 90° white-light scattering to obtain 1-min average PM<sub>2.5</sub>, PM<sub>10</sub>, and PM<sub>10-2.5</sub> mass measurements. The unit was housed within the environmentally controlled shelter with the inlet extending through the shelter roof to a height of 5 m AGL. The T640 analyzer was operated as designated (FEM) and according to the manufacturer provided operator manual.

The composition of non-refractory submicron (NR-PM<sub>1</sub>) particles was continuously monitored by an Aerodyne high resolution time-of-flight mass spectrometer (ToF-AMS) that was housed in a temperature-controlled, mobile sampling trailer. Ambient air was sampled through a PM<sub>10</sub> inlet extending through the trailer roof to a height of ~6 m above ground level. Coarse particles were removed from sampled air by a BGI PM<sub>1</sub> sharp cut cyclone (SSC 2.229) operating at a rate of 16.65 l min<sup>-1</sup>. PM<sub>1</sub> exiting the cyclone was split among several instruments including the AMS using a TSI 4-way flow splitter (mod. no. 370800). A 1.1 l min<sup>-1</sup> bypass flow was used to decrease the total residence time (~10 s) of PM<sub>1</sub> in the sampling line between the splitter and AMS inlet. Sampling lines downstream of the splitter were periodically verified to be free from particle intrusion using a HEPA-filter bypass at the exit of the bypass. Additionally, contributions of gas-phase species to AMS mass spectra were corrected using several sampling periods during which all particles were removed from the air entering the AMS using an in-line HEPA filter. ToF-AMS data were averaged to 5-minute time resolution during UWFPS.

24-hr filter-based PM<sub>2.5</sub> samples were collected daily using Tisch PM<sub>2.5</sub> High Volume Air Samplers over the midnight to midnight (MST) period. Collected filters were sent back to the EPA RTP laboratory to be archived and analyzed in the near future.

Mixing layer height (MLH) measurements in the Cache Valley were obtained with the Vaisala CL51 and the Campbell Scientific CS135 ceilometers. Ceilometers are eye-safe, single laser aerosol backscatter LIDAR's that apply the gradient method to aerosol backscatter signals to obtain MLH measurements. The CL51 was coupled with the Vaisala BLView software package and the CS135 was coupled with the CSL CS135 MLH Software to provide continuous mixing layer height measurements during UWFPS. Operational conditions and procedures are based on recommendations provided in the manufacturer-provided user manuals for both the CL51 and CS135 ceilometers.

Remote sensing for trace gas column amounts was performed using the Pandora Sun Photometer (SciGlob Instruments and Services) during UWFPS. The Pandora system measures total columns of trace gases such as nitrogen dioxide, ozone, and others. Mounted on a microprocessor-controlled azimuth, elevation tracker, the system can point anywhere in the sky to perform direct sun observations. Pandora operating conditions and procedures are based on recommendations provided in the manufacturer-provided user manual and protocols developed during the DISCOVER-AQ mission.

12-hr volatile organic compound (VOC) samples were collected twice daily using 6-liter Summa canisters during the 0600-1800 and 1800-0600 periods (MST). Collected samples were sent back to the EPA RTP laboratory for analysis using a gas chromatography - flame ionization (GC-FID) procedure. Compound identification were determined by comparing observed compound peak retention time to those provided in a developed CALTABLE containing more than 400 compounds. VOC samples were collected from the same glass manifold/inlet system as the trace gas analyzers.

### **Smithfield site (SM)**

SM, UDAQ's main monitoring station in the Cache valley, is located at 675 W. 220 N., Smithfield, UT (41.842778, -111.851944). As part of the Utah air monitoring network, UDAQ routinely monitors PM<sub>2.5</sub>, PM<sub>10</sub>, NO<sub>x</sub> (NO, NO<sub>2</sub>), O<sub>3</sub> and met parameters according to EPA guidelines at this site and operates 24-h Federal Reference Method (FRM) samplers for PM<sub>2.5</sub> for NAAQS compliance. As part of UWFPS, USDA deployed a suite of analyzers to capture emissions from the agricultural sector. The analyzers and samples operated during UWFPS are listed in Table 2.4 along with the analyzer/sampler operation principle.

*Table 2.4 UDAQ/USDA Analyzers/Samplers Operated during UWFPS at SM*

<b>Manufacturer and Model</b>	<b>Operation Principle</b>	<b>Institute</b>
<b>Trace Gas</b>		
Teledyne API T400 (Ozone)	UV Photometric	UDAQ
Teledyne API T200U (NO, NO <sub>2</sub> , NO <sub>x</sub> )	Chemiluminescence	UDAQ
TrsMedor gas chromatograph (Chromatotec) for reduced sulfur compounds	Gas chromatography with electrochemical detection, 10- min	USDA
Auto-GC (SRI) for VOCs and N-VOCs	Tenax trap, gas chromatography with FID/NPD detection, 30-min	USDA
Electrochemical sensors (Cairpol) for H <sub>2</sub> S, NH <sub>3</sub>	sensors, 1-min	USDA
<b>Particulate Matter</b>		
Thermo Scientific 1405-DF (continuous mass)	Two TEOM + two FDMS	UDAQ
FRM PM <sub>2.5</sub> sampler	24-hr filter-based sample	UDAQ

Ambient ion monitor (AIM) (URG) (gas and PM ions)	Gas and particle denuder; Ion chromatography	USDA
TSI Scanning mobility particle sizer (SMPS) (Particle size 10-500 nm)	Particle growth and light scattering, 5-min	USDA
TSI Aerodynamic particle sizer (APS) (Particle size 0.5-20 µm)	Light scattering and aerodynamic sizing, 5-min	USDA
<b>Meteorology Observations</b>		
Weather Station (WS, WD, T, RH, BP, Prec.) (WS, WD, T, RH, BP, Prec.)	Various	UDAQ

Hourly continuous PM<sub>2.5</sub>, PM<sub>10</sub> and coarse PM measurements are made using Thermo Scientific 1405-DF Dichotomous Ambient Air Monitor. This monitor utilizes two tapered element oscillating microbalances (TEOM) and two Filter Dynamics Measurement Systems (FDMS), which can account for volatile and nonvolatile PM fractions. NO<sub>x</sub> (NO and NO<sub>2</sub>) and O<sub>3</sub> are measured using Teledyne API T200U and T400 UV absorption analyzer, respectively. Daily automated precision, zero and span (PZS) checks are performed automatically to monitor any drifts.

Gas and particulate ions were detected and quantified using an ambient ion monitor (AIM). The instrument collects gases using a parallel plate denuder and particulates using steam distillation. Water-soluble ions are detected using cation (Na<sup>+</sup>, K<sup>+</sup>, NH<sub>4</sub><sup>+</sup>, amines) and anion (Cl<sup>-</sup>, NO<sub>2</sub><sup>-</sup>, NO<sub>3</sub><sup>-</sup>, SO<sub>4</sub><sup>2-</sup>, carboxylic acids) chromatography. The instrument sampled gases and particulates hourly.

Reduced sulfur gases (e.g. hydrogen sulfide, dimethylsulfide, methanethiol, dimethyldisulfide) and sulfur dioxide were sampled using a TrsMedor gas chromatograph. The TrsMedor takes a sample every 10 minutes. Gases are separated on a gas chromatography column and detected in an electrochemical flow cell using a redox reaction with chromic acid on platinum electrodes. The TrsMedor has a built in internal standard of permeation tubes to detect changes in instrumental response over time. An internal standards was run every three hours.

Volatile organic compounds were analyzed on an autosampling gas chromatograph. Samples were collected and analyzed hourly. VOC samples were collected on a Tenax-GR trap at 30 °C and desorbed at 200 °C. Gases were separated and detected using a split flow detection by FID and NPD detectors. The FID detected conventional hydrocarbons while the NPD detector detected nitrogen-containing VOCs.

Particle sizing and number concentrations from 10 nm – 20 µm were acquired using a scanning mobility particle sizer and an aerodynamic particle sizer. These instruments detect particles using

light scattering (the SMPS uses butanol to grow small sized particles into the light detection region). Particle size distributions were acquired every five minutes.

Cairpol sensors for hydrogen sulfide and ammonia were deployed to the field site and recorded a sample every minute. These are electrochemical based sensors that have a selective thin film on them allowing only the analyte of interest to pass through and provide a response to the electrochemical cell. While the sensors are quoted for hydrogen sulfide and ammonia, they more likely can be thought of as total reduced sulfur and total reduced nitrogen. The Cairpol sensors have relatively high detection limits (1 ppb for H<sub>2</sub>S and 100 ppb for NH<sub>3</sub>) and are more suited for near-source detection than ambient detection.

## 2.4.2 Salt Lake Valley Sites

### *University of Utah (UU)*

The UU site is located on the top floor of William Browning Building (WBB) on the University of Utah campus, which is situated on the northeastern bench of the SLV, ~150 meters above the valley floor. Most of the analyzers were housed in the Utah Atmospheric Trace Gas and Air Quality (ATAQ) lab except the analyzers for size distribution and HCHO, which were housed within the temperature-controlled penthouse located on the roof of WBB. Table 2.5 gives a list of the measurements made during UWFPS at UU.

*Table 2.5 Samplers operated during UWFPS at UU*

<b>Manufacturer and Model</b>	<b>Operation Principle</b>	<b>Institute</b>
<b>Trace Gas</b>		
Teledyne API T400 (Ozone)	UV Photometric	Dr. Lin's group UU
Teledyne API T200U (NO, NO <sub>2</sub> , NO <sub>x</sub> )	Chemiluminescence	UDAQ
Los Gatos Research (CO <sub>2</sub> , CH <sub>4</sub> , H <sub>2</sub> O)	Cavity Ring-Down Spectroscopy (CRDS)	Dr. Lin's group UU
Thermo 48i CO analyzer	IR absorption spectroscopy	UDAQ
PTR-MS (a suite of VOCs)	Mass Spectrometry	Dr. Baasandorj UU
Aerodyne Mini-TILDAS Formaldehyde Monitor	Multi-pass broad-band absorption spectroscopy	EPA
<b>Particulate Matter</b>		

1400ab ambient particulate monitor (continuous mass)	FDMS TEOM	UDAQ
Ambient ion monitor (AIM) (URG) (gas and PM ions)	Gas and particle denuder; Ion chromatography	Dr. Murphy's group, University of Toronto
TSI Scanning mobility particle sizer (SMPS) (Particle size 10-500 nm)	Particle growth and light scattering, 5-min	Dr. Hallar's group UU
TSI Aerodynamic particle sizer (APS) (Particle size 0.5-20 µm)	Light scattering and aerodynamic sizing, 5-min	Dr. Hallar's group UU
Weather Station (WS, WD, T, RH, BP, Prec.) (WS, WD, T, RH, BP, Prec.)	Various	Dr. Hoch UU

The inlet for most trace gas instrumentation in the lab is located on top of a 7 m meteorological tower located on the roof of WBB, approximately 40 meters above ground level. Air is drawn in at ~13 L/min to a central manifold located in the lab, then distributed out to trace gas instruments for O<sub>3</sub>, NO<sub>x</sub>, CO, CO<sub>2</sub>, H<sub>2</sub>O and CH<sub>4</sub>. Atmospheric CO<sub>2</sub>, CH<sub>4</sub> and H<sub>2</sub>O measurements were performed using a Los Gatos Research Off-Axis Integrated Cavity Output Spectroscopy (Model 907-0011). The instrument is calibrated automatically every three hours using three whole-air, dry, high-pressure reference gas cylinders with known CO<sub>2</sub> and CH<sub>4</sub> concentrations. O<sub>3</sub>, CO, and NO<sub>x</sub> (NO, NO<sub>2</sub>) measurements were performed using a Teledyne API T400, T200U and Thermo 48i CO analyzer respectively. The instruments were calibrated weekly and PZS tests were performed routinely.

A suite of volatile organic compounds (VOCs) including aromatics and OVOCs were measured by University of Minnesota's high sensitivity standard Proton Transfer Reaction-Mass Spectrometer (PTR-MS). The ambient air was drawn in through ~ 8 m long ½" O.D. heated inlet at ~ 10 LPM and the inlet system sub-sampled 700 sccm of the total flow. Automated backgrounds were performed every two hours and calibrations were made every ~ 6 hours.

High-time-resolution measurements of formaldehyde and formic acid were made at the UU site using the Aerodyne Mini-TILDAS Formaldehyde Monitor. A multi-pass broad-band absorption cell that provides optical path lengths up to 76 m allows enhanced sensitivity. The Mini-TILDAS using direct absorption spectroscopy allows for fast (<1 sec) absolute formaldehyde and formic acid concentrations. The Aerodyne Mini-TILDAS was coupled with TDLWintel software to provide instrument control and real-time data analysis. During UWFPS, formaldehyde and formic acid concentrations were averaged to 1-minute time resolution. Automated backgrounds were performed every ten minutes and are excluded from the final data set. The Mini-TILDAS was operated with the Aerodyne inertial inlet to provides particle separation from the sample gas stream with <1 s time response.

Continuous PM<sub>2.5</sub> mass concentrations were determined using 8500 Filter Dynamics Measurement System (FDMS) coupled with TEOM 1400ab ambient particulate monitor. Aerosol size distributions at the UU site were measured with a TSI SMPS 3938 (scanning mobility particle sizer with a TSI 3077 CPC) for particles with diameters between 13 and 615 nm and an Aerodynamic Particle Sizer (APS; TSI Inc, Model 3321) for particles with an aerodynamic diameter between 0.54 and 19.81 microns. The SMPS and APS were installed within a small structure on the roof of the WBB. For the SMPS, sheath and sample flow rates were 4 and 0.3 LPM, respectively. All SMPS distributions were corrected for multiple-charge and diffusional losses. Five-minute scans were collected from the SMPS. With the APS, the aerodynamic particle size was measured from the time of flight of the particle between two (633 nm) He-Ne lasers.

Online measurements of PM<sub>2.5</sub> composition and gas phase precursors were done using University of Toronto's modified Ambient Ion Monitoring System (AIM 9000D, URG Corp, Chapel Hill, NC) coupled with two Ion Chromatographs (Dionex ICS-2000, Thermo Fisher Scientific, Mississauga, ON). A detailed description of the AIM-IC sampling system can be found in [53]. In brief, ambient air was drawn through a PM<sub>2.5</sub> impactor allowing only gases and particles below 2.5 µm to pass through a parallel plate denuder equipped with nylon membranes with 2 mM H<sub>2</sub>O<sub>2</sub> to capture water soluble gases. Particles are hygroscopically grown as they pass through a particle condensation chamber and the dissolved solutes are subsequently collected in sample reservoirs. The inlet system was mounted on the roof to allow for collection of the gas and particle phase compounds with minimal impact to the sample flow, and connected via 20 m sampling lines to the IC systems, which were housed indoors. The AIM-IC system collects continuously and reports measurements every hour at ambient T and pressure.

### **Hawthorne (HW).**

HW is UDAQ's main air monitoring station for Salt Lake City, situated on the valley floor (at ~ 1306 m asl). This site is also part of EPA's Chemical Speciation Network (CSN) and a NCore multi-component monitoring site, where PM (PM<sub>2.5</sub>, PM<sub>10</sub>, PM<sub>10-2.5</sub>), PM<sub>2.5</sub> speciation, trace gases (O<sub>3</sub>, NO<sub>x</sub>, NO<sub>y</sub>), and meteorological parameters are monitored according to EPA guidelines [54]. US EPA deployed Vaisala CL51 ceilometer and the Pandora Sun Photometer (SciGlob Instruments and Services) during UWFPS to obtain the aerosol backscatter profiles and monitor the total columns of O<sub>3</sub>, NO<sub>2</sub> and others. See Table 2.6 and Section 2.4.1 for instrumentation and measurement details.

*Table 2.6 EPA and UDAQ Analyzers/Samplers Operated during UWFPS at HW*

<b>Manufacturer and Model</b>	<b>Operation Principle</b>	
<b>Measurements by EPA</b>		
Vaisala CL 51 Ceilometer (MLH) <sup>1</sup>	Aerosol LIDAR	backscatter

Pandora (NO <sub>2</sub> and O <sub>3</sub> columns)	Sun photometer
<b>Monitoring by UDAQ</b>	
PM (PM <sub>2.5</sub> , PM <sub>10</sub> , PM <sub>10</sub> -PM <sub>2.5</sub> ), PM <sub>2.5</sub> speciation, trace gases (O <sub>3</sub> , NO <sub>x</sub> , NO <sub>y</sub> , SO <sub>2</sub> , CO)	Various
Weather Station (WS, WD, T, RH, BP, Prec.)	Various
Size distribution measurements by SMPS Dr. Kelly, <b>UU</b>	Particle growth and light scattering, 5-min

<sup>1</sup> MLH-mixing layer height

### 2.4.3 Meteorological Observations in the SLV

The observational sites of the Cold-Air Pool Exchange Processes Study, including site names, abbreviations, elevations, type of measurements, and site coordinates are shown in Table 2.7 and Figure 2.7. The key locations for meteorological observations were HW, UU, the University of Utah Mountain Meteorology Laboratory at the mouth of Red Butte Canyon (RB), the Salt Lake City Landfill (LFL), a site near 800 S and 800 E in Salt Lake City (8th&8th), and two sites at the mouth of Parleys Canyon (PAR). Radiosondes were launched twice a day by the National Weather Service (NWS) from the Salt Lake International Airport (KSLC) and additional soundings were released during PCAP conditions from the 8th&8th site. Small and inexpensive temperature data loggers were distributed along an elevation transect running up the northeastern sidewall of the SLV. Additional mobile observation platforms were two instrumented TRAX trains and the KSL news helicopter.

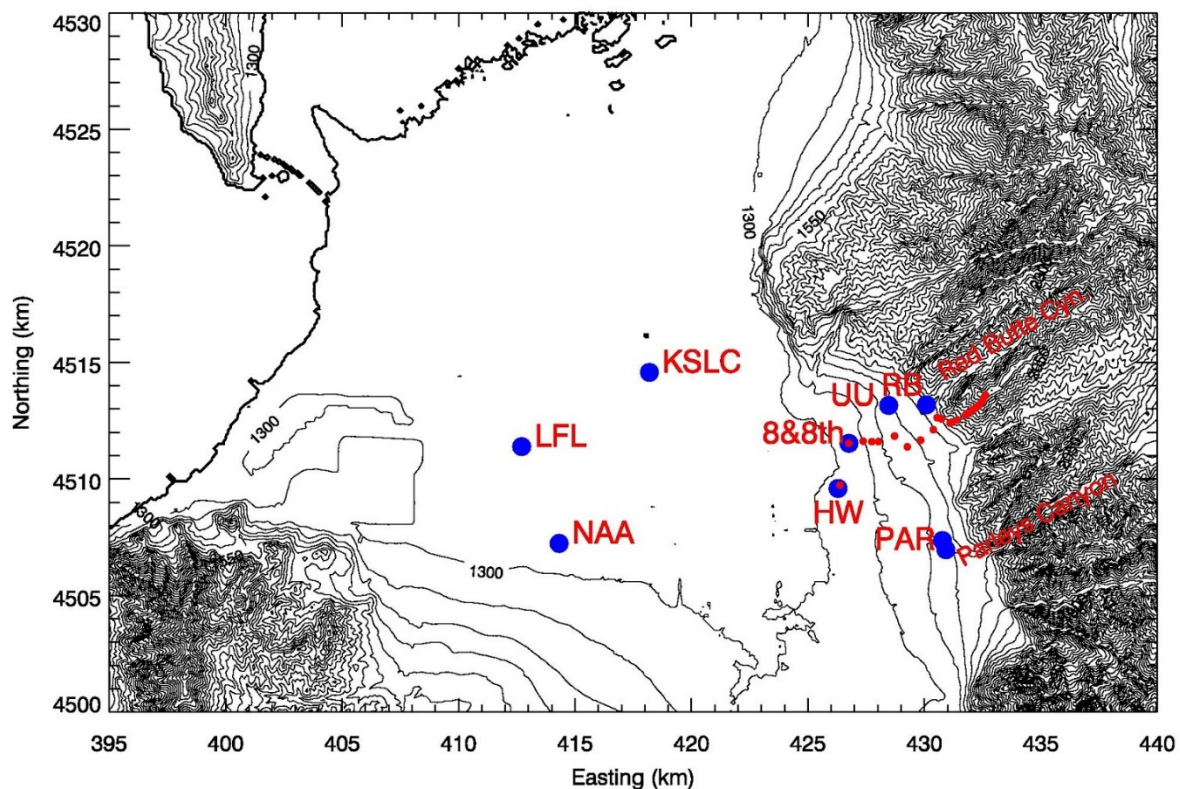


Figure 2.7 Map (UTM grid, 100 m elevation contours) of the northern part of the Salt Lake Valley showing the locations of meteorological observation sites. Blue dots mark sites with multiple meteorological sensors and/or profilers, as described in Table 2.7. Red dots mark automatic temperature data loggers deployed along an elevation transect between ~1300 m and 2150 m ASL. The thick elevation contour approximately shows the coastline of the Great Salt Lake.

Table 2.7 The main meteorological observational sites in the SLV during UWFPS.

Site Name	Abbr	Instrument	Elev (m ASL)	Elev (m AGL)	Lat(°N)	Lon (°W)
University of Utah; William Browning Building	UU (base) and (top)	Temp/RH, Wind, Solar and infrared radiation, turbulence	1442	2	40.766082	111.846752
			1465	30	40.766187	111.847718
Hawthorne Elementary; UDAQ site	HW-LIDAR	Temp, Lidar wind profile, Ceilometer	1310	2	40.735269	111.871889

Salt Lake City International Airport	KSLC	Temp/RH, Wind, Radiosonde	1289	122	40.772436	111.954703
Mountain Meteorology Laboratory; mouth of Red Butte Canyon	RB	Temp/RH, Wind, Ceilometer, O <sub>3</sub> , PM	1522	2	40.7666	111.8284
Salt Lake Landfill	LFL	Sodar Wind Profile, Ceilometer O <sub>3</sub> , PM	1292	-	40.74879	112.03398
Neil Armstrong Academy	NAA	Temp/RH, Wind, O <sub>3</sub>	1301	3	40.71152	112.01448
Parleys Canyon Exit Site 1	PAR	Sodar Wind Profiler	1388	-	40.71423	111.81957
Parleys Canyon Exit Site 2	PAR	Ceilometer O <sub>3</sub> , PM	1433	-	40.7107	111.81778
800 S & 800 E	8th&8th	Radiosonde during PCAP events	1311	-	40.75146	111.86762

### ***Temperature Profiles and Valley Heat Deficit***

Vertical profiles of the atmospheric temperature are necessary to evaluate static stability of the atmosphere and to help to define the strength of diurnal and persistent cold air pools. A good measure of the stability of a valley atmosphere is the Valley Heat Deficit (VHD, see below and Section 1.3 for overview of the winter season). Two independent observations of the temperature structure in the SLV were made to calculate the VHD. The first observation is readily available from the twice-daily radiosonde ascents from KSLC. Radiosondes are launched daily, at approximately 0500 and 1700 MST. Additional soundings were flown during PCAP conditions from the 8th&8th site. The second observation is based on a pseudo-vertical assumption [27], where temperature observations along an elevation transect are interpreted as a proxy for the vertical variation of temperatures within the valley or basin atmosphere. A set of 23 inexpensive temperature data loggers (Hobo© Pro v2, Onset Computers, MA) was deployed housed in 6-plate radiation shields (R. M. Young, MI) along an elevation transect. With the exception of the topmost sensor, they were deployed at a height of approximately 130 to 180 cm above the surface.

Sensors in the upper basin were installed on available dead branches of the vegetation, to avoid any disturbance of the environment. The topmost sensor on the summit of Mt. Wire was installed on the top of a freely accessible tower, approximately 10 m AGL. Temperature data was recorded every 5 minutes and stored on local memory. The location of sensors are given in Table 2.8.

The valley heat deficit (VHD) is a measurement of the amount of energy that would be needed to bring a valley or basin atmosphere to a neutral stratification. Following Whiteman *et al.* [1, 26] it is calculated for the SLV as

$$VHD = c_p \int_{1300\text{ m}}^{2200\text{ m}} \rho(z) [\theta_h - \theta(z)] dz, \quad [\text{J m}^{-2}]$$

where  $\theta_h$  is the potential temperature at height  $h$ ,  $\rho$  and  $\theta$  are the air density and potential temperature from the twice-daily radiosonde sounding, respectively. The specific heat of air at constant pressure is denoted as  $c_p$ , and  $dz$  is 10 m. The VHD is the heat required to warm an atmospheric column with a 1-m<sup>2</sup> base to the potential temperature observed at the top of the basin at height  $h=2200\text{ m}$ , bringing the underlying atmosphere to a dry adiabatic lapse rate. Calculations were performed using the twice-daily radiosondes launched by the National Weather Service (NWS) at the KSLC site, additional radiosondes launched during intensive observational periods, and based on the pseudo-vertical temperature soundings recorded along the northeastern valley sidewall. For the SLV, the elevation range between 1300 m ASL (valley floor) and the height of 2200 m, corresponding with the mean ridge height surrounding the valley, are used. Calculations of VHD reveal the episodes of high atmospheric stability during the passage of high-pressure centers across Northern Utah.

### **Wind Profiles**

Wind profiles, while available from the radiosondes from the KSLC and 8th&8th launch sites, were also continuously recorded using the University of Utah Halo Photonics (UK) Doppler wind lidar and from two Atmospheric Systems Corporation (Santa Clarita, CA) mini-SoDARs. The lidar was installed in a backyard of a local volunteer who lives in the direct vicinity of HW. The installation required a fixed power source and an unobstructed view of sky. The lidar was programmed to scan a Plan Position Indicator (PPI) scan pattern every 10 minutes. The Vertical Azimuth Display (VAD) analysis was used to retrieve the vertical profile of the three-dimensional wind field. This wind field can be overlaid with the aerosol backscatter coefficient of the lidar retrieval or of the co-located ceilometer. Daily quicklooks were produced during the experiment and shared via a web page with the collaborators and interested public.

The two SoDARs were installed at the LFL and PAR sites, recording 10-min average wind profiles up to 200 m AGL with a vertical resolution of 10 m. Regular maintenance was necessary to keep the PAR site sodar running, as it was powered by solar power and snow had to be removed from the antenna housing.

## **Aerosol Backscatter**

Aerosol backscatter profiles were recorded with three ceilometers at three locations in the SLV to resolve spatial differences in the atmospheric aerosol loading and to resolve temporal changes in the aerosol optical properties at these three sites. Ceilometers (Vaisala CL31) were deployed at the Salt Lake Landfill (LFL), at the mouth of Parleys Canyon (PAR), and the Red Butte Canyon Exit (RB) sites. These observations complement the observations at HW and in the Utah and Cache basins made with the EPA deployed Vaisala CL51 ceilometer. The instruments recorded a vertical profile (10-m resolution) of the atmospheric aerosol backscatter coefficient  $\beta$  every 16 seconds. The raw data was averaged to 10-min means for further processing. Daily quicklooks are available for the experiment at the following web site: [http://www.insc.utah.edu/~hoch/AIRQUAL\\_2016-2017/CEILOMETER/](http://www.insc.utah.edu/~hoch/AIRQUAL_2016-2017/CEILOMETER/). Time-height cross sections of aerosol backscatter illustrate changes in the polluted PCAP atmosphere, and visualize mixing processes, layering, and injection of clean air along basin sidewalls or through tributary canyons. Further, phases of quickly intensifying backscatter retrievals may indicate periods of PM<sub>2.5</sub> formation.

*Table 2.8* Locations and elevation of Hobo® automatic temperature dataloggers deployed along an elevation transect in the northeastern Salt Lake City Basin during UWFPS

<b>Identifier</b>	<b>Latitude (° N)</b>	<b>Longitude (° E)</b>	<b>Elev (m ASL)</b>	<b>Serial number</b>
HOBO_01	40.73528	-111.87189	1307	10538180
HOBO_02	40.75146	-111.86762	1311	9889090
HOBO_03	40.75146	-111.86762	1311	9810707
HOBO_04	40.75231	-111.86035	1338	9806339
HOBO_05	40.75216	-111.85593	1372	9806338
HOBO_06	40.75225	-111.85254	1388	9806340
HOBO_07	40.75443	-111.84443	1427	9806358
HOBO_08	40.75032	-111.83782	1429	9784026
HOBO_09	40.75292	-111.83113	1457	9826455
HOBO_10	40.75702	-111.82473	1493	978403
HOBO_11	40.7617	-111.82282	1527	980633
HOBO_12	40.76124	-111.82067	1542	980633
HOBO_13	40.7596	-111.81619	1607	9806342
HOBO_14	40.76007	-111.81534	1662	9784035
HOBO_15	40.76085	-111.81250	1716	9784034
HOBO_16	40.7628	-111.80849	1804	9806354
HOBO_17	40.76373	-111.80695	1888	9806344
HOBO_18	40.76477	-111.80495	1953	9784028
HOBO_19	40.76572	-111.80326	2000	9784029
HOBO_20	40.76664	-111.80176	2048	9784027
HOBO_21	40.76799	-111.80014	2105	9806345
HOBO_22	40.76915	-111.79947	2137	9784030
HOBO_23	40.77055	-111.79835	2181	9806343

### ***Chemical Observations Co-Located with Meteorological Equipment***

Observations at the LFL, PAR and RB sites were co-located with ozone and particulate concentration measurements. The PM<sub>2.5</sub> measurements were recorded by two types of research-grade laser nephelometers manufactured by Met One Instruments: The E-Sampler 9800 or the ES-642 monitors [precision: 3 µg/m<sup>3</sup>, uncertainty: 8%] with sharp cut cyclones at the inlet to restrict particle size sampled to PM<sub>2.5</sub> or smaller. The E-Samplers and ES-642 monitors are calibrated by the manufacturer and have been shown to compare well in match-ups between UDAQ measurements.

The ozone measurements were recorded by a Model 205 Dual Beam Ozone Monitor (O<sub>3</sub>) from 2B Technologies, Colorado (precision: 2% uncertainty: 2%). The 2B Ozone Monitor utilizes UV absorption at 254 nm and is approved by EPA as a Federal Equivalent Method (FEM). The 2B Ozone Monitors were calibrated against UDAQ standards as well as a 2B Technologies Model 306 Calibration Source.

### ***Turbulence Intensity and Vertical Mixing***

Turbulence kinetic energy (TKE) is a measure of turbulence intensity. To evaluate the strength of atmospheric mixing at the valley sidewall (UU) site, turbulence observations were made using a Campbell Scientific CSAT3 ultrasonic anemometer to measure the three-dimensional wind field at 20 Hz. This dataset was processed using the Utah Turbulence in Environmental Studies processing and analysis code (UTESpac).

A second measure of atmospheric mixing and turbulence is the vertical velocity variance ( $\sigma_w$ ) that was derived from vertical stare data collected with the University of Utah Doppler wind lidar.

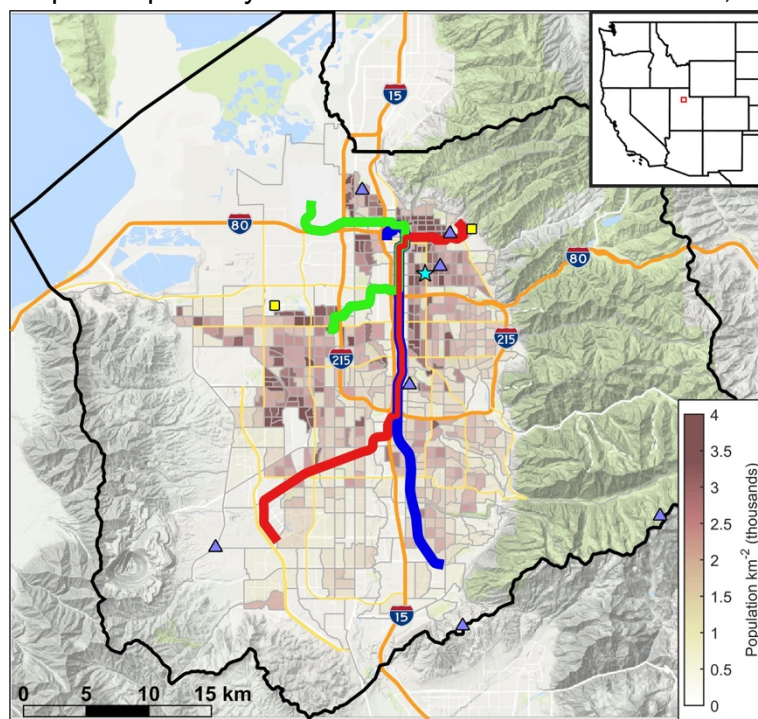
### ***Solar and Infrared Radiation***

Solar incoming and reflected radiation was measured at the University of Utah (UU) site, using pyranometers (CMP21, Kipp and Zonen, Delft, the Netherlands) and in- and outgoing thermal (longwave) radiation were monitored with pyrgeometers (CGR4, Kipp and Zonen, Delft, the Netherlands). Observations of solar radiation can indicate the degree of cloudiness and the amount of radiative energy available to drive photochemical reactions. The surface albedo - the ratio between reflected solar and incoming solar radiation - indicates the surface conditions such as the degree snow cover or bare grass surface. Changes in infrared incoming radiation indicate the degree of cloud cover and cloud height, while the outgoing longwave radiation is a function of surface temperature and emissivity.

## 2.4.4 TRAX Observations

The University of Utah research group has partnered with the Utah Transit Authority (UTA) and installed suites of instruments on two light-rail “TRAX” trains (numbered 1136 and 1104, hereafter TRAX 1 and 2). This measurement project began in December 2014 and is ongoing. Electrified trains are an ideal platform for air sampling because they have zero direct emissions and often run continuously throughout the day. The trains have electric circuitry on their roofs in steel weatherproof boxes, and the instruments were installed in one of the spare boxes (dimensions 1.5 m x 0.5 m x 0.5 m). The sample inlets were 4 m above ground level and 0.5 m above the top of the train. On TRAX 1, PM<sub>2.5</sub> was measured with an E-Sampler aerosol monitor from Met One Instruments, Inc. Carbon dioxide (CO<sub>2</sub>), methane (CH<sub>4</sub>), and water (H<sub>2</sub>O) measurements were made with an Ultra-portable Greenhouse Gas Analyzer from Los Gatos Research (LGR) Inc. The Campbell Scientific CS215-L Temperature and Relative Humidity (RH) probe and CS106 Barometer were used for the meteorological parameters. A Raspberry Pi based data logger collected trace gas data and controlled valve systems for hourly automated calibrations and a Campbell Scientific data logger (CR1000) collected meteorological and PM<sub>2.5</sub> data. TRAX 2 was equipped with a Model 205 Dual Beam Ozone Monitor from 2B Technologies, a NO<sub>2</sub> analyzer from LGR Inc., and an ES-642 Remote Dust Monitor from Met One Instruments, Inc. Data were collected on a Raspberry Pi computer. The PM<sub>2.5</sub> instruments on both TRAX trains are equipped with a sharp cut cyclone and maintain a sample RH of 30% with an internal heater. The observations were collected at frequencies ranging from 1 s to 1 min and transmitted to University of Utah servers every 5 minutes with cell modems.

The TRAX light-rail network has three train lines: Red, Green, and Blue (Figure 2.8). TRAX 1 and 2 operate primarily on the Red and Green train lines, and all of the observations during the



UWFPS come from these two train lines. The TRAX trains had a limited deployment schedule during the UWFPS study period due to maintenance requirements for the train cars, however there are mobile transects on several days that coincide with UWFPS flights. On days when the train cars were not deployed on the train lines they were stationed outside at the light-rail maintenance facility and acted as an additional ground observation site.

*Figure 2.8 The TRAX Red, Green, and Blue train lines in the SLV. The*

University of Utah greenhouse gas monitoring network (blue triangles), University of Utah air quality research sites (yellow squares), and the UDAQ's HW site (cyan star) are also shown. The population density is superimposed in brown shading, and the inset shows the location of the SLV as a red box in the western U.S.

## 2.4.5 Utah Valley Site

### Lindon, UT (LN)

UDAQ's Lindon air monitoring station is located at 50 North Main Street, Lindon, UT (40.3396,-111.7133675). UDAQ routinely monitors 24-h  $PM_{2.5}$ ,  $PM_{2.5}$ ,  $PM_{10}$ , and met parameters according to EPA guidelines at this site (See Table 2.9 or section 2.4.1 for details). 24-h filter based  $PM_{2.5}$  samples were collected using two Thermo 2025 B samplers for  $PM_{2.5}$  organic and inorganic speciation. Collected filters were sent to the EPA RTP laboratory to be archived and will be analyzed in the near future. Additional measurements of  $O_3$ ,  $NO_x$ , aerosol backscatter, and  $O_3$ ,  $NO_2$  column are conducted by EPA at this station during UWFPS as listed in Table 2.9 UDAQ/EPA Analyzers/Samplers Operated during UWFPS at LN. See Section 2.4.1 for instrument and measurement details.

Table 2.9 UDAQ, EPA and BYU Analyzers/Samplers Operated during UWFPS at LN

Manufacturer and Model	Operation Principle
<b>Measurements by EPA</b>	
2B Technologies Model POM ( $O_3$ )	UV photometric
Teledyne API T200UP ( $NO$ , $NO_2$ , $NO_x$ )	Chemiluminescence with photolytic converter
Vaisala CL 51 Ceilometer (MLH) <sup>1</sup>	Aerosol backscatter LIDAR
Pandora ( $NO_2$ and $O_3$ columns)	Sun photometer
<b>Monitoring by UDAQ</b>	
PM ( $PM_{2.5}$ , $PM_{10}$ , $PM_{10-PM_{2.5}}$ ), $PM_{2.5}$ speciation	Various
Weather Station (WS, WD, T, RH, BP, Prec.)	Various
<b>Measurements by BYU</b>	
Organic aerosol monitor (OAM)	TD-GC-MS

<sup>1</sup> MLH-mixing layer height

#### 2.4.6 Passive Ammonia Network

Time-averaged, ambient gas-phase  $\text{NH}_3$  concentrations were measured in the Cache Valley and along the Wasatch Front using a network of Ogawa Model 3300 passive samplers (Ogawa USA, Inc.). A complete description of the passive sampling systems and ultimate quantifications can be found in Roadman *et al.* [55]. Briefly, these portable systems consist of a multi-component sampler, a mounting base, and a rain cover. Commercially-purchased, pre-treated (citric acid-coated) sample pads are loaded into one end of the sampler and held in place by metal screens and a porous cap. Collection of gaseous  $\text{NH}_3$  onto the pads is based on the diffusion of air through a porous end cap and a metal screen to the pad surface and subsequent reaction with the citric acid. Collected  $\text{NH}_3$  is subsequently determined via ion chromatography. A schematic drawing of a component-separated sampler can be found in Figure 2.9. A picture of a sampler as deployed the rural Lewiston (Cache Valley) site is shown in Figure 2.10.

As can be seen in Figure 2.11, 25 and 11 sites were arrayed around Cache Valley and along the Wasatch Front, respectively. Table 2.10 gives the latitude and longitude of each site as well. While the primary goal of the various locations was to adequately characterize the representative airsheds, select locations within the Cache Valley were purposely located near suspected large  $\text{NH}_3$  emissions sources (Franklin East and Lewiston Rural – large poultry facilities; Hyrum 6600 – a commercial fur production facility). The samplers were deployed over three, consecutive 7-day periods beginning on Jan. 26, 2017.

Blank pads were collected during each weekly deployment period at each of the lab sites (USU and UU/UDAQ) while loading the samplers and processing the pads to quantify potential  $\text{NH}_3$  contamination during handling. After exposure, all pads were transferred to individual, label opaque 8 ml HDPE sample bottles and refrigerated ( $<4^\circ\text{C}$ ) until shipment and final quantification via ion chromatography (IC) as performed at the USDA's Agricultural Research Services Food Animal Environmental Research Unit (Bowling Green, KY).

Samples were extracted with 8 mL DDI water. Ammonium cation was determined by ion chromatography (ICS 3000, Dionex Corporation, San Francisco, CA). Samples were injected into IC via an autosampler (Model AS-1, Dionex Corporation). Initial samples were run with a 100  $\mu\text{L}$  injection; subsequent to that, samples with no detection were run with a 500  $\mu\text{L}$  injection volume. Methanesulfonic Acid (20mM, Sigma-Aldrich, St Louis MO) was used as mobile phase for an isocratic run. The mobile phase was pumped at 1.2 mL/min through a 50 mm x 4.00 mm IonPac CG12A Guard and 250 mm X 4.00 mm IonPac CS12A Analytical columns (Dionex Corp, Sunnyvale, CA) held at a temperature of 25  $^\circ\text{C}$ . Detection was performed with a conductivity detector (Model # 061830, Dionex Corporation) and a Cation Self-Regenerating Suppressor (CSRS 300 4-mm Dionex Corp, Sunnyvale, CA). Samples were analyzed in triplicate. The method was calibrated for ammonium from 0.05 to 10 mg/L. The lower detection limit (LDL) for the IC quantification was determined to be 0.05 mg/L (ppm). On the cases wherein the analyzed samples were below the specified LDL, the samples were assigned one-half of the LDL (0.025 mg/L). This IC value is approximately equivalent to an associated ambient value of 1.9 ppb, which

can be taken as the minimum measurable ambient concentration using the above passive sampling protocol.

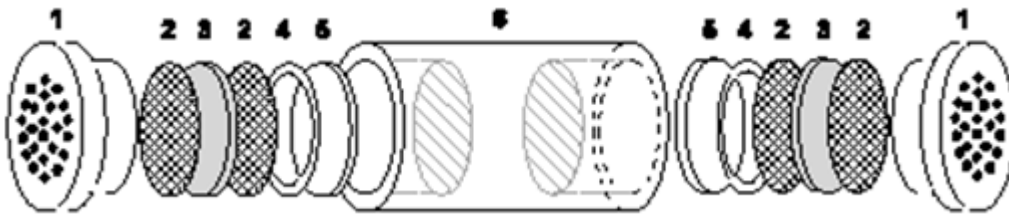


Figure 2.9 Display of the components of the Ogawa Model 3300 passive sampler. Sampler components are: 1) a porous end cap, 2) a stainless steel screen, 3) a sampling pad, 4) a retainer ring, and 5) a base with hollowed ends [55].



Figure 2.10 Passive ammonia sampler as deployed at the rural Lewiston (Cache Valley) sample location – without (left) and with the wind/precipitation cap (right).

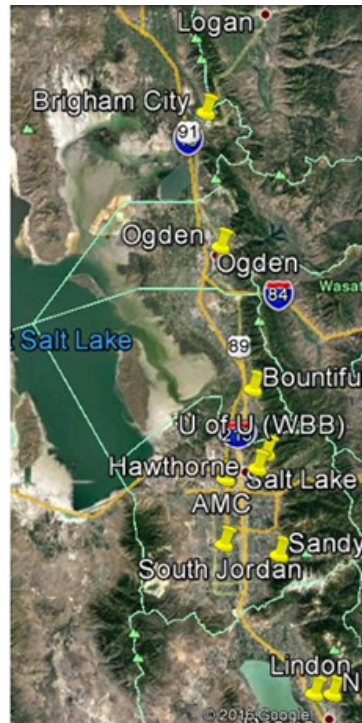
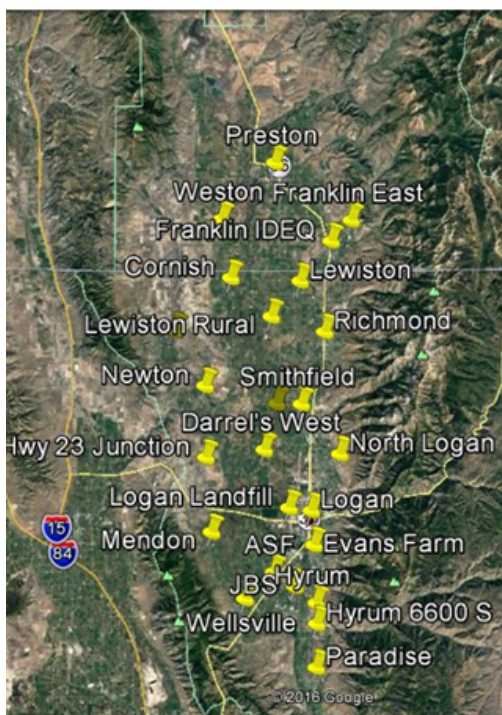


Figure 2.11 Passive ammonia sampler locations in the Cache Valley (left) and along the Wasatch Front (right).

Table 2.10 Latitude and longitude of passive sampling network sites.

Table 2.10 Latitude and longitude of passive sampling network sites.

	Site	Latitude (° N)	Longitude (° E)
Cache Valley	Amalga pole 177	41.8433	-111.8873
	Animal Science Center	41.6661	-111.8912
	Clarkston	41.9200	-112.0317
	Cornish	41.9754	-111.9525
	Daryl West	41.7947	-111.9047
	Evans Farm	41.6950	-111.8345
	Franklin East	42.0355	-111.7818
	Franklin (IDEQ)	42.0137	-111.8102
	HWY 23 JXN	41.7864	-111.9873
	Hyrum Center	41.6344	-111.8310
	Hyrum 6600 S	41.6125	-111.8306
	Lewiston Town	41.9718	-111.8541
	Lewiston Rural	41.9347	-111.8949
	North Logan	41.7903	-111.7981
	JBS	41.6516	-111.8613
	Logan	41.7309	-111.8383
	Logan Landfill	41.7338	-111.8696
	Mendon	41.7081	-111.9791
	Newton Park	41.8617	-111.9886
Paradise	41.5665	-111.8312	

	Preston	42.0963	-111.8901
	Richmond	41.9184	-111.8193
	Smithfield	41.8426	-111.8522
	Weston	42.0370	-111.9654
	Wellsville Park	41.6380	-111.9316
Wasatch Front	AMC	40.7118	-111.9608
	Brigham City	41.4929	-112.0178
	Bountiful	40.9029	-111.8845
	Hawthorne	40.7344	-111.8722
	Lindon	40.3395	-111.7135
	North Provo	40.2528	-111.6627
	Ogden	41.2069	-111.9751
	Sandy	40.5503	-111.8118
	South Jordan	40.5720	-111.9663
	Spanish Fork	40.1384	-111.6655
	University of Utah	40.7665	-111.8477

## 2.5 Model Support and Applications

Four groups have contributed to meteorological and photochemical modeling efforts that relate to UWFPS-2017. A brief overview of the groups and their model platforms is provided here, with more detailed descriptions of their activities and contributions provided in Section 7.

UDAQ modeling has focused on the SIP requirements scheduled for delivery to the U.S. EPA in spring of 2018, and have focused on regulatory model runs of winter cold pool conditions from previous years. UDAQ relies on the CAMx photochemical transport model, driven by high resolution WRF meteorology, for domains covering the state of Utah (4km horizontal resolution) and the Wasatch urban corridor (1.33 km resolution). This effort has led to the identification of model uncertainties, with the most significant being related to meteorological transport during cold pool conditions, emissions of PM<sub>2.5</sub> precursors, and the treatment of oxidation mechanisms within the CAMx model system.

In addition to collecting available meteorological data during UWFPS-2017, the University of Utah (E. Crossman, S. Hoch) has provided meteorological forecasting and interpretive support throughout and after the study. Meteorological comparison studies using the WRF model by UU from several previous winter studies throughout Utah provide a basic understanding of the land-use, terrain effects, and model physics requirements necessary to adequately characterize pollution transport along the Wasatch range.

John Lin (UU, Dept. of Atmospheric Sciences, unfunded) has provided detailed trajectory information for the UU measurement site and the NOAA Twin-Otter aircraft data during UWFPS-

2017. These rely on hourly output from the High Resolution Rapid Refresh analysis fields provided by NCEP (3km horizontal resolution), and the trajectory analysis within the STILT (Stochastic Time-Inverted Lagrangian Transport) model framework. Both trajectory and footprint source information are available through this analysis. Footprint information for surface sources have been provided to date, but footprints from stratospheric or other specific regions are also available.

Finally, NOAA/ESRL/CSD (Stu McKeen et al., unfunded) has completed several simulations of the UWFPS-2017 cold-pool periods using the WRF-Chem photochemical transport model, intended primarily to aid in the interpretation of the NOAA Twin-Otter aircraft observations. This model has fully coupled meteorology and chemistry (both gas and aerosol phase) for a 4km horizontal covering Utah. Figure 2.12 shows this model's domain configuration, illustrating the one-way nesting within a coarser (12km resolution) domain, as well as the NO<sub>x</sub> emissions from the U.S. EPA NEI-2011 emissions inventory used within the simulations. The WRF-Chem model is being used to quantify the dependence of predicted PM<sub>2.5</sub> accumulations to the base WRF meteorological model configuration, the emissions of NO<sub>x</sub> and NH<sub>3</sub> within the inventory, and various assumptions related to gas-phase and heterogeneous phase oxidation mechanisms.

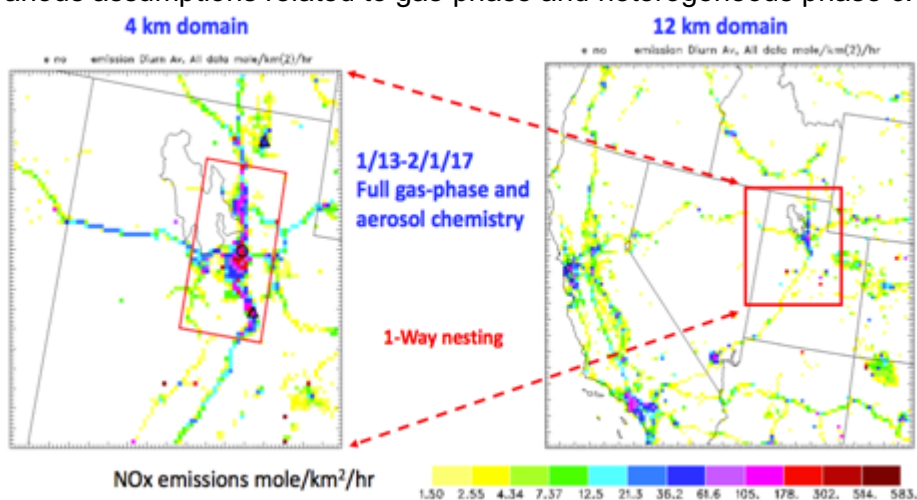


Figure 2.12 4-km (left) and 12-km (right) domains used in the WRF-Chem simulations for the UWFSP-2017 study. Diurnally averaged NO<sub>x</sub> emissions from the NEI-2011 emissions inventory (January, weekday) are also shown. The red box in the 4-km domain demarks the limits used in a diagnostic analysis of the study period.

### 3 Observations of Aerosols and Trace Gases

This section describes the atmospheric chemical observations during the 2016-17 UWFPS intensive measurement campaign. First are described the aerosol measurements, followed by the major classes of trace gases.

#### 3.1 Aerosol Composition and Size Distributions

During the UWFPS field intensive period, we carried out measurements to characterize aerosol composition, size distribution, spatial and temporal evolution from an airborne platform and from several ground sites. We measured the non-refractory chemical composition and size distributions of the aerosol particles in the size range 60 to 1000 nm with an AMS and an UHSAS from the NOAA Twin Otter aircraft. We measured mass concentrations of  $PM_{2.5}$  at the ground sites of Logan, Smithfield, Hawthorne and Lindon, as well as at the University of Utah, together with  $PM_{2.5}$  water-soluble constituents.  $PM_{2.5}$  was also measured from two light rail cars (TRAX) across Salt Lake City. Size distributions in the range from 12 nm to 20  $\mu m$  were measured with a combination of SMPS and APS at the ground site of the University of Utah. In Ogden, we also measured vertical profiles of particle counts with size information from a tethered balloon (see Section 2 for more detailed information on the sites and measurement methods). This section describes the results of these measurements.

##### 3.1.1 Comparison Among the Major Basins

###### *Aircraft Observations*

Figure 3.1 shows three examples of the total aerosol mass loadings overlaid on the Twin Otter flight tracks: two during PCAP events and a third outside a PCAP event. As expected, we observed higher aerosol mass loadings during the PCAP episodes than outside a PCAP event, when clean conditions are expected. The PCAP examples are consistent with the heterogeneity of aerosol mass observations on the ground between the three major valleys, where sometimes the mass loadings are highest in the Cache Valley (18 January, leftmost panel) and other times the highest mass loadings are in the Utah Valley (31 January, middle panel). In fact, the highest mass loadings for the entire study period were observed at the southeastern-most part of the flight tracks above the Utah Valley in the flight shown.

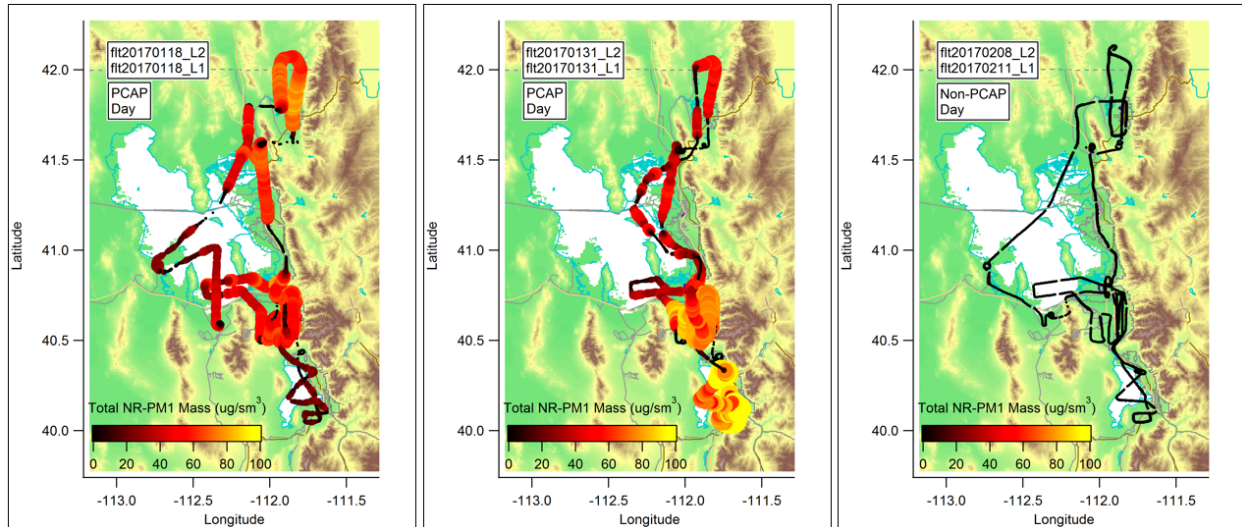


Figure 3.1 Example of Twin Otter flight tracks during PCAP events (left and center) and during a non-PCAP event (right). Size and color of the data points are proportional to the total mass of non-refractory  $\text{PM}_{10}$  measured by the aerosol mass spectrometer (AMS).

The majority of the non-refractory mass of the aerosol particles was ammonium nitrate, in particular when the mass loadings were higher than  $10 \mu\text{g sm}^{-3}$ . As shown in Figure 3.2 during a PCAP event the majority of the aerosol (>70%) was composed of ammonium nitrate, with the organic component of the aerosol particles being around 20%. Sulfate and chloride represented a minor fraction of the mass (<9% and <2%) on average. Outside of PCAP events (clean conditions), the non-refractory particle mass composition was quite variable: ammonium nitrate 16-37%, organic 45-69%, sulfate 16-37% and chloride 0-5%.

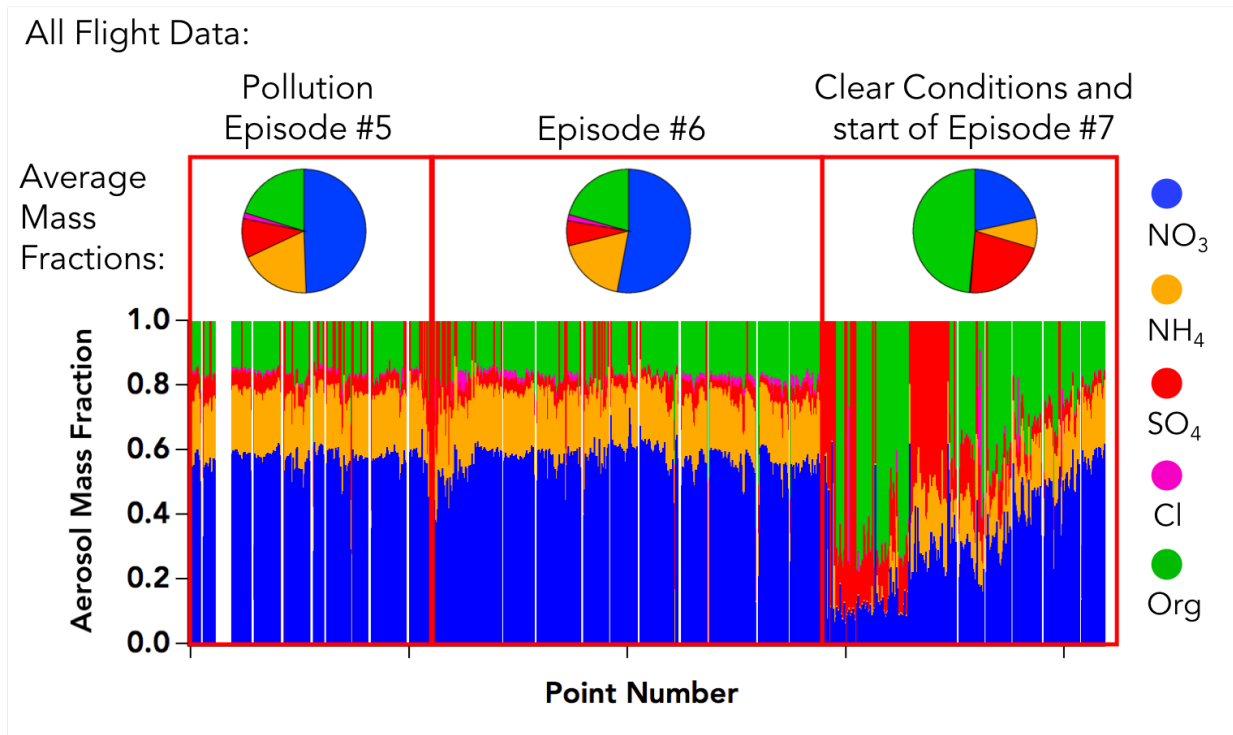


Figure 3.2 Mass fractions of the non-refractory components of the sub-micron aerosol mass measured with the aerosol mass spectrometer (AMS) on the NOAA Twin Otter. At the top panel are shown pie charts of the average mass fractions for the PCAP (pollution) Episode #5, Episode #6 (Table 1.1), and for data measured during clear conditions. In the lower panes are the data as function of point number. Aerosol nitrate is blue, ammonium is orange, sulfate is red, chloride is pink, and organic material is green.

The chemical composition of the aerosol particles was very uniform in all the basins. As shown in Figure 3.3 all the locations show similar features in the mass fraction as a function of total mass. All the basins were dominated by ammonium nitrate when the aerosol mass loadings were larger than  $10 \mu\text{g sm}^{-3}$ . Organic species and sulfate made up for the remaining mass in similar proportions as the ones of the ensemble of the dataset ( $\sim 20\%$  and  $\sim 10\%$  respectively) and the chloride was around 2%. Fine features in the mass fraction versus total mass can be distinguished, e.g. clusters of data with higher chloride in the Great Salt Lake and Salt Lake region or with lower ammonium nitrate and higher organic mass fraction in Ogden and Salt Lake City. Those data require further analysis to assess their nature.

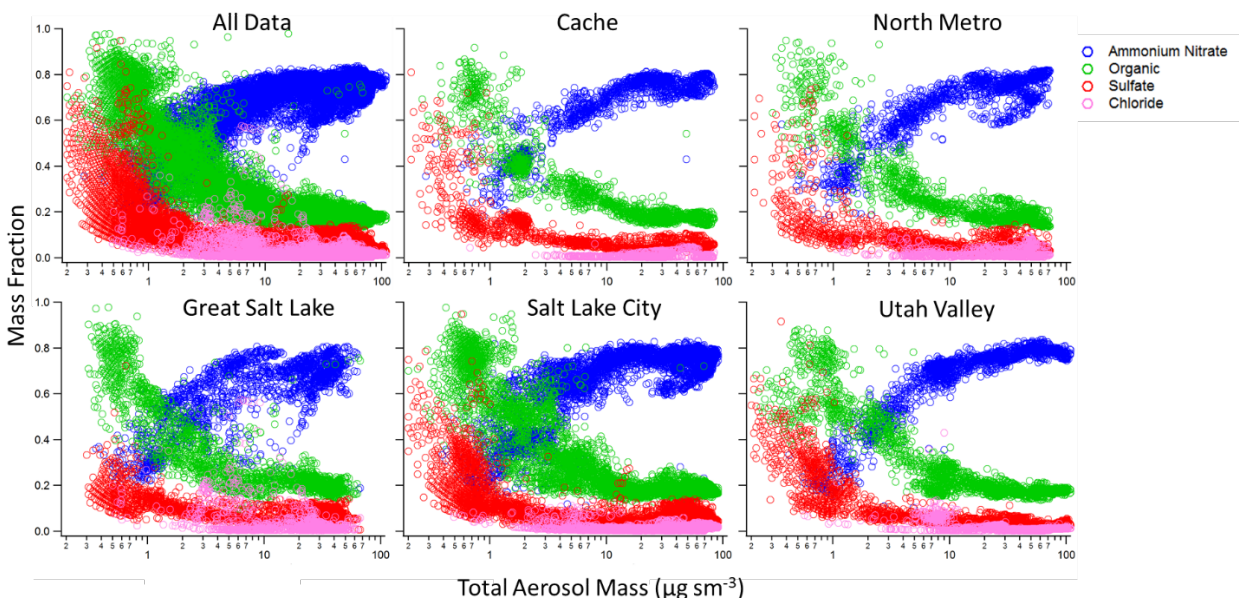


Figure 3.3 Mass fractions as a function of non-refractory, total sub-micron aerosol mass measured with the aerosol mass spectrometer (AMS) on the NOAA Twin Otter. The panel in the upper left corner contains all the data (R1) taken during the UWFPS. In the other panels, the data shown are selected by location. The mass fraction corresponding to ammonium nitrate is shown in blue and calculated as the sum of the nitrate ion ( $\text{NO}_3^-$ ) and the associated ammonium ion ( $\text{NH}_4^+$ ). The organic mass fraction is green, the sulfate mass fraction is red and the chloride mass fraction is light pink.

The comparison between the aerosol particles' total volume, calculated using the UHSAS size distributions and the total mass measured with the AMS (left panel of Figure 3.4) supports the AMS observation that the sub-micron aerosols were composed mainly by ammonium nitrate. The mass density calculated from the slope of AMS mass versus UHSAS volume ( $1.9 \text{ g cm}^{-3}$ ) is, within measurement uncertainties, compatible with the density of ammonium nitrate ( $1.72 \text{ g cm}^{-3}$ ). The AMS ion balance in the right panel of Figure 3.4 supports the conclusion drawn from the analysis of the mass fraction. Except for a handful of data points measured in proximity of the U.S. Magnesium plant that had lower mass fraction of ammonium nitrate, the measured aerosols are completely neutralized, as expected in an environment dominated by ammonium nitrate.

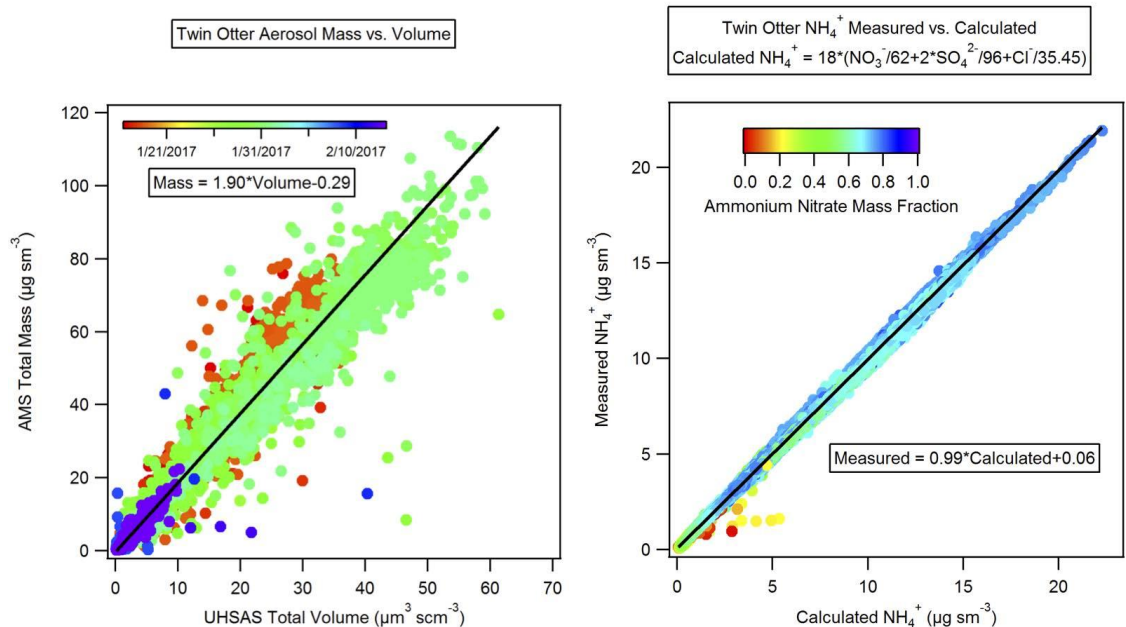


Figure 3.4 Left: Comparison between the total mass measured with the AMS (y-axis) and the total aerosol volume measured with the UHSAS (x-axis). The data are colored by date and time. Right: AMS measured  $\text{NH}_4^+(p)$  versus calculated amount of  $\text{NH}_4^+(p)$  required to neutralize all measured anions. The data are colored by ammonium nitrate mass fraction. The black line is a linear fit through the data.

### Ground-based Observations of Cache Valley $\text{PM}_{2.5}$ and Particulate Nitrate

Figure 3.5 displays the 1-minute average  $\text{PM}_{2.5}$  mass concentrations measured at Logan during the UWFPS. Increased  $\text{PM}_{2.5}$  mass concentrations were observed during PCAPs (17-20 January and 28 January - 3 February). Also displayed in Figure 3.5 is a time series (1-minute average) of the difference between total reactive oxides of nitrogen ( $\text{NO}_y$ ) and  $\text{NO}_x$  ( $\text{NO}_x = \text{NO} + \text{NO}_2$ ). This difference ( $\text{NO}_y - \text{NO}_x$ ) is expected to be dominated by particulate nitrate during this time period in the Cache Valley and as indicated in the figure, is highly correlated with the measured  $\text{PM}_{2.5}$  mass concentrations.

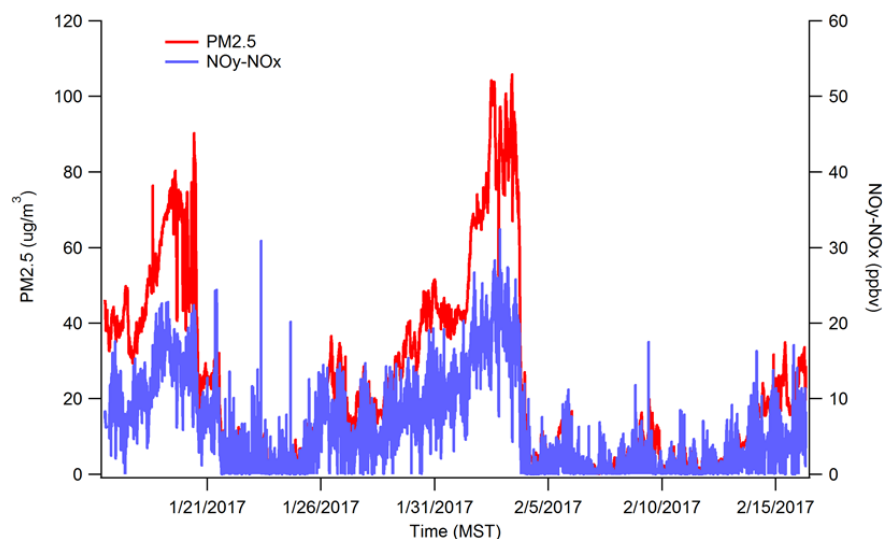


Figure 3.5 Time series showing increased  $PM_{2.5}$  concentrations during PCAPs and the correlation between  $PM_{2.5}$  versus ( $NO_y-NO_x$ ) in Logan, Utah during the UWFPS study period.  $PM_{2.5}$  is expressed in units of  $\mu g m^{-3}$  on the left y-axis and  $NO_y-NO_x$  is expressed in units of ppbv on the right y-axis.

NR- $PM_1$  from the AMS ground-based instrument (L4-AMS) along with  $PM_{2.5}$  concentrations measured at the L4 ground site in Cache Valley are compared in the scatter plot shown in the left panel of Figure 3.6.  $PM_{2.5}$  measurements obtained from the Teledyne T640 were initially averaged to the 5-minute L4-AMS time grid in order to facilitate this comparison. Data points in this comparison plot have been color-coded using the L4-AMS time series in order to show temporal proximity of various data.

Overall, measured NR- $PM_1$  and  $PM_{2.5}$  concentrations are fairly consistent and well correlated. This is particularly true for mass concentrations lower than  $60 \mu g m^{-3}$  (non-PCAP periods) when the agreement between the two measurements is very good. Indeed, a linear regression of NR- $PM_1$  and  $PM_{2.5}$  concentrations calculated for the low mass concentrations (dashed line) has a slope,  $m$ , of 0.91 and intercept,  $b$ , of -1.32. This indicates that a relatively small amount of mass exists between  $PM_{2.5}$  and  $PM_1$  for the lowest mass concentrations and the composition of  $PM_{2.5}$  is likely accurately represented by that of NR- $PM_1$  for these conditions.

While the two measurements of aerosol mass are well-correlated at all mass concentrations, we do note a discrepancy in the agreement between the data at high mass concentrations. Visual inspection of NR- $PM_1$  and  $PM_{2.5}$  time traces suggested a deviation between measurements during the PCAP events (most notably that between 2-4 February 2017) during which  $PM_{2.5}$  concentrations were in excess of  $60 \mu g m^{-3}$ . Linear regression of the NR- $PM_1$  versus  $PM_{2.5}$  concentrations for all of the data (solid line) results in a slope (intercept) of 0.73 (1.52), implying that approximately one-quarter of the  $PM_{2.5}$  mass lies between the size cut of the L4 AMS and the  $PM_{2.5}$  instrument. The cause of this discrepancy is unknown and could stem from either a positive (i.e., overestimation) artifact on the part of the Teledyne T640 or a negative (i.e., underestimation) artifact on the part of the L4-AMS. Given the overwhelming contribution of volatile ammonium nitrate to NR- $PM_1$  during these PCAP episodes, a negative artifact on the part of the L4-AMS appears less likely. This discrepancy at mass concentrations in excess of  $60 \mu g$

$\text{m}^{-3}$  suggests that greater caution must be applied when equating NR-PM<sub>1</sub> and PM<sub>2.5</sub> composition during PCAP episodes.

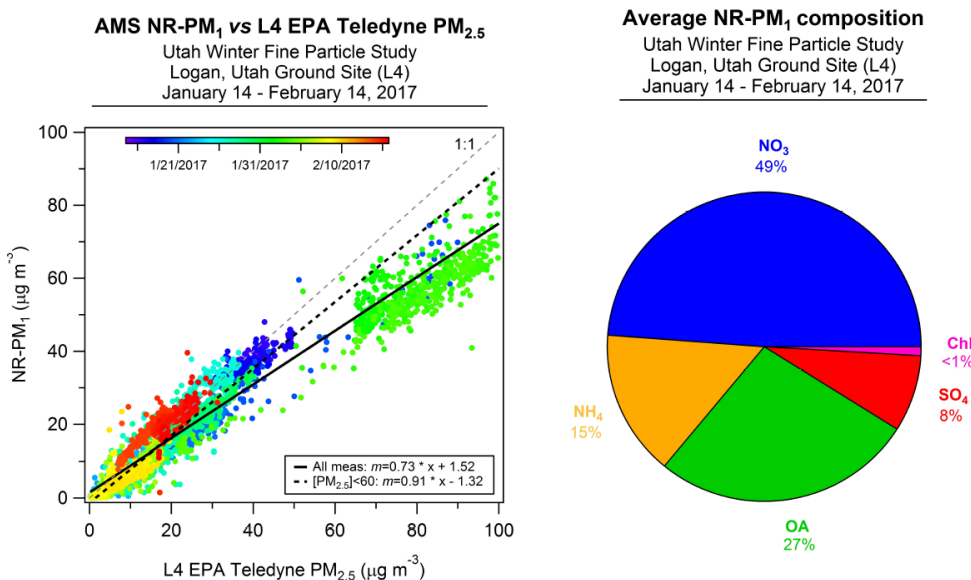


Figure 3.6 Left panel: comparison between the submicron aerosol mass measured by the EPA aerosol mass spectrometer and the PM<sub>2.5</sub> mass, measured using a Teledyne T640 by the EPA at the L4 site in Logan. In color is the date at which the measurements were carried out going from 14 January 2017 (blue) to 14 February 2017 (red). Right panel: chemical composition of the non-refractory mass of submicron aerosol particles measured by the EPA aerosol mass spectrometer at the Logan L4 site. In blue is the nitrate mass fraction, in orange is the ammonium mass fraction, in green is the organic mass fraction, in red is the sulfate mass fraction, and in pink is the chloride mass fraction.

The overall composition of NR-PM<sub>1</sub> throughout the UWFPS study period at the L4 site is presented in the pie chart of Figure 3.6 (right side). Clearly, NR-PM<sub>1</sub> composition was dominated by nitrate which contributes nearly half the mass on average. This nitrate likely exists in the form of inorganic ammonium nitrate although small amounts of nitrate could result from the presence of organic nitrates [56]. On average, one-quarter of NR-PM<sub>1</sub> mass was ammonium and sulfate. Roughly one quarter of NR-PM<sub>1</sub> mass was comprised of organic aerosol while non-refractory chloride (likely ammonium chloride) is present in very small quantities (<1%). Based on the ionic charge balance at the L4 location (Figure 3.7), the vast majority of nitrate and sulfate in fine particles was present as ammonium nitrate and ammonium sulfate, respectively. This is consistent with the aircraft and other ground-based observations over a wider area during the UWFPS sampling period.

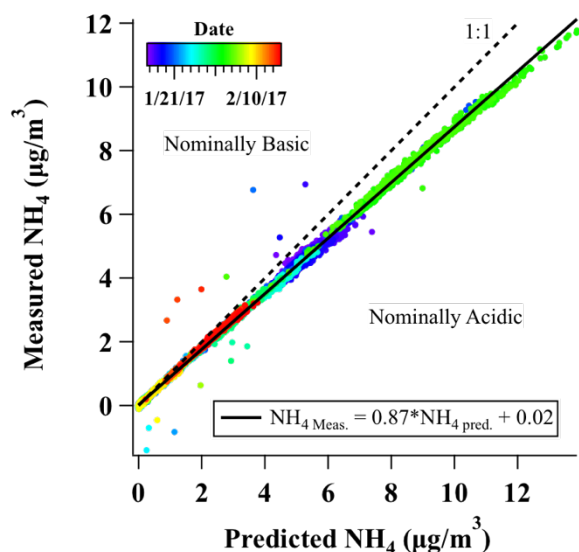


Figure 3.7 AMS measured  $NH_4^+(p)$  versus amount of  $NH_4^+(p)$  required to neutralize all measured anions. Color indicates the date between 14 January and 14 February 2017. Linear fit is shown in relation to the 1:1 line.

### Ground-based Observations with AIM-IC at the University of Utah (UU)

The water soluble  $PM_{2.5}$  constituents measured with the AIM-IC instrument at the UU site are shown in the left panel of Figure 3.8. The inorganic fraction matches previous observations showing the particle composition during PCAP periods was dominated by  $NH_4NO_3$ . Other components that potentially reacted with  $NH_3(g)$  to form particulate species, chloride and sulfate, were very small. A small amount of amines were also detected. Due to the resolution of the chromatography and the prevalence of small amounts of potassium ( $K^+$ ) in the water source, there is a significant overlap of  $K^+$  and amines. By looking at the ion balance for the AIM-IC in the right panel of Figure 3.8, the aerosols appear to be completely neutralized in agreement with the TO-AMS and the L4-AMS observations. Further analysis needs to be done on the chromatograms to accurately report the total  $K^+$  and amine fraction. However, the total  $K^+$  observed does not exceed 5 % of the total mass. The non-volatile cations, calcium ( $Ca^{2+}$ ), magnesium ( $Mg^{2+}$ ), and sodium ( $Na^+$ ), were also observed during PCAP events, suggesting that a fraction of larger-mode primary particles may be present in the total  $PM_{2.5}$  mass. Coarse particles are directly emitted, such as dust, road salt, and lake salt, and typically have short lifetimes in the atmosphere. There is a clear diel pattern of particulate  $Ca^{2+}$ ,  $Mg^{2+}$  and  $Na^+$  during the PCAP periods when the vertical mixing is suppressed (Figure 3.9); however, during clean periods, the amounts observed were very close to the detection limits of the AIM-IC.

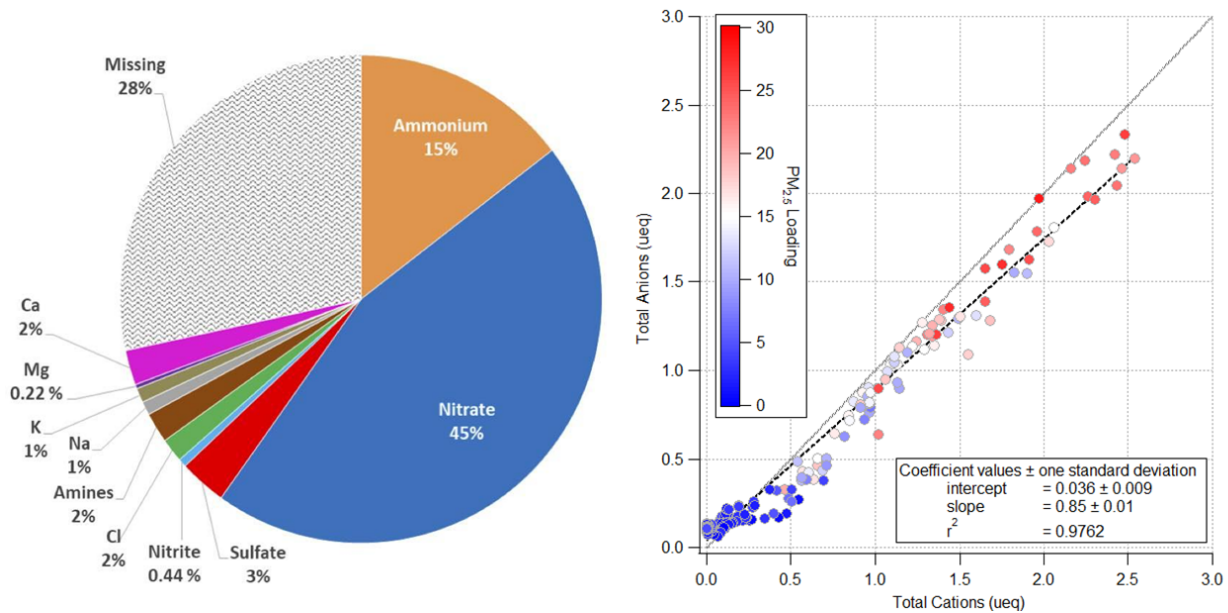


Figure 3.8 Left: Average particle composition of PM<sub>2.5</sub> measured at UU site by AIM-IC for 13-17 February 2017 period. Total PM<sub>2.5</sub> mass was measured by TEOM and matches well the features seen by the AIM-IC, which only resolves the soluble inorganic components. All mass loadings are reported in  $\mu\text{g}$  per standard cubic meter of air. Right: Total  $\mu\text{equivalents}$  of anions ( $\text{Cl}^-$ ,  $\text{NO}_2^-$ ,  $\text{NO}_3^-$ , and  $\text{SO}_4^{2-}$ ) and cations ( $\text{Na}^+$ ,  $\text{K}^+$ ,  $\text{NH}_4^+$ ,  $\text{Mg}^{2+}$ , and  $\text{Ca}^{2+}$ ) measured by the AIM-IC during 13-21 February 2017. The 1:1 ratio is shown in the dashed line. Markers are colored by total measured PM<sub>2.5</sub> mass (not including water).

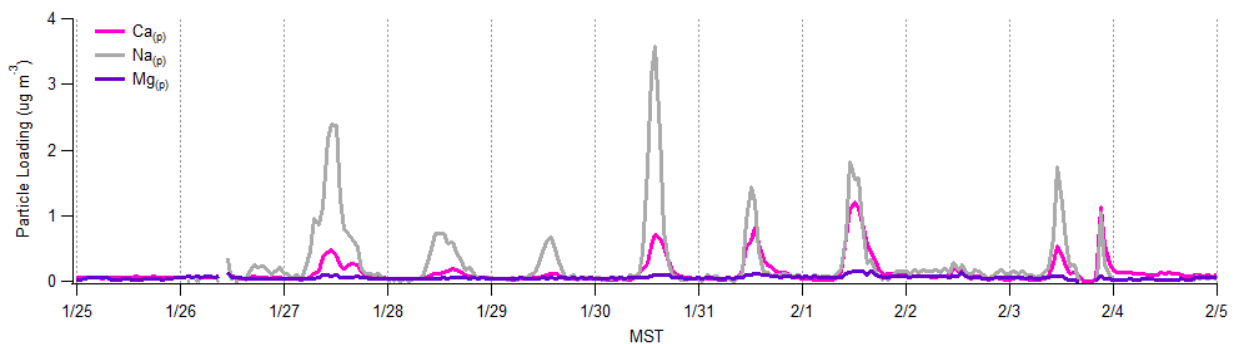


Figure 3.9 Mass concentrations of sodium ( $\text{Na}^+$ ), calcium ( $\text{Ca}^{2+}$ ), and magnesium ( $\text{Mg}^{2+}$ ) in PM<sub>2.5</sub> measured at UU site by AIM-IC for 25 January-5 February 2017 period. All mass loadings are reported in  $\mu\text{g}$  per standard cubic meter of air.

### Ground-based Size Distributions at the University of Utah (UU)

The number size distributions in the range 10 nm to 20  $\mu\text{m}$  measured at the UU site are shown in Figure 3.10. During the strong PCAP event from 26 January – 3 February 2017, there is an obvious diurnal pattern in the aerosol concentration. Particles were persistent throughout the

event and there is clear evidence of overall particle growth from the size distributions. The number concentration was primarily below 900 nm, with extremely high concentrations observed in the range of 30 – 90 nm. The number concentration peaked on 31 January consistent with the trend in PM<sub>2.5</sub> mass concentration (Figure 1.4).

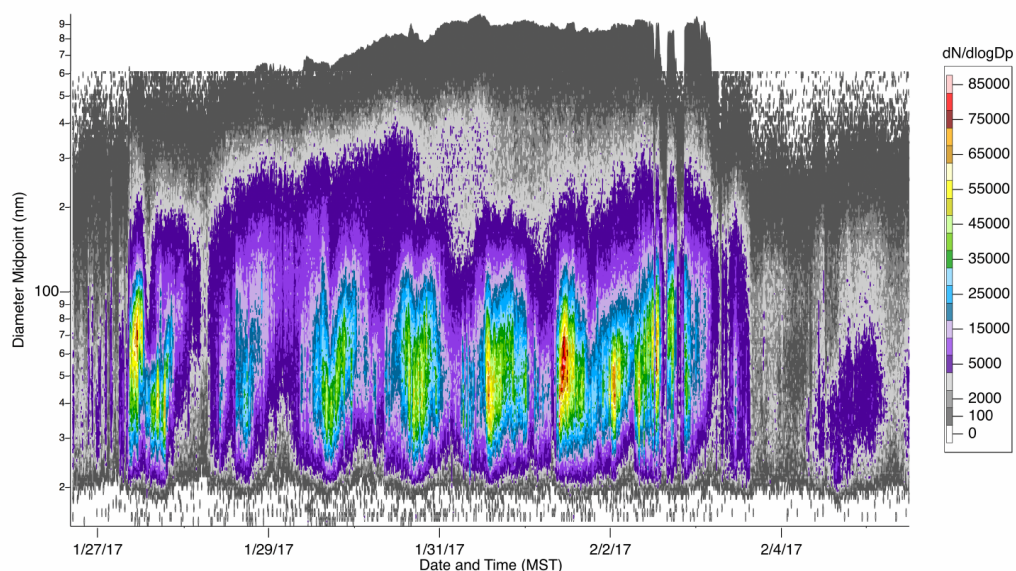


Figure 3.10 Particle size distributions as a concentration matrix, with the x-axis representing time in MST, the y-axis representing the particle size in nm and the colors represent the concentration normalized by size bin ( $dN/d\text{Log}D_p$ ) in number  $\text{cm}^{-3}$ . The data in the figure are from the SMPS and APS instruments at the WBB at UU from 26 January 2017 to 5 February 2017.

### TRAX Observations in the SLV

The TRAX light-rail trains conducted repeated transects across the SLV recording the spatial and temporal evolution of PM<sub>2.5</sub> during PCAP events. An analysis of TRAX data from the previous winter has shown that the spatial pattern of PM<sub>2.5</sub> can be affected by gap flows between the basins, and winds aloft can cause top down erosion of a PCAP boundary layer leading to variable PM<sub>2.5</sub> concentrations across the SLV (Figure 3.11) [57]. In addition, the TRAX train lines pass by several canyon mouths. When air is draining out of the canyons lower PM<sub>2.5</sub> is observed near the canyon mouths, as was observed during a PCAP in December 2016 (Figure 3.12). During the UWFPS study period there was an example of a partial mix-out event on 19 January 2017 where winds aloft scoured out the PM<sub>2.5</sub> from the SLV. This caused ground level PM<sub>2.5</sub> to decrease to  $\sim 10 \mu\text{g m}^{-3}$  for a few hours (yellow shaded region in Figure 3.13) everywhere along the Green TRAX line except at the northern end near the SLC International Airport. After this brief period, the PM<sub>2.5</sub> levels increased again for the rest of the day, and the following day a stronger front completed the mix-out. The TRAX trains also observed inter-basin exchange of polluted air masses with elevated PM<sub>2.5</sub> levels in the morning on 31 January 2017. This case study is shown and discussed in greater detail in section 5.5.

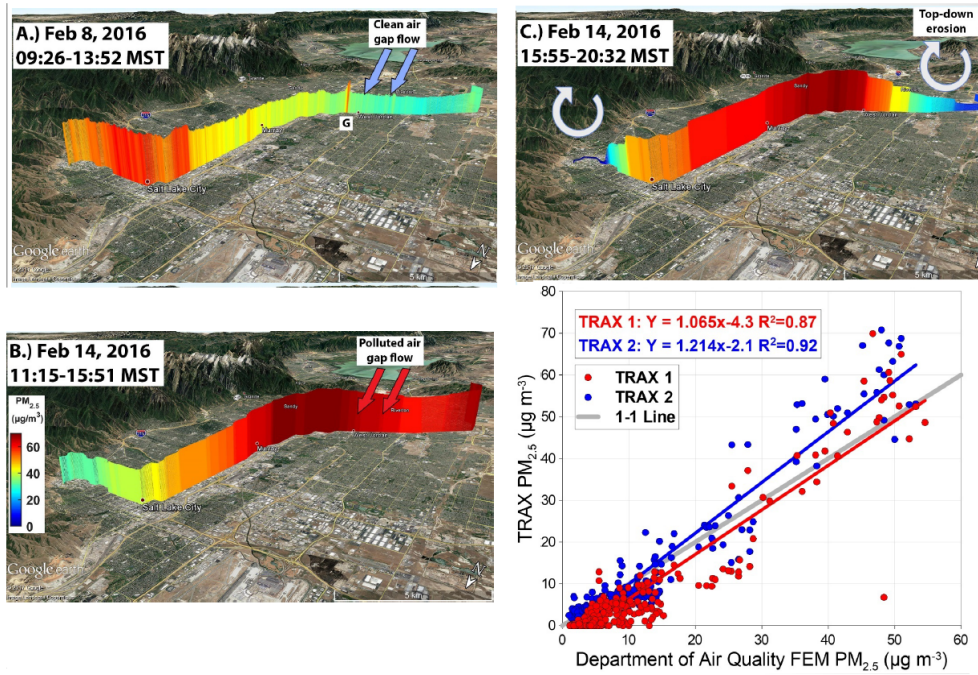


Figure 3.11 Example of different spatial patterns of  $PM_{2.5}$  in the SLV during a PCAP event in February 2016 (panels A-C). Panel D shows the relationship between TRAX observations and the DAQ HW site in February 2016.

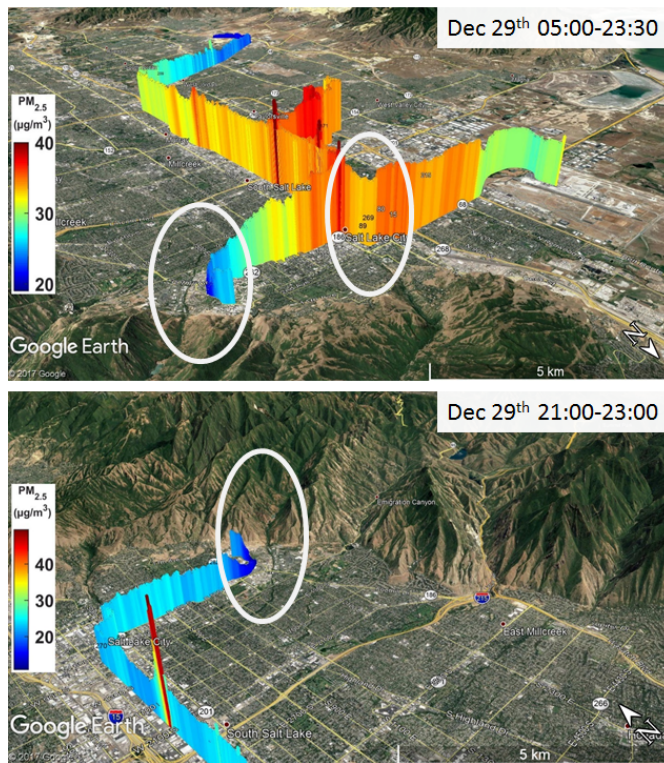


Figure 3.12 Examples of air draining out of the canyons surrounding the SLV with lower concentrations of  $PM_{2.5}$  during a PCAP event in December 2016, indicated by the lower concentrations in the white circles.

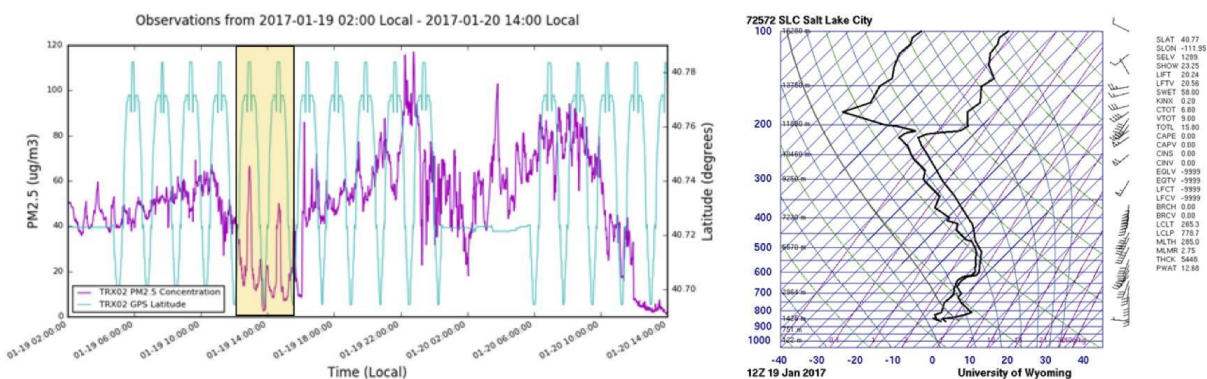


Figure 3.13 Example of a partial mix-out (yellow shaded region in the left panel) on 19 January 2017. During the short period of time when  $PM_{2.5}$  was lower, the spatial pattern observed by TRAX shows higher  $PM_{2.5}$  at the northern part of the Green TRAX line near the SLC airport and lower values elsewhere. The vertical profile indicates moderate winds above the boundary layer that may have scoured the top of the PCAP (right panel).

### 3.1.2 Vertical aerosol distributions

#### Aircraft Results

The study-averaged vertical profiles show, within some variability, decreasing or constant aerosol concentrations as a function of height for all the chemical species measured with the TO-AMS (Figure 3.14). Above about 1700 m ASL, the aerosol mass loadings decrease more markedly and above 2000 m ASL the concentrations are quite low, which is characteristic of the free troposphere.

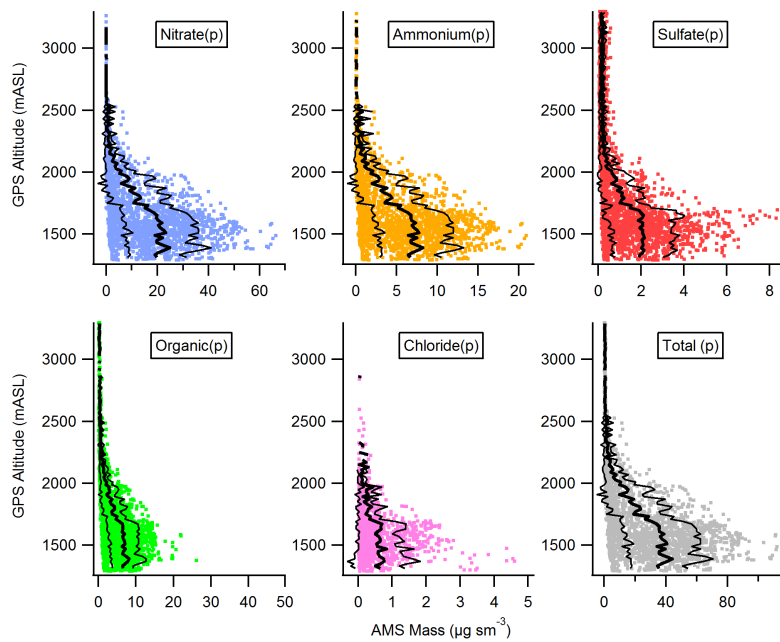


Figure 3.14 Vertical profiles of AMS data (revision R1) obtained from the NOAA Twin Otter aircraft during takeoffs and landings at the SLC airport and selected missed approaches to other airfields in the region. On the x-axes are plotted concentrations of the aerosol nitrate in blue, ammonium in orange, sulfate in red, organic compounds in green, chloride in pink, and the aerosol total mass in grey. On the y-axis is plotted the altitude above sea level. The thick black lines are averages of the concentrations over 20 m steps, the thinner black lines show the variability (one standard deviation) of the averages.

In the SLV the average vertical profile shows a slight increase of mass concentrations with altitude with a maximum at 1650 m ASL (Figure 3.15, left). The average profile relative to Cache Valley shows a constant total aerosol concentration up to 1550 m ASL and a decrease above that height (Figure 3.15, center). In Utah valley, the average mass concentration vertical profile instead decreases rapidly up to about 1800 m ASL (Figure 3.15, right). The clean periods (purple/blue data points) have a decrease in aerosol mass within the first 100 m AGL for the SLV basin. Above that height and at the other locations, the aerosol mass loadings were very low. Although the average profiles indicate general trends during the pollution events, much of the spread in total mass concentrations is due to actual variability in mass loadings over the basins and as a function of height, which was confirmed by higher time-resolution UHSAS measurements along with observations of multiple aerosol layers in some individual vertical profiles. This variability needs to be explored in more detail.

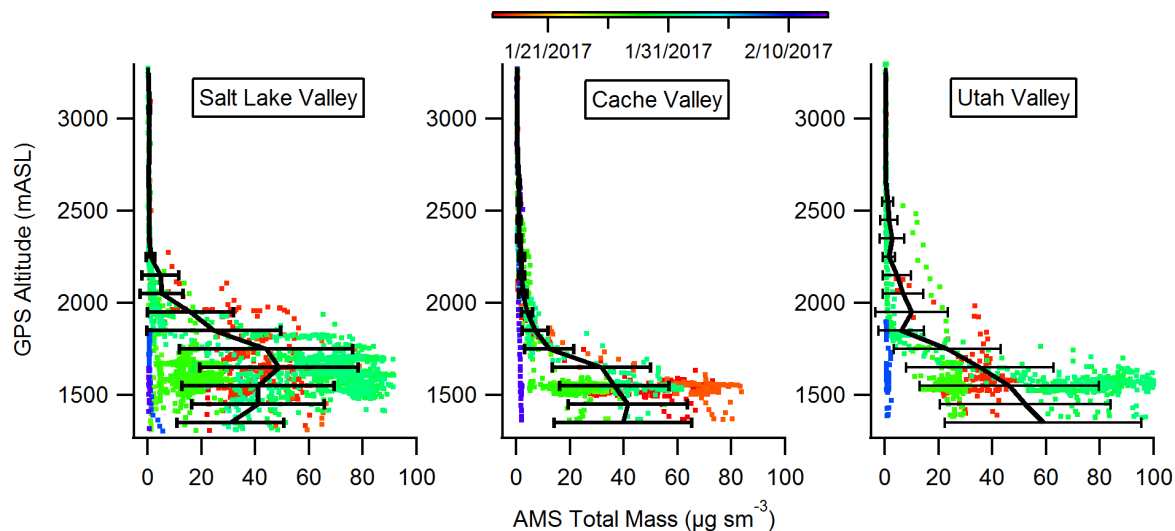


Figure 3.15 Vertical profiles measured using the aerosol mass spectrometer (AMS) on the NOAA Twin Otter (revision R1). On the x-axes are plotted concentrations of the total aerosol mass. On the y-axes is plotted the altitude above sea level. The thick black lines are averages of the concentrations over 100 m steps, the horizontal bars show the variability in the data (one standard deviation). In the left panel are shown data collected during takeoff and landings at the Salt Lake City Airport, in the center are data from missed approaches at the Logan airport in the Cache Valley, and on the right are data from missed approaches at the Provo airport in Utah Valley.

### Balloon Results

Particle counts with size information were collected from balloon measurements near UDAQ's Ogden station as a function of height up to about 175 m AGL at sunrise, mid-afternoon, and sunset. The mid-afternoon data sets show a generally uniform air column with little variation in particle counts from ground to 150 m (500 feet) AGL. The sunset data (typically from about 4:00 p.m. to 30 minutes after sunset) generally show a slow reduction in particulate counts with no clear patterns and no stable layers. The buildup of particulates with sunrise was more interesting, typically exhibiting an altitude dependence and stable layering.

Representative data for two such mornings are shown in Figure 3.16. The top row is from 28 January 2017, a relatively clean day at the beginning of episode #6. The bottom row is day 5 of this event when PM<sub>2.5</sub> levels reached ~ 40 µg m<sup>-3</sup> (Figure 1.4). The GT-526 particulate counter has six channels with channel one measuring 0.3µm-10µm as finest particulates and channel six measuring 5.0µm-10µm as the largest particulates. Three example channels were selected for Figure 3.16. The left column is channel one; the middle column is the channel that measured 1.0µm-10µm particulates; the right column is channel six.

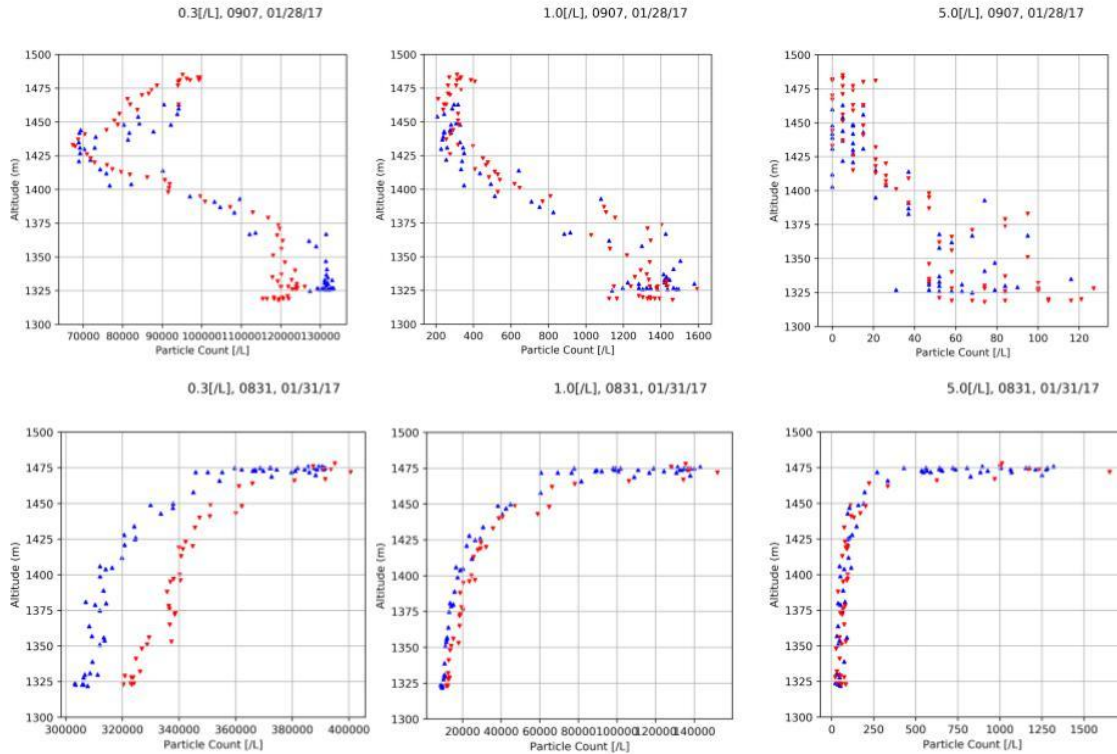


Figure 3.16 The top row is typical of data taken outside of a pollution event (28 January 2017) by the balloon borne Met One GT-526 particle counter. The bottom row is typical of data obtained on the morning of the first day (31 January 2017) of the strongest pollution event that was measured. The particle diameter range for the first column is  $0.3\mu\text{m}-10\mu\text{m}$ , the second column is  $1.0\mu\text{m}-10\mu\text{m}$ , and the third column is  $5.0\mu\text{m}-10\mu\text{m}$ . The blue upward pointing triangles are during ascent, and the red downward pointing triangles are during descent.

At the beginning of pollution events, the primary pattern that was observed had larger PM counts near the ground with the air cleaning out with altitude. Occasional variability could be seen moving through the 150 m (500 foot) vertical column over the course of 20 to 60 minutes. Particulate counts for the six PM size ranges measured by the GT-526 would vary by a factor of 2 to 20. During high pollution events, larger PM number concentrations were typically observed higher in the column. While altitude dependence was clearly observed in the PM counts, the cold air pool appears more uniform for all but the largest sized particulates. The PM counts for the smaller diameter ranges would typically change by factors of 1.3 to 5. The largest particles were different. Sometimes the largest particles exhibited no layering at all, other times there would be 20 times more particulates at 150 m (500 feet) AGL as compared to ground level counts.

As the pollution event settled in, the pattern changed from having the largest counts at higher altitudes to a very uniform air column. This period coincides with the period with plateauing  $\text{PM}_{2.5}$  at the surface in the SLV (Figure 1.4 and Figure 1.6). By the 7<sup>th</sup> day (2 February 2017) of the

event the air column started to display a slight bias towards more particulates near ground level, similar to non-pollution days, but with a smaller spread than observed on non-pollution days.

### News Helicopter Results

Vertical profiles of particulate and ozone pollution were obtained from the KSL-TV helicopter during takeoffs and landings at the SLC airport on the following 10 days (typically ~4-5 pm, but not on all days). These observations enhance other measurements obtained during UWFPS: 16 January, 17 January, 18 January, 20 January, 25 January, 26 January, 27 January, 30 January, 2 February, 3 February 2017.

Two examples of vertical profiles of  $PM_{2.5}$  from the KSL-TV helicopter are shown in Figure 3.17. The vertical structure of the pollution varied considerably during the winter cold-air pools observed during UWFPS, with the variations in pollution layer depth from ceilometers ranging from 100-900 m AGL. On 18 January 2017, the highest pollution concentrations were noted in the lowest 200 m of the boundary-layer, with a deep transition zone where pollution concentrations slowly decreased with altitude within the capping temperature inversion, before the clean air above the inversion was noted around 2200 m ASL. On 3 February, the cold air pool was much shallower based on the gradient in potential temperature, and the depth of the pollution observed by the helicopter was restricted to only between 200 and 300 m AGL (Figure 3.17).

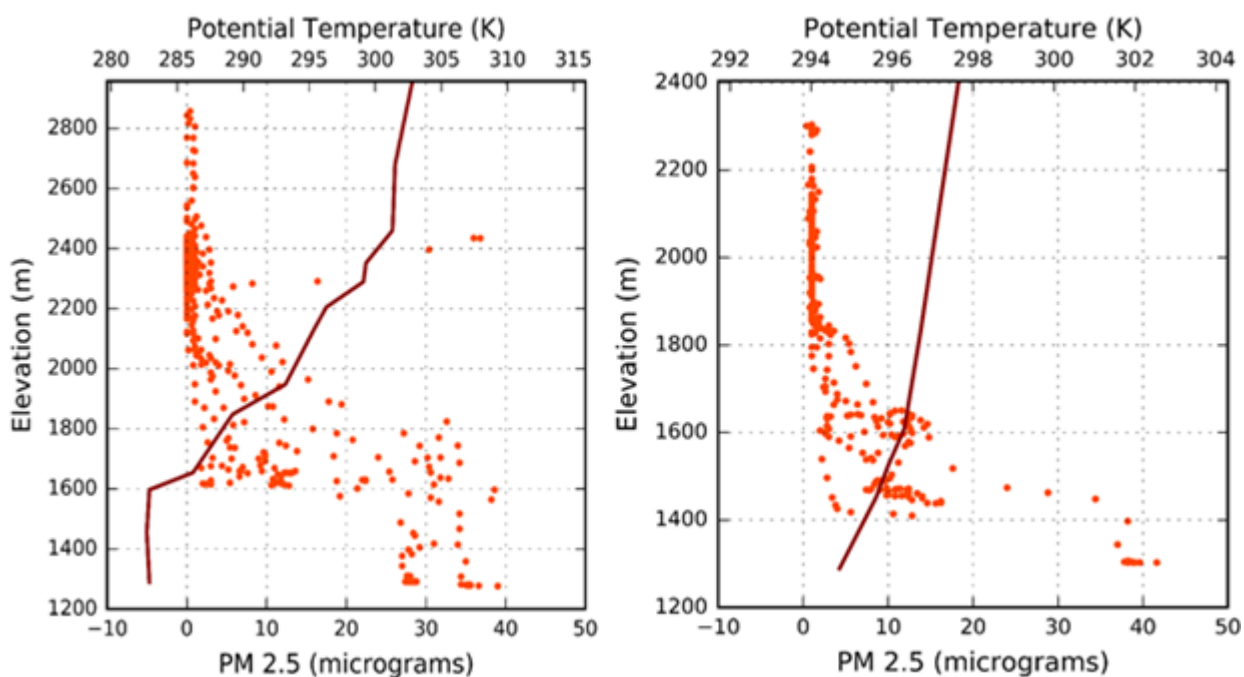


Figure 3.17 Vertical profile of  $PM_{2.5}$  data ( $\mu g m^{-3}$ ) collected in the SLV from KSL-TV helicopter and potential temperature (K, red line) from nearest 0000 UTC rawinsonde observations at the Salt Lake City Airport for helicopter flight periods (left) at 1830-2015 UTC (11:30 am - 1:15 pm MST) on 18 January 2017 and (right) at 2145-2240 UTC (2:45 pm - 3:40 pm MST) on 3 February 2017.

### 3.1.3 Summary and Conclusions

The particle composition during PCAP periods was dominated by  $\text{NH}_4\text{NO}_3$ . While the total mass loadings of aerosols varied with time and location, the relative chemical composition during PCAP events was uniform over all the basins from Cache Valley to the Wasatch front to Utah Valley. This result is supported by observations made by the TO-AMS (Figure 3.2 and Figure 3.3), the L4-AMS (Figure 3.6), the UU AIM-IC (Figure 3.8) as well as by the high correlation of  $\text{NO}_y\text{-NO}_x$  with the measured  $\text{PM}_{2.5}$  in Cache (Figure 3.5). Several measurements showed that the measured ions were balanced, with the number of anions essentially equal to the number of cations (Figure 3.4, Figure 3.7, and Figure 3.8).

Other inorganic species, sulfate and non-refractory chloride (a.k.a. non-lake-salt, non-road-salt, or non-dust), were also present in the aerosol particles, but only as minor components (<9% and <2% on average). These results are supported by the airborne measurements carried out using the TO-AMS, by the ground measurements carried out by the AIM-IC at the UU site, as well as the measurements by the EPA L4-AMS at the Logan ground site. The AIM-IC also consistently detected alkali and alkaline metals (sodium, calcium, and magnesium) in the  $\text{PM}_{2.5}$  size range during the afternoon (Figure 3.9).

The organic fraction measured by both the TO-AMS and the L4-AMS is less than 30% of the total  $\text{PM}_{2.5}$  on average. This observation is consistent with the AIM-IC missing mass, that is 28% and could be from organics, as the AIM-IC does not resolve organic acids or other non-refractory organic material measured by the AMS instruments. The source of the measured organic material in the particulate phase is unknown, however, there may be more information available once the filter samples obtained at Logan and Lindon are analyzed. While black (elementary) carbon could be another aerosol constituent, the aircraft comparison of the measured mass with the measured volume (Figure 3.4) indicates that it is not a large fraction of the mass over the region.

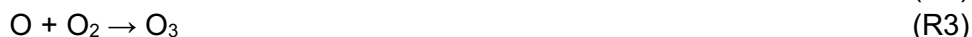
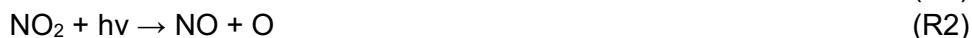
The number concentrations measured at the UU site were primarily for particles smaller than 900 nm, with the highest particle number concentrations observed in the size range of 30 – 90 nm (Figure 3.10). The TRAX trains recorded spatial patterns of  $\text{PM}_{2.5}$  mass across the SLV and when paired with meteorological observations can demonstrate partial mix-out events, “clean” air drainage from the surrounding canyons, and inter-basin exchange of polluted air masses through the Jordan Narrows (Figure 3.11, Figure 3.12 and Figure 3.13).

During high pollution events, PM mass concentrations were higher within the first 500 m AGL (Figure 3.14, Figure 3.15, Figure 3.16 and Figure 3.17). In the SLV, variability in aerosol mass as a function of height above ground suggests the possible presence of elevated aerosol mass concentrations maximizing at altitudes between about 1500-1900 m ASL. In Utah Valley, the vertical concentration profile was at a maximum near the surface. Utah Valley also showed a shallower mixing depth for aerosol species relative to the SLV (Figure 3.14 and Figure 3.15). Cache Valley also presents a shallower mixing depth relative to SLV and a constant mass concentration of aerosols within the first 300 m AGL.

## 3.2 Oxidized Nitrogen and Ozone

Ammonium nitrate ( $\text{NH}_4\text{NO}_3$ ) is formed from the reaction of  $\text{NH}_3$  with  $\text{HNO}_3$ , the latter of which is not directly emitted, but formed by chemical reactions between  $\text{NO}_x$ ,  $\text{O}_3$ , and photochemically produced oxidants from VOCs during the day, or with nitrate-containing aerosol at night [10]. Therefore, a clear picture of the spatial and temporal distribution of  $\text{NO}_2$ ,  $\text{NO}$ ,  $\text{NO}_y$ , and  $\text{O}_3$  is necessary for a full understanding of the formation of ammonium nitrate aerosol, which is the major contributor to  $\text{PM}_{2.5}$  as discussed in Section 3.1.

$\text{NO}_x$  ( $= \text{NO} + \text{NO}_2$ ) is emitted from burning fossil fuels, primarily in the form of  $\text{NO}$  [58]. In the boundary layer,  $\text{NO}$  reacts rapidly (on the time scale of  $\sim 1$ -2 minutes) with tropospheric  $\text{O}_3$  to generate  $\text{NO}_2$  which, during the day, can either photodissociate back to  $\text{NO}$  thus regenerating  $\text{O}_3$  (reactions R1-3), or react further with photochemically produced radicals such as  $\text{OH}$  to make oxidized nitrogen compounds such as  $\text{HNO}_3$  (R4) [59]. In the absence of sunlight,  $\text{NO}_2$  will instead react with  $\text{O}_3$  and then  $\text{NO}_3$  to form  $\text{N}_2\text{O}_5$ , which can further react with nitrate- and chloride-containing aerosol particles to form  $\text{HNO}_3$  and  $\text{ClNO}_2$  (R5-R8) [60].  $\text{NO}$  may also react with  $\text{OH}$  radicals to form  $\text{HONO}$  (R9) [61]. As mentioned above,  $\text{HNO}_3$  can react with gas-phase  $\text{NH}_3$ , which forms a thermodynamic equilibrium with  $\text{NH}_4\text{NO}_3$  in the particle phase (R10) [10, 59].



The sum of all oxidized nitrogen compounds is called  $\text{NO}_y$  ( $= \text{NO} + \text{NO}_2 + \text{NO}_3 + 2\text{N}_2\text{O}_5 + \text{HNO}_3 + \text{ClNO}_2 + \text{HONO} + \text{NO}_3^-(p)$ ) [62] and the evolution in the spatial distribution of both  $\text{O}_3$  and  $\text{NO}_y$  and its components provide a snapshot view of the conversion of  $\text{NO}_x$  emissions to the observed  $\text{PM}_{2.5}$  and can give insight into the chemistry governing this conversion [10, 60]. The instantaneous concentrations of  $\text{O}_3$ ,  $\text{NO}$ , and  $\text{NO}_2$  can also give valuable information about emission point sources, air mass aging, and local chemical conditions [63]. Measurements from all times of day allow us to probe how the diurnal cycle affects  $\text{HNO}_3$  formation, and thus formation of  $\text{NH}_4\text{NO}_3$  [59]. Vertical profiles of these species provide insight into the influence of atmospheric mixing on the formation of  $\text{HNO}_3$  and other  $\text{NO}_y$  compounds. The wide range of compounds measured, platforms utilized (ground sites, aircraft, light rail, remote sensing and balloon sondes), and spatial areas covered allow us to examine how various conditions can lead to  $\text{PM}_{2.5}$  buildup in the northern Utah Valleys.

During the UWFPS campaign, NO<sub>2</sub>, NO, NO<sub>y</sub> (and some of its components), and O<sub>3</sub> were measured with a variety of techniques, yielding a data set spanning a wide horizontal, vertical, and temporal range. Six ground sites (two each in the Cache, Salt Lake, and Utah Valleys) monitored NO<sub>2</sub>, NO, and O<sub>3</sub> continuously throughout the campaign, with two sites also measuring NO<sub>y</sub>. The TRAX light rail instrumentation monitored NO<sub>2</sub> and O<sub>3</sub> on the SLV floor continuously throughout the campaign, with some spatial distribution throughout the valley. NO<sub>2</sub> and O<sub>3</sub> remote sensing column measurements were conducted at one site each in the Cache, Salt Lake, and Utah Valleys. Ozonesondes measured between one and three near-surface vertical profiles of O<sub>3</sub> at varying times of day during pollution episodes #6 and #7 at the end of January and mid-February. The Twin Otter payload included a measurement of NO<sub>2</sub>, NO, total NO<sub>y</sub>, O<sub>3</sub>, HONO, N<sub>2</sub>O<sub>5</sub>, HNO<sub>3</sub>, ClNO<sub>2</sub>, and NO<sub>3</sub><sup>-</sup>(p), with flight tracks detailed in Section 2.1.2 and multiple vertical profiles throughout the boundary layer. This full data set is four-dimensional, spanning the horizontal and vertical directions, and extending through time. By taking “cuts” through one dimension, we can look at evolution of the trace gases (temporal), differing air chemistry in different basins (horizontal), and the distribution of trace gases within the boundary layer (vertical), as summarized in Table 3.1

*Table 3.1* A summary of NO<sub>2</sub>, NO, O<sub>3</sub>, and NO<sub>y</sub> measurements during the UWFPS campaign.

<b>Platform</b>	<b>Species Measured</b>	<b>Temporal Evolution</b>	<b>Horizontal Distributions</b>	<b>Vertical Distributions</b>
Twin Otter	NO <sub>2</sub> , NO, O <sub>3</sub> , total NO <sub>y</sub> , NO <sub>y</sub> components	Compare repeated flight tracks	Separate by valley	Vertical profiles
TRAX	NO <sub>2</sub> , O <sub>3</sub>	1) Track data during stationary periods at train depot 2) Compare repeated rail tracks	Compare regions of the SLV	Compare data near UU and bottom of valley floor
Ground sites	NO <sub>2</sub> , NO, O <sub>3</sub> Total NO <sub>y</sub> at some sites	Track time evolution of each species	Compare ground sites in different valleys	1) Compare UU and HW 2) Compare to Twin Otter overflights
Tethered Balloon Ozonesonde	O <sub>3</sub>	1) Compare repeated sondes 2) Compare surface layer data to ground site	-	Compare to Twin Otter vertical profiles and columns

Pandora Columns	NO <sub>2</sub> , O <sub>3</sub>	Compare repeated columns	Compare different column sites	Compare to Twin Other vertical profiles and ozonesondes
--------------------	----------------------------------	-----------------------------	--------------------------------------	---------------------------------------------------------------

Figure 3.18 shows ground site time profiles for NO<sub>2</sub>, NO, O<sub>3</sub>, and O<sub>x</sub> (= O<sub>3</sub> + NO<sub>2</sub>) in four frames during the main UWFP intensive window. Within each frame, the time traces are separated by valley, as each distinct valley contains a different air mass, and there is reasonably good agreement between the two ground sites in each valley. Frame (a) shows NO<sub>2</sub> time traces for each ground site. While there are some direct sources of NO<sub>2</sub>, the majority is formed by the reaction of NO and O<sub>3</sub>, and is partially depleted by photolysis during the day [58]. For this reason, there is a clear diurnal cycle in the time trace, with a decrease in NO<sub>2</sub> beginning at sunrise, indicated by light yellow bars, superimposed on the general increase in the NO<sub>2</sub> baseline during pollution events. The ground sites within each valley generally agree with each other, with small differences attributable to either local NO<sub>x</sub> sources near each ground site or instrument differences. The sites in the Cache and Utah Valleys used instrumentation that measured NO<sub>2</sub> either via a molybdenum converter (SM and NP) or UV photolysis (LN) followed by chemiluminescence or by direct spectroscopic methods (L4). Previous work has demonstrated a disagreement between the two techniques [64], which may be driving some of this disparity.

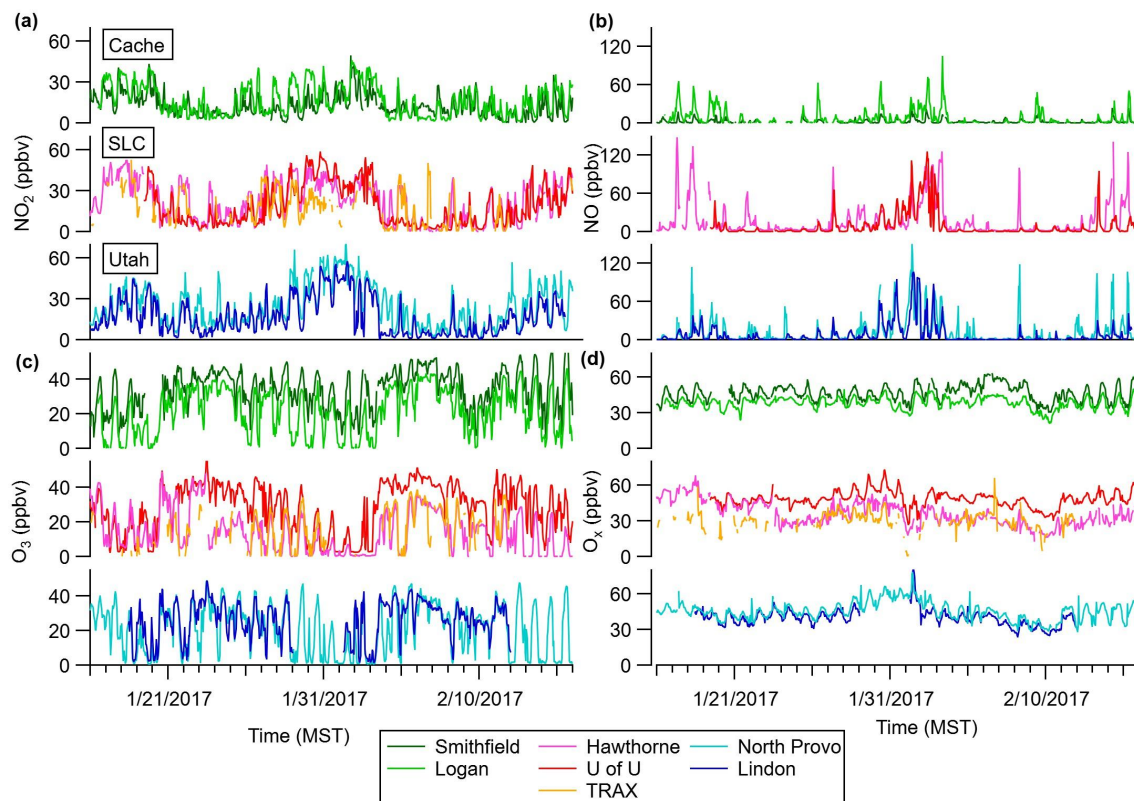


Figure 3.18 Time traces of NO<sub>2</sub>, NO, O<sub>3</sub>, and O<sub>x</sub> measured at the respective ground sites in the three valleys during the main UWFP intensive window. Other UDAQ ground sites in the area (not shown here) also monitor these species continuously.

Frame (b) shows the NO traces. NO is directly emitted by fossil fuel burning, and therefore an NO spike is observed each morning, presumably due to the morning rush hour, which then reacts with O<sub>3</sub> during the day. A corresponding peak during the evening rush hour is not as evident, possibly because the mixing layer height (MLH) is higher in the evenings, thus diluting the NO concentration. In the top trace of frame (b), a comparison between the SM and L4 sites demonstrates the effect of an urban site – L4, located closer to both the city center and to USU, shows much higher NO spikes than the more rural SM site. A similar trend is seen at some points in the comparison of HW and UU. In this case however, the UU site is located at a point partway up the basin wall, and thus this may also represent a vertical spatial difference. Additionally, this site is likely more susceptible to canyon up- and down-flows (see Section 5 for further discussion as well as [15]). For comparison, the NO<sub>2</sub> measurement from the TRAX when it was stationary at the train depot on the valley floor shows close agreement with the nearby HW ground site. In frame (c) ozone displays the inverse trend of NO<sub>2</sub>: a strong diurnal cycle overlaid on a general decrease during pollution episodes. In fact, it is nearly removed in some valleys during pollution episodes, though not in others. Finally, because NO, NO<sub>2</sub>, and O<sub>3</sub> can interconvert during the day (R1-3), it is also useful to consider O<sub>x</sub> (O<sub>3</sub> + NO<sub>2</sub>) in frame (d), which is insensitive to that interconversion [60]. If this interconversion process between NO<sub>2</sub> and O<sub>3</sub> was the only chemistry occurring, we would expect to see this time trace as a flat line. The presence of diurnal variations indicates the presence of other NO<sub>x</sub> reservoirs, additional chemistry, or possibly mixing in of O<sub>3</sub> from aloft.

Averaged diurnal profiles for each of the four species at the six ground sites are shown in Figure 3.19. Profiles were averaged separately for days during pollution episodes (solid lines) and non-pollution events (dashed lines). Overall, NO<sub>2</sub> and NO are higher during pollution episodes, and O<sub>3</sub> is lower, as expected. The O<sub>x</sub> diurnal profiles are slightly higher during pollution episodes in the Salt Lake and Utah Valleys, but fairly similar to non-pollution events in the Cache Valley. It is in these traces that the differences between ground sites become more obvious. For example, the NO diurnal averages appear to be more intense and have earlier onsets in the ground sites closer to morning traffic (L4 vs. SM, and HW vs. UU). The other species have very little variability in shape from valley to valley, only differences in magnitude. The SLC sites have a significant disagreement in the magnitude of their O<sub>x</sub> profiles, which may be due to their locations along the basin wall. The O<sub>x</sub> profiles in the other two valleys are fairly similar to each other.

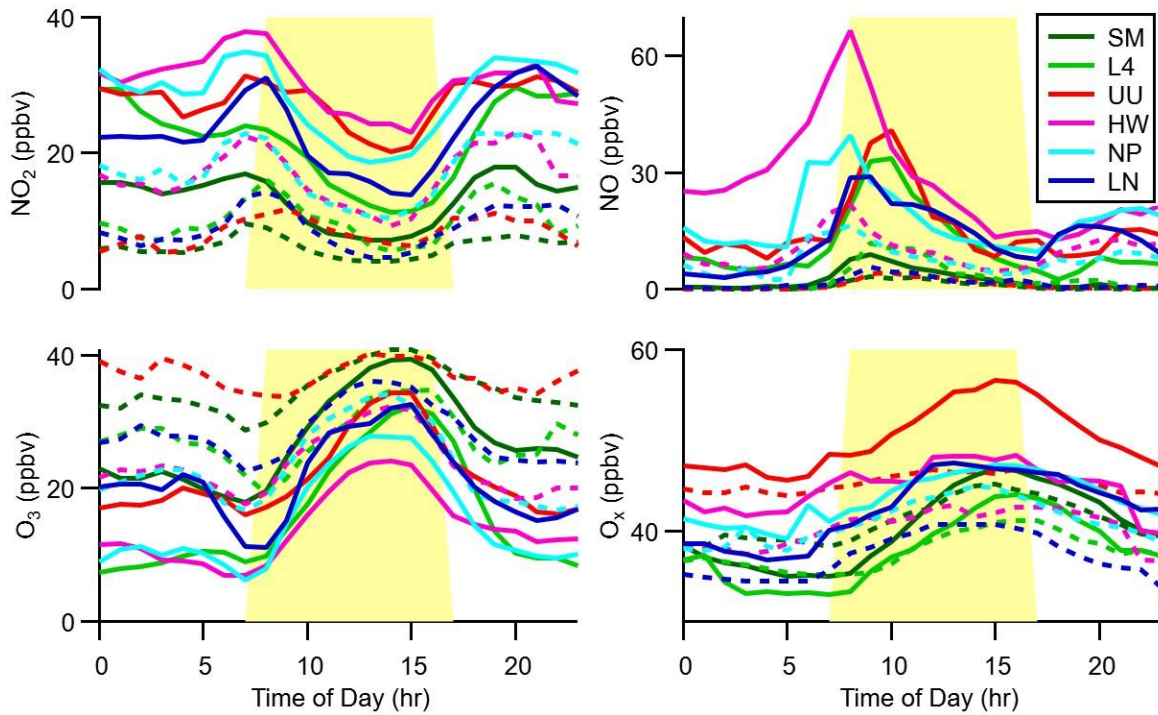


Figure 3.19 Averaged diurnal profiles of  $\text{NO}_2$ ,  $\text{NO}$ ,  $\text{O}_3$ , and  $\text{O}_x$  for the six ground sites from 12/01/2016 - 2/28/2017. Solid lines are diurnal profiles consisting of data taken during pollution episodes, and dashed lines consist of data taken during non-pollution events. The yellow shading indicated daytime hours.

Figure 3.20 shows horizontal distributions of  $\text{NO}_2$  and  $\text{O}_3$  throughout the northern Wasatch Front, as measured by the Twin Otter on repeated flights throughout the area. The four frames each contain a single daytime flight track, colored and sized by either  $\text{NO}_2$  (left) or  $\text{O}_3$  (right). The upper frames show a typical flight during a pollution episode, and the lower frames show a typical flight outside of a pollution episode. It should be noted that these figures contain flight data both within and outside the boundary layer (see Figure 2.3 for typical altitude profiles associated with each flight track). Outside of pollution episodes,  $\text{NO}_2$  is low (generally  $< 2$  ppbv) throughout the region, with the exception of several point sources, and  $\text{O}_3$  is fairly uniform, in the 40-50 ppbv range. During pollution episodes, significant amounts of  $\text{NO}_2$  are detected (upwards of 30 ppbv), particularly in urban areas. The corresponding  $\text{O}_3$  trace shows much more variability, as would be expected given the  $\text{O}_3/\text{NO}_2$  interchange process.

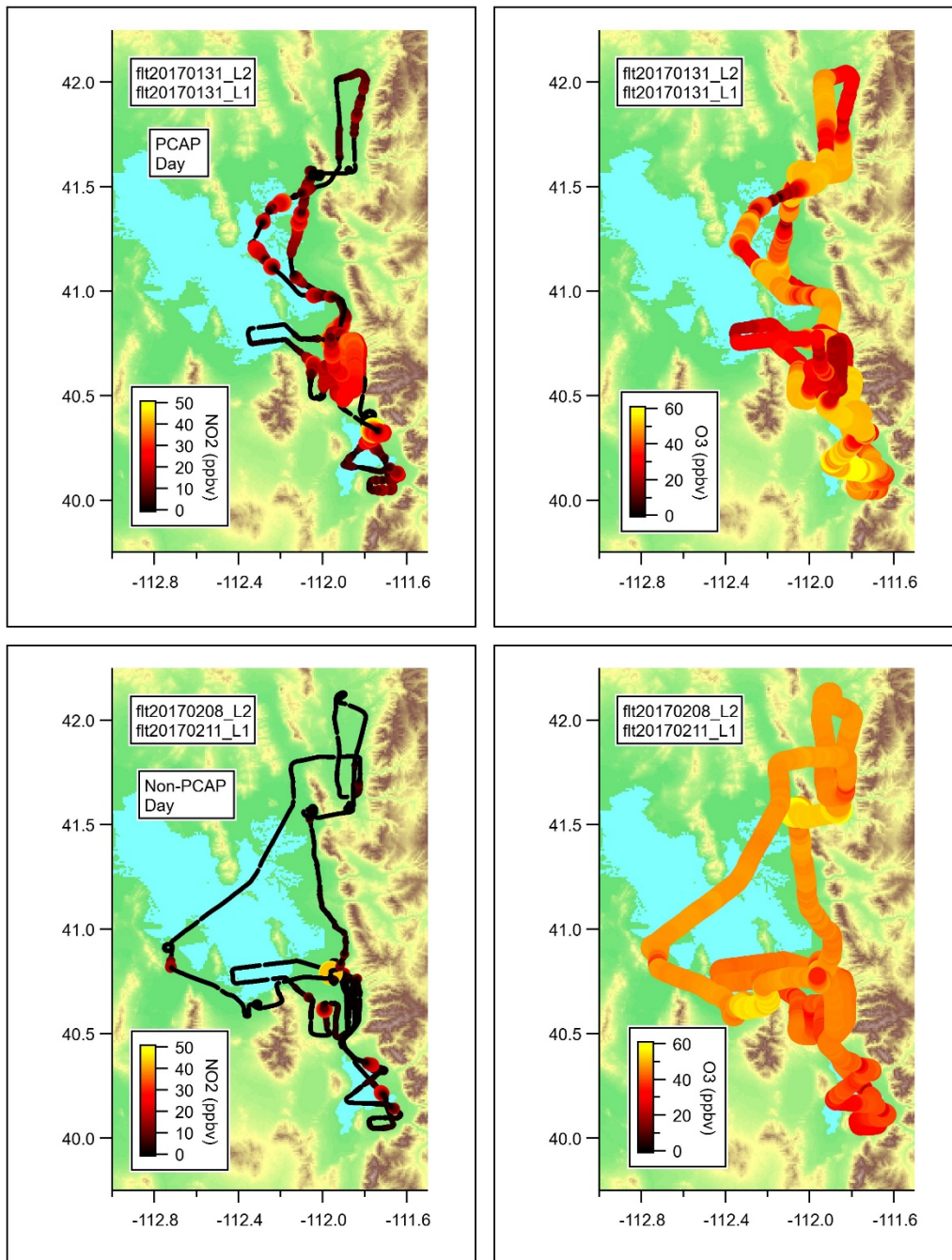


Figure 3.20 A typical Twin Otter flight track, colored and sized by NO<sub>2</sub> (left) and O<sub>3</sub> (right), during a pollution episode (upper) and non-pollution (lower) event.

Figure 3.21 shows an expanded view of the SLV, where the Twin Otter did repeated raster patterns above the city. During some of these flights, the TRAX 2 train car was running throughout the valley on the Red train line. The flight and train tracks are colored by either NO<sub>2</sub> (left) or O<sub>3</sub>

(right) during a typical pollution episode (upper) or non-pollution (lower) event. The TRAX data from a single pass through the city at ~16:00 local time on January 31 (upper panels), and ~07:00 on February 10 (lower panels) are shown in outlined circles. Those dates were selected to provide the closest possible comparison with the Twin Otter flights, which occurred at ~13:00 and ~06:00 on those days, respectively. The TRAX and Twin Otter data agree well for the NO<sub>2</sub> observations, and less so for the O<sub>3</sub> observations, which may be consistent with the pattern of partial O<sub>3</sub> depletion near the ground, closer to local NO<sub>x</sub> sources (see following paragraphs). Similar comparisons can be made for several other Twin Otter flights.

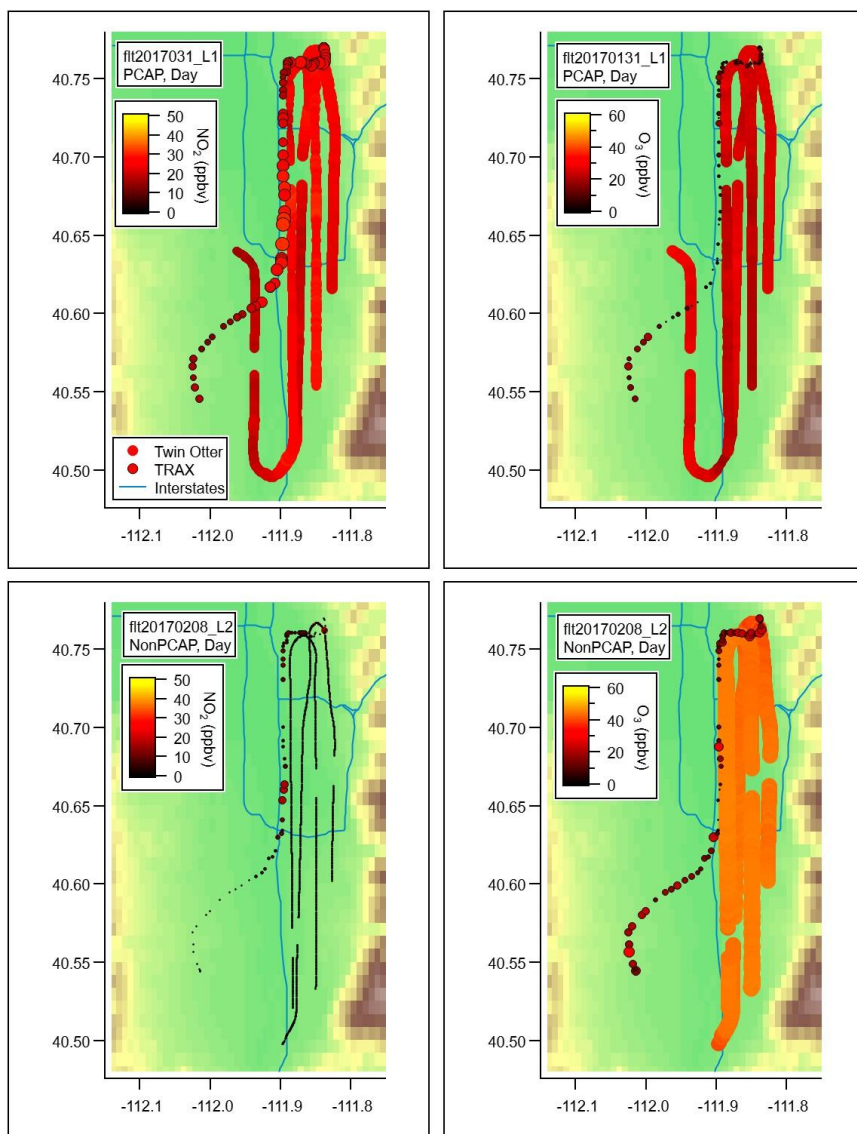


Figure 3.21 A portion of the flight tracks from Figure 3.20 zoomed in on the Salt Lake City region, colored and sized by NO<sub>2</sub> (left) or O<sub>3</sub> (right), during a pollution episode (upper) or non-pollution (lower) event, with a typical TRAX trip overlaid in outlined circles, with the same coloring. Major interstates are shown in blue lines.

The differences between the horizontal distributions in Figure 3.21 at the surface (TRAX) and aloft (Twin Otter) highlights the chemical detail that can be derived by examining vertical distributions of O<sub>3</sub> and NO<sub>x</sub>. Comparisons between a given ground site and the Twin Otter when it flew overhead allow us to probe these vertical distributions, even over areas where the Twin Otter could not do a missed

approach, and thus, lacks the full vertical profile. The aircraft and ground level data are expected to be more correlated during the day, and during non-pollution events, since the boundary layer is well mixed then, though there can still be strong influences of local sources. Figure 3.22 shows three ground sites that had frequent Twin Otter flyovers: SM in the Cache Valley, UU in the SLV,

and LN in the Utah Valley. The ground site data is shown in solid line, with an averaged value from the Twin Otter during the flyover (defined as < 3 km from the ground site) shown in solid circles. In the middle frame, data from UU is shown with both Twin Otter flyover data, and averaged values from when the TRAX passed within 1 km of the University site in triangles. As can be seen in all three frames, the ground site data generally agrees with the Twin Otter and TRAX data, but there are some clear deviations, likely due to actual differences at the surface and aloft. To demonstrate this further, Figure 3.23 shows the O<sub>3</sub> data on the Twin Otter compared directly to the hourly O<sub>3</sub> data from the ground site. In the left frame, all flyovers are shown, at all ground sites, and while a high percentage of the points fall on the 1:1 line shown in dashed line, some are above the line, consistent with O<sub>3</sub> depletion by NO near the surface. In the right frame, only data taken during daytime hours is plotted, and this data falls closer to the 1:1 line, as is to be expected since daytime air is more mixed. However, it should be noted that these plots do not differentiate between pollution episodes and clear conditions.

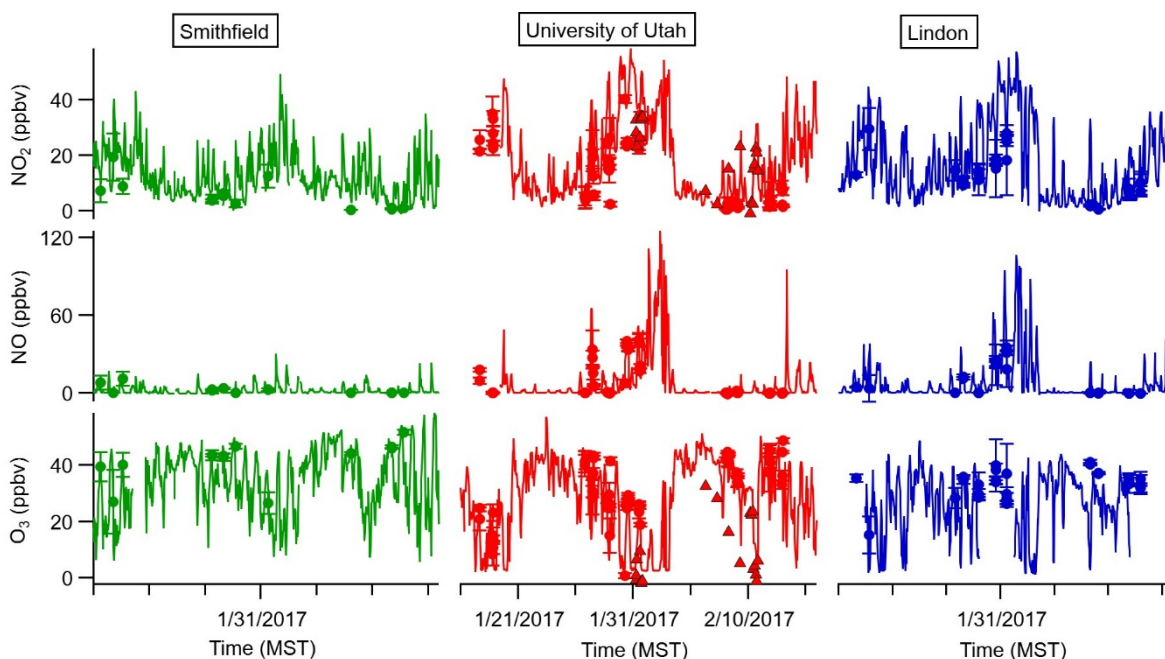


Figure 3.22 Time traces of NO<sub>2</sub>, NO, and O<sub>3</sub> for three representative ground sites are shown in solid line, with averaged values from the Twin Otter and TRAX shown in circles and triangles, respectively, when each vehicle passed nearby the ground site. Similar plots can be made for other UWFPS and UDAQ sites, such as in Figure 3.24 and Figure 3.25.

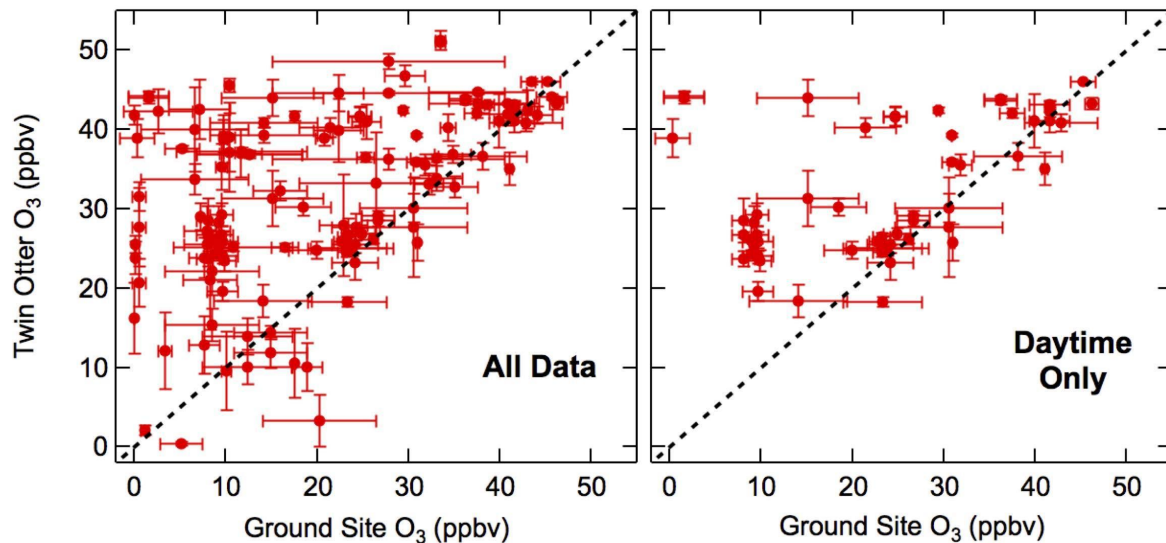


Figure 3.23 Comparison of ozone measurements on the Twin Otter and on the ground. In the left panel, all Twin Otter flyovers at all ground sites are plotted. In the right panel, only daytime flyovers are plotted.

A comparison between a Pandora column  $\text{NO}_2$  measurement and a nearby ground site measurement, shown in Figure 3.24, is a further demonstration of the effect of decreased vertical mixing during pollution episodes. The two panels show the comparison between the 1-min averaged  $\text{NO}_2$  measured at the Logan ground site in grey solid line, with the Pandora total  $\text{NO}_2$  column data in black circles, for a clear day (upper panel) and a polluted day (lower panel). The two traces are comparable in the upper panel, when a convective boundary layer ensures strong vertical mixing, and in the lower panel, there is a wide discrepancy when the boundary layer becomes stable during a pollution event, with much higher  $\text{NO}_2$  concentrations at the surface.

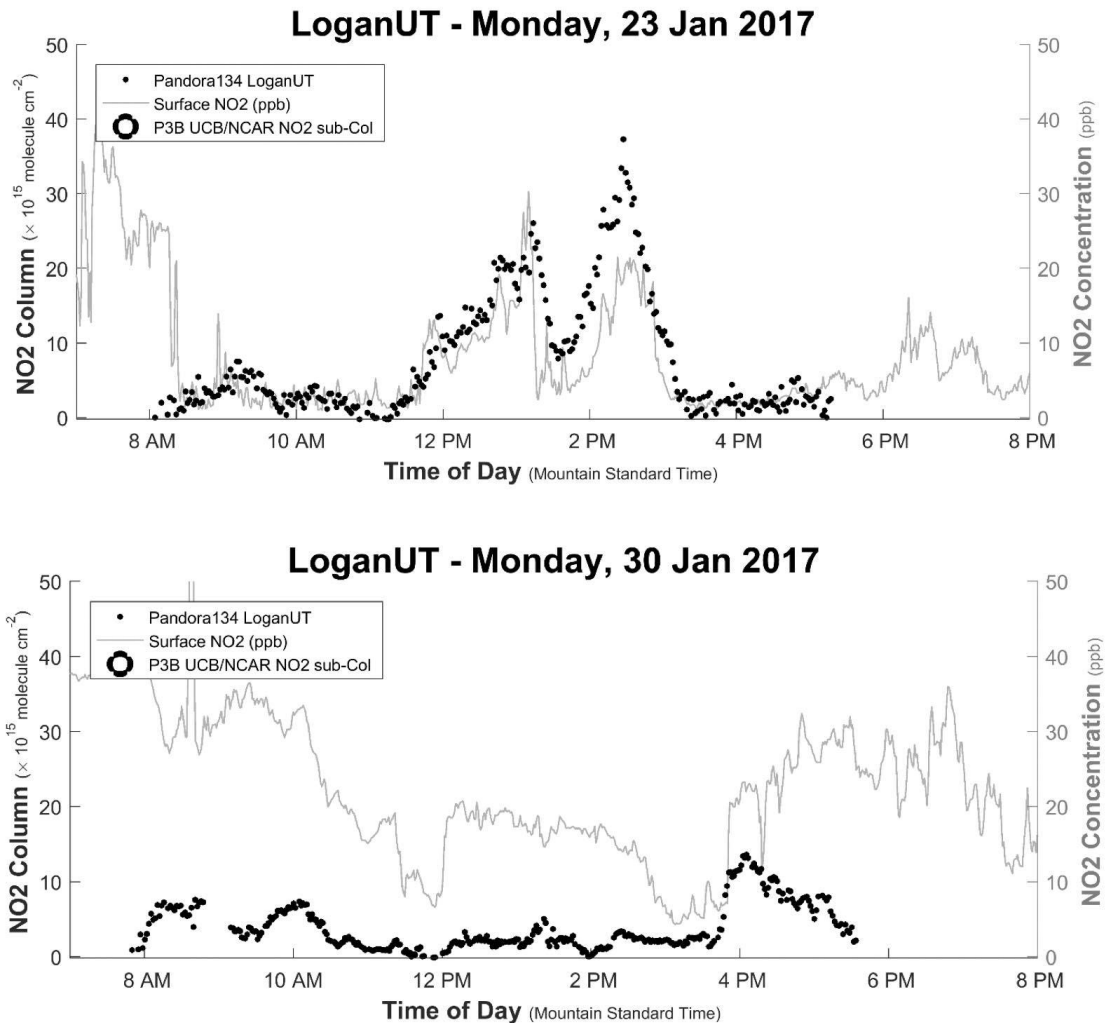


Figure 3.24  $\text{NO}_2$  concentrations on two days in January, as measured at the Logan ground site (grey line), and by the Pandora column in Logan (solid circles).

More detailed information can be derived about the vertical distributions of  $\text{NO}_x$ ,  $\text{NO}_y$ , and  $\text{O}_3$  by examining the balloon ozonesonde data and the Twin Otter during vertical profiles – defined here as a sustained increase or decrease in altitude, by more than 1 m/s for at least 90 seconds. Ozonesondes were taken several times per day during pollution episode #6, and they provide a detailed look at the daily evolution of ozone in the surface layer. The left panel of Figure 3.25 shows a typical set of ozonesonde ascents and descents, taken on the morning of January 29, just after the pollution episode began. The profiles are colored by time, with the red trace corresponding to approximately 07:15 local time, and the purple to 09:30. The  $\text{O}_3$  profile changes dramatically within first 150 m during this time, as the convective boundary layer (CBL) starts to develop. By averaging the data near the surface (as shown in larger circles in the left panel), the ozonesonde data can also be compared to a nearby ground site (the UDAQ Ogden site, which was not an official part of the UWFPS campaign, and as such has not yet undergone final quality control). The two closely agree (right panel), and demonstrate the value of having vertical profile

information during this time to examine the ozone during the layer setup aloft. Additionally, averaged data from the Twin Otter flyovers is shown in blue circles. The UDAQ Ogden site is situated near the Ogden airport, so unlike the other ground sites shown in Figure 3.22, the Twin Otter passed this ground site at very low altitude, near the bottom of the missed approach. Therefore, the blue circles in Figure 3.25 (right) represent Twin Otter data near the surface, and as a result match the ground site data closely. However, there are some discrepancies, likely due to the fact that the Twin Otter always remains higher in altitude than the ground site. The left panel demonstrates how sensitive the  $O_3$  concentration is to small changes in altitude near the surface.

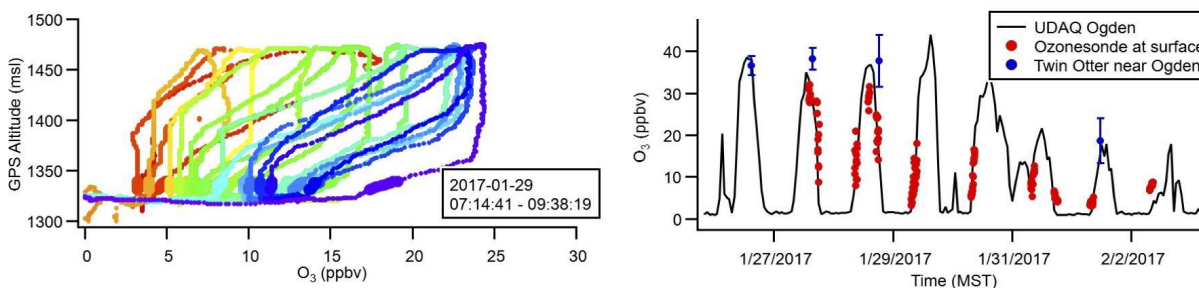


Figure 3.25 A typical ozonesonde (left) with 13 ascents and descents in the morning hours as the CBL starts to develop. By averaging only the data at the surface, indicated by the large circles, the ozonesonde data can be directly compared to  $O_3$  measurements at a nearby UDAQ monitoring site (right). In the right panel, surface level  $O_3$  time traces from both the ozonesonde (red circles) and Twin Otter missed approaches in Ogden (blue circles) are overlaid on the ground site (black line).

In addition to the ozonesondes, vertical profiles of all species measured on board the Twin Otter provide a look at the evolution of the boundary layer during a pollution episode. Figure 3.26 and Figure 3.27 show averaged vertical profiles of  $NO_2$ ,  $NO$ ,  $O_3$ , and total  $NO_y$ , consisting of the averages of all profiles lasting more than 90 seconds within a single valley. Figure 3.26 shows vertical profiles in the SLV on four days just before and during pollution episode #6, spaced approximately two days apart. In the first frame, the pollution episode has not yet begun and the distributions of  $NO_x$  and  $NO_y$  are enhanced to only a few ppbv below 2000 m ASL (700 m AGL). As the episode progresses,  $NO_x$  and  $NO_y$  grow in, and  $O_3$  is depleted at low altitude. This trend is also evident in the ground site data. However, the vertical profiles demonstrate that as the episode progresses, the majority of the  $NO_2$  and  $NO_y$  is aloft. Figure 3.27 shows averaged vertical profiles for the entire UWFPS campaign, both in and out of pollution episodes, for the three major valleys. This figure condenses any time evolution within the pollution episode, but highlights the differences between valleys. In particular, the SLV sometimes displays a higher concentration of  $NO_x$  and lower  $O_3$  aloft during pollution episodes, while the peak of the distribution in the Cache Valley is closer to the ground. These vertical profile shapes may reflect a chemical mechanism, meteorological conditions or emissions source specific to the each valley. A key part of the upcoming analysis will be interpreting these shapes and how they impact the formation of  $PM_{2.5}$ .

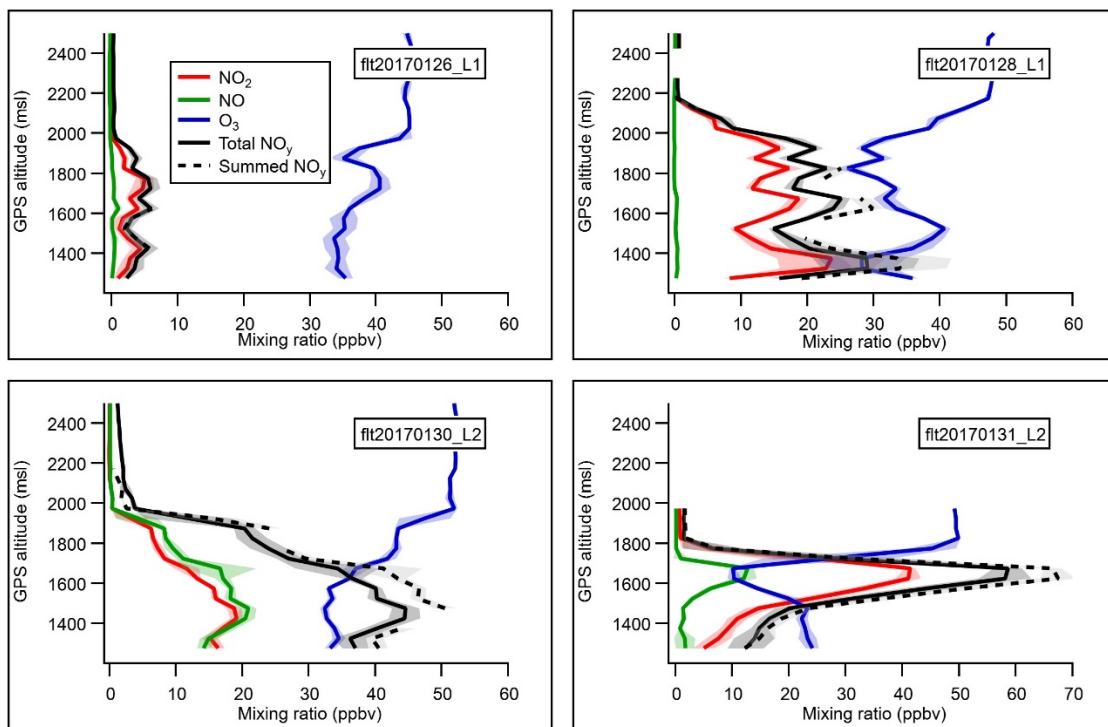


Figure 3.26 Averaged vertical profiles of  $\text{NO}_2$ ,  $\text{NO}$ , total  $\text{NO}_y$ , summed  $\text{NO}_y$ , and  $\text{O}_3$  during sustained ascents and descents in the SLV, on four flights spanning the extent of the major pollution event in late January.

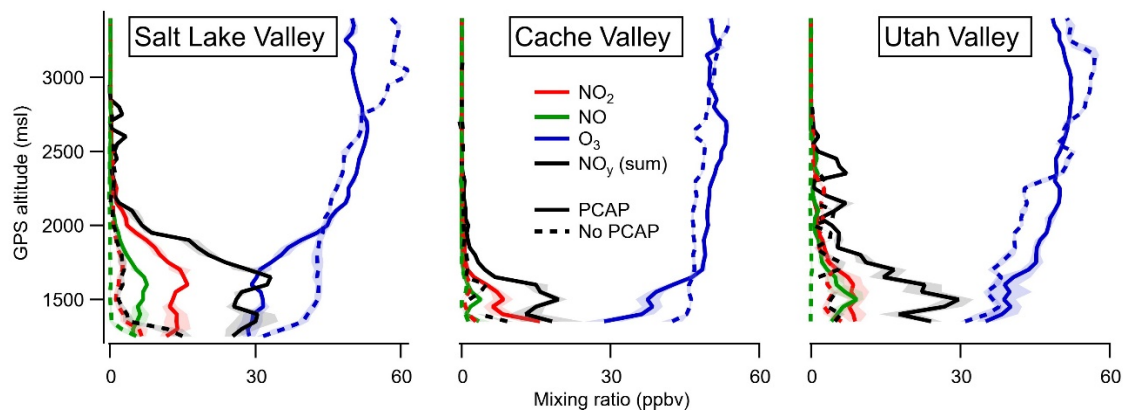


Figure 3.27 Averaged vertical profiles for three major basin in northern Utah. Vertical profiles of  $\text{NO}_2$ ,  $\text{NO}$ , summed  $\text{NO}_y$  and  $\text{O}_3$  for the entire UWFPs campaign are separately averaged for pollution episodes (solid lines) and non-pollution events (dashed lines).

As discussed in the first paragraph of this section, total  $\text{NO}_y$  is defined as the sum of all reactive nitrogen species, and is detected by the NOAA  $\text{NO}_2$  CRDS instrument via thermal dissociation to  $\text{NO}_2$ . Many of the individual components of  $\text{NO}_y$  were also measured on the aircraft by the CIMS and AMS instruments, and can be summed together to yield a summed  $\text{NO}_y$  measurement (sum  $\text{NO}_y = \text{NO}_2 + \text{NO} + \text{HNO}_3 + \text{ClNO}_2 + 2\text{N}_2\text{O}_5 + \text{NO}_3(\text{p}^-)$ ). The  $\text{NO}_y$  channel on the Twin Otter does

not sample 100% of the ammonium aerosol nitrate, so the total  $\text{NO}_y$  is slightly smaller than the summed  $\text{NO}_y$ ; the full characterization of the total  $\text{NO}_y$  channel measurement efficiency is still in progress. The majority of the  $\text{NO}_y$  is  $\text{NO}_x$ ,  $\text{NO}_3^-$ (p), and some  $\text{HNO}_3$ , and thus analogous plots to those displayed in Figure 3.26, as well as comparisons to ground sites, could be derived for each of these species. Section 3.1 contains some of these plots for aerosol phase  $\text{NO}_3^-$ . These vertical profiles provide a more detailed look at the chemistry occurring aloft.

Finally, a critical part of analyzing the observed  $\text{NO}_x$  and  $\text{O}_3$  will be comparison of the observations to modeled emissions. The left panel of Figure 3.28 shows 24-hr averaged modeled emissions (in moles/hr) of  $\text{NO}_x$  (defined here as  $\text{NO} + \text{NO}_2 + \text{HONO}$ ) in the northern Utah Valleys on February 1, 2017, using the SMOKE modeling system. Hotspots are visible near the urban corridors, as expected. In the center and right panels are sample Twin Otter flight tracks colored by observed  $\text{NO}_x$  (defined as  $\text{NO} + \text{NO}_2$ , since the HONO measurement is being finalized and is a minor contributor, usually  $< 300$  pptv), with an example from a pollution episode in the center, and a non-pollution event on the right. While the emissions model reports emissions, and the Twin Otter reports observed  $\text{NO}_x$ , which is a combination of emitted and chemically produced  $\text{NO}_x$ , two images nevertheless show the same regions of elevated  $\text{NO}_x$ , particularly in the urban corridors of SLC, Brigham City, Ogden, and Provo. Further analysis of these models can be found in Section 7.

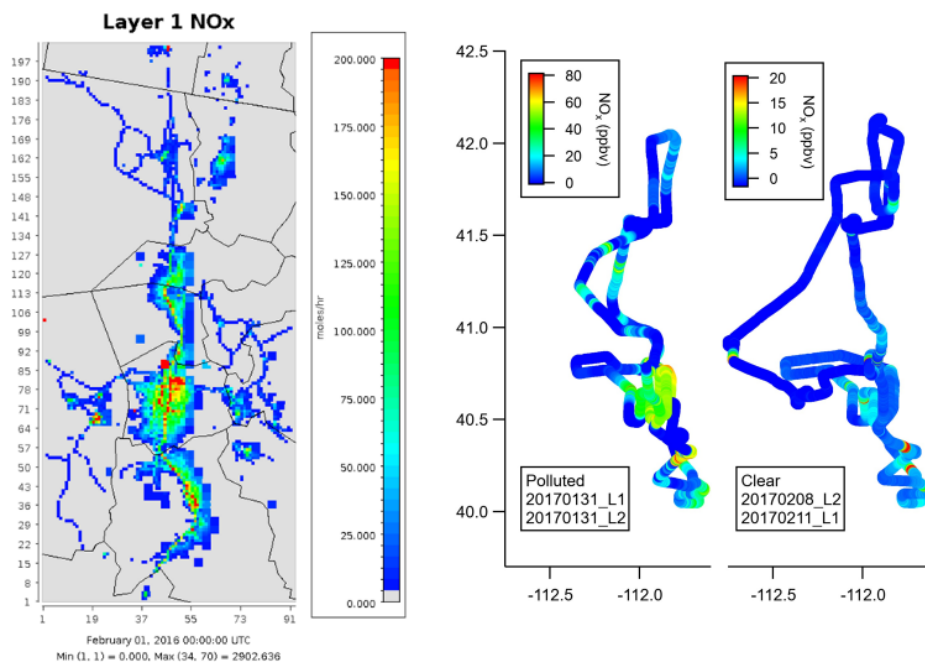


Figure 3.28 Modeled 24-hr averaged  $\text{NO}_x$  emissions with 1.3 km resolution from the SMOKE model for February 1, 2017 are shown on the left. The center and right panels contain sample Twin Otter flight tracks colored by the observed  $\text{NO}_x$  concentration.

### 3.3 Ammonia

#### 3.3.1 Passive NH<sub>3</sub> Sampler Network Measurements

During the 2017 UWFPS campaign, temporally-integrated ambient NH<sub>3</sub> concentrations were obtained for both the Cache Valley and Wasatch Front airshed for three separate, 7-day sampling periods: Jan. 26 – Feb. 2, Feb. 2 – Feb. 9, and Feb.9 – Feb. 16. The individual receptor concentrations can be seen in Figure 3.29 (Cache Valley) and Figure 3.30 (Wasatch Front). As can be seen, the concentrations were typically much higher in the Cache Valley airshed, but also more variable.

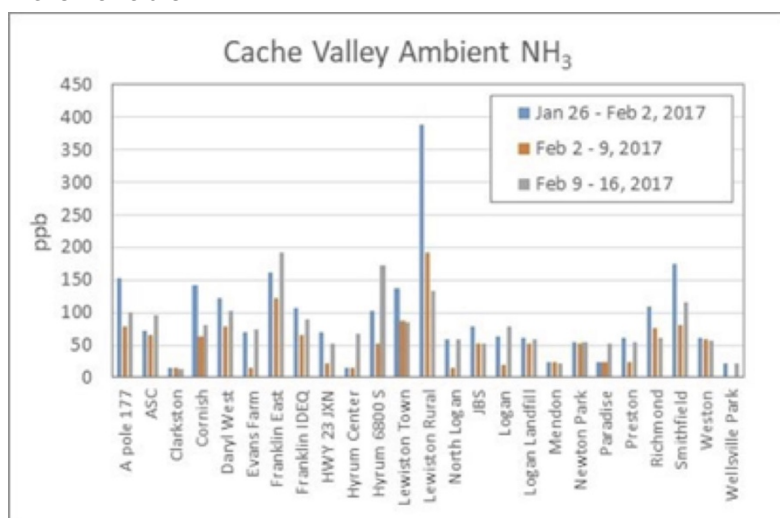


Figure 3.29 Cache Valley ambient NH<sub>3</sub> as measured by the passive sampler network during the 2017 UWFPS.

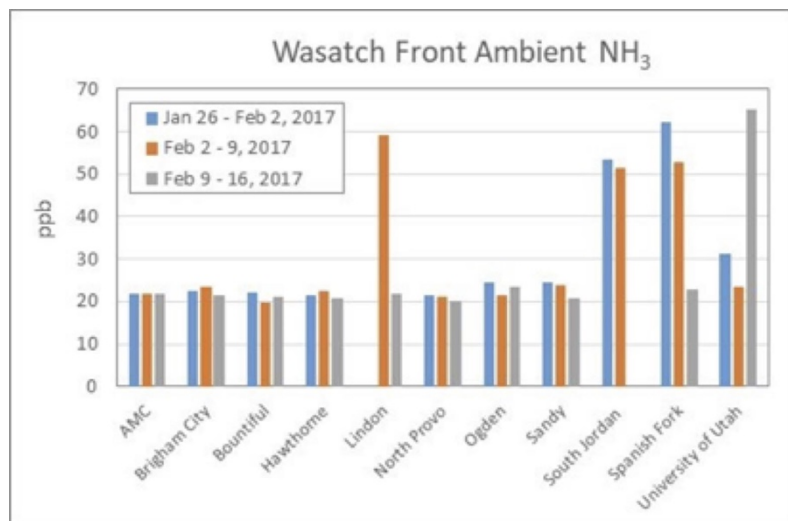


Figure 3.30 Wasatch ambient NH<sub>3</sub> as measured by the passive sampler network during the 2017 UWFPS.

In the Cache Valley, the highest NH<sub>3</sub> concentrations were typically observed near likely agricultural sources (CAFOs), such as, Lewiston Rural and Franklin East – near large poultry facilities, Hyrum 6800 S – near a fur production farm, and SM – immediately adjacent to an active dairy farm. Most of the sites along the Wasatch Front showed NH<sub>3</sub> concentrations consistently near 20 ppb, with four exceptions: average values around 50 ppb at South Jordan; around 40 ppb, but highly variable, values at the UU location; and average values greater than 40 ppb at two of the three more southerly Utah Valley sites - LN and Spanish Fork (SF).

Table 3.2 shows the tabulated average NH<sub>3</sub> concentrations observed at each passive sampling locations, wherein the uncertainty represents the 95% confidence interval about the mean. The overall Cache Valley average NH<sub>3</sub> concentration can be shown to be 75.3 ppb. This average concentration compares very favorably to a similar study conducted in the Cache Valley in the winter of 2016, which found an average ambient NH<sub>3</sub> concentration of 65 ppb. It should be noted that the 2016 study was conducted over five, 7-day sampling periods (Jan. – Feb. 2016), but only consisted of a network of 10 sample locations. The overall average ambient NH<sub>3</sub> along the Wasatch Front from the 2017 study was found to be 29.2 ppb. The 2016 Wasatch Front study, similar to the Cache Valley study, found an average ambient NH<sub>3</sub> concentration of 8 ppb.

For comparison, the National Atmospheric Deposition Program's Ammonia Monitoring Network (AMoN) includes two sites established in 2011 in northern Utah: UT01 (Cache Valley) and UT97 (SLC). The AMoN systems collect 2-week integrated, passive samples (Radiello) and report concentrations in  $\mu\text{g m}^{-3}$ . UT01 is located in the southcentral portion of the Cache Valley near the "Animal Science Farm" location of UWFPS. UT97 is at UDAQ's Air Monitoring Center's (AMC) West Valley City facility. This study's "AMC" site is at the same location. At present, AMoN data are available from the initiation of the sites (Nov. 2011) through early 2015 [65]. From this data set, the wintertime (Jan-Feb.) averages for UT01 and UT97 individual sites can be calculated to be 26.9 ppb and 3.9 ppb, respectively.

Contour plots constructed for both airsheds using the 3-period average at each receptor location is shown in Figure 3.31. As can be seen, the Cache Valley map shows a strong NH<sub>3</sub> concentration gradient, with the highest concentrations primarily in the northern half of the valley and centered near the large poultry egg production facilities previously noted. However, a region of elevated concentrations continues south down the Valley and ends in elevated lobe near another known agricultural production facility. The 2016 contour map resulted in a similar profile, but with less resolution owing to the fewer number of sample sites during that period.

The contour plot for the Wasatch Front, while not showing as much variability as the Cache Valley plot, does show a noticeable gradient with most of the higher NH<sub>3</sub> concentrations being found in the Utah Valley region, seemingly bleeding into the very southern regions of the SLV (South Jordan). This possible inter-valley exchange is further explored in Section 5.

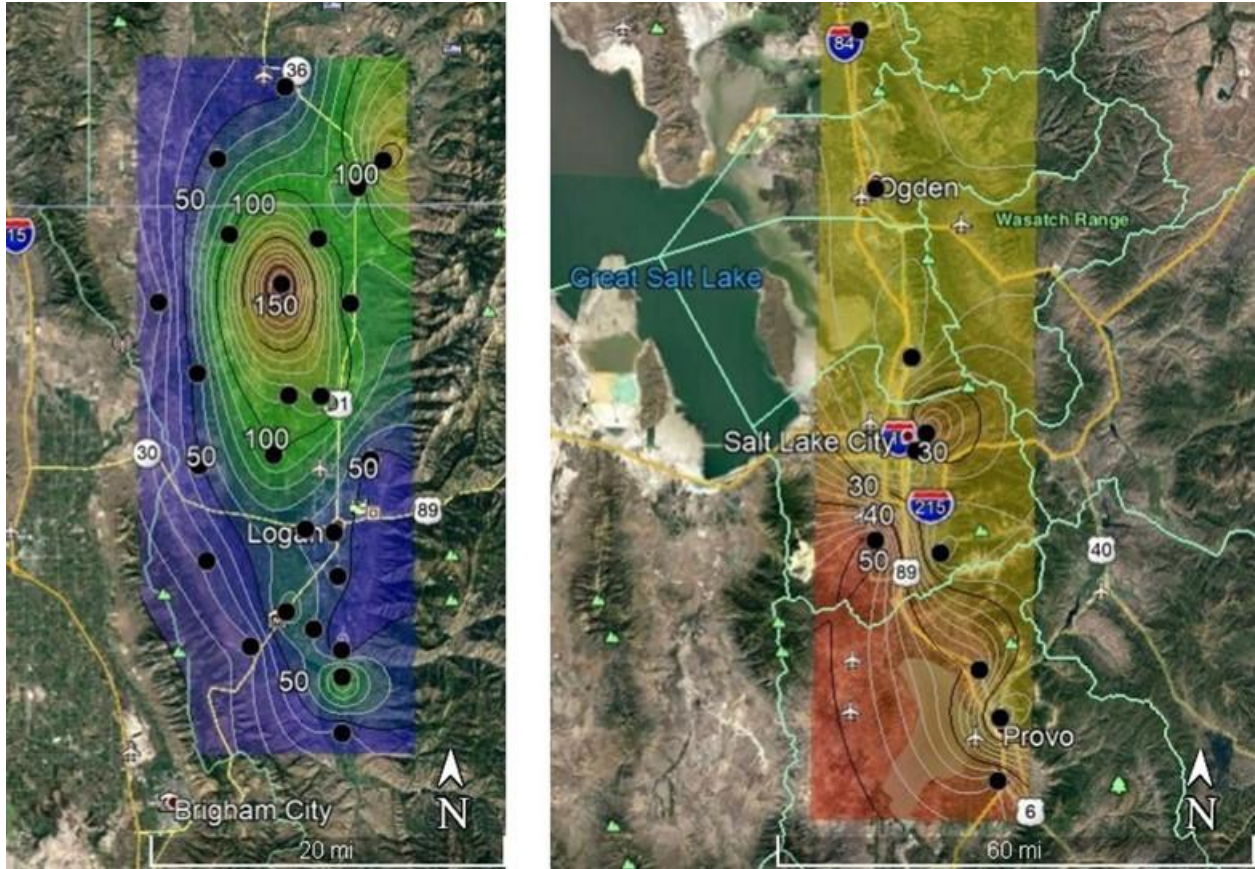


Figure 3.31 Contour plots of the average ambient  $\text{NH}_3$  for Cache Valley and the Wasatch Front during the 2017 UWFPS.

Table 3.2 Average ambient NH<sub>3</sub> (plus/minus 95% CI).

	Site	Ambient NH <sub>3</sub> (ppb)
Cache Valley	Amalga pole 177	110.3 ± 42.5
	Animal Science Center	77.6 ± 18.3
	Clarkston	14.5 ± 1.2
	Cornish	95.3 ± 45.9
	Daryl West	101.3 ± 24.7
	Evans Farm	53.4 ± 37.0
	Franklin East	158.3 ± 40.1
	Franklin (IDEQ)	87.9 ± 23.5
	HWY 23 JXN	47.4 ± 28.2
	Hyrum Center	33.1 ± 34.2
	Hyrum 6600 S	109.4 ± 68.3
	Lewiston Town	103.1 ± 32.9
	Lewiston Rural	237.9 ± 152.5
	North Logan	44.4 ± 27.9
	JBS	61.2 ± 17.8
	Logan	53.3 ± 34.5
	Logan Landfill	57.7 ± 4.7
	Mendon	23.3 ± 1.0
	Newton Park	54.4 ± 1.7
	Paradise	33.7 ± 18.3
Preston	46.4 ± 22.7	
Richmond	82.1 ± 28.6	
Smithfield	123.5 ± 53.3	
Weston	58.1 ± 2.6	
Wellsville Park	15.3 ± 12.9	
Wasatch Front	AMC	21.9 ± 0.1
	Brigham City	22.4 ± 1.2
	Bountiful	21.0 ± 1.2
	Hawthorne	21.7 ± 0.9
	Lindon	40.3 ± 36.7
	North Provo	20.9 ± 0.8
	Ogden	23.2 ± 1.6
	Sandy	23.0 ± 2.1
	South Jordan	52.4 ± 1.9
	Spanish Fork	45.9 ± 23.2
	University of Utah	39.9 ± 25.2

Parallel to the ambient studies, Ogawa passive samplers were also placed in three indoor air locations: the Civil and Environmental Engineering (CEE) office at USU and two private

residences. The home identified as Residence 1 was occupied by two people, 20+ cats, and one dog. The home identified as Residence 2 was occupied by four people, three cats, and one dog. As Figure 3.32 indicates, the CEE office concentrations were consistent and slightly greater than 50 ppb. This is interestingly similar to the outdoor concentration in the area as can be approximated from Figure 3.31. Residence 2, approximately three miles north of the USU campus, showed an average indoor  $\text{NH}_3$  concentration around 177 ppb. Atkins and Lee [66] reported somewhat lower indoor concentrations from United Kingdom residences averaging around 63 ppb. Not unexpectedly, Residence 1, with a large number of domestic cats showed a much higher average  $\text{NH}_3$  concentration (1,095 ppb).

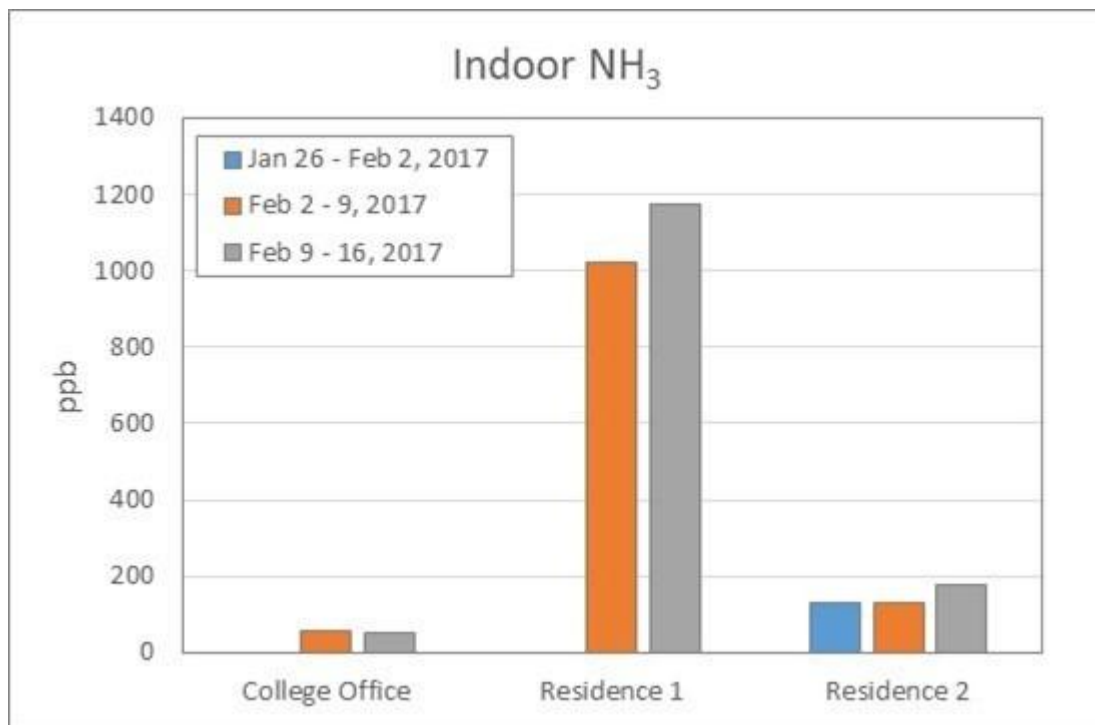


Figure 3.32 Indoor air  $\text{NH}_3$  during the 2017 UWFPS.

### 3.3.2 Ground Based Real Time $\text{NH}_3$ Measurements

#### Cache Valley $\text{NH}_3$ Measurements

Ambient ammonia ( $\text{NH}_3$ ) concentrations were recorded at the Logan EPA trailer location from January 17 to February 14, 2017. During this period, all or parts of three separate pollution events were captured wherein the regulatory, 24-hr average  $\text{PM}_{2.5}$  concentrations, as reported by UDAQ at SM varied from  $< 1.0 \mu\text{g}/\text{m}^3$  to  $75.7 \mu\text{g}/\text{m}^3$  (Figure 1.4 and Figure 1.6) [67].

Figure 3.33 shows the ambient gas-phase  $\text{NH}_3$  throughout the sample period as measured at the EPA trailer Logan location. For comparison, collocated measurements of total  $\text{PM}_{2.5}$  mass and particulate-bound ( $\approx\text{PM}_1$ ) ammonium ( $\text{NH}_4^+$ ) by US EPA are also shown (discussed more fully in Section 3.1 and 4). As shown, the ambient  $\text{NH}_3$  concentrations ranged from occasional levels below the instrument detection limit (0.5 ppb) during clean periods to over 80 ppb during the pollution events. During the two main pollution episodes #6 and #7, the ambient  $\text{NH}_3$  averaged 46.7 ppb, compared to 10.3 ppb during the non-pollution periods.

The time series of particulate-bound ammonium is also shown in Figure 3.33. The  $\text{NH}_4^+(\text{p})$  concentrations ranged from below detection to greater than 20 ppb during the strongest PCAP event. During the two main pollution episodes #5 and #6, the  $\text{NH}_4^+(\text{p})$  averaged about 7.7 ppb, compared to 0.9 ppb during the clean period. Summing the  $\text{NH}_3$  and  $\text{NH}_4^+$  into a combined  $\text{NH}_x$  showed averages of 54.4 and 11.2 ppb, respectively, for the pollution and non-pollution periods. On average, this suggests the particulate-bound  $\text{NH}_4^+$  accounted for 14.1 and 8.0% of the atmospheric  $\text{NH}_x$ , respectively.

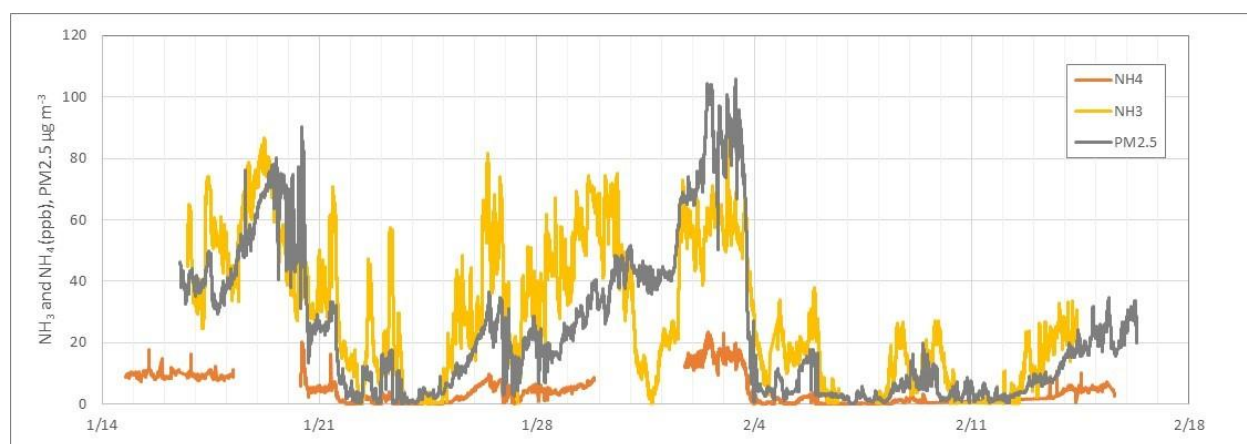


Figure 3.33 Cache Valley ambient  $\text{NH}_3$ , particulate-bound  $\text{NH}_4$ , and  $\text{PM}_{2.5}$  as measured at the Logan EPA trailer location during the 2017 UWFPs.

It is also interesting to note that the rates of change of the ambient ammonia and ammonium appear to be significantly different during the concentration increases during a pollution episode. A more detailed examination of the period from Jan. 25 - 29, when both  $\text{NH}_3$  and  $\text{NH}_4^+(\text{p})$  data are available, show positive slopes of 6.1 and 0.6 ppb day<sup>-1</sup> for  $\text{NH}_3$  and  $\text{NH}_4^+(\text{p})$ , respectively. This indicates a buildup of ammonia 10 times faster than the increase in  $\text{NH}_4^+(\text{p})$ , supporting an excess of ammonia gas in relation to ammonium nitrate (p) formation.

Solid-state chemical sensors were used to monitor ammonia at SM. The sensors are not typically used for ambient detection of ammonia because they have relatively high detection limits  $\sim 100$  ppb more appropriate to source emissions experiments. The SM site is adjacent to several farming operations, including a dairy directly to the north. Chemical sensor data for ammonia is shown in Figure 3.34 and shows that the site routinely gets exposed to high concentrations of ammonia for several hours at a time, often exceeding 1 ppm.

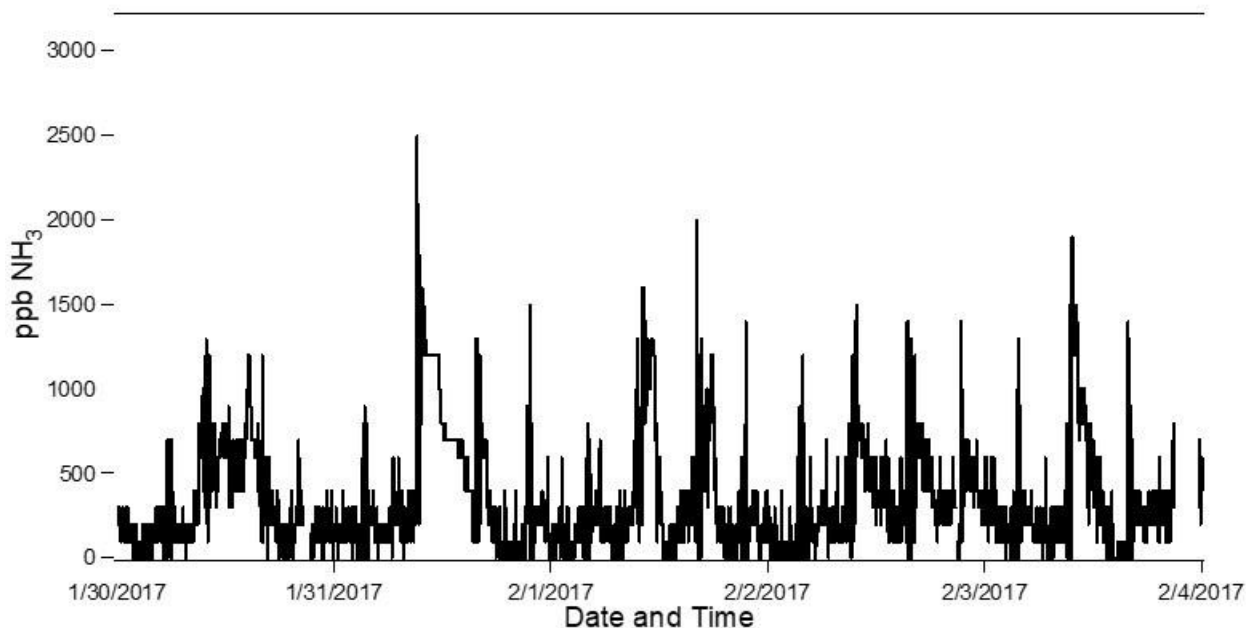


Figure 3.34 Ammonia time series at SM as measured by low-cost solid-state NH<sub>3</sub> sensor.

### **The SLV (UU) NH<sub>3</sub> Measurements**

The behavior of NH<sub>3</sub>(g) - NH<sub>4</sub><sup>+</sup>(p) partitioning was observed from 21 January to 21 February, consisting of two main pollution episodes #5 and #6 (Figure 3.35). During the episode #6 that occurred 27 January to 4 February, there was a marked rise in NH<sub>4</sub><sup>+</sup>(p) loading with small consistent levels of ambient NH<sub>3</sub>(g). Towards the end of the period where the cold air pool becomes unstable (1 Feb), there is an increase in observed NH<sub>3</sub>(g) concentrations with a delayed decrease in NH<sub>4</sub><sup>+</sup>(p), by a few hours. This observed increase in NH<sub>3</sub> cannot be from partitioning out of the particle phase exclusively. A closer look at the trend of total NH<sub>x</sub> (= NH<sub>4</sub><sup>+</sup>(p) + NH<sub>3</sub>(g)) shows there is still an overall buildup of total NH<sub>x</sub> with a diurnal trend before the clean out period. On January 29, 30, and 31, there is a midday peak in NH<sub>x</sub> that is dominated by NH<sub>4</sub><sup>+</sup>(p). On Feb 1, the same midday peak occurs but the contributions for the particle and gas phase are comparable. By February 2-3, the gas phase dominates over the particle phase for NH<sub>x</sub>. This period, where a strong weather front mixes out the cold air pool, which may explain the observed decrease in PM<sub>2.5</sub> before the complete mix out of NH<sub>3</sub>. This is also in line with the observed mix out of other trace gases measured in the SLV.

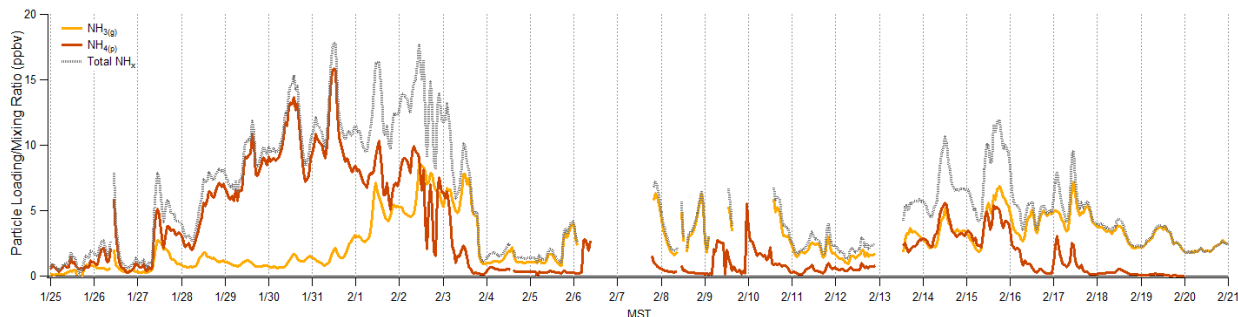


Figure 3.35 Observed  $\text{NH}_3(\text{g})$ ,  $\text{NH}_4^+(\text{p})$ , calculated total  $\text{NH}_x$  in the SLV during Jan 25 to Feb 21. Particle loading and ambient concentration are given in ppbv.

Due to technical difficulties, high-quality  $\text{HNO}_3$  and particulate  $\text{NO}_3^-(\text{p})$  levels are only available from February 13-21, which includes the last episode #7 in mid-February (Figure 3.36). During episode #7, the particle composition was dominated by  $\text{NH}_4\text{NO}_3$ , as previously reported. There is significantly more nitrate in the particle phase than in the gas phase. The  $\text{NH}_3$ -  $\text{NH}_4^+(\text{p})$  behavior in this shorter episode was different compared to the previous episode, #6. The 24-hr total  $\text{PM}_{2.5}$  average did not exceed  $30 \mu\text{g m}^{-3}$  and only persisted for 2-3 full days, which is roughly half the particle loading and duration of the episode #6. The levels of  $\text{NH}_4^+(\text{p})$  are similar to  $\text{NH}_3(\text{g})$  during episode #7. On Feb 16-17, the  $\text{NH}_4^+(\text{p})$  levels drop, while the gas phase levels remain close to what is observed during "clean" periods. Total  $\text{NH}_x$  shows the same trend of accumulation during the pollution event and then a drop back to "clean" levels. It is possible the PCAP did not persist long enough for nitrate to build up sufficiently to pull the majority of gas phase  $\text{NH}_3$  into particles before being transported out of the valley.

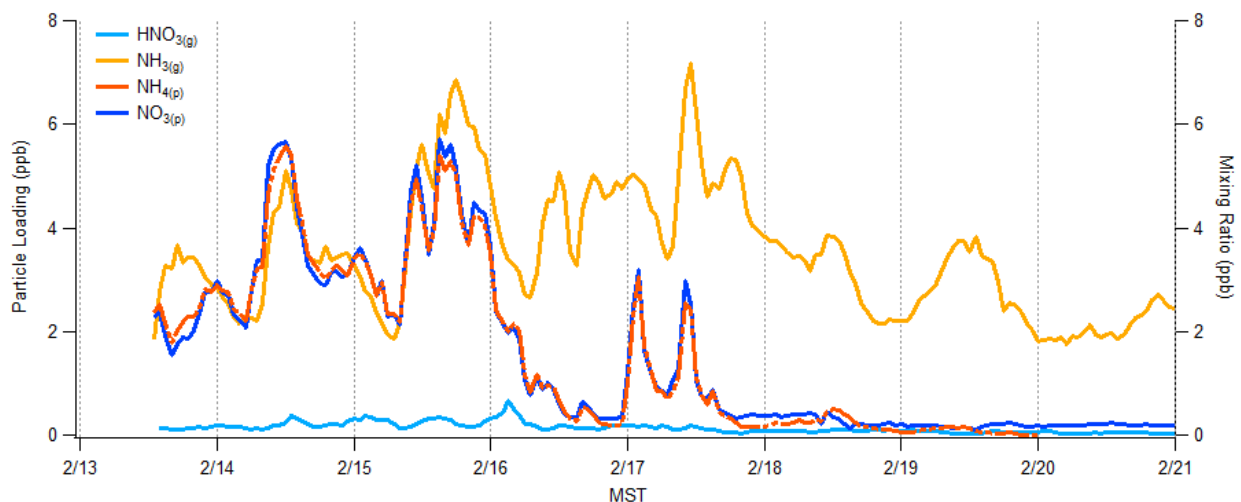


Figure 3.36 Time series of  $\text{HNO}_3(\text{g})$ ,  $\text{NH}_3(\text{g})$  and  $\text{NO}_3^-(\text{p})$  and  $\text{NH}_4^+(\text{p})$  during episode #7 captured during UWFPS. Particle loading and ambient concentration are given in ppbv.

### 3.3.3 Aircraft NH<sub>3</sub> Measurements

The spatial distribution of NH<sub>3</sub> was measured aboard the Twin Otter aircraft using a QC-TILDAS spectrometer (see Section 2.1.1). The instrument was operational on all but the two flights on 31 January 2017. Data shown here passed through an extensive quality control resulting in some data gaps. All together data from 2320 out of total 3207 flight minutes (72%) could be retrieved.

#### Prevailing NH<sub>3</sub> Mixing Ratios for Different Regions

The frequency distributions of NH<sub>3</sub> mixing ratios measured for different regions is shown in Figure 3.37 for both PCAP and non-PCAP conditions. Mixing ratios were filtered to only include those from the lowest steady flight level for a better comparison between regions. The histograms reveal low NH<sub>3</sub> regions with typical mixing ratios less than 10 ppb: Salt Lake City, North Metropolitan Area, Bear River Valley, Great Salt Lake, Tooele and Utah Valley. Among these, the North Metropolitan Area, Bear River Valley, Tooele and Utah Valley also show sporadic high NH<sub>3</sub> mixing ratios up to 30 ppb, indicating the presence of local emission sources (see also Section 6.1 on NH<sub>3</sub> emissions). Ammonia mixing ratios observed in Utah valley were on average higher than in the other low NH<sub>3</sub> regions but still mainly below 10 ppb. Highest NH<sub>3</sub> levels were found in Cache valley reaching up to 75 ppb marking it as a distinct high NH<sub>3</sub> region.

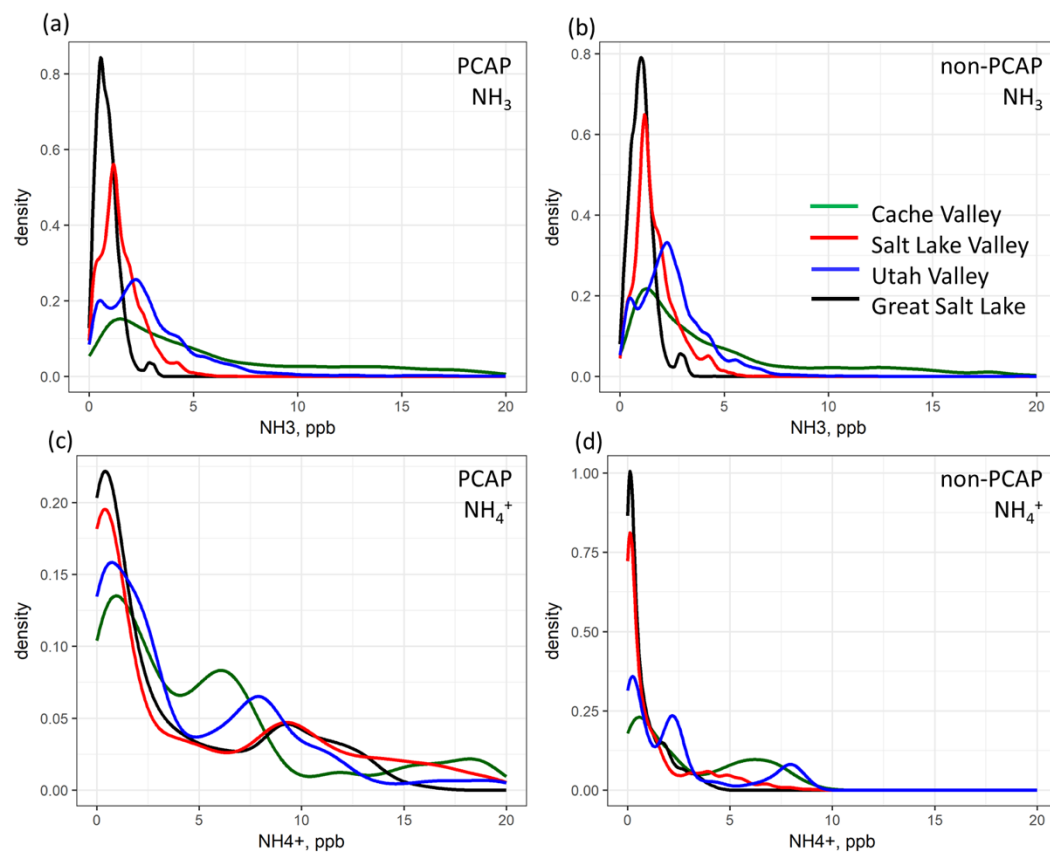


Figure 3.37 Frequency distributions of NH<sub>3</sub> and NH<sub>4</sub><sup>+</sup>-aerosol mixing ratios measured from the Twin Otter airplane for different regions under PCAP and non-PCAP conditions.

### ***Differences between Polluted and Clean Conditions***

Frequency distributions reveal clear differences in  $\text{NH}_3$  between polluted and clean conditions (Figure 3.37). For low  $\text{NH}_3$  regions, the maximum density during pollution events is shifted to lower  $\text{NH}_3$  mixing ratios than during clean conditions, with exception from the North Metropolitan Area where the distribution is very similar for both conditions. The lower  $\text{NH}_3$  values during polluted conditions matches with increased  $\text{NH}_4^+(\text{p})$  concentrations and can therefore be explained by a higher partitioning into the particle phase. In Cache Valley, the maximum density is at about 4 ppb during pollution events while outside PCAP conditions the maximum density is at less than 1 ppb. At the same time, mixing ratios above 10 ppb were also observed much more frequent during PCAP conditions. Both observations indicate a local strong source of  $\text{NH}_3$  Cache Valley. The higher density of  $\text{NH}_3$  mixing ratios between 5 and 20 ppb in Utah Valley also indicates strong emission sources there.

### ***Ammonia Mixing Ratios during Individual Flights***

Figure 3.38 and Figure 3.39 show the  $\text{NH}_3$  mixing ratios measured for both North and South flight pattern, respectively (see Table 2.2). Again, mixing ratios were filtered to only include mixing ratios from the lowest steady flight level. These figures underline the regional distributions from Figure 3.37 described above, with Cache Valley being the major hotspot for  $\text{NH}_3$  and the lowest average mixing ratios above the Great Salt Lake. The measurements also reveal that the spatial distribution in Cache Valley is very heterogeneous (Figure 3.38) consistent with the findings of the passive  $\text{NH}_3$  network. In many cases the Eastern side of the valley shows higher  $\text{NH}_3$  mixing ratios (flights 1, 4 and 10). Also  $\text{NH}_3$  mixing ratios tend to be higher in the Logan area, however, local hotspots shift between flights and the data has to be evaluated further also regarding to wind directions and footprint areas. Flights in the south sector (Figure 3.39) show that  $\text{NH}_3$  is distributed quite homogeneously over the Salt Lake City area. In contrast, there is more variability in Utah Valley, with lower mixing ratios above Utah Lake (flight 13) and hotspots near Spanish Fork and Linton. Peaks near Linton at the North Eastern section of Utah Lake are associated with emissions from an ammonia factory and a power plant (see also Section 6.1).

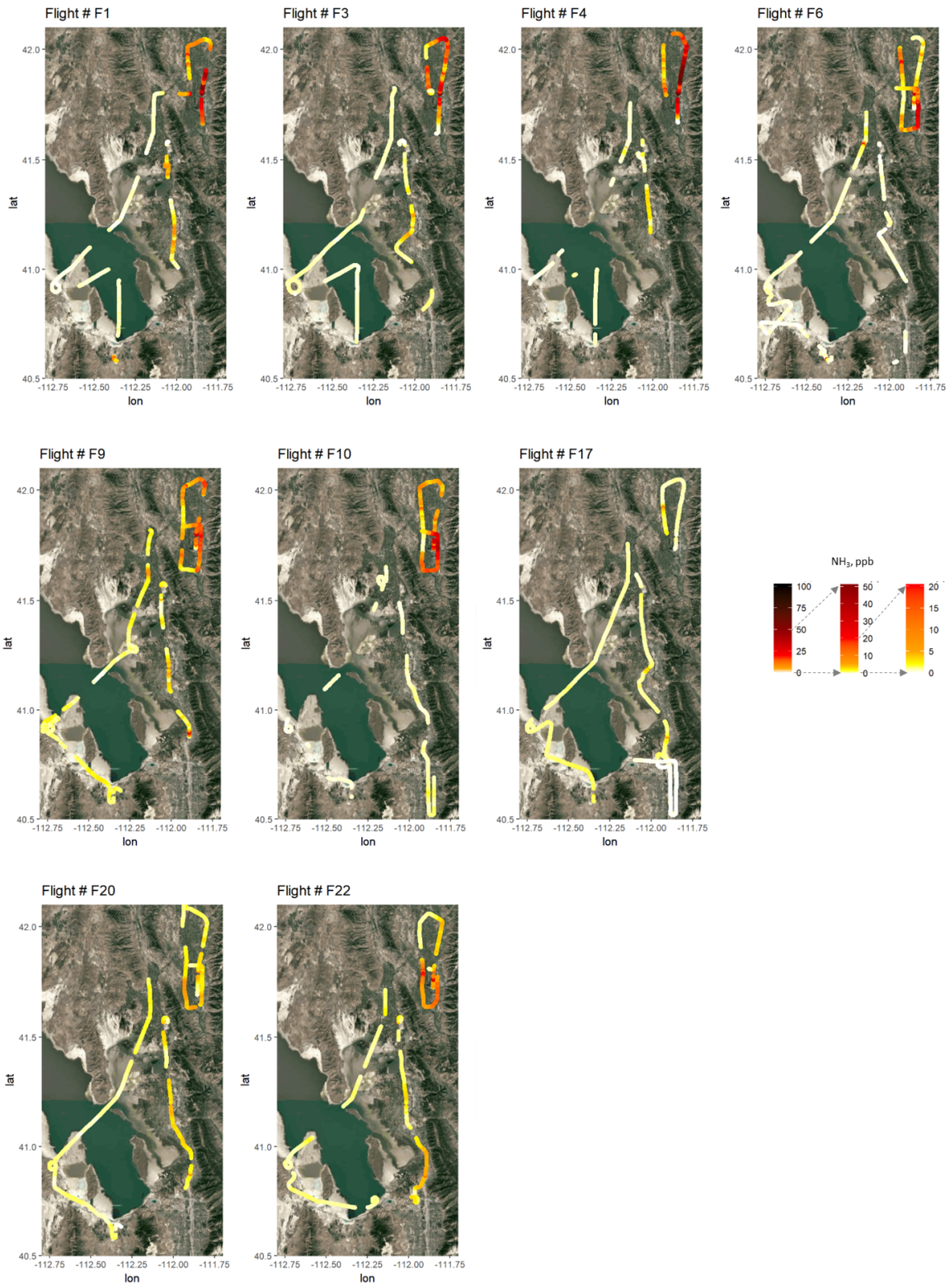


Figure 3.38 Ammonia mixing ratios measured from the Twin Otter airplane for the North flight pattern. Only data from the lowest steady flight level is shown.

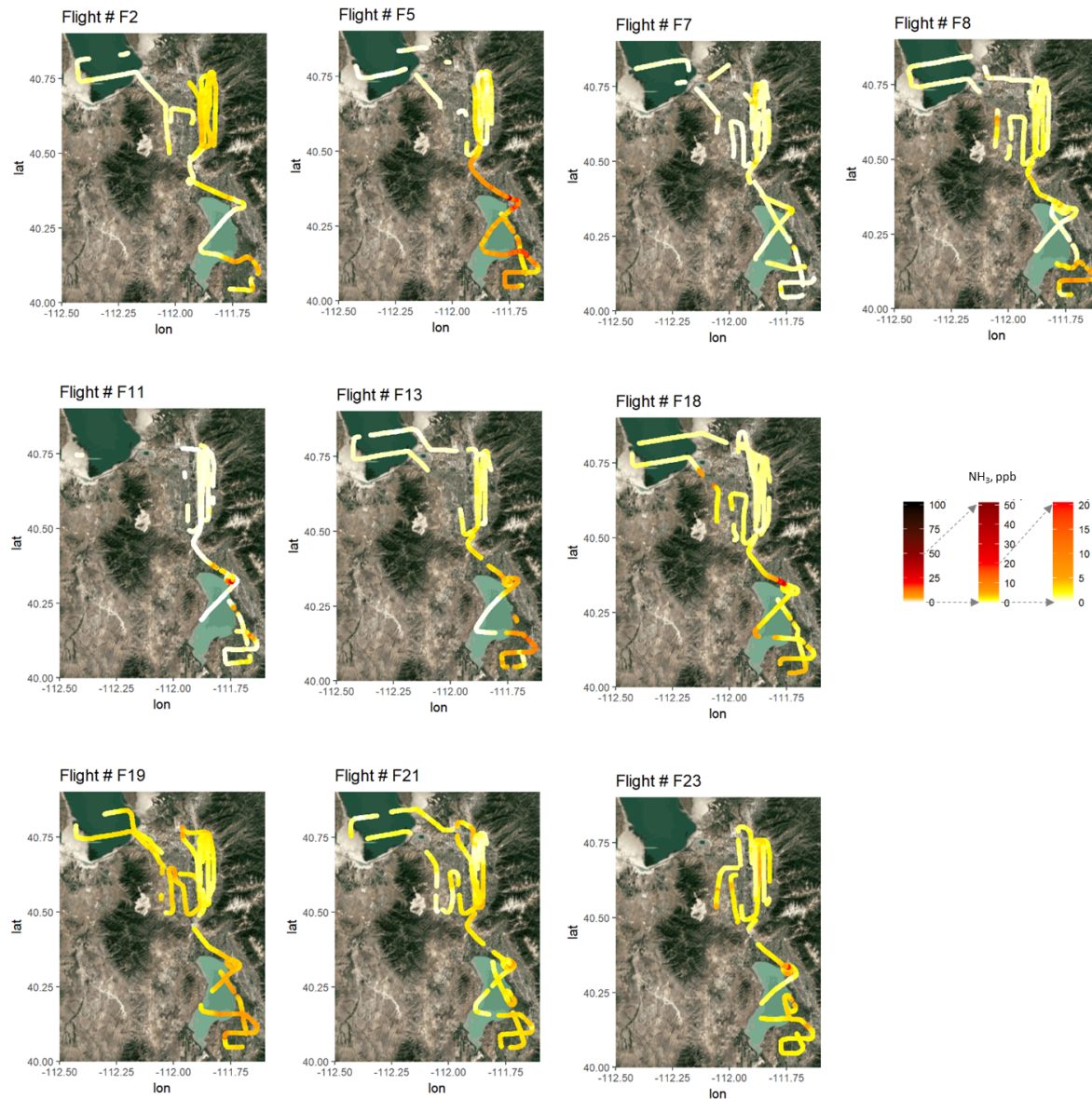


Figure 3.39 Ammonia mixing ratios measured from the Twin Otter airplane for the South flight pattern. Only data from the lowest steady flight level is shown.

### Near Surface NH<sub>3</sub> Mixing Ratios

NH<sub>3</sub> near the surface was measured during the missed approaches at various airports in the region. Figure 3.40 shows the average NH<sub>3</sub> mixing ratios for each missed approach at the different airports. At Logan airport in Cache Valley, the difference between pollution (16, 17 and 18 January) and non-pollution periods is most prominent, with average mixing ratios between 30 to

45 ppb during polluted conditions. At both Provo and Spanish Fork a clear increase of  $\text{NH}_3$  mixing ratios at the surface at the start of the pollution episode #6 (28 to 30 January) is visible.

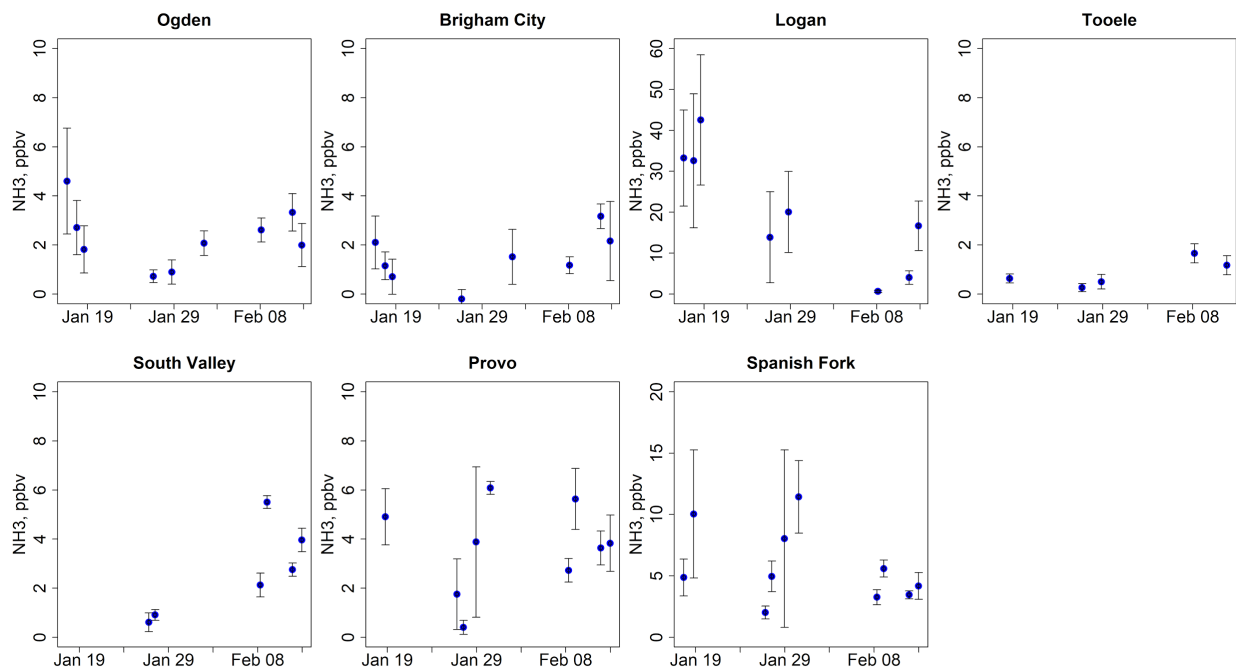


Figure 3.40 Ammonia mixing ratios during missed approaches at different airports in the region.

### Comparison with Ground Site Measurements

Ammonia mixing ratios from the Twin Otter are compared with the continuous measurements at the Logan and the UU ground sites. For comparison with the Logan ground site the data from the missed approaches at Logan airport was used as it represents best the near surface levels of  $\text{NH}_3$  (Figure 3.41).  $\text{NH}_3$  mixing ratios from the Twin Otter follow the trend from the ground measurements well with (1) high mixing ratios around 50 ppb during PCAP 5, (2) medium and highly variable mixing ratios in the moderate polluted period end of January, and (3) lower mixing ratios in February. The direct comparison shows that mean values from the Twin Otter are roughly a factor of two lower than values from the ground site measurements. This is most likely due to the lower  $\text{NH}_3$  levels further above the ground during ascents and descents of the missed approaches. For that reason, maximum values represent better the ground level mixing ratios, which is supported by their closer 1:1 correlation with the data from the Logan ground site.

To compare  $\text{NH}_3$  mixing ratios from the Twin Otter with measurements from UU, a horizontal 1 km x 1km grid around the ground site was used to filter the Twin Otter data (Figure 3.42). As the flight levels were mostly constant, the variability of  $\text{NH}_3$  mixing ratios from the Twin Otter is much less compared to the missed approaches. Again, the Twin Otter measurements follow the trend of the continuous ground site measurements. The direct comparison shows that  $\text{NH}_3$  mixing ratios

mainly follow the 1:2 line, indicating the lower mixing ratios at the flight level compared to the ground. However, a clear relationship of the differences with altitude could not be found. During two periods (9 February, 0:33 and 1:34 am MST),  $\text{NH}_3$  values observed from the Twin Otter were significantly higher than at the ground site. This could have been caused by limited vertical mixing during the night, but has to be further investigated.

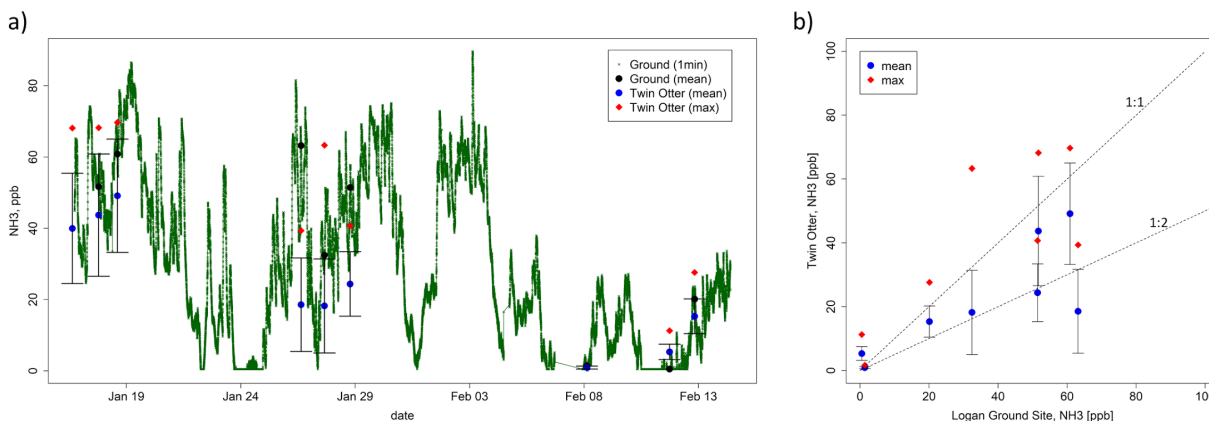


Figure 3.41 Comparison of  $\text{NH}_3$  mixing ratios between Twin Otter measurements and the Logan ground site as a) time series and b) direct comparison of the respective time periods. Twin Otter data shown represents the missed approaches at Logan airport, located approximately 3 km NW of the Logan ground site. Mean values (blue dots, with standard deviations) are the average  $\text{NH}_3$  mixing ratios between 1 km before and 1 km after the start and end of the runway. Maximum values (red diamonds) were observed directly above the runway and are most representative for the  $\text{NH}_3$  mixing ratios at ground level.

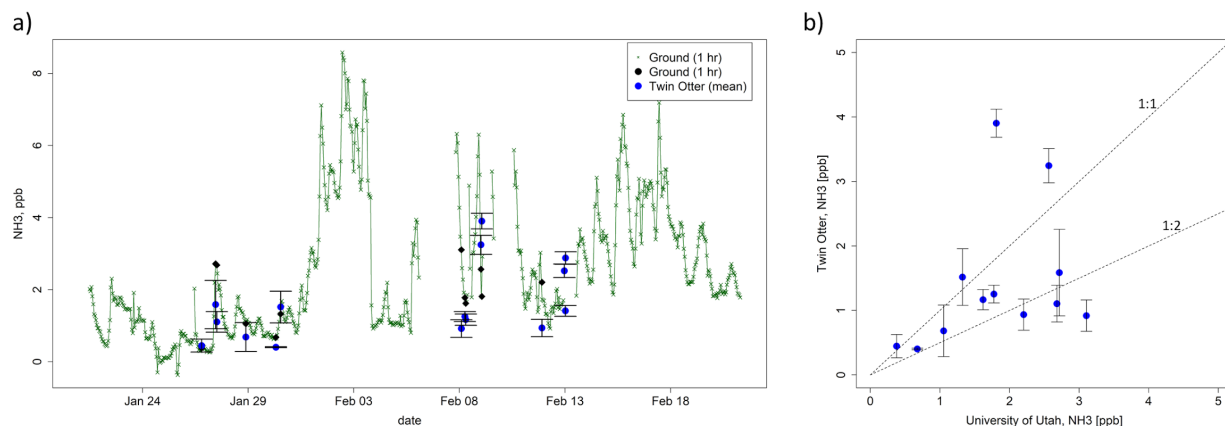


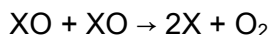
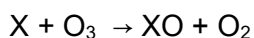
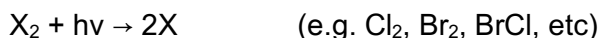
Figure 3.42 Comparison of  $\text{NH}_3$  mixing ratios between Twin Otter measurements and the UU ground site as a) time series and b) direct comparison of the respective time periods. Mean values (blue dots, with standard deviations) are the average  $\text{NH}_3$  mixing ratios within a horizontal 1 km x 1 km grid around the ground site. Corresponding  $\text{NH}_3$  mixing ratios from the ground site (black dots) represent the mean concentration during the 1 hour sampling interval.

### 3.4 Halogens

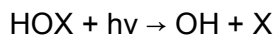
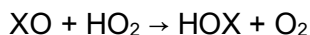
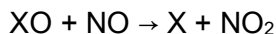
The Salt Lake City and surrounding region is unique compared to other inland urban areas with significant natural and anthropogenic sources of common atmospheric halogens (Cl, Br, I). Potential sources include spray from the Great Salt Lake, playa dusts from dry salt beds, industrial processes, such as alkali earth metal extraction (e.g. magnesium) and chlorine production, and energy production such as coal-fired power plants, among others.

Molecular halogens have the potential to act as radical sources important for driving photochemical production and destruction of ozone both directly and indirectly. Halogen radicals (e.g. Cl $\cdot$ , ClO $\cdot$ , BrO $\cdot$ , etc) affect the lifetime of hydrocarbons (RH) and reactive nitrogen, drive the production of organic peroxy radicals involved in ozone formation and can participate in catalytic cycles which destroy ozone (e.g. [68, 69]). Example reactions that occur in these cases are listed below.

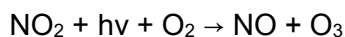
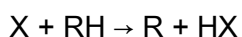
#### Ozone Destruction



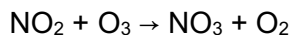
#### HO $_x$ and NO $_x$ Perturbations



#### Ozone Formation



Moreover, in the presence of excess ammonia (NH $_3$ ), HCl will partition to aerosol particles thereby contributing to PM $_{2.5}$  mass concentrations through the formation of ammonium chloride (NH $_4$ Cl). The enhanced partitioning of reactive chlorine to the particle phase (NH $_4$ Cl) in turn alters the rate and product branching of nocturnal nitrogen oxide chemistry.



These effects can be significant to local wintertime air quality even when the molecular halogen precursors are at sub parts per billion levels. Thus, constraining the sources and distribution of halogens throughout the Salt Lake City region was a key measurement objective for UWFPS.

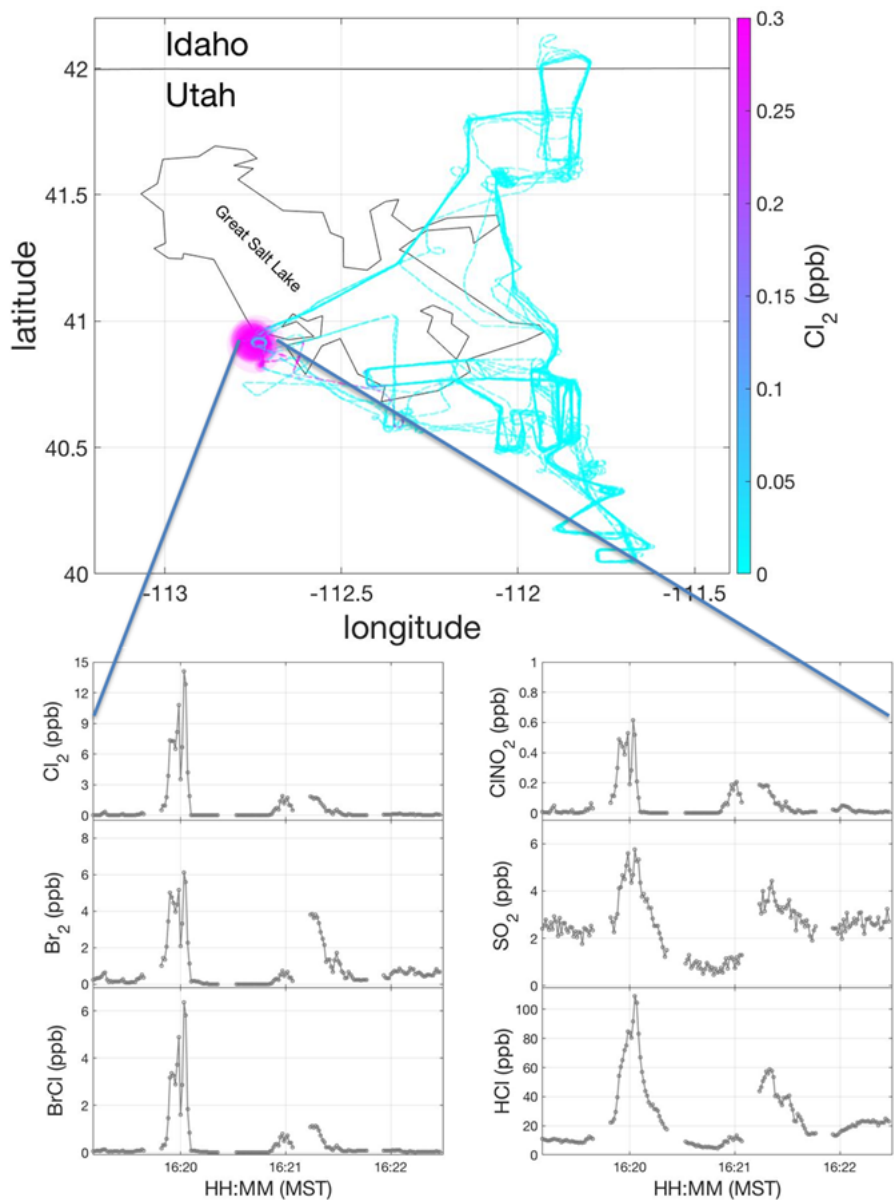
The UWFPS campaign had several instruments, both on the Twin Otter aircraft and at the Logan (Cache Valley) ground site, which provide real-time measurements of gas and particulate inorganic halogen containing compounds. Two high resolution time of flight chemical ionization mass spectrometers (I<sup>-</sup> ToF CIMS) instruments provided measurements of hydrochloric acid (HCl), hypochlorous acid (HOCl), molecular chlorine and bromine (Cl<sub>2</sub> and Br<sub>2</sub>), bromine chloride (BrCl), and nitryl chloride and bromide (ClNO<sub>2</sub> and BrNO<sub>2</sub>) in the gas-phase aboard the Twin Otter and at the Logan ground site [45, 70]. The I<sup>-</sup>ToF CIMS instruments were directly calibrated to most of these gas-phase reactive halogen species in the field or just before or after the UWFPS campaign. The I<sup>-</sup> ToF CIMS instruments also detect other halogen species (such as ClO, BrO, and ClONO<sub>2</sub>) which can be used as qualitative tracers of reactive halogen constituents. Tests to assess whether the corresponding signals can be used as quantitative measures of these species are ongoing. In addition, the aerosol mass spectrometer (AMS) also deployed aboard the Twin Otter and at the Logan ground site, measures non-refractory chloride (generally assumed to be as NH<sub>4</sub>Cl) mass concentrations in PM<sub>1</sub>.

Our survey of the data collected by these instruments, suggests both that chlorine and bromine compounds are ubiquitous over the region at levels often as high as coastal urban areas, and that the U.S. Magnesium plant is a substantial direct anthropogenic source of these halogens. We observed multiple events where boundary layer ozone is depleted to levels below detection limits of the aircraft instrument and that correspond in space and time to elevated reactive halogen species. Similarly, we observe significant contributions of aerosol chloride to PM<sub>2.5</sub> episodes as well as ClNO<sub>2</sub>, a source of radicals for daytime photochemical production of secondary pollutants such as ozone and nitrate.

In this section, we present example observations of (1) halogen measurements from the CIMS instrument aboard the Twin Otter near the U.S. Magnesium plant and other point sources, (2) ozone depletion events correlated with reactive halogens measured aboard the Twin Otter, (3) an overview of ClNO<sub>2</sub> and Cl<sub>2</sub> distributions throughout the region, and (4) comparisons between the Twin Otter and the Logan ground site measurements.

The U.S. Magnesium facility is located on the western edge of Stansbury Bay of the Great Salt Lake, due west of the northern tip of Stansbury Island. On several Twin Otter flights during UWFPS a plume rich in halogens was detected at and just downwind of this facility. The highest concentrations of most halogens were measured in the U.S. Magnesium plume during UWFPS.

See Figure 3.43 for a map of all  $\text{Cl}_2$  observations from the Twin Otter with a color scale that saturates at 0.3 ppb. The single highest  $\text{Cl}_2$  mixing ratio measured in the vicinity reached >500 ppb in a plume intercepted at night (not shown).  $\text{Cl}_2$  was often the halogen species with highest mixing ratios in the plumes, typically reaching from 30 to 100 ppb. An example plume transect is shown in the bottom panel of Figure 3.43. Due to variations in wind speed and direction, photolysis frequencies, and possibly in emissions from the facility, there was variability in the measured



composition during each transect of the U.S. Magnesium facility plume.  $\text{Br}_2$  ranged from ~ 1 to >10 ppb, and  $\text{BrCl}$  mixing ratios were often in between those of  $\text{Br}_2$  and  $\text{Cl}_2$  within the plume. These are some of the highest mixing ratios of dihalogens reported from wintertime aircraft observations.

Figure 3.43 Top panel: spatial distribution of  $\text{Cl}_2$  mixing ratios obtained on 22 Twin Otter flights. The color scale is proportional to mixing ratio, but saturates at 0.3 ppb to make the distribution visible over the entire domain. See text for details on  $\text{Cl}_2$  mixing ratios near the U.S. Magnesium facility. Bottom panel: example time series of several halogen species and  $\text{SO}_2$  from an afternoon

intercept of the plume from U.S. Magnesium facility.

$\text{HCl}$  and  $\text{HOCl}$  were also observed to be elevated in the vicinity of the U.S. Magnesium, but not as reproducibly as the dihalogens, perhaps because direct emissions of these occurred from separate processes and/or were smaller than the subsequent production from chemical

transformations of the dihalogens. For example, in the afternoon intercept shown in Figure 3.43 HCl reaches 100 ppb, higher than the Cl<sub>2</sub> on this intercept. As noted above, other intercepts, especially at night, the relationship is often the reverse.

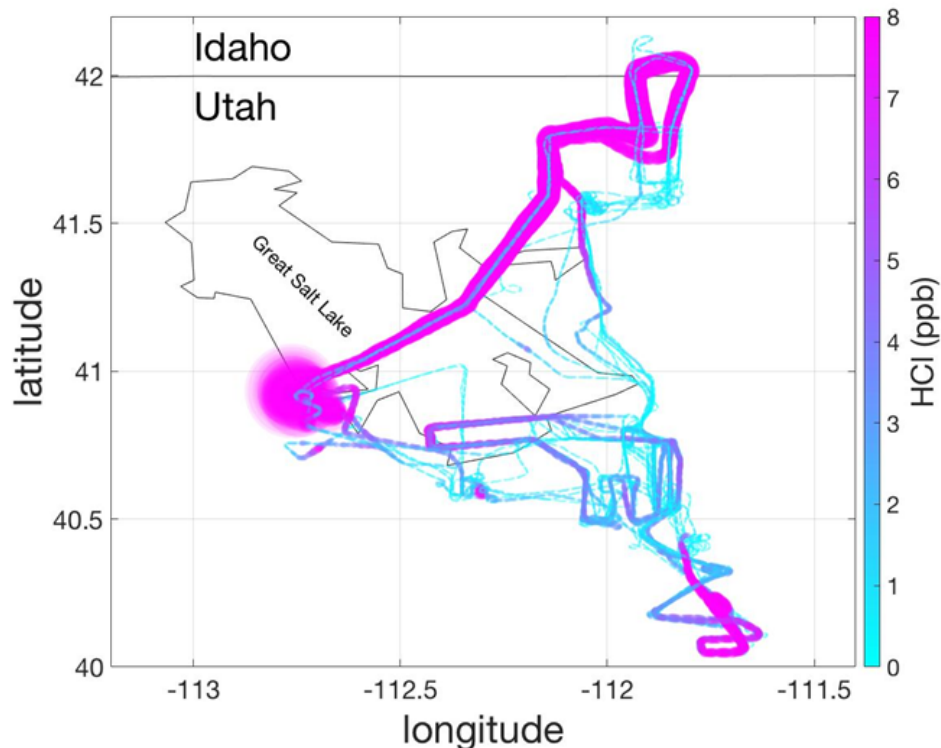


Figure 3.44 shows the spatial distribution of HCl mixing ratios from all Twin Otter flights with a color scale that saturates at 8 ppb. HCl mixing ratios are more uniformly distributed throughout the region than are the dihalogens, likely in part due to its longer atmospheric lifetime and distributed sources.

*Figure 3.44 Spatial distribution of HCl during the UWFPS campaign aboard the Twin Otter. The color scale saturates at 8 ppb, the thickness of the lines is directly proportional to mixing ratio.*

A goal in forthcoming analyses is to use the observed enhancements of halogens near the U.S. Magnesium plant to estimate the emission rates of halogens and compare to existing emissions inventories. In one approach, observed ratios of halogens to independently measured NO<sub>x</sub> (measured by CRDS) and/or SO<sub>2</sub> (see Figure 3.45) (measured by the CIMS) will be compared to the emissions ratios in the inventory. In another approach the emission rate will be estimated from the plume maximum concentration, distance downwind from the plant, and measured wind field together with a model of plume dispersion.

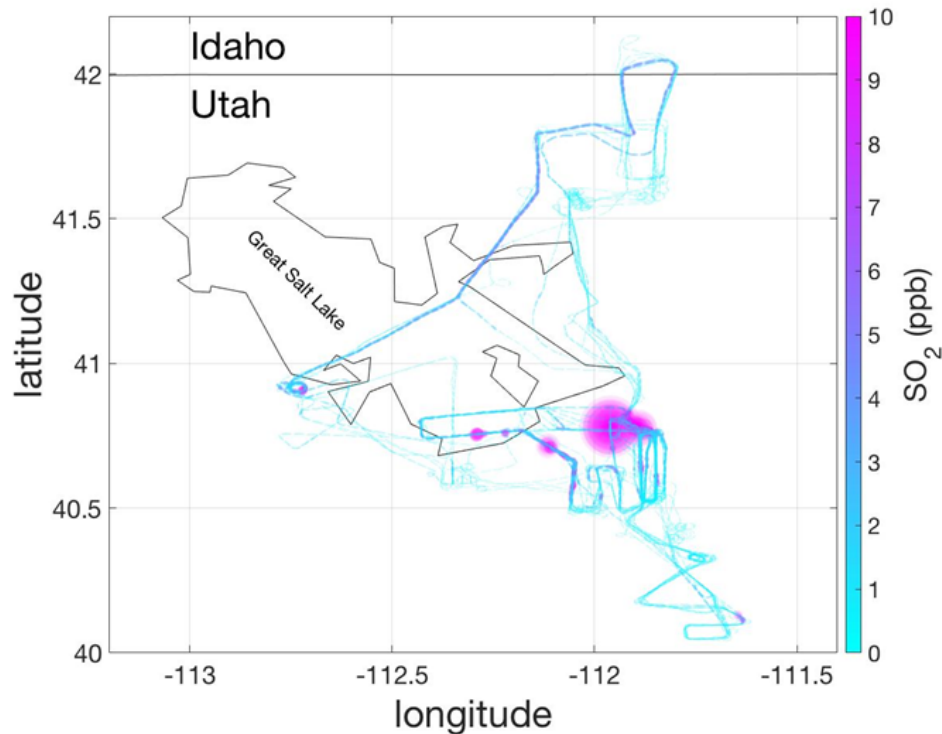


Figure 3.45 Spatial distribution of  $\text{SO}_2$  as measured by the I ToF CIMS on Twin Otter during UWFPS. Individual point sources associated with power generation and other industries are clearly observable. The relatively small enhancement mean the U.S. Magnesium facility can be useful for constraining halogen emissions.

It is clear from surveying the data collected by the Twin Otter flights that U.S. Magnesium is largest point source of reactive halogens in the UWFPS domain. There are two other smaller but detectable point sources in the Utah Valley that show elevated  $\text{Cl}_2$ . One of these is located on the northeast edge of Utah Lake, where there was also a natural gas power generation unit and a fertilizer plant located. The co-enhancement of  $\text{NO}$  suggests a co-located combustion source, but whether the  $\text{Cl}_2$  was from one of those or a different, co-located source is not yet clear. The other source is located to the southeast of Utah Lake, near the Spanish Fork area at  $40.13^\circ\text{N}$ ,  $-111.64^\circ\text{E}$ . The data illustrated in Figure 3.46 were obtained during a daytime flight. The emissions inferred from such data will be biased low due to the photolysis of  $\text{Cl}_2$ .

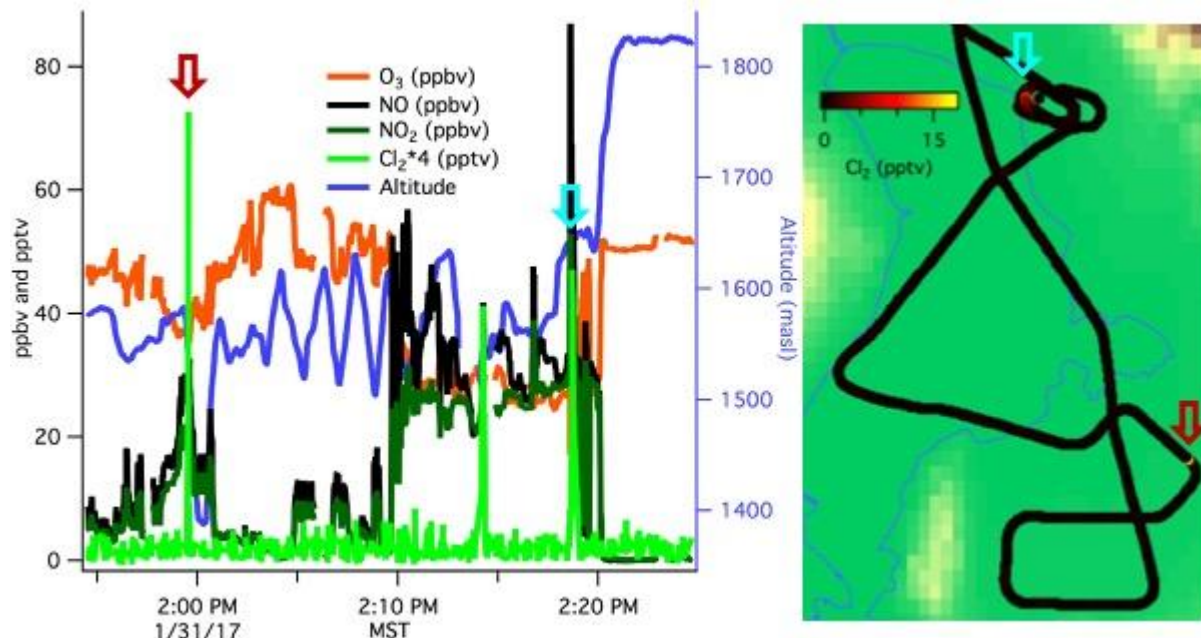


Figure 3.46 Chlorine concentration in the Utah Valley. There are two places that show consistent spikes in chlorine across multiple flights through the Utah Valley. In the map, the blue outline is Utah Lake and the arrows correspond to the arrows in the time series. The second increase in chlorine, which is not marked with an arrow is directly below the third on the map. While these sources are much smaller than U.S. Magnesium, they appear to be consistent sources of chlorine in the Utah Valley and may affect the chemistry.

Ongoing analyses are assessing the role of photochemical transformations of dihalogens within the plume. During the day, the dihalogens photolyze on the timescale of 30 minutes to produce Cl and Br atoms, which in turn participate in radical cycling which can produce or destroy ozone depending upon the abundance of NO. In multiple flights of the Twin Otter complete or nearly complete O<sub>3</sub> depletion events were observed as shown in Figure 3.47. The O<sub>3</sub> depletion events were most often spatially and temporally correlated with the dihalogen measurements as well as CIMS signals (counts per second) of ions having compositions consistent with the corresponding halogen oxide radicals (ClO and BrO) known to be central in the catalytic destruction of O<sub>3</sub>. There were also events attributed to nighttime emissions of NO, but the largest titration of O<sub>3</sub> occurred within the vicinity of the U.S. Magnesium plant during daytime (see Figure 3.47 and Figure 3.48), and could not be explained by measured NO, consistent with a role for reactive halogen chemistry.

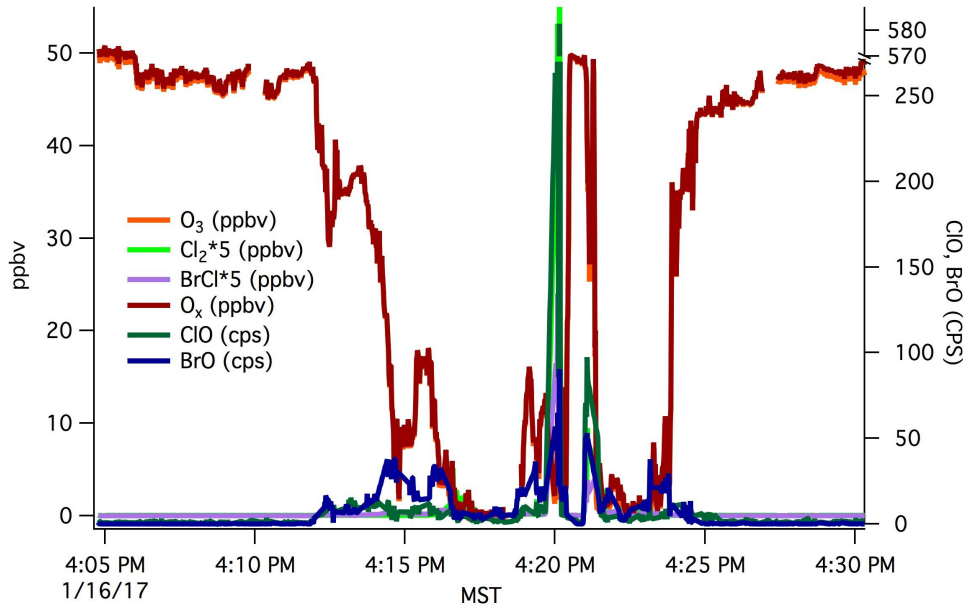


Figure 3.47 Ozone depletion event observed on 16 January. Graph shows data from near U.S. Magnesium plant with observed dihalogen mixing ratios ( $Cl_2$ ,  $BrCl$ ) and halogen oxides ( $BrO$ ,  $ClO$ ) well above background.  $O_x$  ( $O_3 + NO_2$ ) shows an inverse relationship with the halogen oxides. This episode was the lowest observed  $O_x$  during the campaign, but there were many other observations of  $O_x$  being depleted when halogen oxides were high.

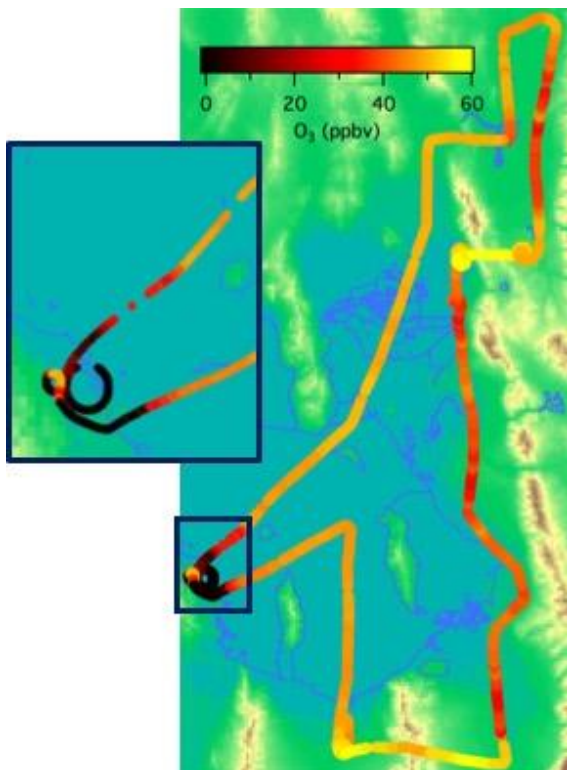


Figure 3.48 Map of flight from 16 January. The flight track is colored by  $O_3$  mixing ratio. The lowest observed  $O_3$  was in proximity to the U.S. Magnesium plant. The expanded portion of the map shows the area included in the time series in Figure 3.47.

In contrast to halogen catalyzed  $O_3$  depletion, in the presence of sufficient  $NO_x$ , halides tend to contribute to photochemical oxidation and the formation of secondary pollutants such as  $O_3$ . In particular, chloride containing aerosol particles promote the nighttime conversion of  $N_2O_5$  to  $ClNO_2$  which photolyzes during the next day into  $Cl$  atoms and  $NO_x$  thereby contributing to the oxidant budget and  $NO_x$  recycling. Consistent with the dependence upon  $NO_x$  availability, the Twin Otter CIMS measurements show that  $ClNO_2$  is typically elevated over Salt Lake City and Provo urban regions, reaching mixing ratios  $> 0.8$  ppb at night (see Figure 3.49). These  $ClNO_2$  mixing ratios approach those measured in polluted coastal regions (e.g., [22, 71]). Similar levels of  $ClNO_2$  were detected in the U.S. Magnesium plant plume, but  $ClNO_2$  was always a very small fraction of the total halogen concentrations measured in that facility's plume.

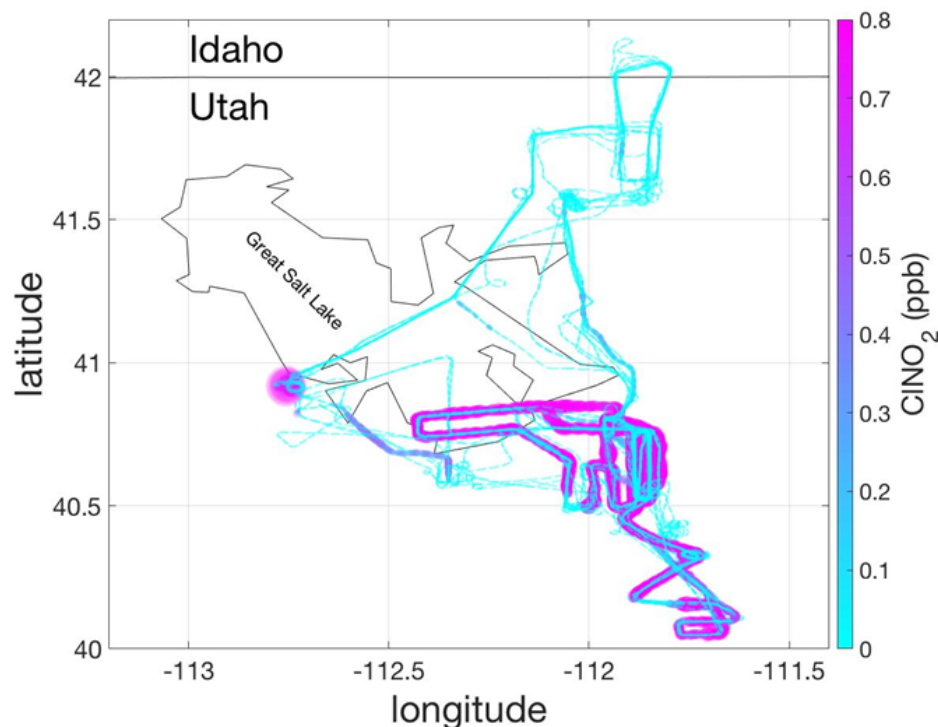


Figure 3.49 Spatial distribution of  $ClNO_2$  measured by the CIMS on 22 Twin Otter flights during the UWFPS campaign. The color scale saturates at 1 ppb.

As noted above, nearly identical CIMS instruments operated on the Twin Otter and at the Logan ground site. As illustrated in Figure 3.50  $ClNO_2$  at the Logan ground site were elevated at

night, as expected, and typically below 200 pptv except for a four day period between January 31 and February 3, 2017 during episode #6 where daily maximum mixing ratios reached between 300 and 1200 pptv.  $Cl_2$  was more episodic at the Logan ground site, with only two short events ( $< 3$  hours in duration) where  $Cl_2$  exceed 200 pptv. The sources of these  $Cl_2$  events at Logan are not known. In the event that occurred on February 4, 2017, the  $Cl_2$  mixing ratio increased, after  $ClNO_2$  began to decrease, and remained elevated for part of the morning as shown in Figure 3.51

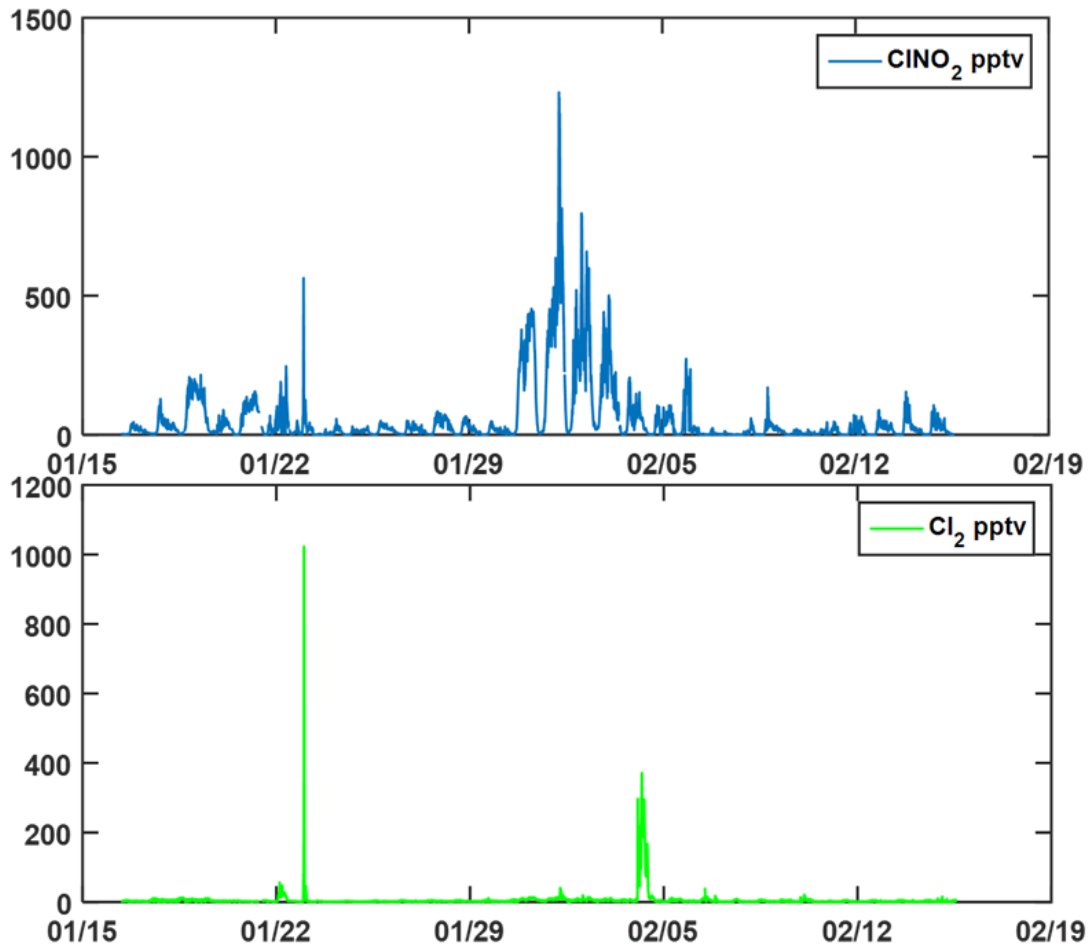


Figure 3.50 CINO<sub>2</sub> (top) and Cl<sub>2</sub> (bottom) mixing ratios measured by I-ToF CIMS at the Logan (Cache Valley) ground site during the UWFPS 2017 campaign.

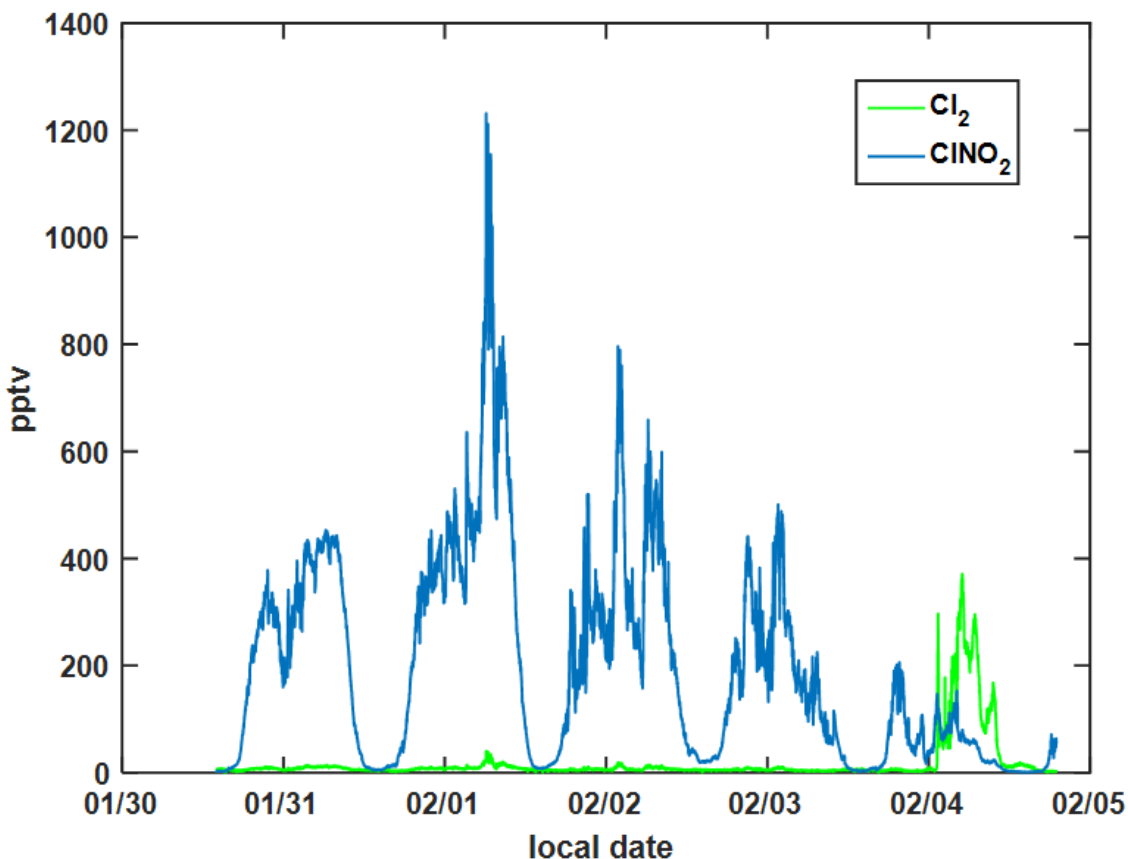


Figure 3.51 ClNO<sub>2</sub> and Cl<sub>2</sub> mixing ratios from the Logan ground site measurements during a stagnation event with the highest sustain mixing ratios of ClNO<sub>2</sub>. The Cl<sub>2</sub> was usually much lower and more episodic than the ClNO<sub>2</sub> though during this event a unique period occurred with Cl<sub>2</sub> greater than ClNO<sub>2</sub> for several hours. The cause of this change in Cl<sub>2</sub>:ClNO<sub>2</sub> is not yet known.

The Twin Otter routinely made missed approaches at the Logan-Cache airport approximately 4 km from the ground site. These missed approaches allow measurement of the vertical profiles of trace gases and particles, and by comparison with the ground site can inform how chemical and physical processes vary with altitude. A comparison between ClNO<sub>2</sub> measured at the Logan ground site and on the Twin Otter at the minimum altitude reached during missed approaches at Logan-Cache airport illustrate that while normally within factors of 2 of each other (Figure 3.52), the Logan ground site typically measured higher ClNO<sub>2</sub>. Cl<sub>2</sub> comparisons show the same relationship of higher mixing ratios at the ground site, with lower observations from the Twin Otter (Figure 3.53). Ongoing analyses aim to determine whether this difference is related to calibration differences between the two instruments, changes in chemistry between the minimum altitude of the Twin Otter, or due to changes occurring between the two locations (ground site and airport). Notably, the comparison of N<sub>2</sub>O<sub>5</sub> mixing ratios reported by the two instruments show the opposite relationship (lower at the ground site than on the Twin Otter), as shown in Figure 3.54. This is a typical vertical profile for N<sub>2</sub>O<sub>5</sub> (e.g., [72]), which has both suppressed production at the surface

due to reactions of fresh NO emissions with  $\text{NO}_3$ , and significant losses due to deposition and higher relative humidity.

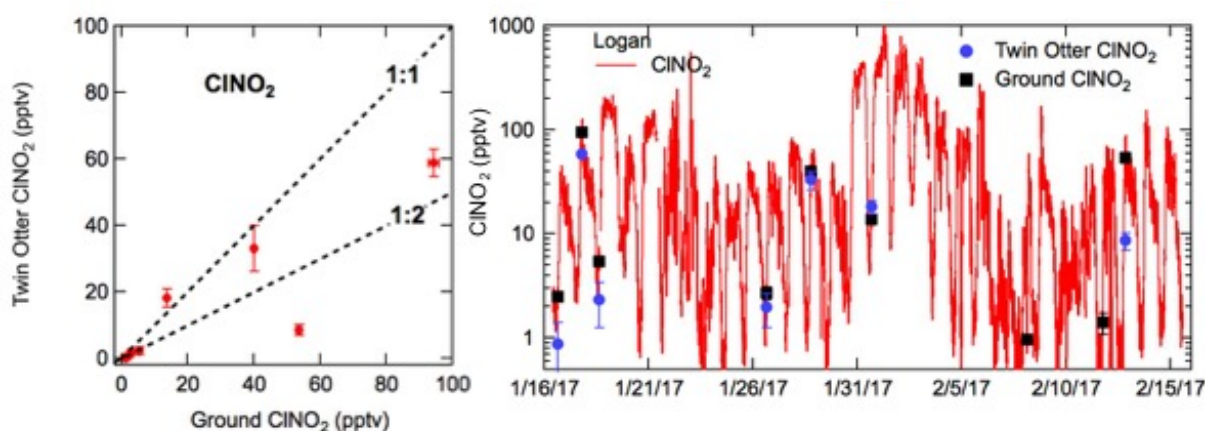


Figure 3.52 Comparison of  $\text{ClNO}_2$  at the Logan ground site and from Twin Otter missed approaches at the Logan-Cache airport. The ground site shows, generally, higher  $\text{ClNO}_2$  than measured aloft by the Twin Otter. Work is ongoing to determine if this variation in measurement is real or instrumental differences.

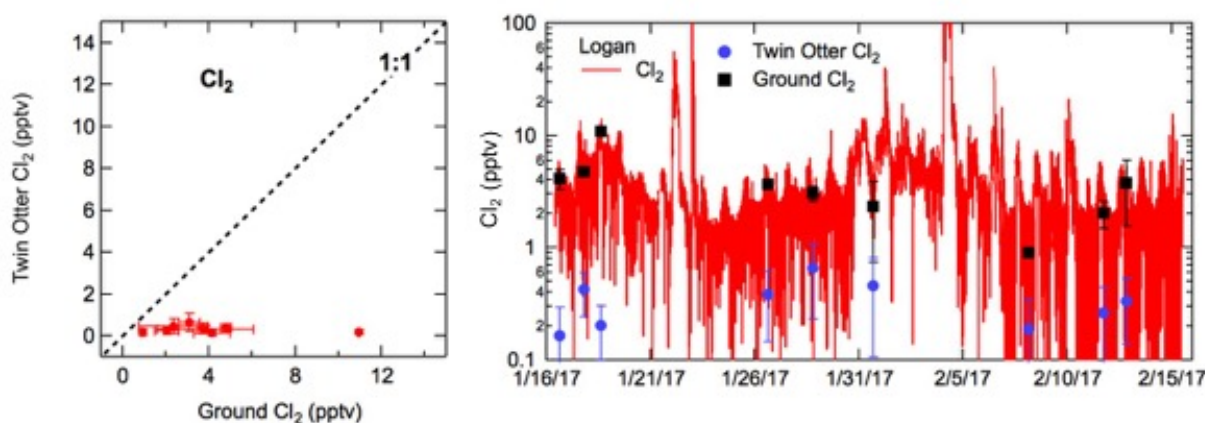


Figure 3.53 Comparison of  $\text{Cl}_2$  at the Logan ground site and from Twin Otter missed approaches at the Logan-Cache airport. The Twin Otter CIMS routinely shows  $\text{Cl}_2$  at or below the detection limit in this area, while the CIMS based at the Logan ground site indicates  $\text{Cl}_2$  mixing ratios up to 10 pptv.

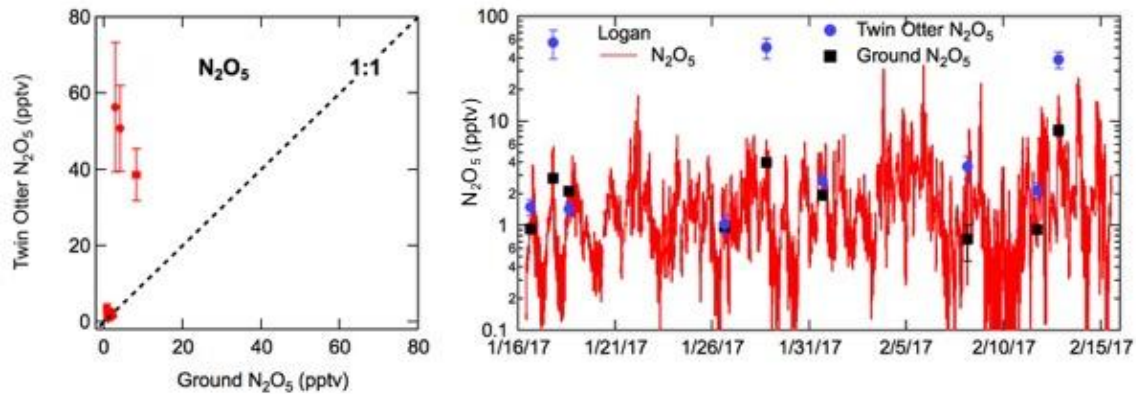


Figure 3.54 Comparison of  $N_2O_5$  at the Logan ground site and from Twin Otter missed approaches at the Logan-Cache airport.  $N_2O_5$  observed from the Twin Otter showed higher mixing ratios than observations from the ground site. This is consistent with past observations. At the surface,  $NO + NO_3$  is a more important  $NO_3$  pathway and there is increased loss of  $N_2O_5$  due to deposition and higher relative humidity.

### 3.5 Greenhouse Gases

The SLV is home to the longest continuous urban  $CO_2$  measurement network in the world. Started under the supervision of Dr. Jim Ehleringer at the University of Utah in 2001, the Utah Urban  $CO_2$  Network (UUCON, [air.utah.edu](http://air.utah.edu)) measures  $CO_2$  mole fraction in a variety of land use types at 6 sites in the valley. Recent efforts have modernized and expanded the network into neighboring areas, including Cache Valley, Heber Valley and a mountain top site located on Hidden Peak at Snowbird Ski Resort in a network of 9 total sites along the Wasatch front (Figure 3.55).

Studies utilizing the data collected from this network, as well as others, have identified greenhouse gases as a useful indicator of localized pollutants [73-75], urban growth and changes in local emissions [57], as well as to constrain uncertainties in emission inventories [73, 76-78], identify atmospheric transport processes [74, 75, 79-81], provide insight into meteorological process during PCAP conditions [73], and provide evidence for the co-emission of particulate precursors like  $NH_3$  [82, 83].

Additionally, many mobile greenhouse gas and pollutant measurements have been conducted in the SLV using van and light rail based platforms (Figure 3.55). The combination of in-situ and mobile measurements in the SLV has provided an insight into the distribution and temporal variability of trace gases, which are discussed in detail in Mitchell *et al.* [57]

During the 2017 UWFPS, carbon dioxide ( $CO_2$ ) and methane ( $CH_4$ ) were also measured at Logan site in the Cache Valley, using a Picarro G2508 CRDS. The 1-minute average values are shown in Figure 3.56 and Figure 3.57 along with  $PM_{2.5}$  mass concentration. As shown in Figure 3.56,  $CO_2$  concentrations track  $PM_{2.5}$  mass concentrations fairly well, reaching maximum levels during

PCAP periods. However, CO<sub>2</sub> does not increase at the same rate as the PM<sub>2.5</sub>. This is likely due to the strong enhancement of the PM<sub>2.5</sub> via secondary production pathways, while the CO<sub>2</sub> is limited to direct emissions. As can be seen in Figure 3.57, CO<sub>2</sub> shows temporal and diurnal variability, but averaged around 456 ppm during PCAP events and 420 ppm during the non-PCAP periods. These values are similar to those observed in the SLV during this study (not shown) and those reported in previous studies, however concentrations observed in the SLV tend to be ~25 ppm higher during PCAP conditions than to those observed at Logan [73, 84]. This is not surprising given the significantly greater amount of anthropogenic emissions in the SLV compared to Cache Valley.

CH<sub>4</sub> concentrations measured throughout the study period also showed generalized increases during the PCAP periods, but did not increase to the extent of the CO<sub>2</sub> and PM<sub>2.5</sub> (Figure 3.57). This could be reflective of the relative source strengths for each species. CH<sub>4</sub> concentrations averaged around 3.3 ppm during PCAP events and 2.6 ppm during the non-PCAP periods at the Logan site. Not surprising given the amount of agricultural activity in Cache Valley, these values are higher those observed in the SLV during this study and those observed in previous studies, where average concentrations of approximately 2.2 and 2.0 ppm during non-PCAP and PCAP events respectively [73, 84].

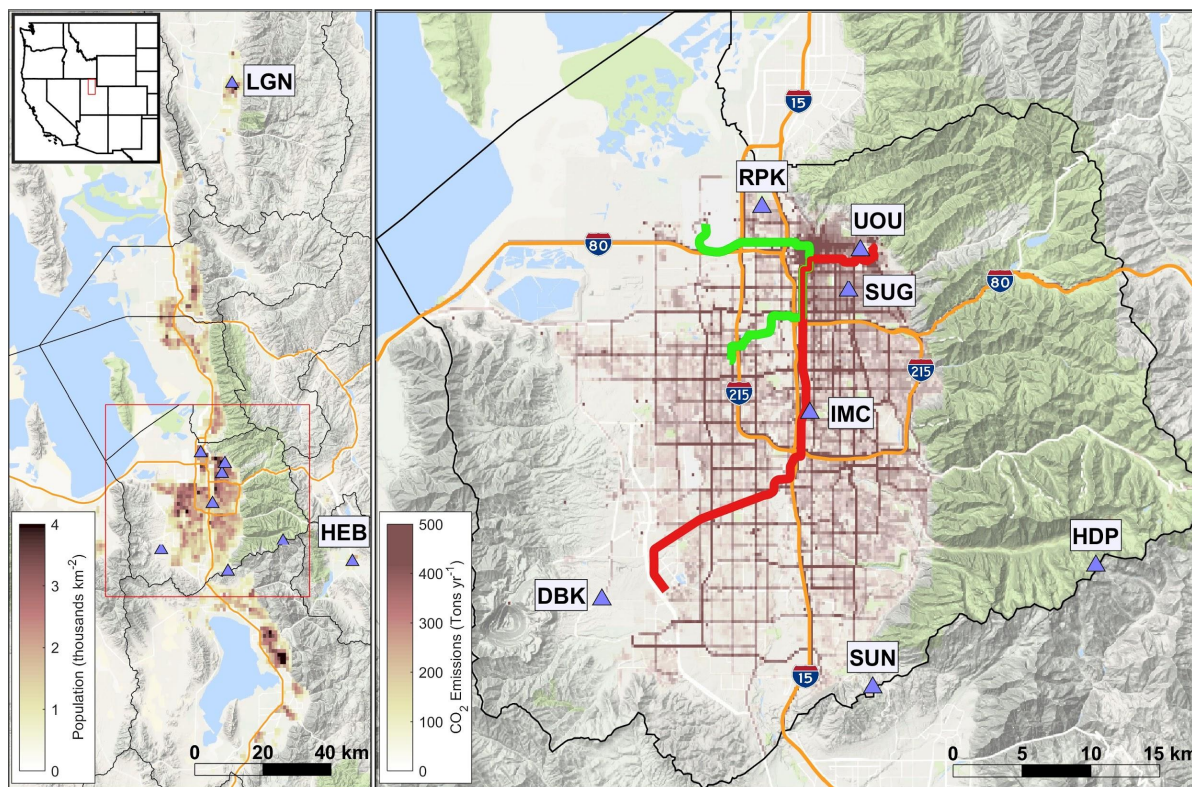


Figure 3.55 Map of the Utah Urban CO<sub>2</sub> Network (UUCON) measurement sites along the Wasatch front (Blue triangles) and TRAX lines (Red and Green) indicating light rail based mobile GHG measurements.

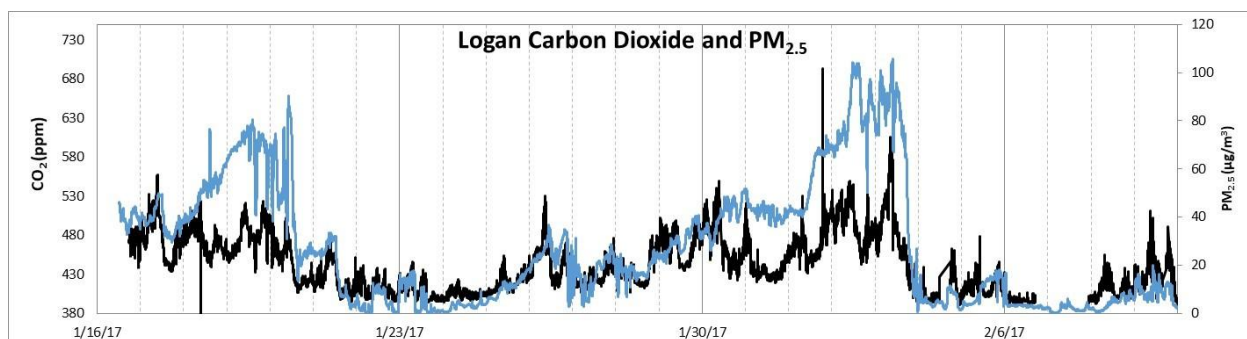


Figure 3.56 CO<sub>2</sub> and PM<sub>2.5</sub> measured at the EPA Logan trailer during the 2017 UWFPS. The black line shows CO<sub>2</sub> ppm (left axis) and the blue line shows PM<sub>2.5</sub> (right axis).

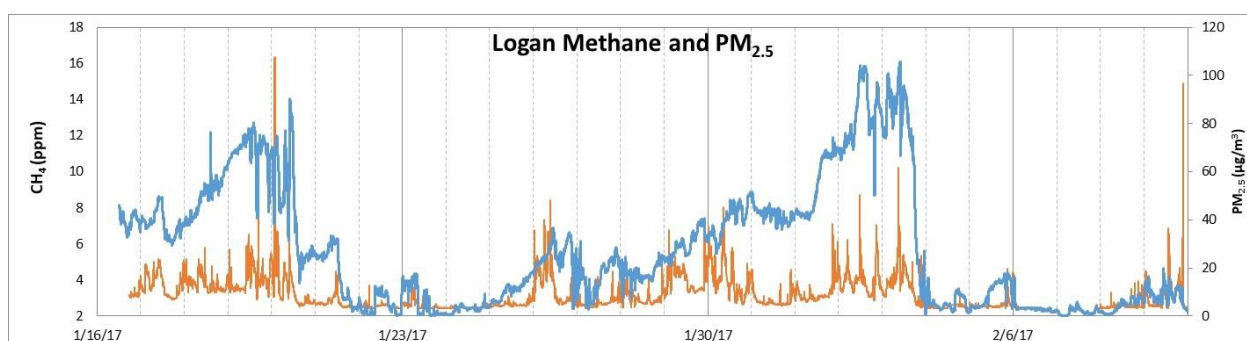
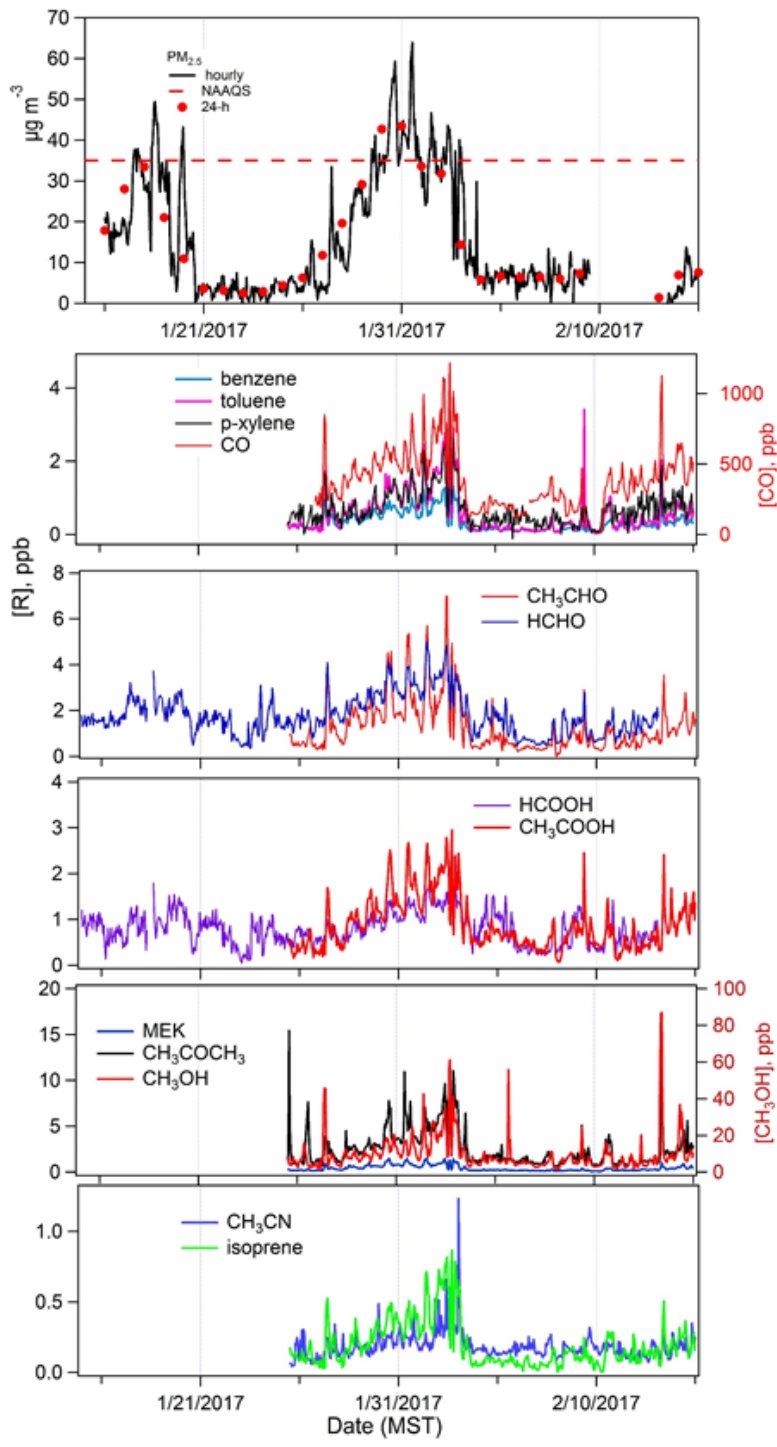


Figure 3.57 CH<sub>4</sub> and PM<sub>2.5</sub> measured at the EPA Logan trailer during the 2017 UWFPS. The gold line shows CH<sub>4</sub> ppm (left axis) and the blue line shows PM<sub>2.5</sub> (right axis).

### 3.6 Volatile Organic Compounds

Real-time VOC measurements were conducted at UU site during UWFPS. Figure 3.58 shows time series of BTX compounds (benzene, toluene, sum of xylenes as p-xylene), aldehydes (HCHO, CH<sub>3</sub>CHO), acids (HCOOH, CH<sub>3</sub>COOH), carbonyls (acetone, methylethyl ketone (MEK)), CH<sub>3</sub>OH, isoprene and CH<sub>3</sub>CN along with observed PM<sub>2.5</sub> and CO. Figure 3.59 and Figure 3.60 compare the diurnal and weekly trends of key VOCs with those of NO, CO, CH<sub>4</sub>, and PM<sub>2.5</sub>. As the pollution builds up during PCAPs, enhancements in all VOCs and CO were observed (Figure 3.58 and Figure 3.59). The concentrations of BTEX compounds ranged from 0.08 ppb during clean periods to 2 - 3 ppb during the pollution episodes with highest values of 1.5, 3.1, and 4.5 for benzene, toluene, and p-xylene, respectively. These values are within the range of BTEX levels measured at Bountiful (BV) and West Valley City as part of air toxics campaigns [85, 86] High concentrations of oxygenated volatile organic compounds (OVOC's) including HCHO, CH<sub>3</sub>CHO, CH<sub>3</sub>COCH<sub>3</sub>, and CH<sub>3</sub>OH are seen at this site with hourly values reaching as high 5, 7, 14, and 100 ppb, respectively.

As shown in Figure 3.59, BTEX compounds, isoprene,  $\text{NO}_x$ , and CO exhibit a morning peak ~ 10 AM, indicative of the emissions from mobile sources in the urban corridor and transport across the valley up to the sidewall, UU location. In contrast, surface  $\text{PM}_{2.5}$  show enhancements ~ 11 AM during pollution episodes as the convective boundary layer develops around that time and mixes the  $\text{PM}_{2.5}$  rich air from upper part of PCAP to the surface [15] and  $\text{O}_3$  reaches its daytime maxima ~ 2 PM MST. OVOCs reach their peaks around 10 - 11 AM, earlier than  $\text{O}_3$ , which suggest the importance of primary sources of OVOCs within the SLV valley. Consistently, weekly trends of these species show high values during midweek compared to the weekends, pointing to the influence of anthropogenic activities (Figure 3.60).  $\text{CH}_3\text{CHO}$ , acids ( $\text{HCOOH}$ ,  $\text{CH}_3\text{COOH}$ ) and carbonyls (e.g.  $\text{CH}_3\text{COCH}_3$  and MEK) appear to show a second, smaller peak later in the day indicating a small contribution from secondary sources. Reactive species such as isoprene and BTEX compounds are present during the day, reflecting the low levels of oxidants available during pollution episodes (Section 3.2).



Both  $\text{CH}_3\text{COCH}_3$ , and  $\text{CH}_3\text{OH}$ , common solvents, show peaks  $\sim 10 - 11$  AM like other OVOCs, but they also show sporadic, rapid enhancements during weekdays, often at night. This may indicate nearby sources or solvent usage in the vicinity of UU.  $\text{CH}_4$ , associated with emissions from natural gas activities, exhibit a broader peak between 9 - 11 AM, consistent with valley wide sources with some located closer to UU.

Figure 3.58 Time series of hourly averaged VOCs measured at UU along with  $\text{PM}_{2.5}$  and CO during UWFPS.

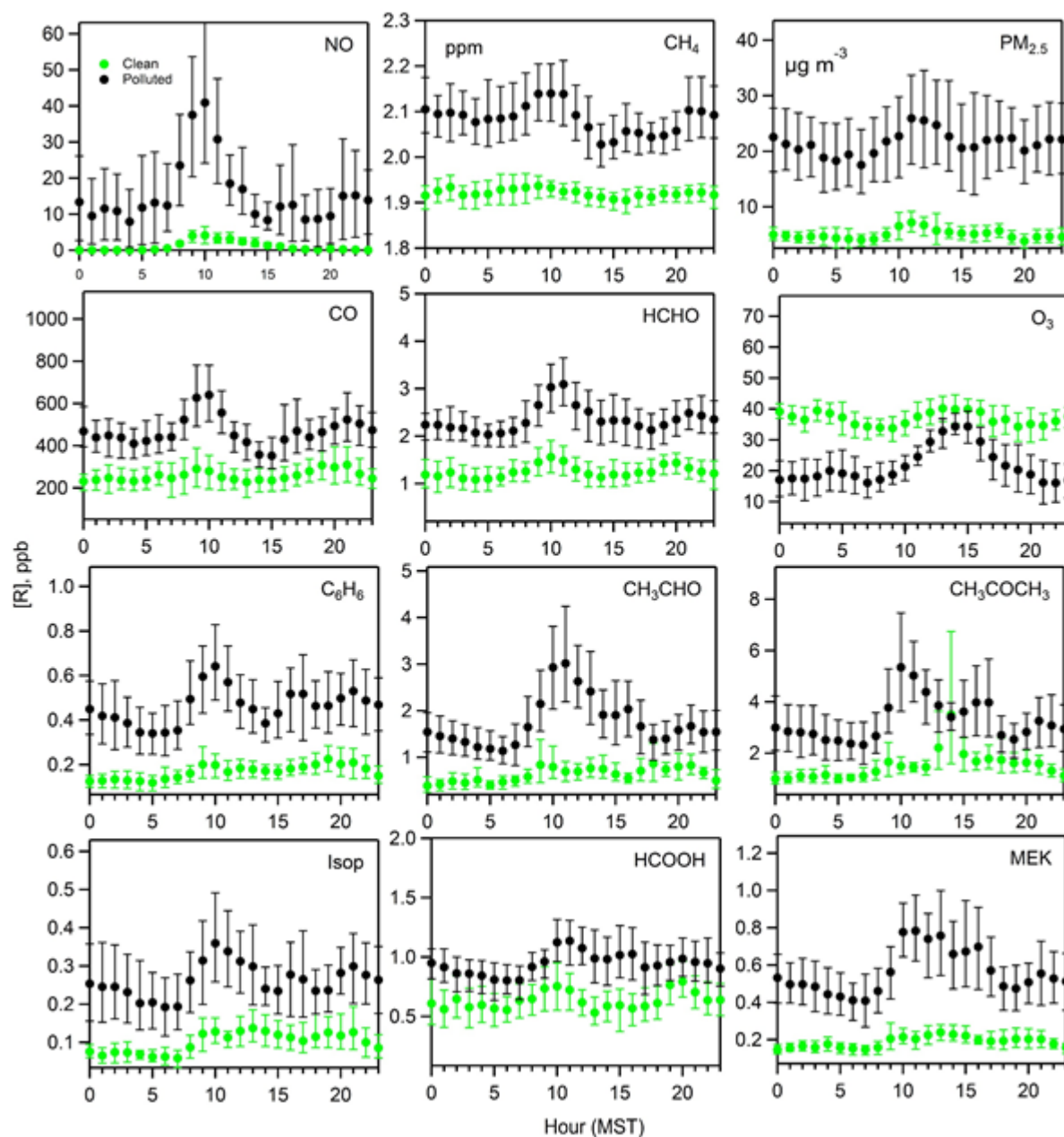


Figure 3.59 Diurnal trends of key VOCs, PM<sub>2.5</sub>, O<sub>3</sub>, CH<sub>4</sub> and CO measured at UU during polluted and clean conditions.

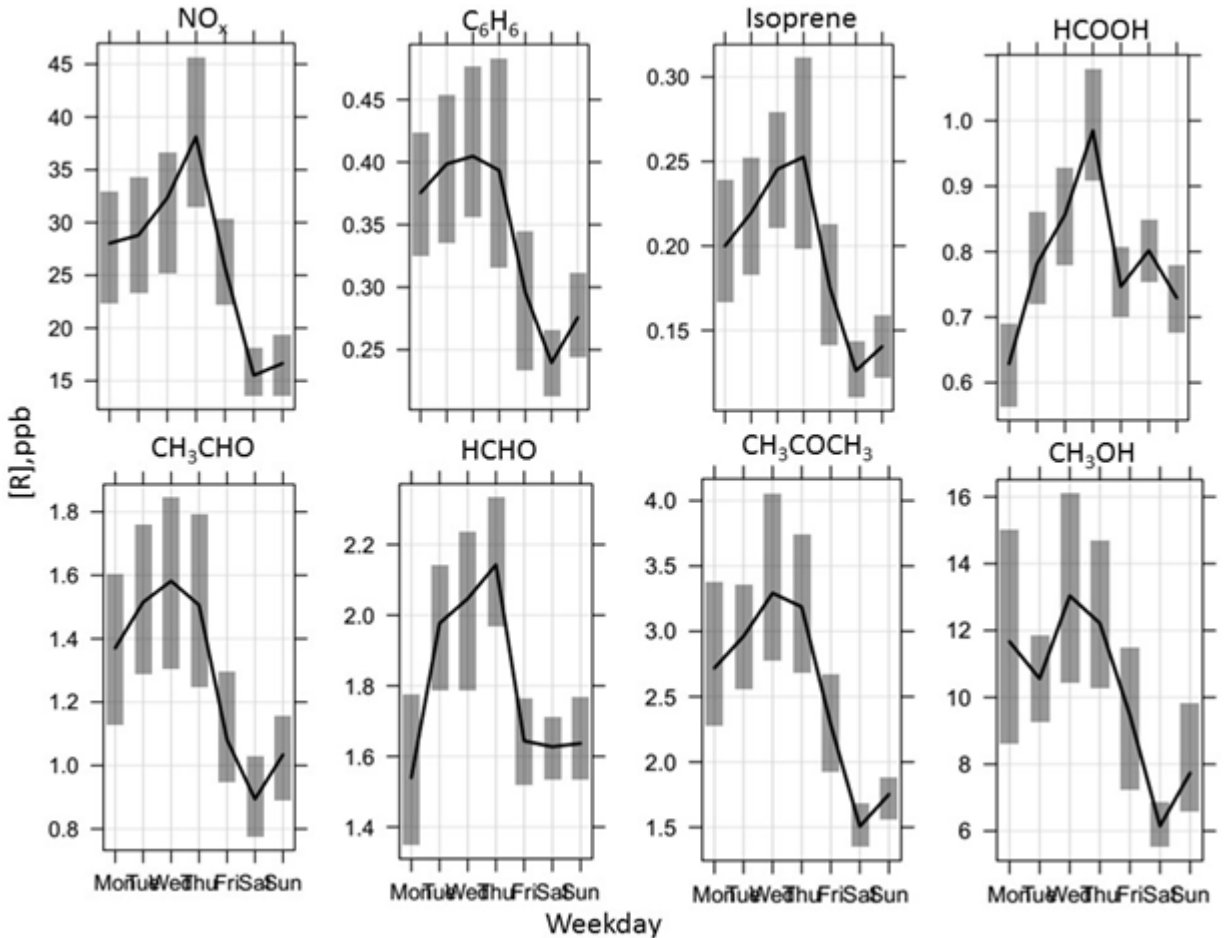


Figure 3.60 Weekly trends of key VOCs and  $\text{NO}_x$  at UU.

UDAQ's 2015 special air toxics study [85] noted high levels of HCHO and  $\text{CH}_3\text{CHO}$  reaching 15-20 ppb at Bountiful site and attributed them to emissions from the nearby industries located in the North Salt Lake City. According to the HCHO inventory from the 2014 NEI, mobile sources are the largest reported category of direct emissions, followed by residential wood combustion. Assuming a 20 km x 40 km and 400 m PBL, an emission rate of 71 lbs/hour and a 24-hr lifetime, ambient HCHO levels are expected to be around 2.2 ppb, which is within the range observed during UWFPS. This emission rate estimate does not include biogenic, wildfire and prescribed fire emissions of HCHO, which are negligible in winter. However, when photochemical losses are taken into consideration, it is estimated that these emissions would contribute to only ~ 0.5 ppb of HCHO. The estimated photolysis lifetime is ~5 hours based on the calculated midday photolysis rate. This discrepancy between the observed and estimated HCHO may indicate underrepresentation of HCHO sources.

In order to examine the importance of photochemical sources, the relationship between OVOC's and CO is examined in detail. The effects of emissions and transport processes are evident in the diurnal trends CO, NO<sub>x</sub> and OVOC's as seen in Figure 3.59, masking the photochemical contributions to ambient OVOCs. The ratio of VOC of interest-to-CO can be used to isolate the effect of photochemical formation [87]. Figure 3.61 shows diel trends of enhancement ratios of OVOC-to-CO under polluted condition. The higher enhancement ratios seen in the afternoon may indicate the importance of the secondary formation of these species in the afternoon during pollution episodes. There is also a second peak seen in the ratios of HCHO and HCOOH vs. CO around 4 AM.

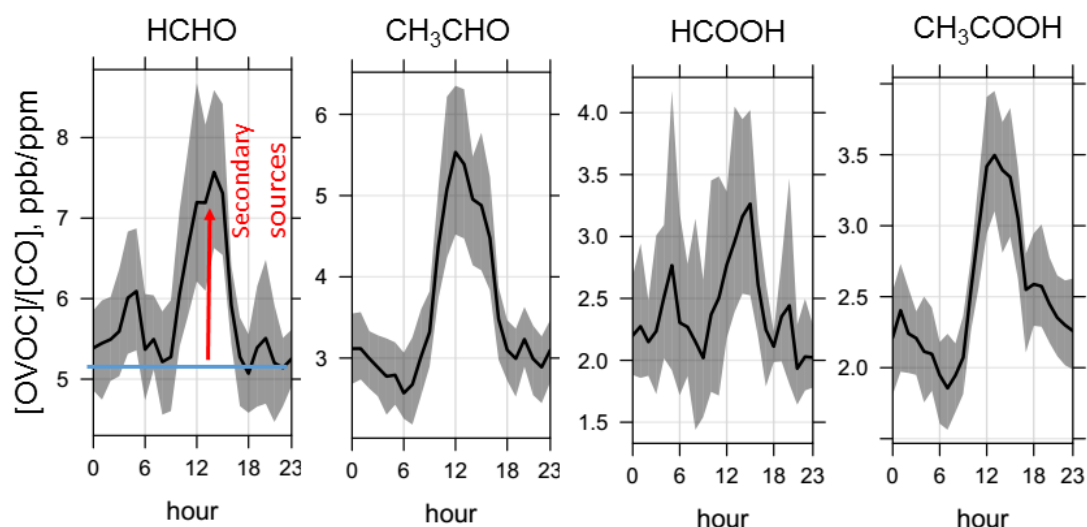


Figure 3.61 Diurnal trends of the ratios of HCHO, CH<sub>3</sub>CHO, HCOOH and CH<sub>3</sub>COOH versus CO.

Our observations indicate direct emissions as well as secondary production of HCHO and CH<sub>3</sub>CHO during the pollution episodes. High concentrations of HCHO and CH<sub>3</sub>CHO with 24-hr values of 3 - 4 ppb on average observed at UU during pollution episodes can influence the atmospheric chemistry significantly acting as a source of radicals during the day. Observations of the relevant radicals and photolysis parameters will be essential to quantify their contribution to the radical budget.

## 4 Limiting and Excess Reagents for Ammonium Nitrate

Ammonium nitrate ( $\text{NH}_4\text{NO}_3(\text{p})$ ) is formed from the equilibrium reaction of gas-phase nitric acid ( $\text{HNO}_3(\text{g})$ ) and ammonia ( $\text{NH}_3(\text{g})$ ), following Reaction 1. Under cold and dry wintertime conditions, the formation of particulate  $\text{NH}_4\text{NO}_3$  is thermodynamically favorable and its formation potential is proportional to the product of  $\text{NH}_3(\text{g})$  and  $\text{HNO}_3(\text{g})$  (e.g. [10, 88, 89]). During wintertime in Northern Utah,  $\text{PM}_{2.5}$  is mainly composed of  $\text{NH}_4\text{NO}_3$  (Section 3.1) and its effective mitigation will require that the limiting precursor reagent ( $\text{HNO}_3(\text{g})$  or  $\text{NH}_3(\text{g})$ ) be identified and its concentrations reduced.



Previous UDAQ modeling efforts, developed for State Implementation Plans, reported excess  $\text{NH}_3(\text{g})$  in all Non-Attainment Areas (NAA) of Northern Utah [7, 90, 91]. Additional sensitivity studies confirmed these results, in which  $\text{PM}_{2.5}$  concentrations were only sensitive to “very large” reductions in  $\text{NH}_3(\text{g})$  emissions. Excess gas-phase  $\text{NH}_3$  indicates that there are sufficient amounts of  $\text{NH}_3$  to first neutralize the acidic components (mainly sulfuric acid) in the aerosol phase and subsequently react with  $\text{HNO}_3(\text{g})$  via R1. Under these conditions,  $\text{NH}_4\text{NO}_3$  particle formation is limited by the presence of gas-phase  $\text{HNO}_3$ , which is formed from the atmospheric oxidation of  $\text{NO}_x$  (Section 3.2). Additional ground-based observational studies have similarly concluded that during pollution episodes, aerosol particles in the Salt Lake City region are neutralized (ion balance of 1) [9] and that air in both Salt Lake and Cache Valleys is  $\text{NH}_3$ -rich [10, 11, 92]. Prior to this study, an analysis of excess  $\text{NH}_3(\text{g})$  vs.  $\text{HNO}_3(\text{g})$  in Utah Valley had not been undertaken.

In the following section multiple methods are used to preliminarily identify the limiting reagent to  $\text{NH}_4\text{NO}_3(\text{p})$  formation as a function of location within Northern Utah, time of day, and whether pollution conditions are present.

### 4.1 Method #1 - Molar Ratios of Oxidized to Reduced Nitrogen

Since gas-phase  $\text{NH}_3$  and  $\text{HNO}_3$  are in a thermodynamic equilibrium with their particulate equivalents ( $\text{NO}_3^-(\text{p})$  and  $\text{NH}_4^+(\text{p})$ ), the limiting reagent is inferred from observations of the ratio of total nitrate ( $\text{HNO}_3(\text{g}) + \text{NH}_3^-(\text{p})$ ) to total reduced nitrogen ( $\text{NH}_x = \text{NH}_3(\text{g}) + \text{NH}_4^+(\text{p})$ ), shown in Equation 1. This ratio does not account for other contributing aerosol components such as  $(\text{NH}_4)_2\text{SO}_4$ ,  $\text{NH}_4\text{HSO}_4$ , and  $\text{NH}_4\text{Cl}$ , but should generally represent the  $\text{NH}_4\text{NO}_3$  aerosol system when particulate concentrations of sulfate and inorganic chloride are low, as was observed during pollution events in 2017 (Section 3.1). Under these conditions, a nitrogen ratio greater than 1 indicates that oxidized nitrogen is in excess and  $\text{NH}_4\text{NO}_3$  particle formation is limited by the presence of  $\text{NH}_3(\text{g})$ . Conversely, a ratio smaller than 1 indicates that formation is limited by the presence of  $\text{HNO}_3(\text{g})$  (which itself is limited by the oxidation rate of  $\text{NO}_x$  - Section 3.2).

$$\text{Ratio} = \frac{\text{HNO}_3(g) + \text{NO}_3^-(p)}{\text{NH}_3(g) + \text{NH}_4^+(p)} \quad (\text{E1, Nitrogen Ratio})$$

#### 4.1.1 Twin Otter Observations

##### **Salt Lake Valley**

During the UWFPs campaign, the NOAA Twin Otter conducted 50 box patterns over the North-South extent of the SLV, east of Interstate I-15 (Figure 4.1). Flights occurred day and night, during two different pollution episodes (#5 & #6) as well as “clear conditions” after February 5, 2017. Figure 4.2 shows a time series of the nitrogen ratios for this region, calculated from the measurements of gas and particle compounds, averaged over each individual box pattern. Based on this analysis of available data,  $\text{NH}_4\text{NO}_3$  particle formation over eastern SLC (highlighted in Figure 4.1) is predominantly limited by  $\text{HNO}_3(g)$ . There is one night during pollution Episode #6, however, that displays  $\text{NH}_3(g)$  limitation. This result is in contrast to all previous ground-based observations that show exclusive  $\text{HNO}_3(g)$  limitation in SLV [7, 9]. One explanation for this discrepancy is that nitrogen ratios could change as a function of time of day and altitude above the ground since vertical atmospheric transport times, sources of  $\text{NO}_x$  oxidants, and emissions of  $\text{NO}_x(g)$  and  $\text{NH}_3(g)$  all have clear diurnal cycles (Section 3.2). The shading in Figure 4.2 indicates whether the box patterns were flown during the day or after dark (as defined by solar zenith angle ( $\text{SZA} \geq 90^\circ$ )), while the color of each point indicates the average altitude above sea level (meters ASL) of that box. Figure 4.2 shows that although there were day-to-day variations in the nitrogen ratio, there were small differences between boxes flown repeatedly over the course of one day or night (i.e. 3 boxes on the night of Jan. 28), suggesting little time-of-day or altitude dependence of

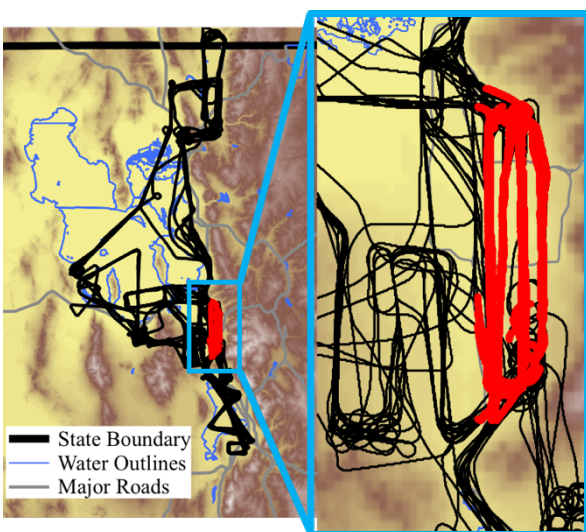


Figure 4.1 UWFPS flight track with Salt Lake City “Box Pattern” shown in red.

the nitrogen ratio. Figure 4.2. also shows that the system is close to the transition zone between these two regimes during pollution episodes. During these events, the nitrogen ratio also appears to increase over time. This may indicate that during long-lasting episodes the system is likely shifting from  $\text{HNO}_3$ -limited to  $\text{NH}_3$ -limited regime over time. Additional studies with a larger sampling size and longer duration will be important to investigate this further.

An additional comparison indicates that there was a larger excess in  $\text{NH}_x$  relative to total nitrate during clear conditions than during pollution episodes (lower nitrogen ratio) in this region of SLV. The smaller mass fraction of  $\text{NH}_4\text{NO}_3$  (Figure 3.2), however, also suggests a different dominant aerosol formation mechanism

during clear conditions than during pollution events. Further analysis is required to investigate factors driving this difference.

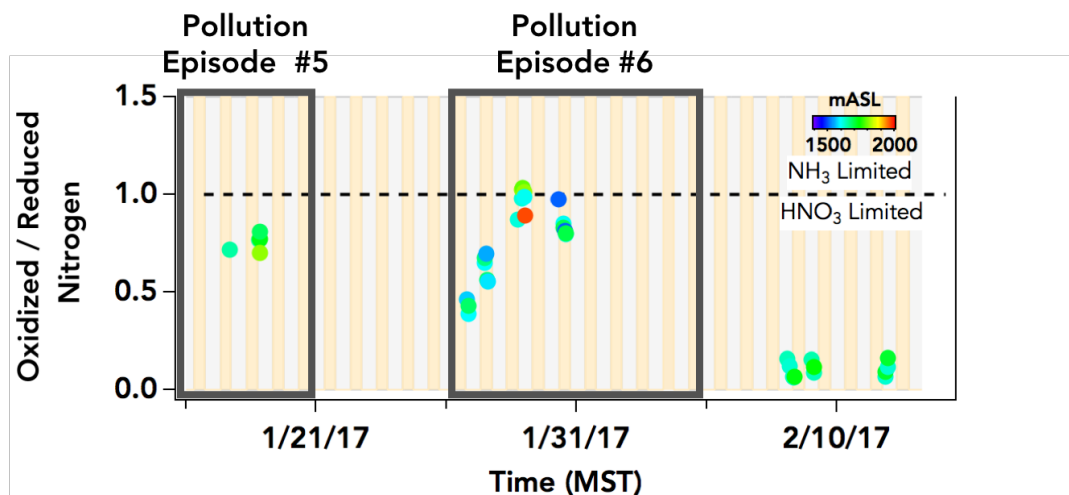


Figure 4.2 Time Series of Nitrogen Ratio from Salt Lake City. Each point represents the average ratio for a single “box-pattern” shown in Figure 4.1. Yellow/Gray shading indicates day/night as defined by  $SZA \geq 90^\circ$ . Time period of pollution episodes events are shown by gray boxes. Color scale shows the average altitude above sea level (meters ASL) of each box.

### Cache Valley

The NOAA Twin Otter conducted 10 flights into the Cache Valley during both polluted and clear conditions. Aircraft measurements collected at a 1-Hz time resolution were split into level, 30-second average intervals (Figure 4.3) in order to minimize any influence from rapid altitude changes.

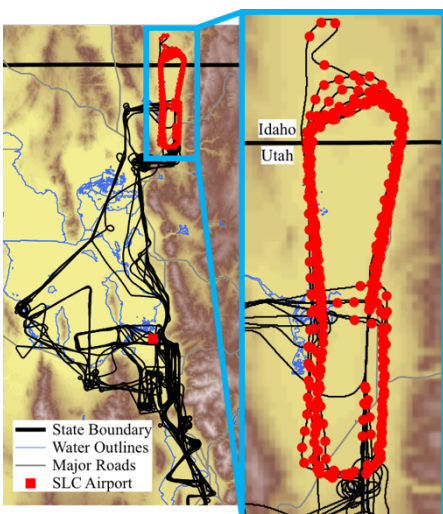


Figure 4.3 UWFPs Flight track with level, 30-second average intervals shown in red.

30-second average intervals (Figure 4.3) in order to minimize any influence from rapid altitude changes. The nitrogen ratio for each 30-second interval is shown as a time series in Figure 4.4, similar to Figure 4.2. These results are in agreement with previous ground-based studies that have observed  $\text{HNO}_3(\text{g})$ -limited conditions in the Cache Valley [11, 90, 92]. Although a smaller range of altitudes was sampled in Cache than in Salt Lake or Utah Valleys, the color scale in Figure 4.4 does not indicate a strong dependence of the nitrogen ratio on either altitude or time-of-day. The range of nitrogen ratios is also larger within a single flight than between flights, which indicates that the strongest factor influencing the nitrogen ratio may be location within the valley relative to  $\text{NO}_x(\text{g})$  and  $\text{NH}_3(\text{g})$  emission sources. Similar to the Salt Lake City boxes, the nitrogen ratio was lower during clear conditions, suggesting

a smaller excess of  $\text{NH}_x$  relative to total nitrate during pollution episodes, the reasons for which will require further investigation.

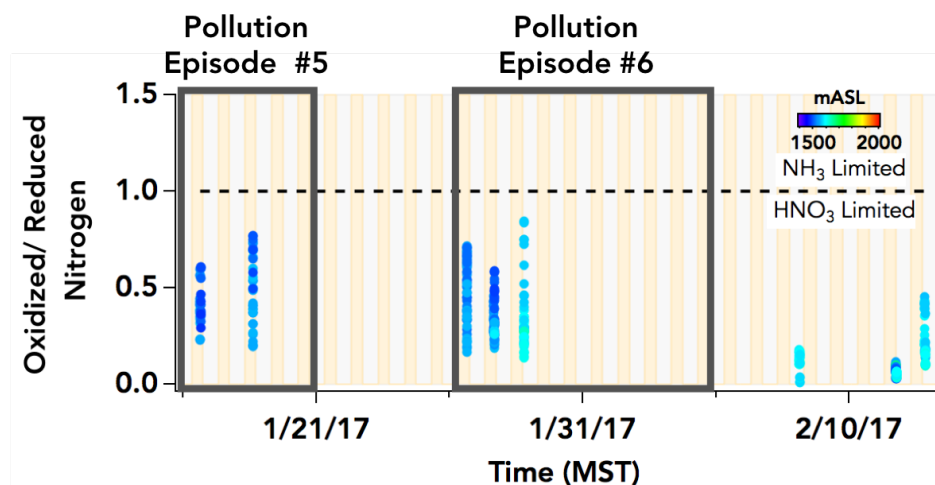


Figure 4.4 Time Series of Nitrogen Ratio from Cache Valley. Individual points represent 30-second averages over constant altitudes. Yellow/Gray shading indicates day/night as defined by  $\text{SZA} \geq 90^\circ$ . Time period of pollution episodes are shown by gray boxes. Color scale shows the average altitude above sea level (meters ASL).

### Utah Valley

The NOAA Twin Otter conducted 12 flights over the Utah Valley during both polluted and clear conditions. Similar to the Cache Valley data, 1-Hz measurements were split into level, 30-second average intervals as shown in Figure 4.5. The nitrogen ratio for each 30-second interval is shown in Figure 4.6. These are the first field-based results examining the limiting reagents of  $\text{NH}_4\text{NO}_3(\text{p})$

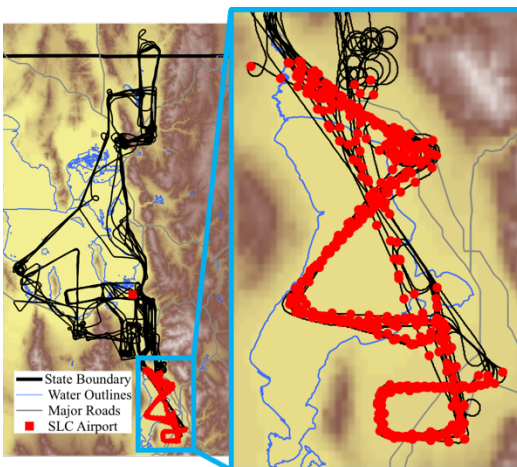


Figure 4.5 UWFPs Flight track with level, 30-second average intervals shown in red.

formation in Utah Valley. Similar to the Salt Lake City boxes,  $\text{NH}_4\text{NO}_3$  particle formation in Utah Valley appears to be limited mainly by  $\text{HNO}_3(\text{g})$  with one period of  $\text{NH}_3(\text{g})$  limitation observed during pollution episode #6 with several cases approaching 1. The  $\text{HNO}_3(\text{g})$  limitation is in agreement with previous emission inventory-based modeling studies [91]. Periods of  $\text{NH}_3(\text{g})$  limitation on the night of Jan. 28 occurred at some of the highest sampled altitudes. Ratios approaching 1, however, were observed at lower altitudes on the previous and subsequent flight days, obscuring any clear altitude dependence. In addition,  $\text{NH}_3(\text{g})$  limitation was only observed one night during UWFPs 2017 making it difficult to draw a definitive conclusion about the altitude or time-of-day

dependence of the observed nitrogen ratios in Utah Valley. Yet, as in the SLV, this can also indicate a time evolution of the system toward a more  $\text{NH}_3$ -limited regime as a pollution episode progresses. Similar to Cache Valley, the largest factor determining the nitrogen ratio within the  $\text{HNO}_3$ -limited regime (ratio < 1) appears to be location within the valley. In addition, as with the two other regions, there is also a smaller excess in  $\text{NH}_x$  relative to total nitrate during pollution episodes than during clear conditions.

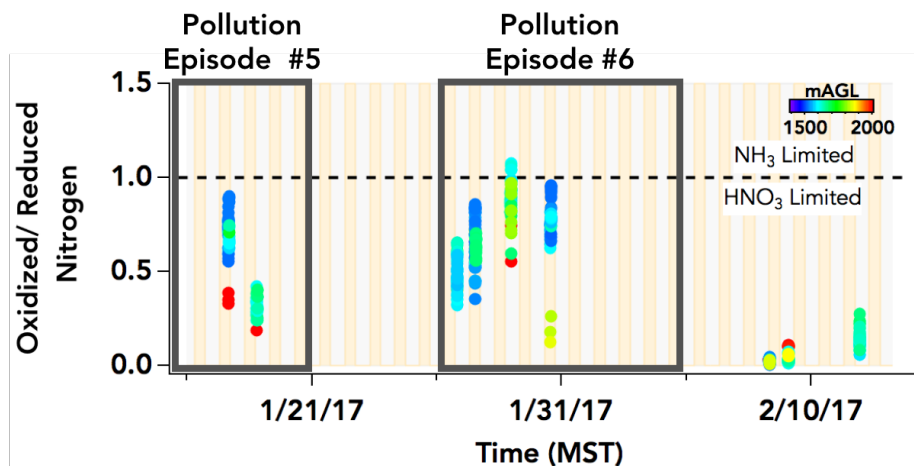


Figure 4.6 Time Series of Nitrogen Ratio from Utah Valley. Individual points represent 30-second averages over constant altitudes. Yellow/Gray shading indicates day/night as defined by  $\text{SZA} \geq 90^\circ$ . Time period of pollution episodes are shown by gray boxes. Color scale shows the average altitude above sea level (meters ASL).

#### 4.1.2 Ground Site Observations

##### Salt Lake Valley – UU Site

Ambient gas concentrations and particle composition were measured using an AIM-IC (Section 2.4.2) at the UU. Due to technical difficulties, high-quality  $\text{HNO}_3(\text{g})$  and particulate  $\text{NO}_3^-(\text{p})$  data are only available from February 13-21 and do not overlap with any Twin Otter flights. Comparing the total level of nitrates ( $\text{HNO}_3(\text{g}) + \text{NO}_3^-(\text{p})$ ) with the total  $\text{NH}_x$  ( $\text{NH}_3(\text{g}) + \text{NH}_4^+(\text{p})$ ) during pollution episode #7, however, clearly shows an excess of  $\text{NH}_x$  (Figure 4.7), which is in agreement with ratios derived from the Twin Otter flights during a short-lived episode #5 or beginning of episode #6. An ion balance based on total particle anions and cations measured by the AIM-IC during February 13-21 (Figure 3.8) additionally shows that aerosol particles at the UU ground site were fully neutralized, as expected in an  $\text{NH}_3$ -rich region and previously observed [9]. Figure 4.7 also shows that variability in the nitrogen ratio does not correlate with time of day, suggesting a different driving factor. The totals displayed in this figure only account for gases and particles smaller than  $2.5 \mu\text{m}$ . There is evidence of significant coarse mode particle mass during the previous episode (#6), but no information about their composition.

In addition to showing a clear  $\text{HNO}_3$  limitation, Figure 4.7 also shows that the nitrogen ratio was larger during pollution episode #7 than during clear conditions. This trend was also observed in the Twin Otter data for all three Northern Utah Valleys and suggests that the availability of total nitrate relative to  $\text{NH}_x$  is greater during pollution episodes, but not enough to transition the region to a  $\text{NH}_3$  limited regime during short-lived episodes. Although currently an open question as to why this change occurs, it is possible that  $\text{HNO}_3$  reactions with mineral/coarse mode particles may play an important role in limiting the availability of  $\text{HNO}_3$  during these events. Elucidating this effect on  $\text{NH}_4\text{NO}_3(\text{p})$  formation would require further investigation of gas-particle partitioning of nitrate and composition of coarse mode particles. An alternative explanation could be the heterogeneity of  $\text{NH}_3$  sources in the SLV and the stable conditions during the pollution episodes that can inhibit the dispersion of  $\text{NH}_3$  throughout the valley and the transport of  $\text{NH}_3$  between the valleys as discussed in section 5.

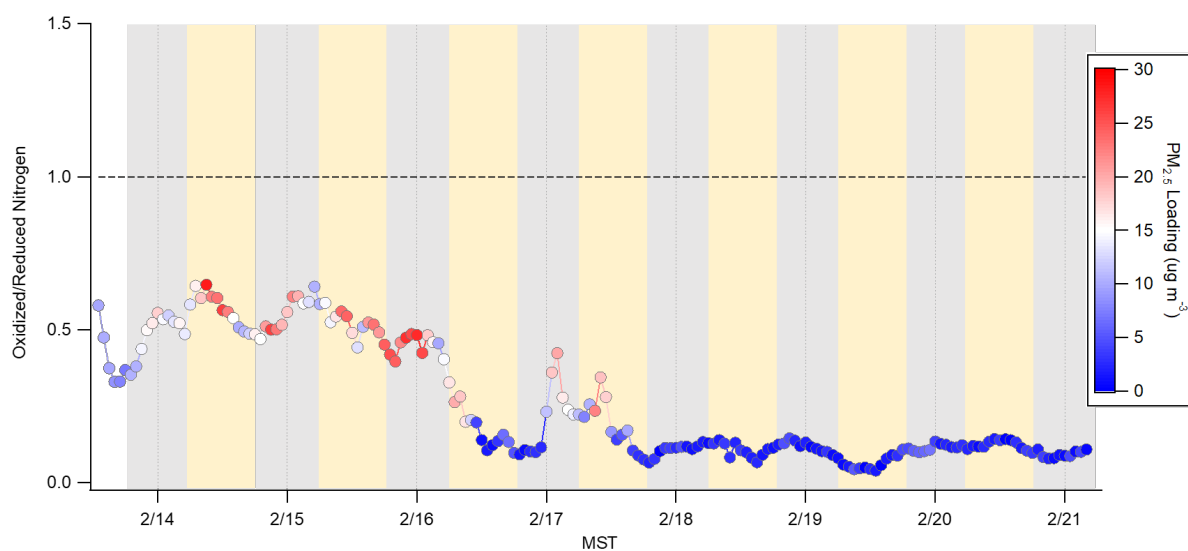


Figure 4.7 Ratio of Oxidized to Reduced Nitrogen for pollution episode #7 and clear (after 18 Feb.) periods in mid-February. Yellow/Gray shading indicates day/night as defined by  $\text{SZA} \geq 90^\circ$ . Markers are colored by the total measured  $\text{PM}_{2.5}$  aerosol mass (not including water).

### Cache Valley – Logan (LGN) Site

Measurements of particle composition were collected by an EPA Aerosol Mass Spectrometer operated at the Logan ground site (Section 2.4.1). Additional measurements of gas-phase  $\text{HNO}_3$  were collected by an EPA Chemical Ionization Mass Spectrometer and  $\text{NH}_3(\text{g})$  was measured by the USU's PICARRO instrument. The nitrogen ratio was calculated as described above and shown in Figure 4.8. Individual dots represent 5-second averaged data, which correspond to the reported time resolution of the AMS. It should be noted that AMS  $\text{NH}_4^+(\text{p})$  measurements are from the analysis of unit mass resolution data and therefore do not account for the possible presence of organonitrates, organosulfates, or amines. Similar to the aircraft observations (presented above) and previous ground-based studies [11, 92], Cache Valley was exclusively  $\text{NH}_3$ -

rich/ $\text{HNO}_3$ -limited during the 2017 study. An ion balance based on AMS data in Figure 3.7 additionally shows that aerosol particles in Cache Valley during UWFPS 2017 were fully neutralized, as expected in an  $\text{NH}_3$ -rich region. In contrast to the aircraft observations, however, there is no distinct difference between the nitrogen ratio during pollution episodes and clear conditions. Overall, the nitrogen ratios are also lower than those observed from the aircraft. This may suggest that the excess  $\text{NH}_x$  relative to total nitrate is always larger at ground level than aloft ( $> 1500\text{m ASL}$ ) in Cache Valley, regardless of whether pollution conditions are present.

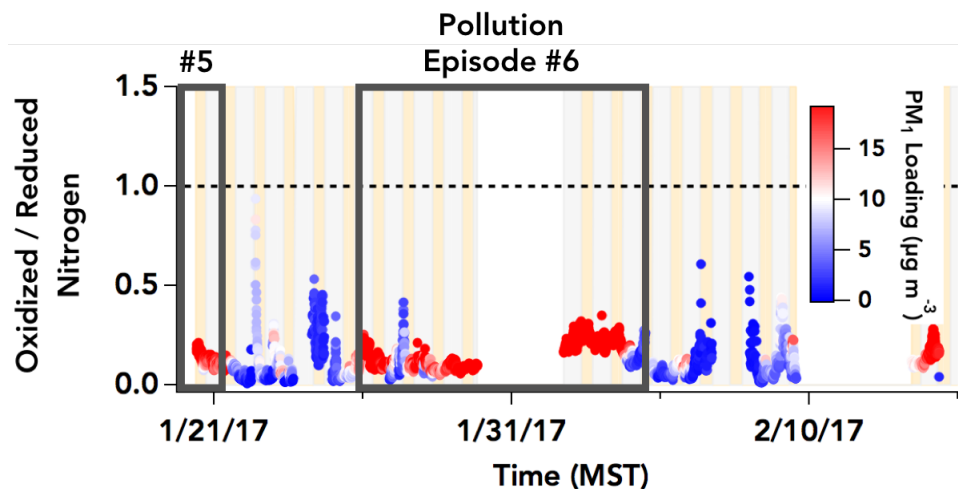


Figure 4.8 Time series of Nitrogen Ratio at the Logan Ground Site. Black dots represent 5-minute averages. Yellow/Gray shading indicates day/night as defined by  $\text{SZA} \geq 90^\circ$ . Time period of pollution episodes are shown by gray boxes.

## 4.2 Method #2 - Thermodynamic Modeling

The main measurements used for this comparison were:  $\text{HNO}_3(\text{g})$  and  $\text{HCl}(\text{g})$  measured using an I-CIMS,  $\text{NH}_3(\text{g})$  measured with a QC-TILDAS, and the chemical composition of the non-refractory component of the sub-micron aerosol particles with an AMS (Section 2.1.1). This analysis uses ISORROPIA (v2.1) to determine the aerosol to gas phase partitioning of inorganic compounds. ISORROPIA is a model that assumes thermodynamic equilibrium. The aerosol particles are assumed to be internally mixed, meaning that all particles are of the same size and have the same composition [93, 94].

ISORROPIA was run in “forward mode” in order to predict the particle-gas partitioning of each component starting from the user-provided inputs of measured concentrations of total nitrate ( $\text{HNO}_3(\text{g}) + \text{NO}_3^-(\text{p})$ ), total ammonium ( $\text{NH}_x = \text{NH}_3(\text{g}) + \text{NH}_4^+(\text{g})$ ), total chloride ( $\text{HCl}(\text{g}) + \text{Cl}^-(\text{p})$ ), total sulfate ( $\text{SO}_4^{2-}(\text{p})$ , assuming  $\text{H}_2\text{SO}_4(\text{g})$  was negligible), together with ambient temperature and relative humidity. The model output consists of the concentrations of the gas phase components ( $\text{HNO}_3(\text{g})$ ,  $\text{NH}_3(\text{g})$  and  $\text{HCl}(\text{g})$ ) along with the aerosol phase components, further divided into solid

and liquid phases. In this analysis, the focus is on the partitioning between the gas and aerosol phase, disregarding whether the species are solid or liquid within the aerosol phase.

The thermodynamic model here was restricted to using AMS data for aerosol species, which typically does not measure sodium salts (e.g., sodium chloride, nitrate, or sulfate). These salts have extremely low saturation vapor pressures and it was assumed that their low vapor pressures do not affect the partitioning of the acidic gases when the corresponding ammonium salts were observed. Hence, sodium and its corresponding salts were not included in the model. It is recognized, however, that the presence of sodium and other alkali and alkaline earth metals (such as potassium, calcium, and magnesium) could affect the partitioning of the acidic gases in this environment (e.g., acid displacement of  $\text{HNO}_3(\text{g})$  from sodium chloride that generates  $\text{HCl}(\text{g})$ ).

#### **4.2.1 Results from All Regions (All Twin Otter Data)**

First, data from all Twin Otter flights were compared with the model output (Figure 4.9). The comparison between the model results (y-axis) and the measurements (x-axis) shows a good agreement for the gas- and particle-phase  $\text{NH}_x$  and nitrate species, as shown in the top two rows of Figure 4.9. Gas phase nitric acid (plot in the center) had time periods where the model seemed to overestimate the concentrations. However, this could be due to the relatively small fraction of total nitrate in the gas phase compared to the aerosol phase, which appeared mostly represented accurately by the model. There is a less than satisfactory agreement for the chloride species.  $\text{HCl}(\text{g})$  is moderately underestimated and  $\text{Cl}(\text{p})$  is grossly overestimated by the model as seen in the bottom, right two panels of Figure 4.9. This discrepancy requires further investigation, however is most likely related to the model itself, as ISORROPIA previously overestimated the aerosol  $\text{Cl}(\text{p})$  up to 40% while simultaneously behaving well for ammonium and nitrate species [94]. This chloride-partitioning trend has also been observed in the Extended-AIM aerosol thermodynamics partitioning model. Note that the subsequent sensitivity analyses are affected by the model's calculation of chloride partitioning, especially when the total nitrate (gas+particle) is reduced.

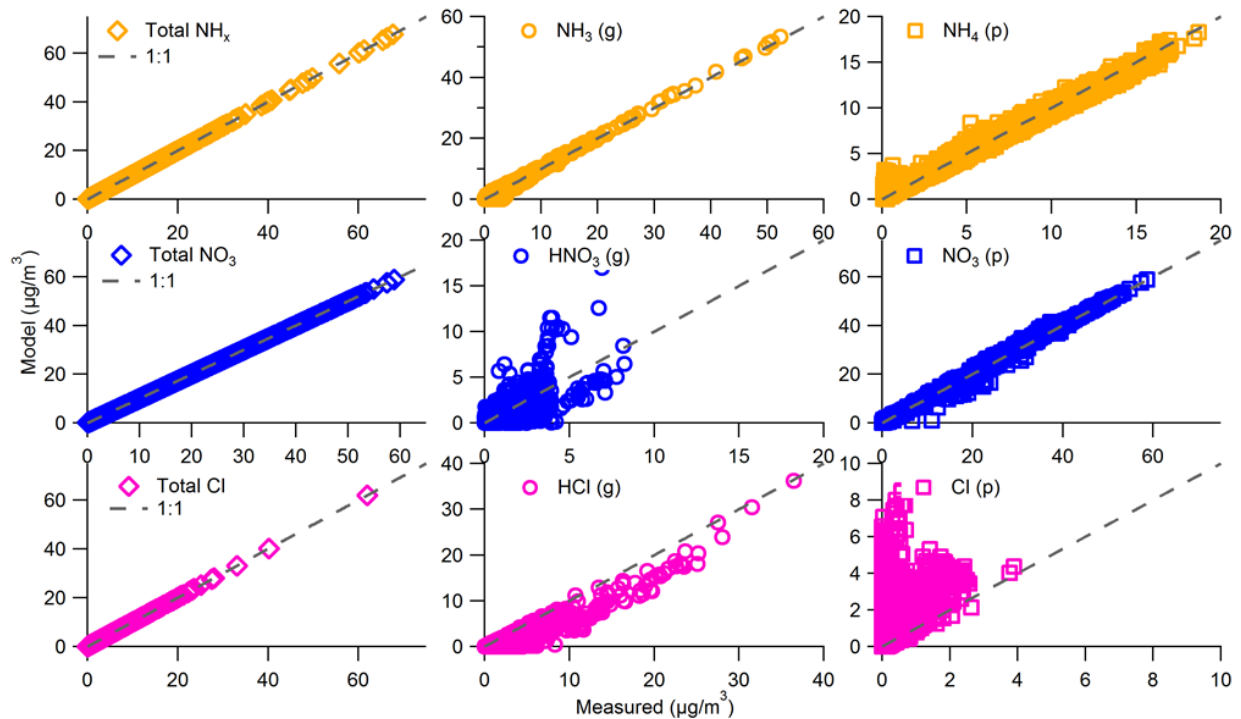


Figure 4.9 Comparison between measurements (x-axis) and model results (y-axis) of the phase partitioning of ammonium (yellow), nitrates (blue) and chloride (pink). All Twin Otter data are shown. The leftmost column shows the total  $\text{NH}_x$ , nitrate, and chloride (gas+aerosol) and constitutes the input of the model. The central and rightmost columns show the gas and aerosol phase predicted by the model using measured temperature and relative humidity.

In the second part of this analysis, two tests were conducted to assess the sensitivity of the system to reductions in  $\text{NO}_x(\text{g})$  and  $\text{NH}_3(\text{g})$  emissions, carried out by decreasing the inputs of total nitrate (Figure 4.10, left column) and total ammonium (Figure 4.11, left column) by a factor of two. In each of the remaining figures, the x-axis represents the “base case” results (the model output with the available measurements as inputs) shown in Figure 4.9 above, while the y-axis shows the model results from each sensitivity study.

In the nitrate-reduction case (Figure 4.10),  $\text{HNO}_3(\text{g})$  and the  $\text{NO}_3^-(\text{p})$  decreased by roughly the same amount, as expected. The  $\text{Cl}^-(\text{p})$  slightly increased, pointing towards some replacement of  $\text{NH}_4\text{NO}_3$  with  $\text{NH}_4\text{Cl}$  in the particle phase. The  $\text{NH}_3(\text{g})$  increased, reflecting the evaporation of part of the  $\text{NH}_4\text{NO}_3$  in the aerosol phase. There appear to be two responses of  $\text{NH}_4^+(\text{p})$ , one where the  $\text{NH}_4^+(\text{p})$  decreases and one where it doesn't. It would be expected that a reduction of available nitrate (i.e. reduced input nitrate) would subsequently reduce particulate  $\text{NH}_4^+$  if the aerosol composition was predominantly  $\text{NH}_4\text{NO}_3$  and its formation was nitrate-limited (as shown by results of the nitrogen ratio analysis). Therefore, this result is unexpected and will require further investigation.

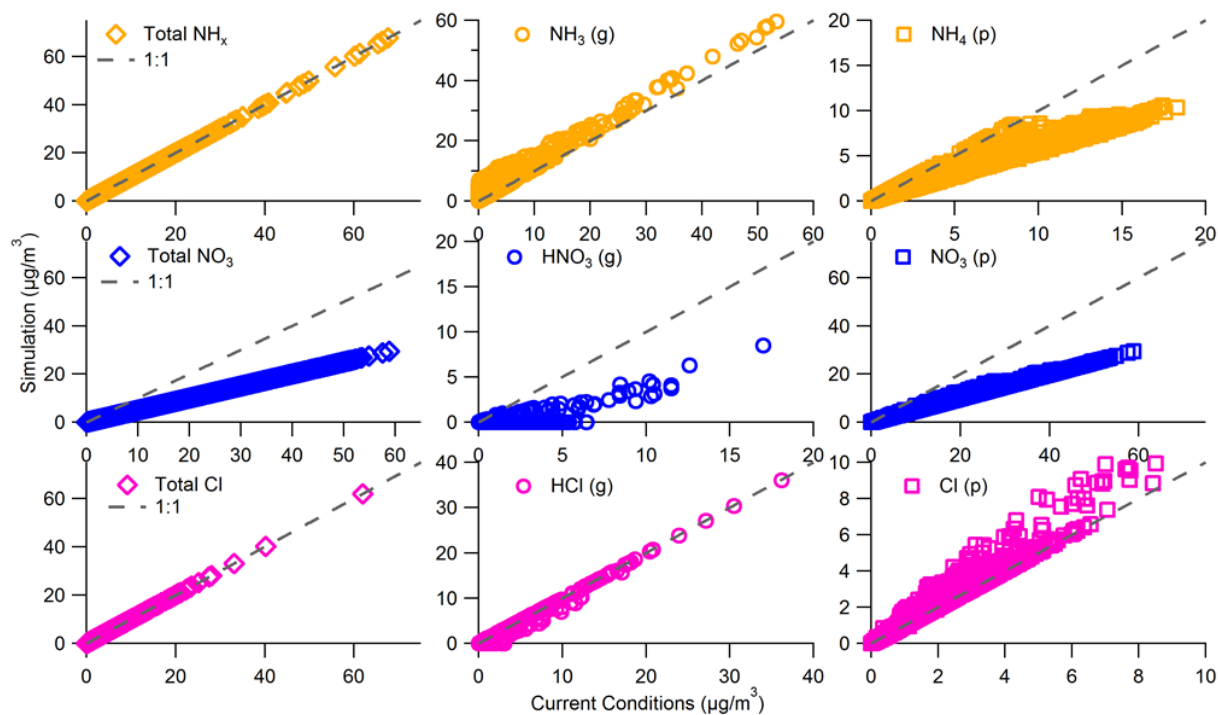


Figure 4.10 Comparison between original model results (from Figure 4.9, here on the x-axis) and the simulation case where the input of total nitrate is divided by 2 (y-axis). All Twin Otter data are shown. The leftmost column shows the concentrations of total  $\text{NH}_x$ , nitrate, and chloride (gas+aerosol). The central and rightmost columns show, respectively, the gas and aerosol phase predicted by the model for the new conditions using measured temperature and relative humidity.

In the ammonium-reduction case (Figure 4.11),  $\text{NH}_3(\text{g})$  decreased markedly, as expected, while  $\text{HNO}_3(\text{g})$  and  $\text{HCl}(\text{g})$  increased, reflecting the partial evaporation  $\text{NH}_4\text{NO}_3(\text{p})$  and  $\text{NH}_4\text{Cl}(\text{p})$ . Interestingly, there appear to be two responses, one where there is a reduction in  $\text{NH}_4^+(\text{p})$  and  $\text{NO}_3^-(\text{p})$  and one where there is no reduction (Figure 4.11, right column). As in the nitrate-reduction case, this dual response is not expected for nitrate-limited  $\text{NH}_4\text{NO}_3(\text{p})$  formation and requires further investigation.

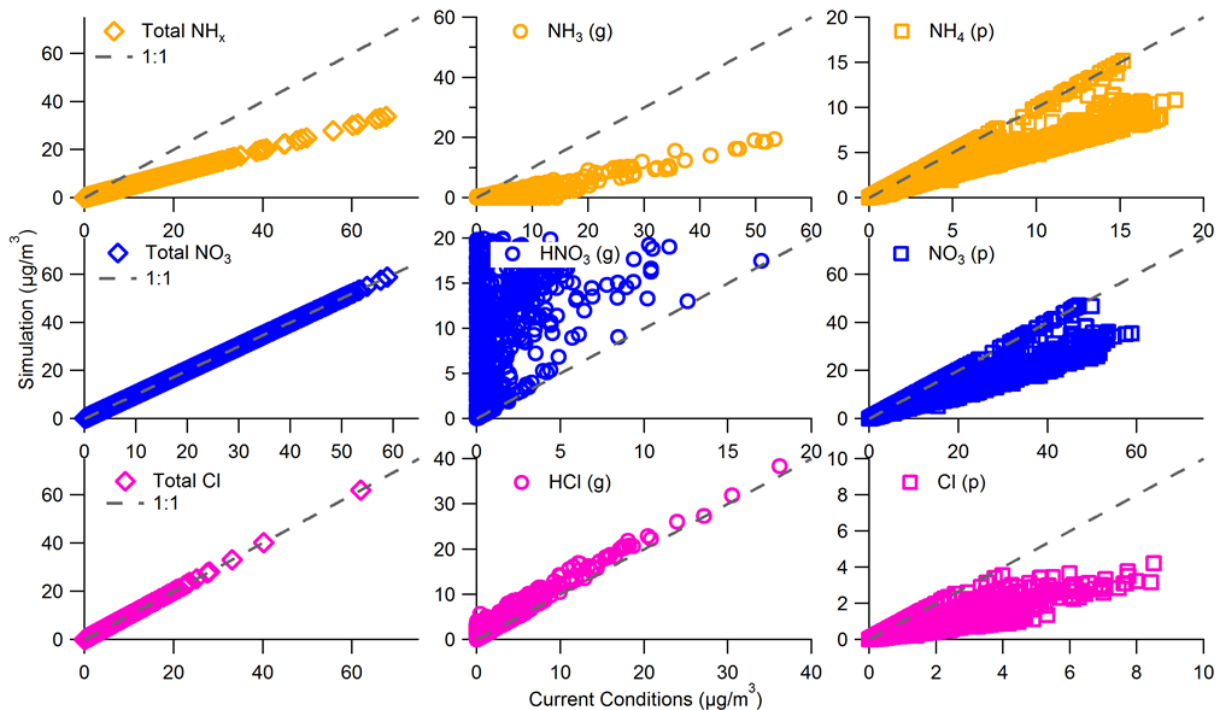


Figure 4.11 Same as Figure 4.10, except the input of total  $\text{NH}_x$  is divided by 2.

#### 4.2.2 Salt Lake Valley

Results for the nitrate-reduction case for SLV data are shown in Figure 4.12 and appear similar to those described above for the ensemble of the data. The most striking feature is that modeled  $\text{HNO}_3(\text{g})$  is reduced to nearly zero  $\mu\text{g m}^{-3}$  when the total nitrate input is halved, while the concentrations of  $\text{NH}_3(\text{g})$  increase, reflecting the evaporation of part of the  $\text{NH}_4\text{NO}_3$  in the aerosol phase. The  $\text{HCl}(\text{g})$  decreased and the  $\text{Cl}^-(\text{p})$  increased, pointing towards the replacement of  $\text{NH}_4\text{NO}_3$  with  $\text{NH}_4\text{Cl}$  in the particle phase. The  $\text{NH}_3(\text{g})$  increased, reflecting the evaporation of part of the  $\text{NH}_4\text{NO}_3$  in the aerosol phase. These results suggest that  $\text{NH}_4\text{NO}_3$  aerosol formation in SLV is limited by the availability of nitrate.

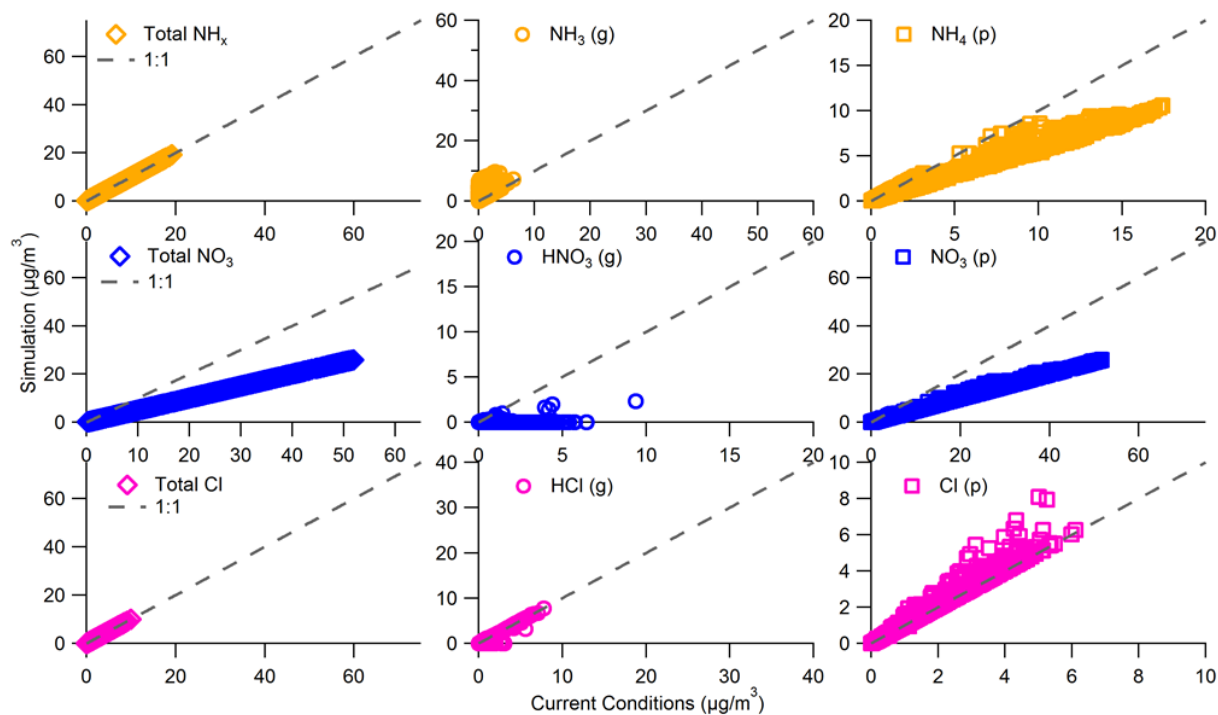


Figure 4.12 Comparison between original model results (from Figure 4.9, here on the x-axis) and the case where the input of total nitrate is divided by 2 (y-axis), for Salt Lake Valley only. The leftmost column shows the total  $\text{NH}_x$ , nitrate, and chloride (gas+aerosol). The central and rightmost columns show the gas and aerosol phase predicted by the model for the new conditions using measured temperature and relative humidity.

In the ammonium-reduction case (Figure 4.13), the  $\text{NH}_3(\text{g})$  decreased, as expected, while the  $\text{HNO}_3(\text{g})$  and  $\text{HCl}(\text{g})$  increased, reflecting the evaporation of part of  $\text{NH}_4\text{NO}_3$  and  $\text{NH}_4\text{Cl}$  in the aerosol phase. The  $\text{NH}_4^+(\text{p})$  and the  $\text{Cl}^-(\text{p})$  decreased. Interestingly, only some of the data show a decrease in  $\text{NO}_3^-(\text{p})$  (Figure 4.13, middle row, right column). Currently, this result does not have a straightforward interpretation but could indicate that a 50% reduction in total  $\text{NH}_x$  could push Salt Lake City into a  $\text{NH}_3$ -limited regime. Further investigation is required to understand this result and its implication for  $\text{HNO}_3(\text{g})$  vs.  $\text{NH}_3(\text{g})$  limitation in SLV.

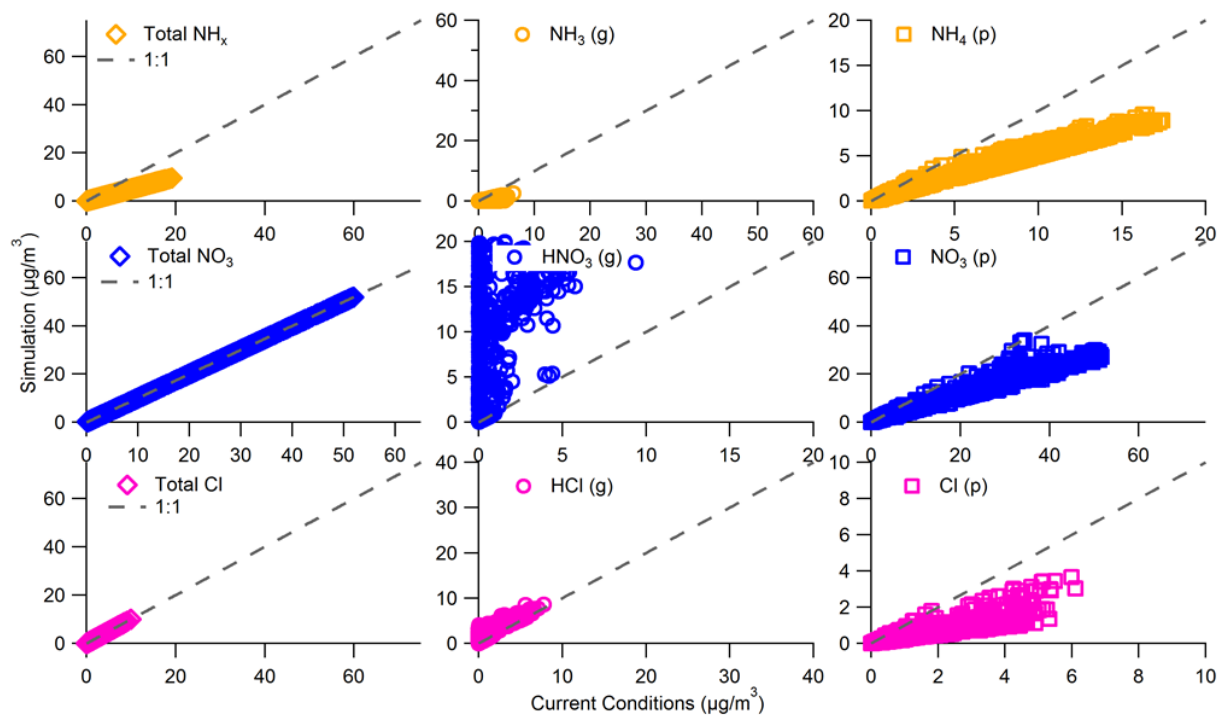


Figure 4.13 Same as Figure 4.12, except the input of total  $\text{NH}_x$  is divided by 2.

### 4.2.3 Cache Valley

Results for the nitrate-reduction case for Cache Valley are shown in Figure 4.14. As in SLV, the most striking feature is that modeled  $\text{HNO}_3(\text{g})$  is reduced to zero  $\mu\text{g m}^{-3}$  when the total nitrate input is halved. Again, the concentrations of  $\text{NH}_3(\text{g})$  increase, reflecting the evaporation of part of the  $\text{NH}_4\text{NO}_3$  in the aerosol phase. As expected,  $\text{NO}_3(\text{p})$  decreased by roughly the same amount as the total nitrate. The  $\text{HCl}(\text{g})$  partially decreased and  $\text{Cl}(\text{p})$  partially increased, pointing towards replacement of some of the  $\text{NH}_4\text{NO}_3$  with  $\text{NH}_4\text{Cl}$  in the particle phase. For this region, the total chloride available was lower than the other two regions. The Cache Valley basin seems to be the only region that responded to the reduction in input total nitrate with a uniform reduction in  $\text{NH}_4^+(\text{p})$  and  $\text{NO}_3^-(\text{p})$ . This suggests that the Cache Valley is  $\text{HNO}_3(\text{g})$ -limited, consistent with the nitrogen ratio results from the Logan ground site and Twin Otter aircraft measurements presented above.

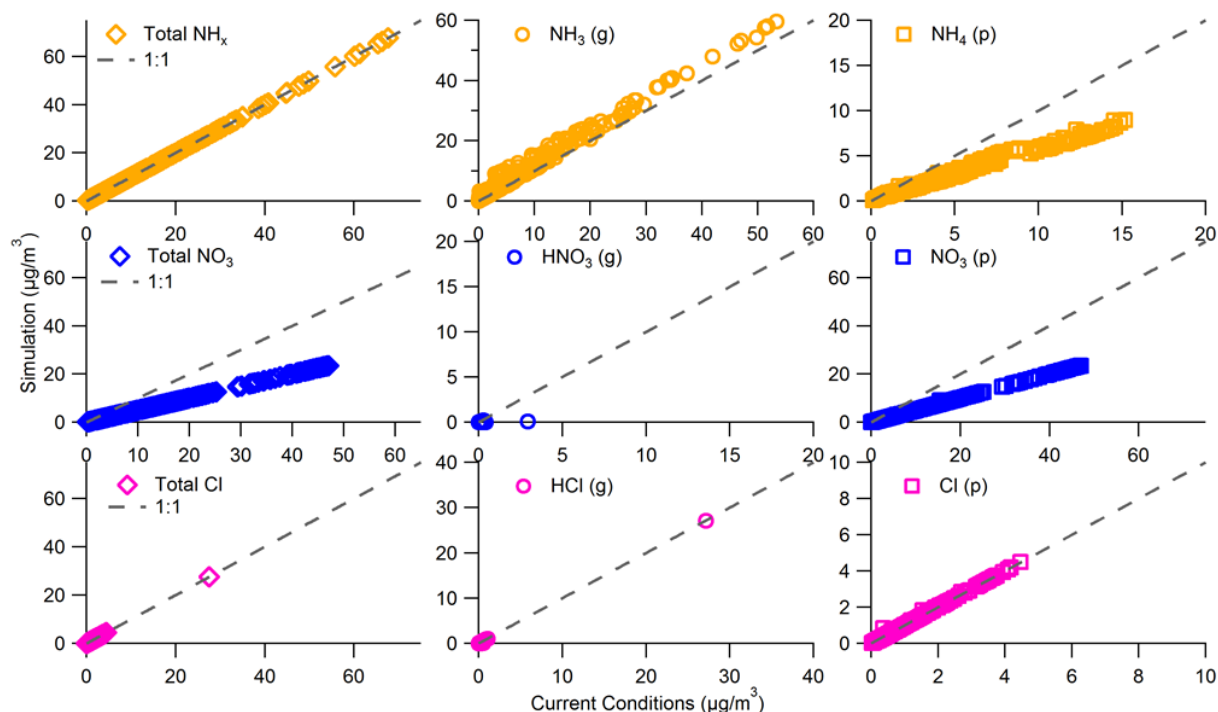


Figure 4.14 Comparison between original model results (from Figure 4.9, here on the x-axis) and the case where the input of total nitrate is divided by 2 (y-axis), for Cache Valley only. The leftmost column shows the total  $\text{NH}_x$ , nitrate, and chloride (gas+aerosol). The central and rightmost columns show the gas and aerosol phase predicted by the model for the new conditions using measured temperature and relative humidity.

In the ammonium-reduction case, data from the Cache Valley (Figure 4.15) show a marked decrease in  $\text{NH}_3(\text{g})$  and increase in  $\text{HNO}_3(\text{g})$ . The aerosol phase seems to have a dual behavior. One cluster of data seems to respond to the decrease in total  $\text{NH}_x$  showing a decrease in  $\text{NH}_4^+(\text{p})$ ,  $\text{NO}_3^-(\text{p})$ , and  $\text{Cl}^-(\text{p})$ . At the same time another cluster of data shows no change with respect to 'base case' concentrations.

These results for Cache Valley suggest a sensitivity in  $\text{NH}_4\text{NO}_3$  concentrations (i.e.  $\text{NH}_4^+(\text{p})$  and  $\text{NO}_3^-(\text{p})$ ) to a reduction in total nitrate, is expected in a  $\text{HNO}_3$ -limited/ $\text{NH}_3$ -rich regime, as was shown by the nitrogen ratio analysis from ground and aircraft observations (Section 4.1 above). The full implication of these modeling results, however, will require further investigation.

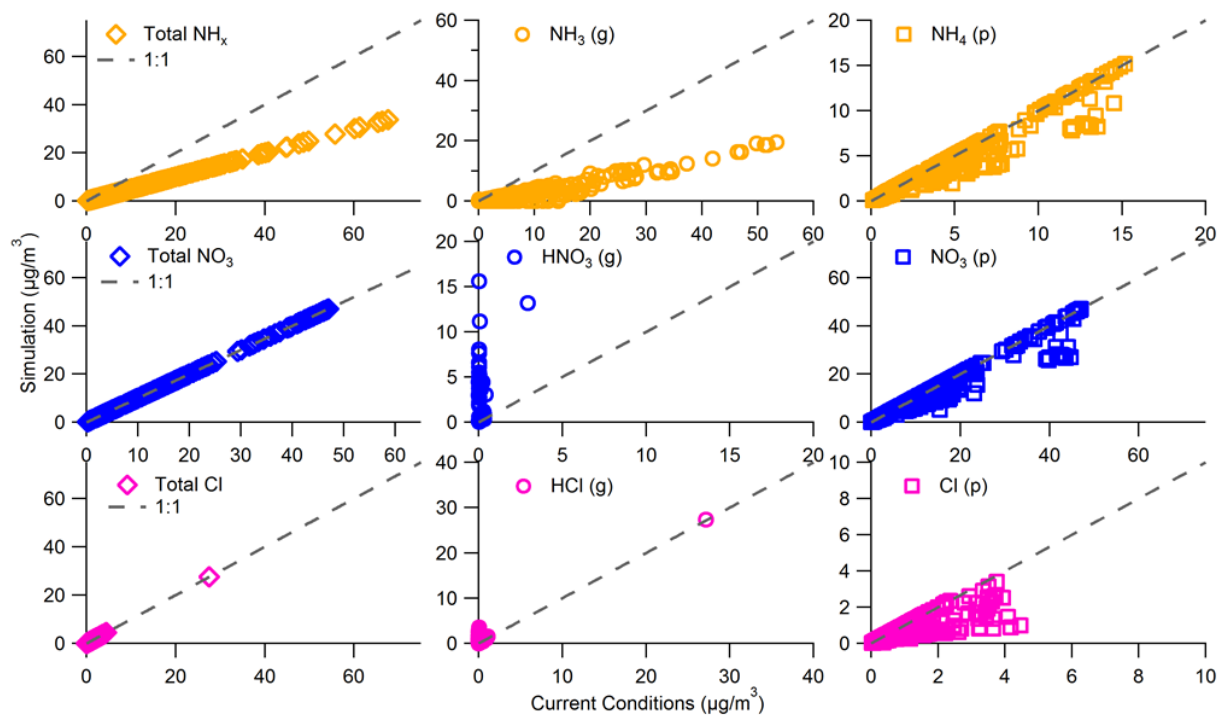


Figure 4.15 Same as Figure 4.14, except the input of total NH<sub>x</sub> is divided by 2.

#### 4.2.4 Utah Valley

In the nitrate-reduction case, data from Utah Valley (Figure 4.16) show an increase in NH<sub>3</sub>(g), decrease in HNO<sub>3</sub>(g), a decrease in NO<sub>3</sub><sup>-</sup>(p) to nearly zero, a slight decrease in NH<sub>4</sub><sup>+</sup>(p), and a very slight increase in Cl<sup>-</sup>(p). The increase NH<sub>3</sub>(g), possibly reflects the evaporation of part of the NH<sub>4</sub>NO<sub>3</sub> in the aerosol phase. The lack of decrease in some NH<sub>4</sub><sup>+</sup>(p) and the small increase in Cl<sup>-</sup>(p) points towards the replacement of some NH<sub>4</sub>NO<sub>3</sub> with NH<sub>4</sub>Cl in the particle phase.

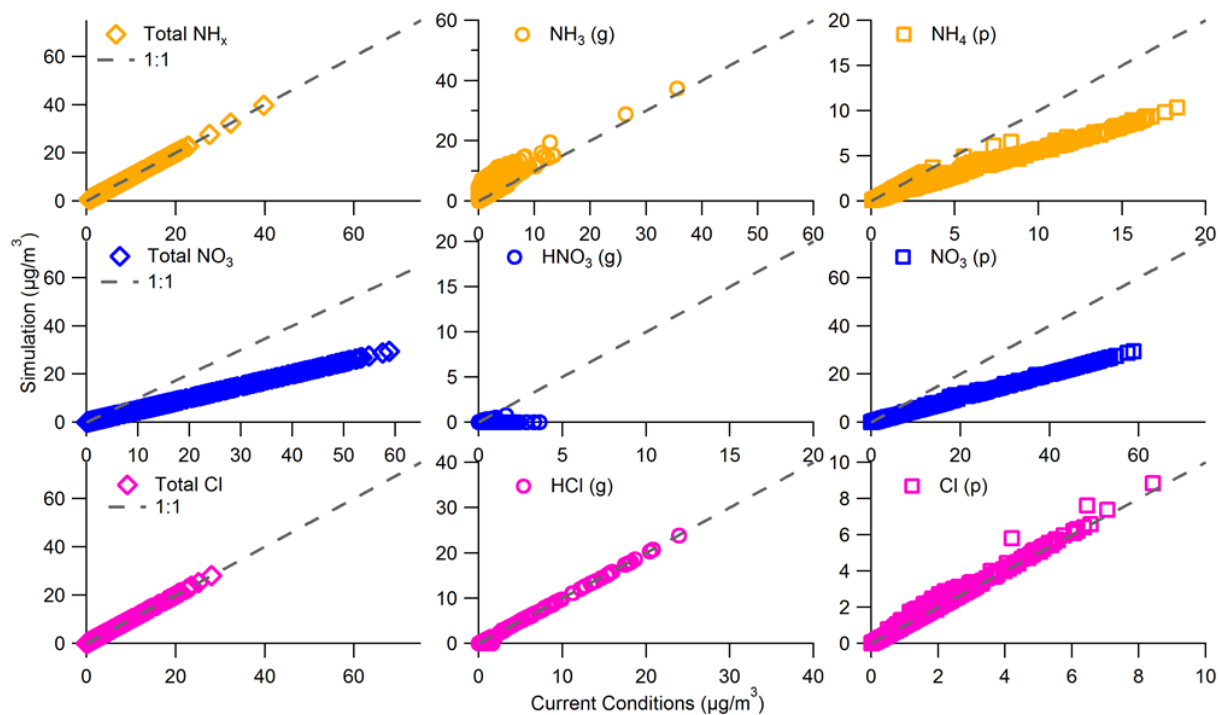


Figure 4.16 Comparison between original model results (from Figure 4.9, here on the x-axis) and the case where the input of total nitrate is divided by 2 (y-axis), for Utah Valley only. The leftmost column shows the total  $\text{NH}_x$ , nitrate, and chloride (gas+aerosol). The central and rightmost columns show the gas and aerosol phase predicted by the model for the new conditions using measured temperature and relative humidity.

In the ammonium-reduction case, data from Utah Valley (Figure 4.17) show a marked decrease in  $\text{NH}_3(\text{g})$  and an increase in  $\text{HNO}_3(\text{g})$ . The aerosol phase seems to have again two responses where in some cases no change in mass for any of the species is observed, and some cases where all decrease. The magnitude of the decrease in each compound scales with the magnitude of the 'base case' (x-axis) concentrations. These results suggest some sensitivity to  $\text{NH}_x$  that is not expected for a nitrate-limited regime and will require further analysis.

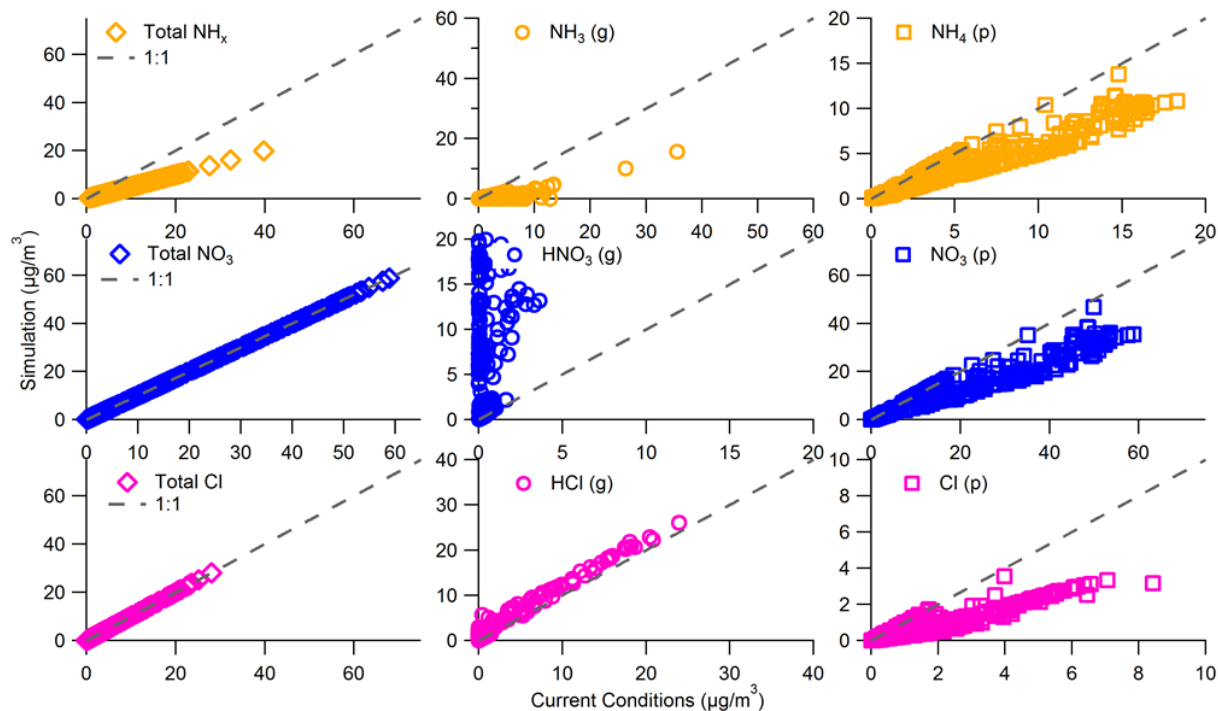


Figure 4.17 Same as Figure 4.16, except the input of total  $\text{NH}_x$  is divided by 2.

### 4.3 Summary, Future Analyses and Outstanding Questions

Effective mitigation of  $\text{NH}_4\text{NO}_3$  aerosol requires identification and reduction of its limiting precursor reagent. Presented here are two types of analyses (nitrogen ratio and thermodynamic modeling) used to preliminarily address this question. Combined, all results suggest that  $\text{NH}_4\text{NO}_3(\text{p})$  formation in Cache Valley is limited by the availability of  $\text{HNO}_3(\text{g})$ , although the amount of excess  $\text{NH}_x$  to total nitrate may be larger at the surface than aloft (>1500 m ASL). The aircraft based results for Salt Lake and Utah Valleys show that both regions are predominantly  $\text{HNO}_3$ -limited, but may also have periods of  $\text{NH}_3$ -limitation later in a pollution episode if the pollution event persists longer. The ground-based UU observations did not observe  $\text{NH}_3(\text{g})$ -limited conditions during a short lived pollution episode. In addition, the excess amount of  $\text{NH}_x$  to total nitrate appears to decrease during pollution events relative to clear conditions. None of the analyses indicate that the limiting precursor is time-of-day dependent, but that it is more strongly influenced by location within a valley or the presence of polluted conditions and number of days into the pollution episode. These results suggest a general limitation by nitrate across northern Utah, but with some variation in the degree of this limitation. Longer pollution events exhibit an indication of  $\text{NH}_3$ -limitation in the SLV and Utah Valley. This may suggest that these valleys, particularly the SLV, is a system close to the transition between  $\text{HNO}_3$ -limited and  $\text{NH}_3$ -limited regimes.

Major remaining questions include identification of which factors drive changes in the  $\text{HNO}_3/\text{NH}_3$ -limited regimes in Salt Lake and Utah Valleys, as well as the change in excess  $\text{NH}_x$  to total nitrate consistently observed between polluted and clear conditions. The role of gas/particle surface deposition and coarse-aerosol should be considered. If  $\text{NH}_4\text{NO}_3(\text{p})$  formation throughout Northern Utah is consistently limited by the presence of  $\text{HNO}_3(\text{g})$ , the dominant formation (e.g. day vs. nighttime oxidation chemistry) and loss processes of  $\text{HNO}_3(\text{g})$  should be identified in order to inform the most effective  $\text{PM}_{2.5}$  mitigation strategies. If the Wasatch Front, particularly the SLV, is a mixed system close to the transition regime,  $\text{NH}_3$  reduction could potentially result in an overall reduction of  $\text{NH}_4\text{NO}_3(\text{p})$ .

It should be finally noted that further analyses are required to fully address the question of limiting reagents throughout Northern Utah. The nitrogen ratio calculation for data from the aircraft should be updated to account for additional  $\text{NH}_4$ -containing aerosol species not measured by the AMS such as  $\text{NH}_4\text{Cl}$  and  $(\text{NH}_4)_2\text{SO}_4$ . Additionally, analysis of the thermodynamic model indicates an over-prediction in the amount of aerosol chloride observed, affecting the partitioning of aerosol species in the sensitivity studies. The ISORROPIA results should be further compared to additional thermodynamic models such as E-AIM, to evaluate its performance and better understand and interpret its results. Lastly, the effect of sodium as a source of the measured aerosol chloride from heterogeneous reactions with nitrogen oxides remains an open question. Additional analyses that address these uncertainties and further evaluate aerosol formation in Northern Utah are expected in upcoming scientific manuscripts.

## 5 Exchange Processes

The NSF-funded meteorological component of UWFPS allowed the installation of equipment at the interfaces between the Salt Lake Valley and two tributary canyons (Red Butte Canyon and Parleys Canyon) and between the SLV and the Great Salt Lake. Further, LiDAR and radiosonde observations monitored the evolution of the thermal and dynamic structure of the PCAP at the center of the basin.

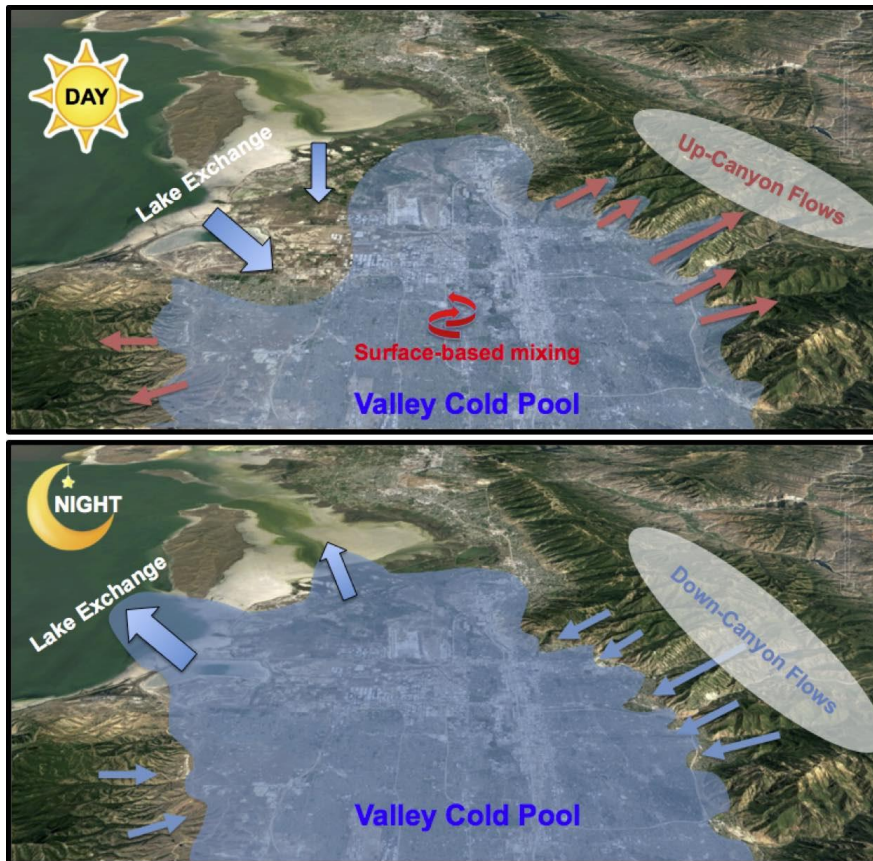


Figure 5.1 Schematic Illustration of diurnal exchange processes affecting the evolution of a PCAP in the SLV.

The Red Butte Canyon site (RB) was equipped with surface wind sensors, a ceilometer, and  $PM_{2.5}$  and ozone observations, the Parleys Canyon (PAR) and Landfill (LFL) sites were augmented with additional SoDAR wind profilers. The goal was to investigate the linkages between up-canyon or down-canyon thermally driven flows at RB and PAR, particulate pollution, and ozone concentrations. Further, the role of air mass exchange with the boundary layer over the Great Salt Lake - both through thermally-driven lake breezes and synoptically forced flows - was targeted with the observations at LFL and NAA. Insufficient funding was obtained to target

meteorological inter-basin-exchange processes but careful analysis of existing data sets such as Mesowest [95] allows for a limited characterization of these flows.

In the following, examples of these various exchange processes are highlighted through selected case studies.

## 5.1 Down-Canyon Flows

Thermally-driven down-canyon flows are strongest during clear nights and synoptically quiescent conditions, when radiative surface cooling is strong and synoptic pressure gradients are weak. The onset of the 25 January to 4 February 2017 pollution episode was characterized by increasing influence of cloudiness from 27 January (clear) to 30 January (strong influence of cloud cover), reducing the effectiveness of night-time radiative cooling (not shown) in these initial days. Thermally-driven flows were observed during the three nights at both the Parleys and Red Butte Canyon exits, as illustrated in Figure 5.2 (winds in down-canyon directions, 110 and 70 degrees, respectively) However, the strength of the flows decreased with increasing cloud effects (see wind speeds).

Winds at HW and UU also show signatures of diurnal thermal wind forcing, with nocturnal northeasterly downslope and daytime west-southwesterly upslope flows at UU and nighttime southeasterly and daytime northwesterly down- and up-valley flows. The near-surface wind speeds, however, are highest during the day and suggest a downward transport of momentum from aloft, while wind speeds are highest during the night at the canyon exits.

The time series of  $PM_{2.5}$  and ozone are shown in the bottom panels of Figure 5.2, and indicate a reduction in particulate concentrations and an increase in ozone concentrations during the night when the down-canyon flows transport air that with lower aerosol concentration and higher ozone mixing ratio into the PCAP.

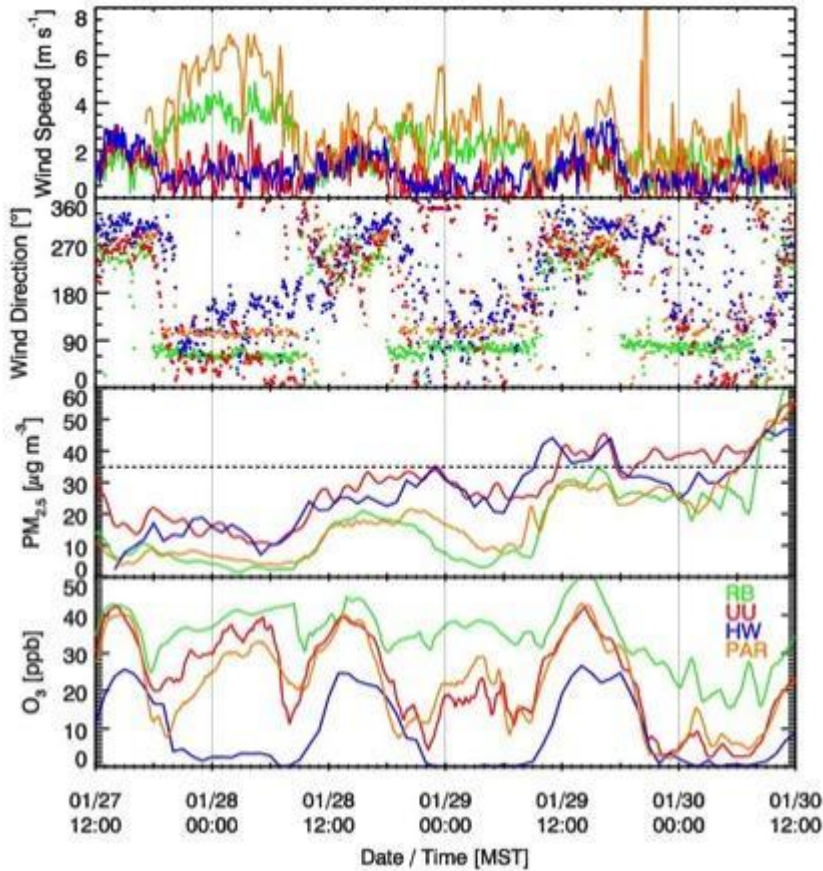


Figure 5.2 Time series of wind speeds, wind direction, PM<sub>2.5</sub> and ozone concentrations collected at four selected sites near the mouths of tributary canyons (PAR, RB), the valley sidewall (UU) and the basin floor (HW) during the onset of a particulate pollution episode.

Thermally-driven down-canyon flows are expected to occur on clear nights within all tributary canyons leading into the Salt Lake, Utah and Cache Valleys. These include the Bells Canyon, Little Cottonwood, Big Cottonwood, Parley Canyon, Mill Creek, Red Butte, and City Creek drainages in the SLV, Weber and Ogden Canyons to the north of Salt Lake City, and the Provo and American Fork Canyons in Utah Valley. Strong influences of drainage flows are expected through Logan and Blacksmith Canyons in Cache Valley. The relative strength of the canyon flows and how far and at what height above the Valley floors they extend into the PCAP atmosphere is largely unknown but likely a complex function of basin depth, slope, land cover, and other meteorological factors such as thermal stratification and the strength of synoptic flow. Signatures of possible injections of aerosol-scarce air reaching the HW site in the Salt Lake Basin, and the LN site in Utah Valley can be found in the ceilometer backscatter profiles collected at these sites (not shown).

## 5.2 Daytime Sidewall Ventilation - 29 January 2017

Even under PCAP conditions, a convective boundary layer (CBL) develops at the basin floor and along the basin sidewall during daytime. The depth of the convective mixing strongly depends on the surface net radiation, and thus on surface snow cover and cloud conditions. The development of the CBL can be seen in the vertical and pseudo-vertical temperature profiles, ceilometer backscatter profiles, and lidar-retrieved  $\sigma_w$  (Section 2.4.3).

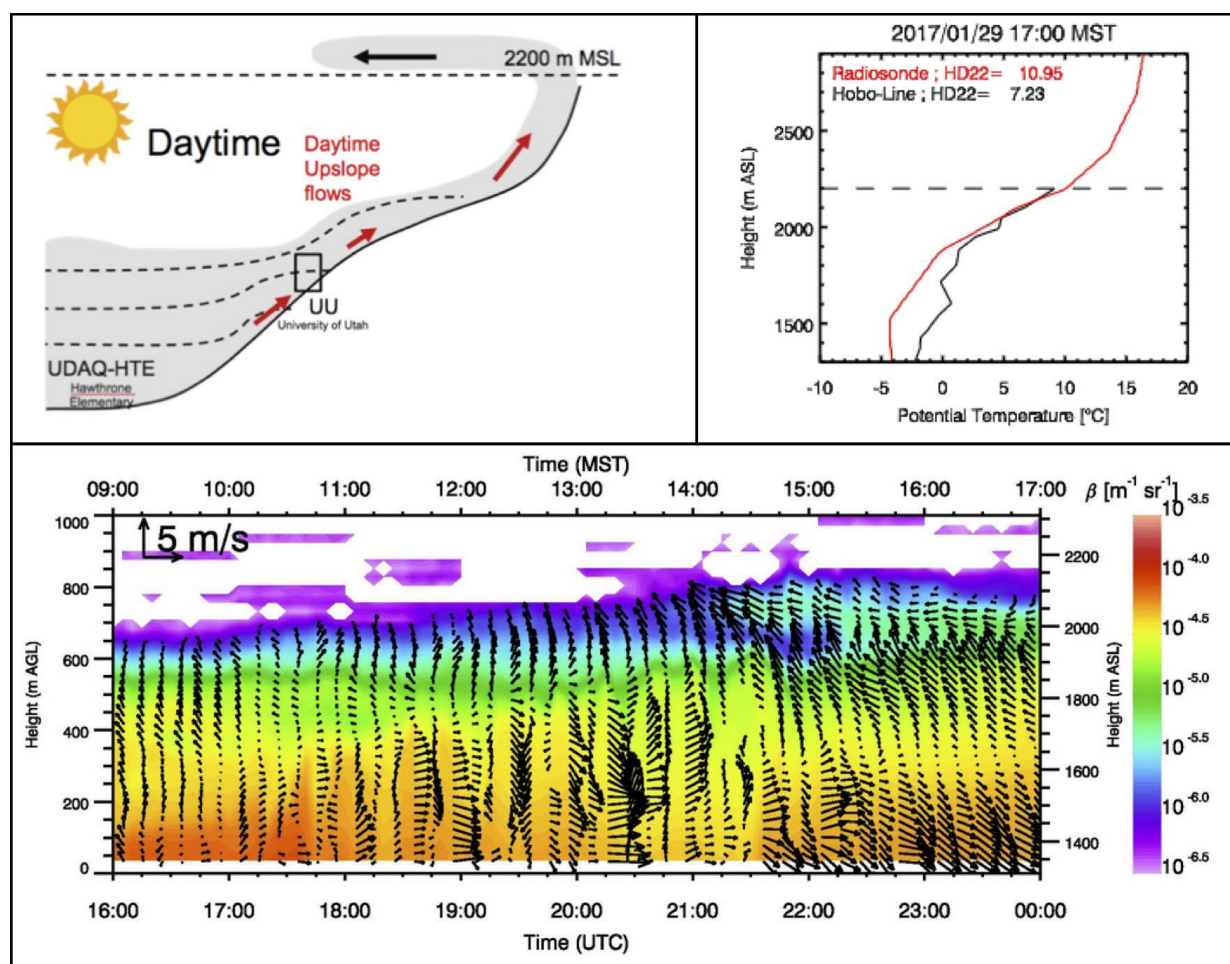


Figure 5.3 Illustration of basin sidewall ventilation on 29 January 2017. A schematic of the process is shown in the top left panel. Vertical (red) and pseudo-vertical temperature profiles (black) are shown for 1700 MST in the top right. The evolution of the convective boundary layer is shown in the lidar backscatter (bottom). The recirculation of sidewall-ejected aerosols at  $\sim 2050$  m ASL reaches HW shortly after 1400 MST.

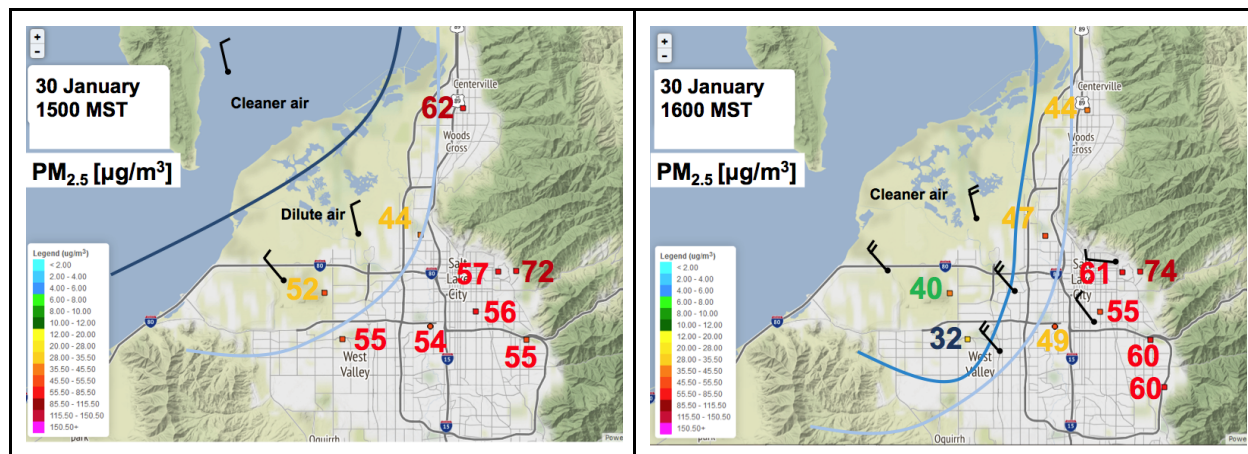
Surface heating on the sun-exposed northeastern basin sidewalls is expected to drive upslope and up-canyon flows. While these flows were not directly targeted in the meteorological observations, they can be seen in time series of wind speed and direction at the canyon exit sites (PAR, RB, see Figure 5.2). The thermal forcing, however, can be inferred from the difference

between the balloon-based temperature soundings and the pseudo-vertical temperature profiles collected along the northeastern basin transect, as shown for the afternoon of 29 January 2017 (Figure 5.3). LiDAR backscatter collected at HW during this day shows the growth of the CBL. Aerosols ventilated along the basin sidewall are recirculated with the easterly flow above 2000 m ASL and are picked up in the backscatter profile at HW after 1400 MST.

### 5.3 Lake Breeze Circulation - 30 January 2017

Figure 5.4 illustrates a lake breeze event that developed on 30 January 2017 (day 4 of episode #6). In the afternoon, the thermal contrast between a warmer valley boundary layer and the cold air over the lake forced a lake breeze front to penetrate into the northern part of the SLV. The lake atmosphere brought aerosol-scarce air into the basin, leading to decreasing PM<sub>2.5</sub> concentrations as the breeze advanced.

The flight of the instrumented KSL news helicopter [52] flown in the northern part of the valley revealed the depth of the lake breeze. The last panel of Figure 5.4 shows a smoothed profile of the averaged PM<sub>2.5</sub> observations as the helicopter ascended within and descended back into the PCAP. It reveals how shallow the lake breeze is as it undercuts the more heavily polluted valley air mass.



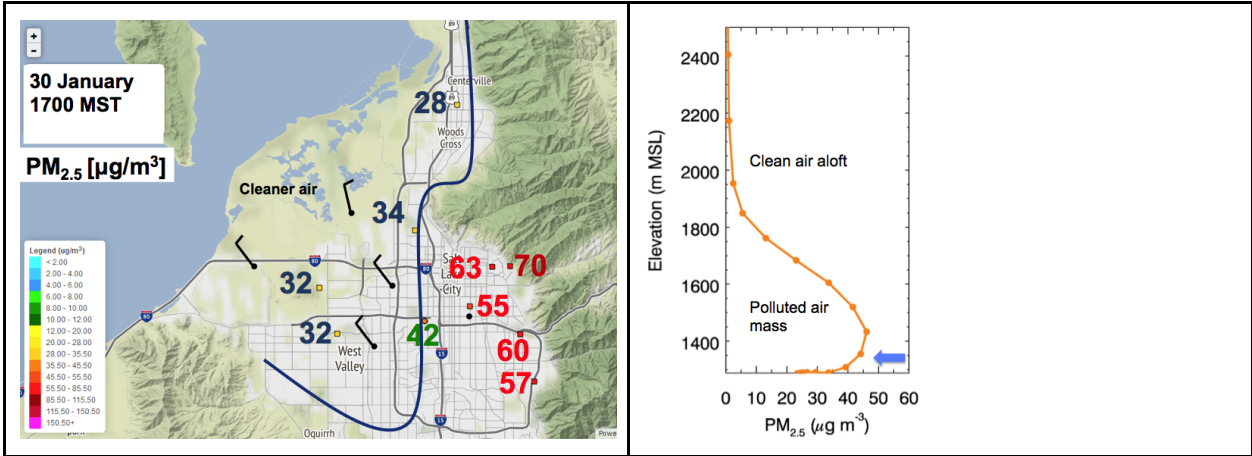
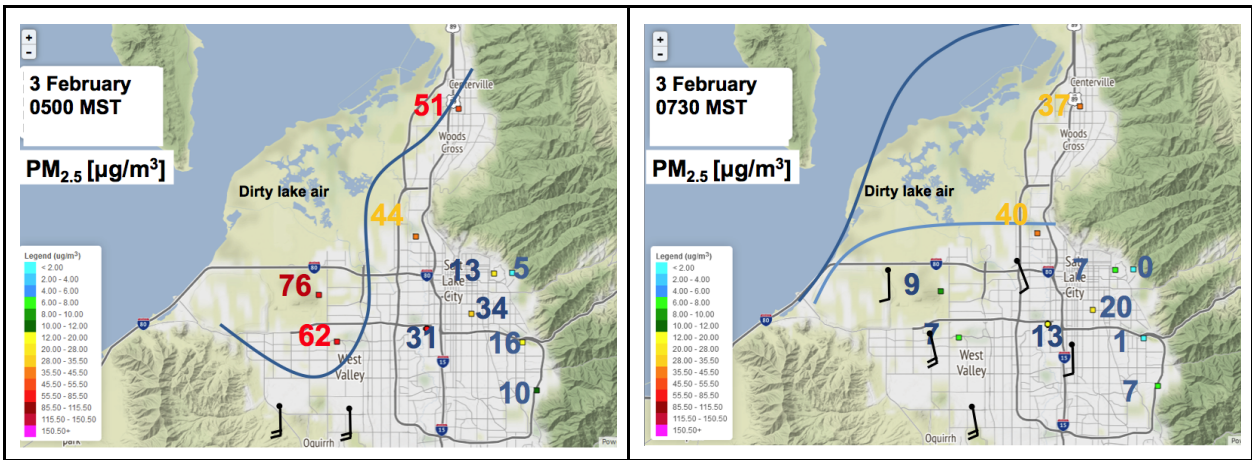


Figure 5.4 Analysis of the surface wind field and surface  $\text{PM}_{2.5}$  concentrations during the 30 January 2017 lake breeze event. The last panel shows a smoothed vertical profile of  $\text{PM}_{2.5}$  concentrations from observations on a local news helicopter taken in the northern part of the basin.

## 5.4 Synoptically-Forced Lake Exchange

A schematic of the wind field and particulate concentrations during a synoptically-forced lake exchange event is shown in Figure 5.5. In the morning of 3 February 2017 (day 8 of episode #6), strong southerly flow scoured out the pollution from the Salt Lake basin, starting at the benches (0500 MST), and eventually eroding the entire PCAP in the basin (0730 MST). Polluted air was pushed north over the Great Salt Lake.



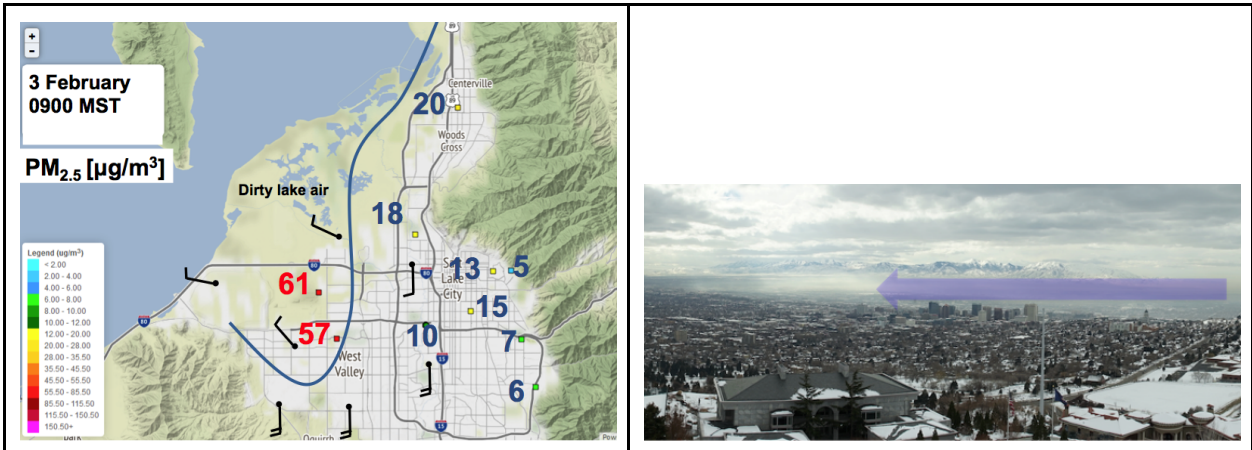


Figure 5.5 Analysis of the surface wind field and surface  $PM_{2.5}$  concentrations during the 3 February 2017 lake “recharge” event. The last panel shows a photograph of the shallow tongue of polluted air “recharging” the basin.

By 0900 MST, however, the flows weakened and colder and aerosol-rich air penetrated back into the lowest areas of the Salt Lake basin, leading to a “recharge” of the pollution at those locations. The last panel shows a photograph of the pollution tongue penetrating back into the basin.

## 5.5 Inter-Basin Exchange

Inter-basin exchange through synoptically forced and / or thermally driven circulations may play an important role in the import and export of pollutants, pollutant precursors, and oxidants. Initial plans to place additional equipment at the Jordan Narrows could not be realized due to limited funding. Nevertheless, data from MesoWest stations, TRAX-based measurements, and large gradients in pollutants between the Salt Lake and Utah Basins can indicate the role of such inter-basin exchange processes.

Initial analysis of West Valley Air Toxics data shows that the highest  $NH_3$  concentrations at NAA are associated with periods of inter-basin exchange [86]. During most nights during the UWFPS study, a period of southerly flow was observed by a Utah Department of Transportation Weather station in the Jordan Narrows gap (Figure 5.6). However, periods when that exchange persisted for longer duration were also observed. The following periods were identified as having both a PCAP and significant prolonged south-to-north (from Utah Valley into SLV) from Mesowest observations (Figure 5.6): January 17-20, 28-31 and February 1-2 2017.

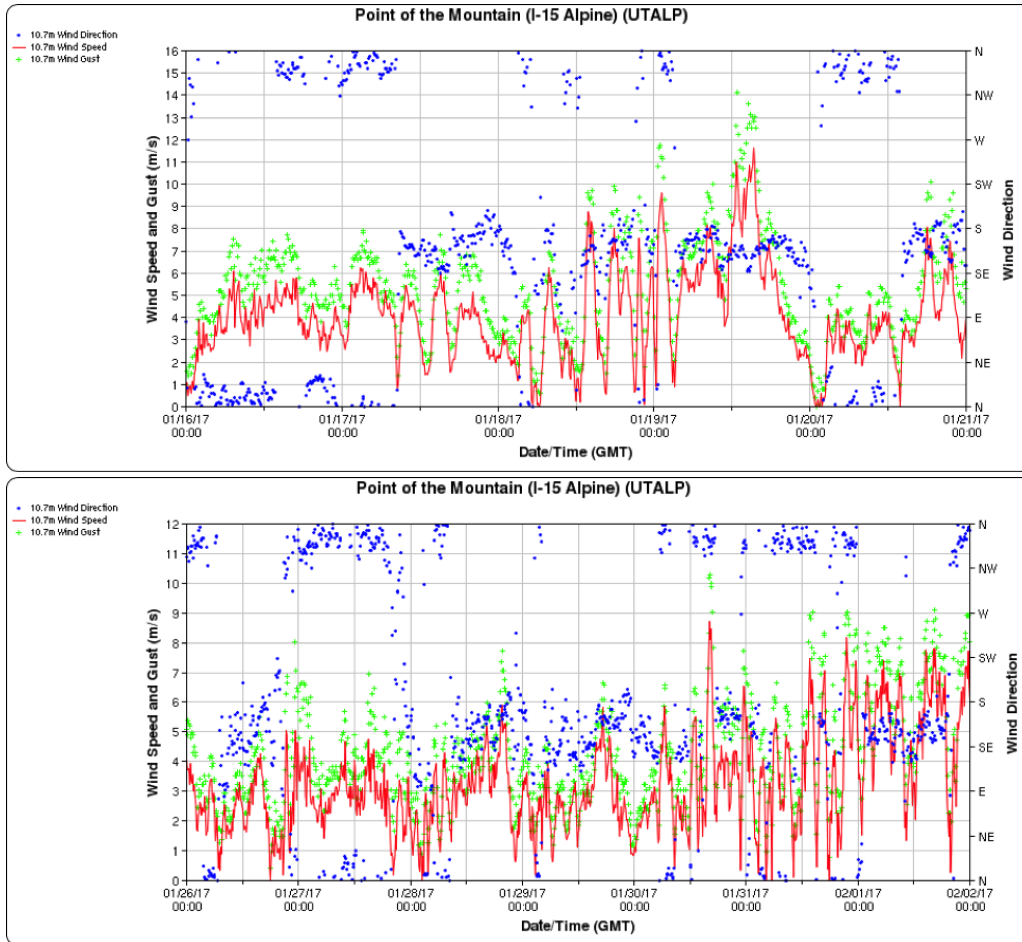


Figure 5.6 Wind speed ( $m s^{-1}$ ) and wind direction at the Point of the Mountain Utah Department of Transportation weather station between 16-21 January 2017 (top) and 26 January- 2 February 2017 (bottom).

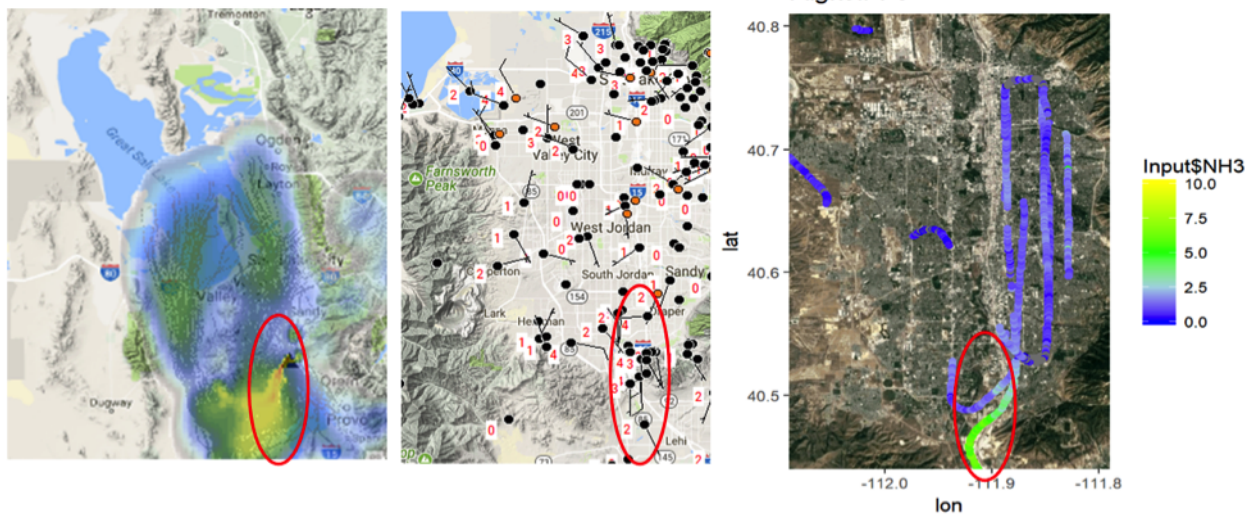


Figure 5.7 Analysis of HRRR-STILT backward trajectories (left panel), Mesowest surface wind speeds (middle panel, barb and red value, in  $\text{ms}^{-1}$ ) and  $\text{NH}_3$  concentrations from the NOAA Twin Otter during the afternoon of 17 January 2017. The red circled region indicates the region of southerly inter-basin from the Utah Valley into the SLV and the associated high  $\text{NH}_3$  concentrations ( $\text{NH}_3$  figure courtesy Alex Moravek and Jennifer Murphy).

Another valuable resource for determining the southerly flow are particulate and ozone sensors onboard the TRAX light-rail train [57]. On 31 January 2017, the TRAX sensors intersected a plume of air with higher particulate concentrations flowing into the SLV from the Utah Valley. Mesowest observations and HRRR-STILT analyses verify that the source of the polluted air observed by TRAX was from the Utah Valley (Figure 5.8).

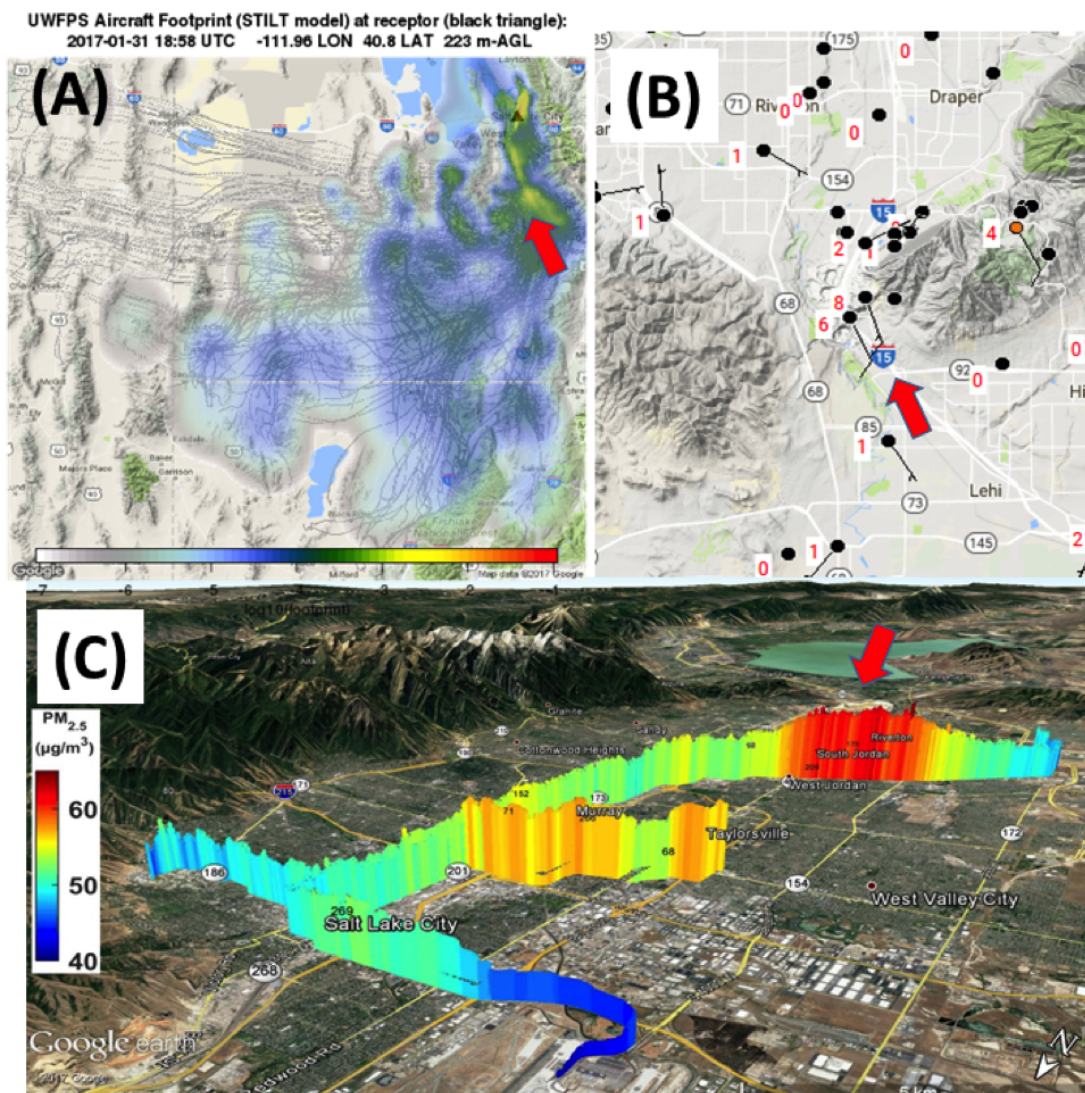


Figure 5.8 (a) analysis of HRRR-STILT backward trajectories, (b) Mesowest surface wind speeds (barb and red value, in  $\text{m s}^{-1}$ ), and (c) TRAX  $\text{PM}_{2.5}$  concentrations during mid-morning hours on 31 January 2017.

# 6 Emissions

## 6.1 Ammonia emissions

Current knowledge on ammonia emissions in the study region is reflected in the UDAQ emission inventory. The inventory is based on the 2014 NEI emission inventory and was processed with SMOKE for temporal and spatial allocation of sources within a 1.33 km modelling domain. Figure 6.1 illustrates the estimated emissions of NH<sub>3</sub> by different sectors for several Northern Utah counties. In all counties, area sources constitute the largest fraction of NH<sub>3</sub> emissions. E.g. in Cache County NH<sub>3</sub> from animal waste accounts for more than 70% of the total NH<sub>3</sub> emitted. In Salt Lake County about one third of emitted NH<sub>3</sub> is estimated to be from mobile sources. The spatial distribution of NH<sub>3</sub> sources is illustrated in Figure 6.2, showing total emissions together with emission from each sector. NH<sub>3</sub> emissions from point sources are only minor compared to NH<sub>3</sub> from area sources, however, they may have a large local impact.

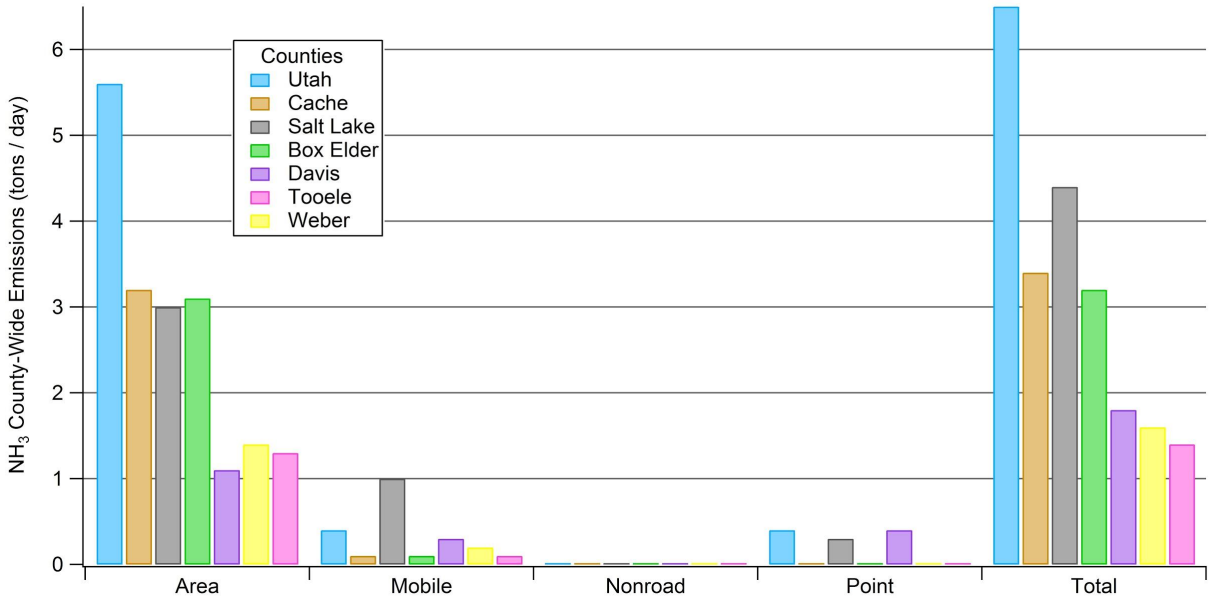


Figure 6.1 2014 NEI NH<sub>3</sub> emissions totals (tons/day) for several Northern Utah counties. Emission totals have been temporally processed to reflect a typical winter weekday.

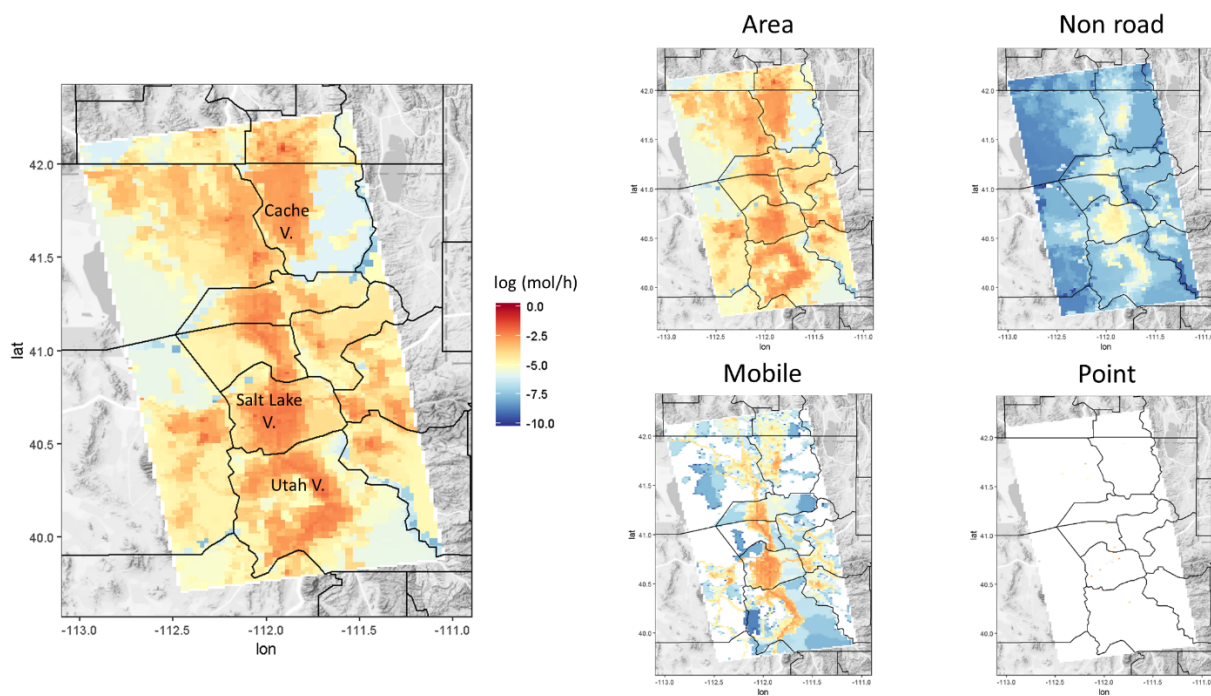


Figure 6.2 24-hour average of 2014 NEI  $\text{NH}_3$  emission rates (moles/hr) allocated across a 1.33 km Northern Utah modeling domain. Emission rates reflect a typical winter weekday in February. The left panel shows emissions at the surface and the right panel shows the sum of all emissions from all the layers above the surface. Shown are the total emission rates (large map) and the contributions from different emission sectors (small maps).

The aim of the UWFPS study was to provide further insight into  $\text{NH}_3$  emissions from  $\text{NH}_3$  measurements in the region. To evaluate potential sources of  $\text{NH}_3$ , we examine tracer relationships using other commonly measured gas phase species that are emitted from a variety of sources (Figure 6.3 and Figure 6.4). The sum of gas and particle phase  $\text{NH}_x$  is used as a better conserved tracer than  $\text{NH}_3$  alone. Recent measurements of  $\text{NH}_3/\text{CO}_2$  ratios from mobile sources in on-road [96] or simulated [97] on-road conditions are in the range of 0.17 - 0.35 ppb/ppm. This is a bit higher than the ratio observed in SLV (0.12 ppb/ppm), suggesting that there may be other sources of  $\text{CO}_2$  that are not significant sources of  $\text{NH}_3$ . In Nowak et al. [89] the slope between  $\text{NH}_3$  and CO was measured to be 0.03 - 0.05, and this was attributed to mobile sources. In the SLV, this ratio appears to be slightly lower (0.016 ppb/ppb), again suggesting another source of CO that emits relatively less  $\text{NH}_3$ . Based on the NEI 2014 inventory, the molar ratio of  $\text{NH}_3$  to  $\text{NO}_x$  emissions in Salt Lake County is 0.16, which is in relatively good agreement with the observed slope of 0.12 ppb/ppb seen in Figure 6.3. Note that the molar ratio of  $\text{NH}_3$  to  $\text{NO}_x$  from the mobile emissions sector is 0.074. Based on UDAQ's inventory, mobile emissions constitute half of the total  $\text{NO}_x$  emissions in Salt Lake County, but only one quarter of the  $\text{NH}_3$  emissions.

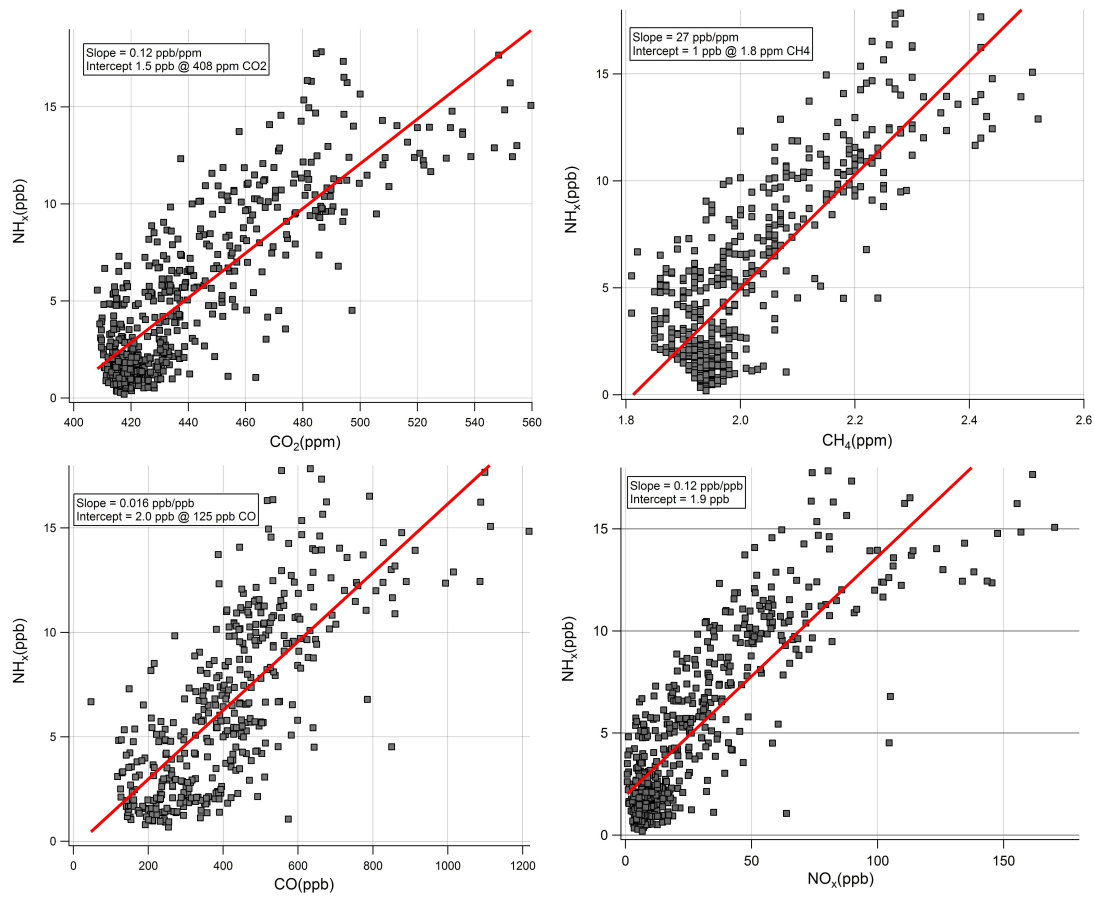


Figure 6.3 Scatterplots of  $\text{NH}_x$  vs other gas phase compounds ( $\text{NO}_x$ ,  $\text{CO}_2$ ,  $\text{CO}$  and  $\text{CH}_4$ ) measured at the UU ground site.

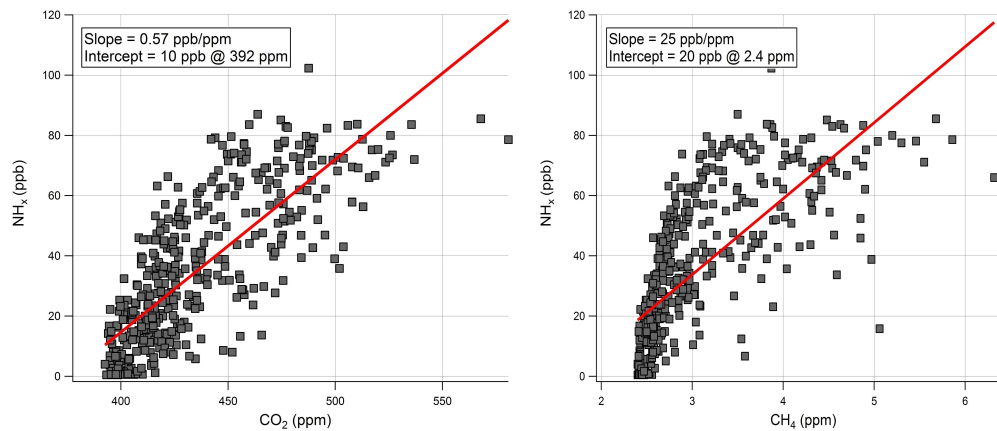


Figure 6.4 Scatterplots of  $\text{NH}_x$  vs other gas phase compounds ( $\text{CO}_2$  and  $\text{CH}_4$ ) measured at the Logan ground site.

In contrast to the SLV, the slope between  $\text{NH}_x$  and  $\text{CO}_2$  at the Logan site, 0.57 ppb/ppm, is much higher than expected from mobile sources. The simplest fit to the  $\text{NH}_x$  vs  $\text{CH}_4$  data gives a slope that is similar to that seen in SLV, but the relationship does not appear linear. There seem to be additional sources of  $\text{CH}_4$  in Cache Valley that are not sources of  $\text{NH}_3$ . In Eilerman et al. [98], the relationship between  $\text{NH}_3$  and  $\text{CH}_4$  in the Colorado Front Range during summer was in the range of 100 - 1000 ppb/ppm.

Other results include the comparison of  $\text{NH}_3$  measurements from the Twin Otter with the UDAQ emission inventory. For example, the high  $\text{NH}_3$  mixing ratios observed in the Cache Valley suggest, that  $\text{NH}_3$  emissions are largely underestimated by the inventory in that region. At the submission date of this report, this investigation was still ongoing and results will be made available in a later publication.

## 6.2 Residential Wood Combustion

The contribution of residential wood combustion to  $\text{PM}_{2.5}$  has been a topic of several recent studies in Utah valleys. These studies are based on Positive Matrix Factorization (PMF) analysis of 24-h filter samples collected at UDAQ's sampling sites, with exception of Cropper *et al.* [99] and Baasandorj *et al.* [86] who used hourly speciated particulate organic and inorganic composition data from BYU campus and West Valley City, respectively. Kelly et al. [9] found primary  $\text{PM}_{2.5}$  contributions for wood smoke to be 40% and 20 - 70% at HW and BV, respectively, and 40 % at LN on days when  $\text{PM}_{2.5}$  exceeded  $20 \mu\text{g m}^{-3}$ . The authors reported that these values are larger than UDAQ's inventory estimates, as important as the gasoline exhaust contributions to primary  $\text{PM}_{2.5}$  at these sites during PCAPs. The authors also noted that the sampling sites could be influenced by wood smoke more due to their location in older residential neighborhoods. Kotchenruther *et al.* [100] estimated, using PMF analysis of 2007 - 2014 chemical speciation network (CSN) data, that 12% and 9% of total  $\text{PM}_{2.5}$  come from primary wood smoke during December and January months at BV and LN respectively. Based on this analysis, total primary and aged wood smoke contributions are estimated to be  $3.3 \mu\text{g m}^{-3}$  on average, 22% and 17.8 % of total winter  $\text{PM}_{2.5}$  at the respective sites. Recent radiocarbon analysis from ground sites in the Salt Lake Valley at the University of Utah, Hawthorne, and Rose Park indicate that fossil fuels were the dominant sources of carbonaceous aerosol during winter, contributing to 58% (48-69%) of the organic carbon in aerosols, with RWC contributing to less than half of organic aerosol in winter [101]. UDAQ's recent wood-smoke quantification study found a significant spatial and temporal variability in the residential wood combustion contribution to  $\text{PM}_{2.5}$ . According to the PMF analysis of December 2015 to February 2016 filter-based speciation data, the wood combustion contribution to  $\text{PM}_{2.5}$  varied from 21.2% and  $2.53 \mu\text{g m}^{-3}$  at North Provo to 11.1% and  $2.01 \mu\text{g m}^{-3}$  at SM, on average during a winter. The percentage contribution is lower during days with elevated  $\text{PM}_{2.5}$ , however wood smoke mass contribution is higher with values ranging from  $\sim 2$  to  $2.73 \mu\text{g m}^{-3}$  on these days. The residential wood combustion is estimated to contribute to  $\sim 1.3 \mu\text{g m}^{-3}$  and 16.2% of total  $\text{PM}_{2.5}$  at HW on average during a winter, with contribution of 1.2

$\mu\text{g m}^{-3}$ , equivalent to ~6% of total  $\text{PM}_{2.5}$  on mandatory no burn days when  $\text{PM}_{2.5}$  levels are high [102].

Cropper *et al.* [99] recently reported hourly measurements of fine particulate organics between January - February 2015 on BYU campus located in Utah valley, using GC-MS organic aerosol monitor (OAM), and estimated the wood combustion contribution to be  $\sim 5.05 \mu\text{g/m}^3$  and 29.9 % total  $\text{PM}_{2.5}$  on average during the study period [99]. This value is higher than the estimated contribution in North Provo [102] and those based on the long-term CSN data from Lindon [9, 100]. A similar suite of measurements including speciated fine particulate organics, inorganics,  $\text{PM}_{2.5}$  mass, and trace gas measurements was conducted at Neil Armstrong (NAA) as part of West Valley City High Time Resolution Air Toxics Monitoring campaign between December 2015 and February 2016. The PMF analysis of hourly NAA data indicate that the residential wood smoke accounted for an average mass of  $0.7 \mu\text{g m}^{-3}$  and 3.5% of total  $\text{PM}_{2.5}$  on average during 2015-2016 winter in West Valley City [86]. This value is significantly lower than the estimated wood combustion contribution in other neighborhoods, HW [102] and BV [9, 100].

During the UWFPS study, the total measured non-refractory mass from the Twin Otter AMS data averaged about 20% organic and was fairly consistent between the different basins during the PCAP episodes when the total aerosol mass was more than  $10 \mu\text{g sm}^{-3}$  (Figure 3.3). Biomass burning aerosols are sometimes distinguished in the AMS data by elevated signals at  $m/z$  60, which is representative of levoglucosan, and can be as high as 4% of the total organic signal in ambient wildfire plumes [103]. However, this marker of biomass burning aerosols is quite variable for different fuels and decreases with aging [104]. The  $m/z$  60 fraction of the organic signal in the Twin Otter data was nearly always less than 1% and averaged around 0.3%, which is typical of background values [103]. At the EPA's ground site in the Cache Valley, the study averaged organic mass fraction from the AMS instrument was 27%, with an  $m/z$  60 fraction as high as 2% at times and usually <1%. Therefore, on the ground there may have been some times where the biomass burning influence on the organic aerosol was clear. As seen in the previous studies, smoke from wood combustion can have a large local impact, especially at night during PCAP events when pollutants are trapped closer to the ground. Since it is possible that some of the regional organic aerosol mass was due to biomass burning aerosols, the overall AMS findings about biomass burning aerosols from the UWFPS study are inconclusive.

The findings of previous studies suggest that the contribution of residential wood combustion to  $\text{PM}_{2.5}$  can vary significantly from neighborhood to neighborhood within a valley, with higher contributions in older residential areas. Due to active wood burning at night and the formation of nocturnal boundary layer, the sites in residential areas are exposed to the emissions from wood combustion longer while the sites located farther away see the signatures associated with the wood combustion only later in the day when convective boundary layer develops. The overall contributions of residential wood combustion to total  $\text{PM}_{2.5}$  buildup within a valley and regionally that include both direct and indirect effects are still uncertain, and require further investigation.

## 7 Models of Northern Utah Winter Air Quality

As discussed above, the two NAA's along the Wasatch Front have been re-designated as "serious", a designation more critical than "moderate". Being responsible for serious nonattainment areas means the State of Utah must do more to find and develop effective control strategies that bring future-year levels of air pollution down.

Under the Federal Clean Air Act, The State of Utah is mandated to demonstrate attainment of the federal standard at a future date; usually five-years out from a present-day "base" year. The demonstration of federal attainment is determined using regional air quality modeling. This process involves sophisticated software that numerically simulates the complex physics and chemistry that contribute to aerosol formation.

There is always a level of uncertainty and bias inherent in air quality modeling. However, air quality models remain our best tools for forecasting regional air pollution. Fortunately, the performance of air quality models are improving over time. Important areas of air quality modeling where improvements are always welcome include:

1. Estimates of precursor emissions (e.g, NO<sub>x</sub>, VOC, NH<sub>3</sub>, SO<sub>2</sub>)
2. The spatial and temporal allocation of emission sources
3. Meteorological simulations of near-surface air stability during persistent cold air pools
4. The chemical mechanism schemes that produce secondary aerosol

For example, capturing the vertical temperature structure during a persistent cold air pool is critical. If the planetary boundary layer is not well simulated, particulate matter may not realistically build-up during a PCAP in the model.

Often times, the information available to guide modelers on where to place precursor emissions sources in space and time is limited or coarse. And if precursor emissions are not well quantified in the first place, then it could affect our ability to determine effective regulatory strategies. Likewise, if the chemical processes in the atmosphere are not well replicated in the air quality model, inaccuracies in the amount of secondary aerosol formed compromises the model's usefulness for assessing emission control strategies.

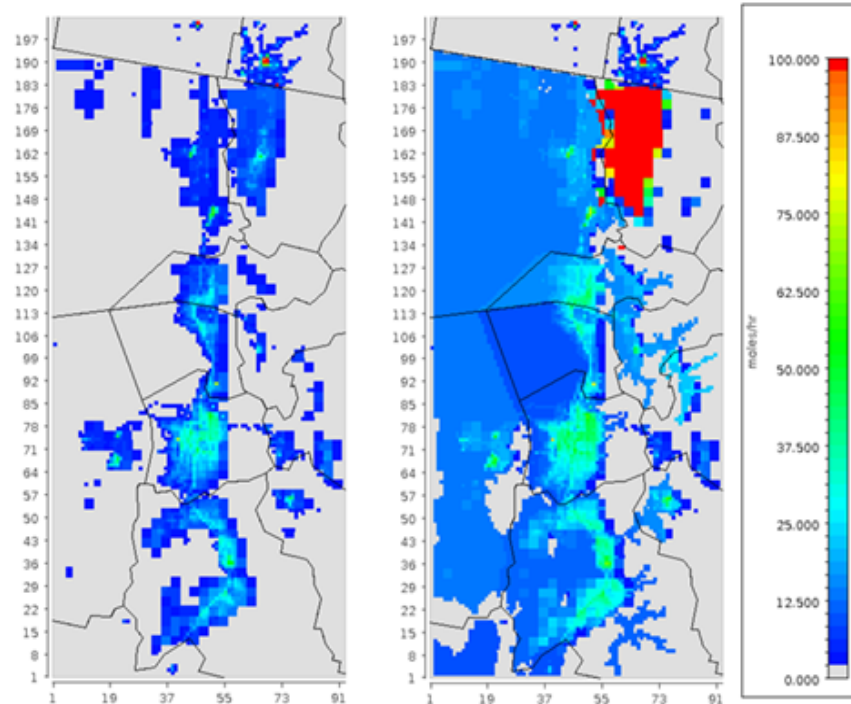
The best way to constrain uncertainties in the air quality model, as well as mark a direction for future model improvements, is by comparing modeled results to chemical and meteorological observations. For this reason, the Utah Winter Fine Particulate Study is highly valuable. It is a unique opportunity to have a study as broad in scope, yet as focused on wintertime pollution episodes in Northern Utah as the UWFPS.

## 7.1 Utah Regulatory Modeling Progress

UDAQ is in the process of conducting regulatory modeling of Wasatch Front air quality for the PM<sub>2.5</sub> State Implementation Plan (SIP). This is the third major photochemical modeling study that UDAQ has undertaken to develop plans for PM<sub>10</sub> and PM<sub>2.5</sub> attainment demonstrations. During this period UDAQ has used new air quality models as they have continued to be improved by the scientific community. It currently uses the Comprehensive Air Quality Model with Extensions (CAMx 6.30 [105]). As in past studies, the biggest technical challenge has been simulating a realistic level of ammonium nitrate, the largest component of PM<sub>2.5</sub> mass during high wintertime pollution events in Northern Utah.

The role of NH<sub>3</sub> as a limiting precursor to ammonium nitrate has come into sharper focus during the last several years through field campaign measurements [15] and model sensitivity analyses. Measurements of ambient ammonia in Utah are limited, but UDAQ discovered a significant low bias in simulated ammonia from their modeling work. Low concentrations of ammonia in the air quality model could be due to a low estimate of inventoried ammonia. Another possibility contributing to low modeled ammonia concentrations may be caused by a poor representation of the ammonia dry deposition mechanism in the CAMx model [106] or overestimation of SO<sub>2</sub>.

To address the issue of low modeled NH<sub>3</sub> concentrations, as well as poor ammonium nitrate performance, UDAQ injected ammonia in low elevation regions (< 6,000 ft ASL) of the modeling domain. Ammonia was added to individual counties in proportion to the difference between ambient ammonia measurements and modeled results. For example, NH<sub>3</sub> was injected in greater



amount to Cache County, because the difference between measured and modeled NH<sub>3</sub> was highest there (Figure 7.1, right panel).

Figure 7.1 (Left panel) Gridded 1.33 km NH<sub>3</sub> emissions prior to ammonia injection. (Right panel) Gridded NH<sub>3</sub> emissions after NH<sub>3</sub> injection. County borders shown by thin black lines. The large red feature (right panel) in the northern region of the modeling domain implies much more NH<sub>3</sub> was injected into Cache County.

### 7.1.1 Effect of Ammonia Injection on Model Performance

Comparing speciated 24-hour  $PM_{2.5}$  filter measurements to model output for January 7, 2011, we see that total  $PM_{2.5}$  mass was well simulated for that day (Figure 7.2). The  $NH_3$  injection contributed to excellent particulate ammonium ( $NH_4^+(p)$ ) performance. However, modeled  $HNO_3(g)$  was still biased low, while modeled  $SO_4^{2-}(p)$  was biased quite high.

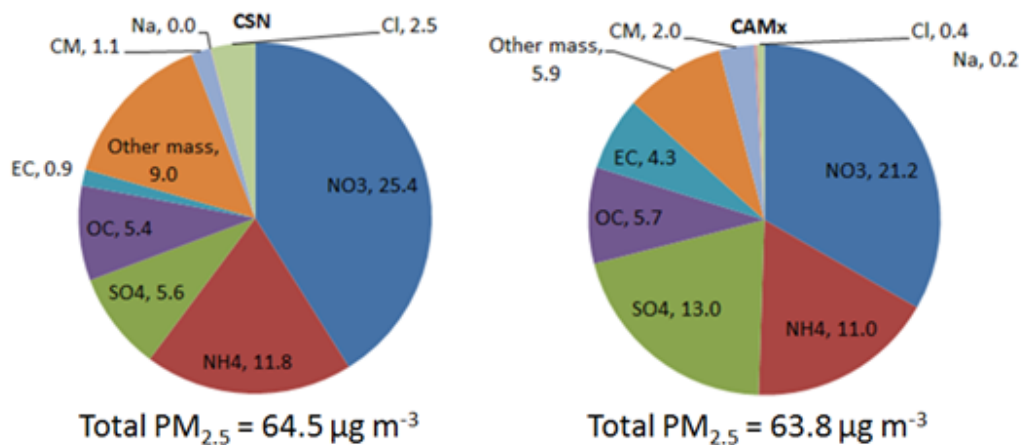


Figure 7.2 (Left panel) Measured  $PM_{2.5}$  aerosol species ( $\mu g m^{-3}$ ), for January 7, 2011, an example pollution day, at HW. (Right panel) Modeled  $PM_{2.5}$  aerosol species.

The  $NH_3$  injection led to a relatively slight increase in  $NO_3^-(p)$  ( $0.7 \mu g m^{-3}$ ) compared to modeled results where  $NH_3$  injection was not applied. Coupled with a significant increase in  $SO_4^{2-}(p)$  ( $7.1 \mu g m^{-3}$ ), this result was surprising. A plausible reason for the  $SO_4^{2-}(p)$  increase is that the injected  $NH_3$  neutralized sulfuric acid ( $H_2SO_4(g)$ ) concentrated in the simulated near-surface clouds that appeared on January 7 (Figure 7.3, courtesy of Erik Crosman, University of Utah). The presence of near surface fog/clouds in the simulation allowed more  $SO_2(g)$  to dissolve in cloud water, thus higher  $SO_4^{2-}(p)$  that can use up  $NH_3(g)$ . This aqueous chemical pathway was included in the CAM<sub>x</sub> chemistry mechanism.

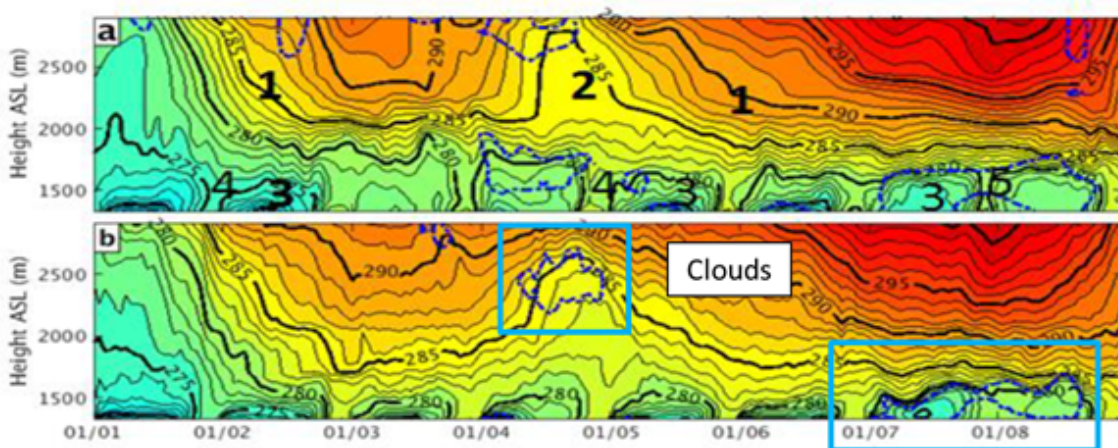


Figure 7.3 (Top) Observed potential temperature (K) and RH (90% threshold, dashed blue line). (Bottom) Modeled potential temperature (K) and cloud water mixing ratio ( $0.1 \text{ g kg}^{-1}$  threshold, dashed blue line). Presence of clouds and large  $\text{NH}_3(\text{g})$  emissions could lead to increased oxidation of  $\text{SO}_2(\text{g})$  to  $\text{SO}_4^{2-}(\text{p})$ .

### 7.1.2 Effect of Meteorological Modeling on Model Performance

Although model performance for total  $\text{PM}_{2.5}$  was great on January 7 when  $\text{PM}_{2.5}$  concentration exceeded  $60 \mu\text{g m}^{-3}$ , there was a low model bias for most of the simulated episode. Model performance during January 4 - 5 was particularly poor (Figure 7.4).

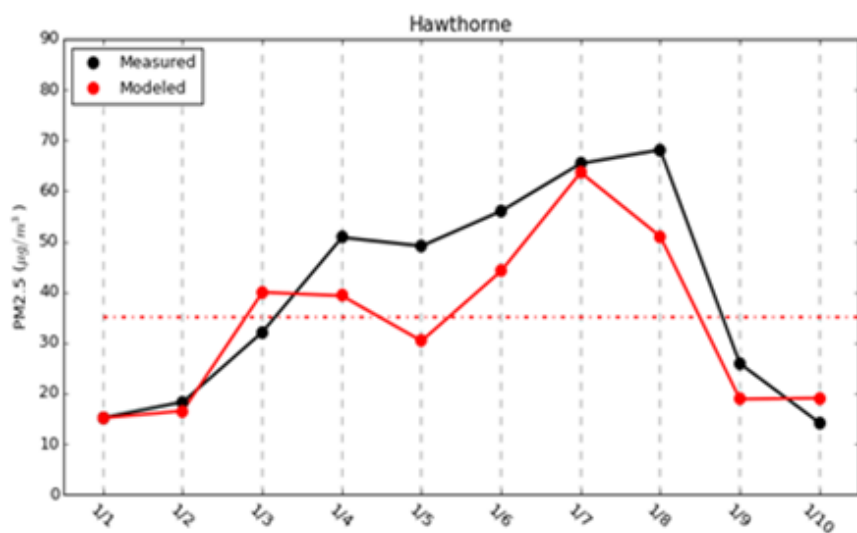


Figure 7.4 Modeled concentrations of 24-hour  $\text{PM}_{2.5}$  ( $\mu\text{g m}^{-3}$ ) at the 1.33 km grid cell collocated with UDAQ's HW monitor (red). Observations of 24-hour  $\text{PM}_{2.5}$  from UDAQ's HW monitor (black). Red dashed line shows NAAQS ( $35 \mu\text{g m}^{-3}$ ). The period simulated is January 1, 2011 to January 10, 2011.

On January 4-5, the WRF meteorological model did not correctly simulate the mid-level clouds that were present near HW at this time. These clouds, observed in the SLV, trapped heat near the surface and increased the height capping inversion and resulted in well mixed-layers between 300 and 600 m in depth in the boundary layer during both day and night during this period (Figure 7.5). Because of increased air stability in the CAMx simulation due to the absence of clouds (daytime mixed layers were only ~200 m deep, with essentially no vertical mixing at night), modeled  $PM_{2.5}$  concentrations were significantly higher than what was observed (Figure 7.6). Further analysis indicated that increased air stability in the CAMx simulation due to the absence of clouds played a part in this result. To compensate for unrealistically high  $PM_{2.5}$ , UDAQ increased vertical diffusion rates in the CAMx model for the lower atmosphere. As a result, aerosol deposition was quicker and modeled  $PM_{2.5}$  concentrations were now lower than measured (Figure 7.4). Although the increased vertical diffusion introduced a pronounced low model bias in  $PM_{2.5}$  mass for January 4 – 5, modeled  $PM_{2.5}$  composition revealed a more realistic balance between organic compounds and ammonium nitrate (not shown).

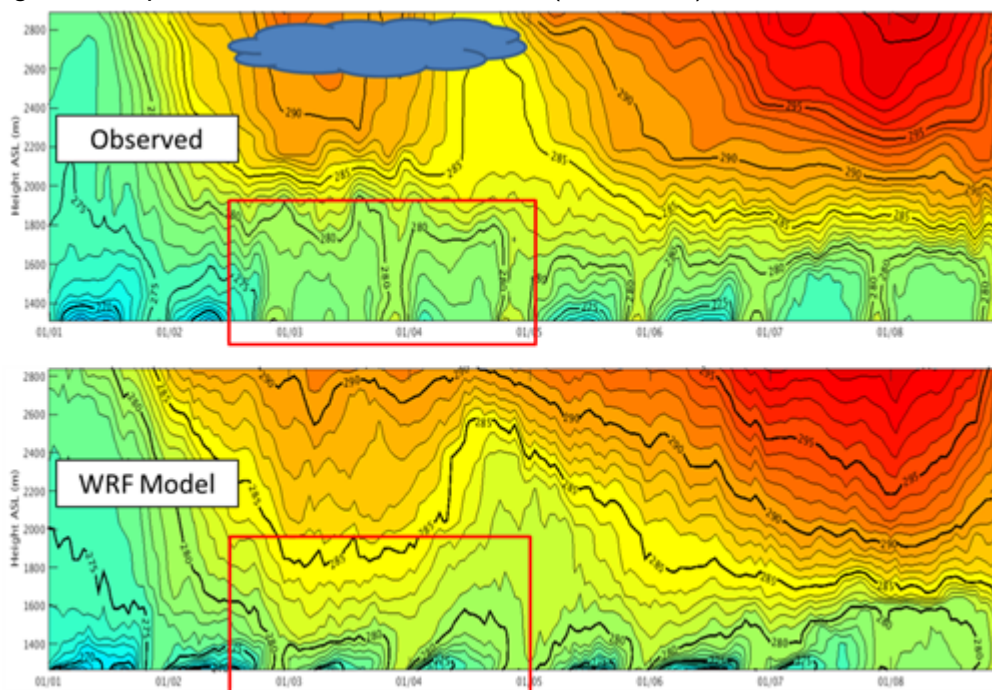


Figure 7.5 (Top) Observed temperature at HW compared to (bottom) modeled temperature for January 1 – January 8, 2011 (UTC). Red boxes highlight the near-surface vertical temperature structure for January 4 and January 5. Differences between simulated and observed temperature gradients are likely due to mid-level clouds observed, but absent in the WRF simulation.

Even during the non-cloudy periods on other days, the nighttime stable layers were a bit too tight in WRF versus observations. Increasing the vertical diffusion rates for CAMx had a positive impact on model performance for most of the episode.

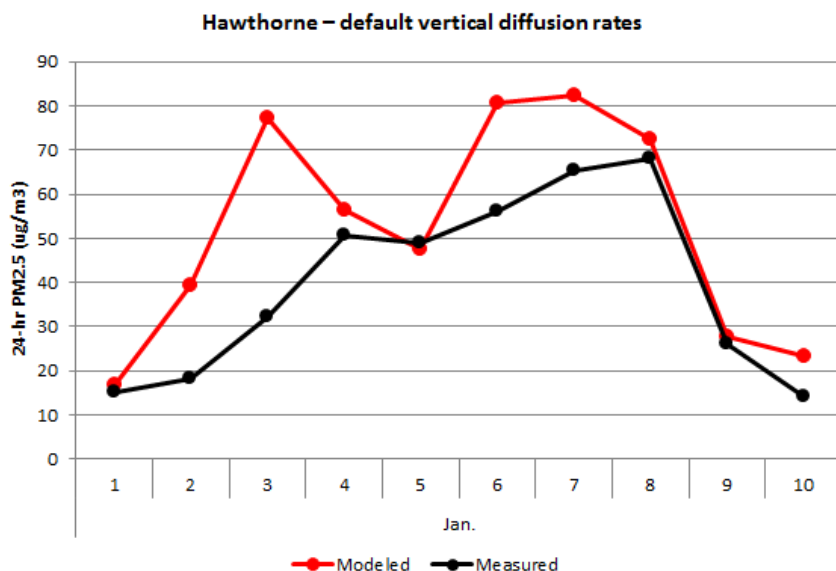


Figure 7.6 Modeled 24-hour  $PM_{2.5}$  performance at HW before increasing vertical diffusion rates in the model (red). Observations of 24-hour  $PM_{2.5}$  from UDAQ’s HW monitor (black). Modeled  $PM_{2.5}$  on January 3 is particularly high due to the incorrect simulation of clouds in WRF.

It is likely that regional air quality models will always fall short in their ability to accurately reproduce observations. But considering the regulatory implications, improving model performance is certainly worthwhile. The development of effective emissions control strategies in the face of complex air chemistry and meteorology is advanced by improved model performance. Data and analyses from the UWFPS should aid Utah’s air quality modeling efforts by improving model inputs and informing model development.

## 7.2 WRF/Chem Modeling for UWFPS-2017

Intended primarily to aid in the interpretation of aircraft measurements, the WRF/Chem photochemical transport model (<https://ruc.noaa.gov/wrf/wrf-chem/>) was applied to the 1/13/17 through 1/31/17 time period over Utah. Run in research mode, it can be used to identify uncertainties in WRF meteorology, emissions, photochemical and physical mechanisms related to UWFPS-2017 that may prove useful to UDAQ model efforts. Previous applications of WRF/Chem for the winters of 2012 and 2013 demonstrated its ability to simulate cold-pool conditions, resulting pollutant buildup, and high ozone formation from oil and gas production within the Uintah Basin [76]. Here, the same modeling framework is moved ~200km west, and configured to address the problem of  $PM_{2.5}$  formation along the Wasatch Front. The WRF/Chem model is unique in that all photochemical species are transported exactly the same way as heat and moisture, at each time step, within the WRF forecast calculation. Though coupling between radiation and aerosol/chemistry is an option within WRF/Chem, initial modeling for UWFPS-2017 does not include this coupling.

The basic WRF meteorology model contains a dozen PBL physics options, along with several options for surface layer physics, land use, boundary/initial conditions, radiation, microphysics, noise filtering etc. Examining the full parameter space within WRF is computationally unfeasible. Yet recent comparisons of WRF simulations for the Wasatch Front [32] have shown that wintertime forecast winds and temperature can depend strongly on the accurate placement of the Great Salt Lake and urban albedo effects within the WRF input data. Thus, determining the WRF settings that best reproduce the meteorological observations is a key, and ongoing activity. As such, WRF/Chem modeling efforts to date are preliminary, at least until “the best” meteorology settings have been determined. Though there are also several chemistry/aerosol options within WRF/Chem, here we utilize the mechanisms used in previous successful comparison studies, the gas-phase mechanism described in *Ahmadov et al.* [76] coupled with the aerosol mechanism of *Ahmadov et al.* [107].

### 7.2.1 WRF/Chem Configuration

Table 7.1 lists many of the relevant options and details of the WRF/Chem configuration used to simulate the UWFPS-2017 study. Aside from several model updates, the settings are identical to those used in the Uintah Basin study of *Ahmadov et al.* [76]. The most recent version of WRF/Chem (version 3.9) is used, which has the option of calculating on the older (sigma) or newer (hybrid) vertical coordinate system. The newer coordinate system is designed to minimize or eliminate numerical noise near the model top (50 mb), and comparison tests show very little impact below 5km on the chosen coordinate system.

Several perturbations to the base configuration in Table 7.1 have been performed in order to quantify model uncertainty of meteorological and chemical forecasts with comparisons to UWFPS-2017 observations. These perturbations and comparison results, are presented in detail in the two “results” sections below.

*Table 7.1* WRF/Chem settings used in the base configuration for UWFPS-2017 simulations.

Version - Release Date	Version 3.9 - 4/17/17
Vertical Coordinate System	Hybrid
Horizontal Resolution	4-km and 12-km
Vertical Levels	59 (surface to 50 mb), 20 from 0 to ~1.0km
Met Driver	NCEP RAP reanalysis (initial, 6hr LBCs)
PBL physics	Mellor-Yamada Nakanishi and Nino
Surface Layer physics	MYNN
Land Use parameterization	Noah

---

Land Use dataset	MODIS
Microphysics	WRF Single-Moment 5-class
Convection Physics	Grell-Freitas
Chemistry	RACM-ESRL (opt. 108)
Aerosol	MADE-VBS-SOA (modal)
Photolysis	Madronich (TUV)
Overhead ozone	290 Dobson units (OMI obs.)
SW radiation	RRTMG
Long wave radiation	RRTMG
Aerosol-Meteorology Feedback	No
Aerosol impact on photolysis	Yes – 2-stream approximation
Anthropogenic Emissions	NEI-2011 version 1
Biogenic Emissions	BEIS 3.14 (winter)
Chem. Boundary Conditions	12km – Default, 4km – forced by 12km
Horizontal Diffusion	WRF default (diff_opt=1) with km_opt=4

---

The WRF/Chem simulations contain a couple additional modifications necessary for the wintertime conditions encountered during UWFPS-2017. First, snow was on the ground throughout the simulation period along the Wasatch front, and this snow is also present within the model simulations. As discussed in Ahmadov et al. [76] photolysis rate calculations within WRF/Chem are modified to use a surface albedo of 0.85 over snow covered surfaces, which has a strong impact on daytime OH radical production rates. Second, the PBL mixing schemes under highly stable conditions with near-zero vertical mixing, leads to extremely large concentrations at the lowest model level (0-10 m) and near zero concentrations above 10 m. This is in clear contrast to the Twin-Otter observations which typically exhibit well mixed or partially mixed layers of pollutants in the lowest 200 to 300 m AGL. Vertical diffusion coefficients for emitted species were therefore modified to have a minimum value of 3 m<sup>2</sup>/s below 300 m for urban and suburban grid cells, using a criteria of CO emissions > 50 mole/km<sup>2</sup>/hr. This corresponds to a 2-hr characteristic time for mixing in a 0-300m layer, and is designed to account for the impact of anthropogenic heat sources on vertical mixing in a very crude ad-hoc manner. Third, all deposition velocities for gas and aerosol species have been artificially forced to zero in these initial model studies. This is partly because of the large uncertainties in deposition rates over snow, but also to discard deposition effects on the budget analysis of nitrogen species within these preliminary model studies.

### 7.2.2 Emissions

A critical yet highly uncertain component to the UWFPS-2017 simulations is the precursor emission dataset used to drive the photochemical and aerosol formation mechanisms. County level emissions are those used in Ahmadov et al. [76], and are based on the U.S. EPA NEI-2011 (version 1) inventory [108]. NOAA/ESRL/CSD provides an hourly, 4-km gridded inventory derived from the NEI-2011 on a public web-site [109]. Details on the methodology and EPA datasets used to derive the temporal and spatial allocation factors and VOC speciation profiles are contained within a “readme.txt” file that comes with that gridded inventory. January average weekday emissions are used in the simulations and analysis presented here. Examples of NO<sub>x</sub> emissions from this inventory were shown in Figure 3.28. It should be noted that the 4-km WRF/Chem model grid coincides exactly with the 4-km EPA spatial allocation grid in order to eliminate any numerical smoothing of emissions due to unequal grid spacing.

The most critical emissions related to the UWFPS-2017 aerosol observations are for NO<sub>x</sub> and NH<sub>3</sub>. Table 7.2 shows January weekday average emissions for 6 counties along the Wasatch front from the NEI-2011 inventory. Analysis of the 4 main EPA emission sectors (point, mobile-onroad, mobile-nonroad, and area) shows that NH<sub>3</sub> emissions are dominated by agricultural sources in the area emission category. About 59% of the total NO<sub>x</sub> emissions comes from the mobile-onroad sector, with 12%, 14% and 16% from the mobile-nonroad, area and point sectors, respectively. Although there are significant differences between individual counties, an inventory average NH<sub>3</sub>/NO<sub>x</sub> molar emission ratio of 0.300 is derived from the totals in Table 7.2 for comparisons with observations discussed below.

*Table 7.2 NEI-2011 Emissions (January weekday) for select Utah counties. Units are short tons per day, NO<sub>x</sub> as NO<sub>2</sub>.*

County	Total NO <sub>x</sub>	Onroad NO <sub>x</sub>	Total NH <sub>3</sub>	Onroad NH <sub>3</sub>	Area NH <sub>3</sub>
Salt Lake	96.86	52.19	5.06	1.23	3.61
Cache	10.13	6.15	7.14	0.11	7.02
Utah	44.23	31.11	6.39	0.54	5.65
Weber	19.82	11.73	1.58	0.24	1.33
Davis	26.58	16.76	1.89	0.34	1.17
Morgan	5.69	1.56	0.51	0.02	0.48
Total	203.31	119.5	22.57	2.48	19.26

### 7.2.3 Uncertainties Related to Meteorology

The 4-km resolution WRF meteorological forecasts are primarily limited by grid resolution. Though differences between 12km and 4km simulations are available for analysis, topographic features along the Wasatch front may require much finer grid structure, depending on specific meteorological requirements [32]. 4 km is the finest resolution possible for the photochemical

calculations since this is the highest resolution defined within the U.S. EPA spatial allocation database currently available.

Instead of presenting detailed meteorological statistics based on comparisons with all the surface, sonde and aircraft measurements available during UWFPS-2017, the focus here is on larger-scale, basin-wide, multi-day transport characteristics specific to the cold-pool periods. A convenient quantity, defined in section 2.4.3 and used in previous Wasatch studies [1, 28, 110] to represent basin-wide inversion strength is VHD (Valley Heat Deficit) calculated from the twice-daily NWS balloon-sonde launches at Salt Lake City airport (KSLC). This quantity expresses the deficit of heat content below 2200 m ASL (units of MegaJoule/m<sup>2</sup>), a level that corresponds with the height of the Oquirrh Mountains west of the SLV. Values of VHD greater than 4.1 are considered cold-pool conditions, and directly correlate with PCAP events in the valley during 2017 as shown in Figure 1.3.

Heat deficit calculations for UWFPS-2017 based on KSLC sonde data are available at [111] Figure 7.7a shows these observations and WRF model derived values for 3 different model cases during the simulation period. Case MYNN-default uses the MYNN PBL scheme and default horizontal diffusion options that come with WRF or WRF/Chem. Case MYNN-Kh=0 uses the MYNN PBL scheme and forces all horizontal diffusion terms in WRF to zero. Case YSU-Kh=0 uses the YSU PBL scheme, using an option designed specifically for cold-pool conditions and all horizontal diffusion terms forced to zero. The strong cold-pool conditions observed during the 1/17-1/18/17 period and the 1/29-2/1/17 period of UWFPS-2017 have much lower heat deficits when the default horizontal diffusion options are used, though all model cases significantly underestimate heat deficits during the second period. The choice of PBL scheme (MYNN versus YSU) has very little impact compared to the diffusion option used. Note that the meteorology in the model is reinitialized at 00:00 UTC each day, accounting for spikes close to observations at this time. All model cases tend to drift quickly away from the 00:00 UTC specification in the same direction, suggesting some bias or drift in the simulations between reinitializations.

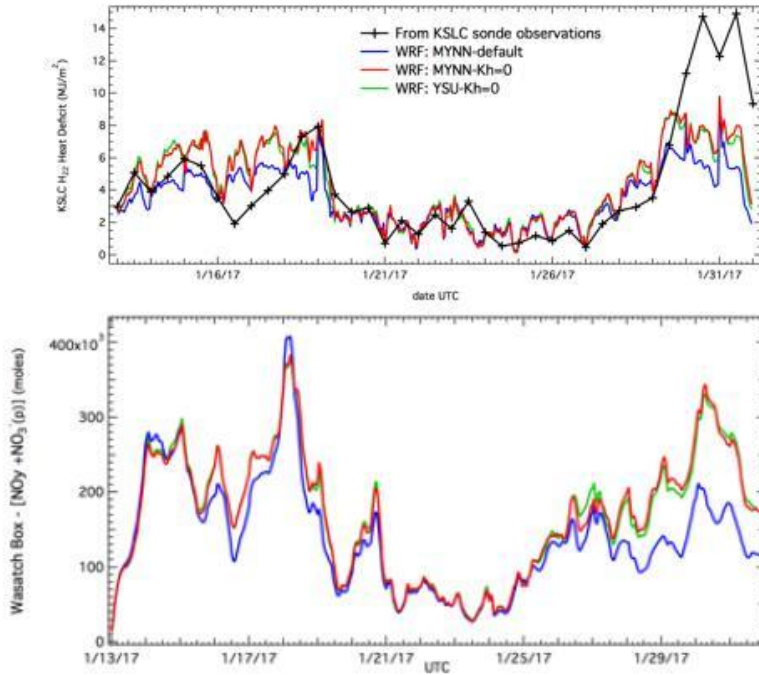


Figure 7.7 (a) Heat Deficit at KSLC from observations and 3 model cases. (b) Column sum of total oxidized nitrogen over the Wasatch Box from the WRF/Chem simulations for 3 model cases described in the text.

Figure 7.7b compares the corresponding sum of all oxidized nitrogen species over the Wasatch box defined in Figure 4.1 for the three model cases. This quantity is conserved within the WRF/Chem configuration, determined only by the emissions in Table 7.2 and horizontal transport in and out of the defined box. As expected, this column sum correlates with the heat deficit values in Figure (a). Model differences are small in the 1/19 – 1/26/17 time period when three cold fronts and accompanying high winds kept the Valley from accumulating NO<sub>x</sub>. Departures on the order of 20% begin to occur for the cold-pool conditions that begin on 1/27/17, gradually leading to ~60% differences during peak confinement on 1/30/17. These 2 figures illustrate the sensitivity of the forecasts to the horizontal diffusion configuration within WRF, and suggest that eliminating all horizontal diffusion terms may be more consistent with the KSLC heat deficit observations. Again, the choice of PBL scheme (MYNN versus YSU) is of minor consequence for these comparisons.

#### 7.2.4 Uncertainties Related to Emissions and Photochemistry

Several WRF/Chem simulations, designed to characterize predicted NO<sub>x</sub>, NH<sub>3</sub>, and ammonium nitrate formation, were performed to test the sensitivity of the results to various assumptions related to photochemistry within the WRF/Chem runs. The main motivation for these perturbation runs is to address and answer the following questions:

- (1) Can daytime photochemistry alone explain the ammonium nitrate levels observed during UWFPS-2017?

- (2) What impact could heterogeneous night-time photochemistry have on PM<sub>2.5</sub> levels?
- (3) What impact could heterogeneous conversion of NO<sub>2</sub> on the snow surface have on PM<sub>2.5</sub> levels?

These perturbation runs were done using only the MYNN-default case of the WRF configuration. Full chemistry/emission perturbations and comparisons with Twin Otter observations using a WRF option with minimal horizontal diffusion, as shown in Figure 7.7, are still in progress. The results derived to date still give some quantitative estimates related to questions 2) and 3) above from a 3-D model perspective.

### ***Emission Perturbations***

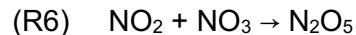
NO<sub>x</sub> emissions within the NEI inventories are known to have large uncertainties and long-term trends, particularly in relation to mobile onroad sources [112]. The 2011 inventory used here was based on 2010 census data, yet the Wasatch front is one of the fastest growing regions in the U.S. As discussed in Section 4, UWFP-2017 aircraft and surface observations suggest the ammonium nitrate levels throughout the Wasatch front are often times, but not always, limited by nitrate rather than NH<sub>3</sub>. The sensitivity of predicted PM<sub>2.5</sub> to NO<sub>x</sub> emissions is therefore of primary interest, and a perturbation run with onroad emissions of NO<sub>x</sub>, CO and VOC was performed. It should be noted that the mobile onroad CO/NO<sub>x</sub> emission ratio for Salt Lake County in the NEI-2011 inventory (molar ratio = 10.3) closely matches linear fits through the hourly HW site data during UWFP-2017.

As discussed in Sections 3.3 and 6.1, NH<sub>3</sub> emissions are highly uncertain within the inventory. The high spatial variability of NH<sub>x</sub> seen in the Twin Otter data (Section 3.3.3) implies limited spatial overlap with NO<sub>x</sub> sources, and Table 7.2 likewise shows large differences in the NH<sub>3</sub>/NO<sub>x</sub> emission ratios between individual counties. Looking at the Twin Otter measurements as a whole (all January flights, altitudes < 300m AGL), median values of NH<sub>x</sub> and (NO<sub>x</sub>+HNO<sub>3</sub>+NO<sub>3</sub><sup>-</sup>(p)) are 8.7 ppbv and 14.1 ppbv, respectively. This ratio (0.62) is about a factor of 2 higher than the NH<sub>3</sub>/NO<sub>x</sub> emission ratio from the inventory totals given in Table 7.2. This ratio is also much higher than that derived from the UU ground site observations (0.12, see section 3.3.2), which may be a result of less regional, and more local influence at the UU site. To test the sensitivity to NH<sub>3</sub> emissions a perturbation case with all NH<sub>3</sub> emissions uniformly multiplied by 4 was run to represent an extreme upper limit to possible emission uncertainty.

Photolysis of HONO can be a major OH radical source, especially after sunrise and if HONO builds up overnight [113]. Sources of HONO include mobile emissions, and HONO/NO<sub>x</sub> emission ratio as high as 0.017 have been reported [114]. From Twin Otter nighttime measures of HONO and NO<sub>x</sub> during USWP-2017 over the Salt Lake City region, very distinct correlations of HONO and NO<sub>x</sub> are observed on 5 separate occasions. The median of the slopes of these correlations yields a HONO/NO<sub>x</sub> ratio of 0.023. The possible impact of these emissions is quantified assuming an upper limit of 0.025 for this ratio.

### ***Heterogeneous Nitrate Formation***

Section 3.2 lists 2 possible reaction pathways where aerosol acts as catalyst for nitrate formation:



The photochemical/aerosol mechanism used in the simulations does not contain explicit treatment of either of these mechanisms, nor chlorine/chloride chemistry. An upper limit to the impact of (R7) was calculated by simply modifying the photochemical mechanism to force all  $\text{N}_2\text{O}_5$  formed from (R6) into 2  $\text{HNO}_3$ . The applicability of this assumption depends on the available aerosol surface area and the sticking coefficient for  $\text{N}_2\text{O}_5$  [115]. But given the high aerosol loading during the PCAP events, this upper limit assumption may be somewhat realistic.

Conversion of  $\text{NO}_2$  to nitrate and nitrite on surfaces has been known to occur from controlled laboratory studies and atmospheric measurements (e.g. Finlayson-Pitts et al., [116]). Pusede et al. [117] have proposed a generic stoichiometry consistent with recent studies:



Evaluating the impact of this mechanism was done by modifying the WRF/Chem code to accommodate it and assuming the surface resistance of  $\text{NO}_2$  to snow at the molecular interface to be zero (i.e. only aerodynamic and laminar layer resistance determine deposition velocity). Uncertainty with the deposition velocity of  $\text{NO}_2$  onto snow forces this upper limit calculation.

For determination of model impacts, median values of each model species are compared for model points along the January Twin Otter flight tracks, windowed for altitude < 300m AGL. This represents ~4700 points, with disproportionate sampling over the Salt Lake City urban corridor. Only relative model differences are given here, with direct observational comparisons awaiting completion of the “final” simulations. These percentage model differences are also likely to change with updated WRF settings.

Table 7.3 summarizes the relative impact of the emission/photochemistry perturbations listed above have on total nitrate. The snow albedo effect is significant, and brings into question how accurately photolysis rates are treated in the photochemical models. Without radiation measurements on the aircraft, one can only speculate on vertical gradients of UV radiation through optically thick aerosol layers, and if high UV irradiance at the layer top could make “hot spots” for rapid photochemical nitrate formation. The emission perturbations are relatively small

in this model configuration, with NH<sub>3</sub> perturbations requiring very large modification to affect median nitrate levels. Conversion of NO<sub>2</sub> to HNO<sub>3</sub> and HONO at the snow surface could have a moderate impact on the simulations, but conversion of N<sub>2</sub>O<sub>5</sub> on aerosol is clearly a significant mechanism that must be considered in photochemical modeling of the PCAPs.

*Table 7.3 Percentage increase in NO<sub>3</sub><sup>-</sup>(p) + HNO<sub>3</sub> due to model perturbation (upper limits).*

Snow Albedo = 0.85 (from 0.15)	60%
Onroad NO <sub>x</sub> , CO & VOC emissions X 2	25%
NH <sub>3</sub> emissions X 4	44%
Onroad HONO/NO <sub>x</sub> emiss. Ratio = 0.025	4%
Add heterogeneous N <sub>2</sub> O <sub>5</sub> -> 2HNO <sub>3</sub>	100%
Add deposition: 2 NO <sub>2</sub> -> HONO+HNO <sub>3</sub>	25%

### 7.2.5 Comparing with Column Integrated Data from Twin Otter Missed Approaches

Twin Otter flight plans were unique in that missed approaches over several airports along the Wasatch front were performed during UWFPS-2017, with nearly all of them showing a sharp transition between very clean conditions aloft and pollution in the lowest few hundred meters. Vertically integrating gas and particulate species concentrations allows a simple comparison to model results and obfuscates complexities introduced by layer structuring and incomplete vertical mixing. Figure 7.8 shows an example of total nitrate columns versus NO<sub>x</sub> columns for both the observations and coincident model results. Integrals are from 1 km to 30m AGL or below and for vertical profiles having more than 75% data coverage. This particular model simulations shows a distinctively different pattern to the relationship compared to the observations. The measurements with highest NO<sub>x</sub> columns are over Salt Lake City during local morning commuting times, and highest total nitrate columns occur at intermediate NO<sub>x</sub> column values on the edges of the main Provo-Salt Lake City urban area. In contrast the model tends to have highest nitrate over the highest NO<sub>x</sub> source region, and does not produce the high nitrate amounts at intermediate NO<sub>x</sub> column levels seen in the measurements. The column determinations shown in this figure illustrate the valuable constraints the missed approach profiles provide to UWFPS-2017, challenging the photochemical models to reproduce these features adequately.

Figure 7.8 also shows theoretical traces of a conceptual model relating column NO<sub>x</sub> to (HNO<sub>3</sub>+NO<sub>3</sub><sup>-</sup>(p)) under the simplifying assumption of first-order chemical conversion and basin-wide meteorological dilution. This results in a coupled system of ordinary differential equations with column (HNO<sub>3</sub>+NO<sub>3</sub><sup>-</sup>(p)) related to column NO<sub>x</sub> through the ratio of the first-order rates, and the initial condition specified from the observed highest NO<sub>x</sub> column. Results of the simple theory for relative rates of chemistry/dilution equal to 0.5 and 1.25 are shown, and envelope most of the observed data. Though this simple system ignores important details such as recirculation, transient meteorology and deposition, it provides a conceptual picture that generally relates the residence time under PCAP conditions to the characteristic time of chemical NO<sub>x</sub> conversion.

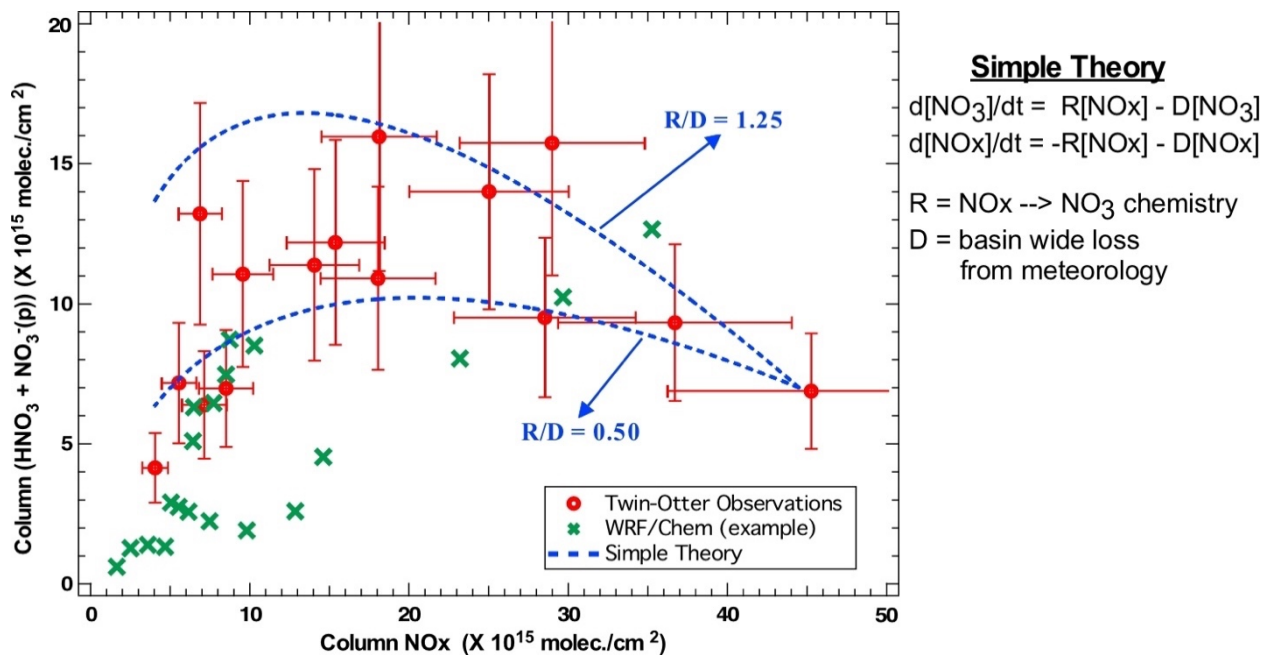


Figure 7.8 Column Nitrate versus column NO<sub>x</sub> from Twin Otter missed approaches and landings from observations and a representative model simulation. Integrals are over altitudes < 1 km AGL. The simple theory assumes nitrate is formed by a first-order loss of NO<sub>x</sub>, both nitrate and NO<sub>x</sub> are removed by a first-order meteorological process, and initial conditions are from the measurement with highest column NO<sub>x</sub>.

### 7.3 University of Utah Trajectory Information

University of Utah (Atmospheric Sciences Dept.) has provided a very useful data set and graphics collection to assist in source identification during the field study. These are based on the Stochastic Time-Inverted Lagrangian Transport (STILT) model, as described in Lin et al. [118]. STILT is a Lagrangian particle dispersion model that simulates atmospheric transport with ensembles of stochastic air parcels represented by computational particles. In most applications STILT simulates air parcels backward in time, from a receptor of interest, to map out the source region, or footprint, affecting the receptor.

Back-trajectory and source footprint calculations using this framework were applied to the Twin Otter aircraft, or the location of the William Browning Building measurement site, University of Utah campus. Calculations for the aircraft are for all Utah flights during the study, and from 1/1/17 through 2/28/17 for the WBB site. STILT was driven by NOAA-NCEP's High Resolution Rapid Refresh (HRRR) meteorological fields, which are gridded at 3-km spacing over CONUS. The HRRR-STILT model carried out runs with 200 particles starting from each receptor and transported backward in time for 24 hours. For aircraft data, calculations are performed roughly every minute of flight time, while the surface calculations are done hourly.

The complete set of trajectory output are available at: [http://home.chpc.utah.edu/~lin/UWFPS\\_STILT/STILT\\_foot\\_trajs/](http://home.chpc.utah.edu/~lin/UWFPS_STILT/STILT_foot_trajs/). Separate folders contain back-trajectory/footprint data for the aircraft and surfaces sites, and more detailed information regarding file formats, organization, and naming conventions is supplied in readme.txt files. For each calculation (in time and/or space), graphical output is supplied for both the back-trajectories and source footprints, as well as data in digital format. Figures 5.7 and 5.8 show examples where the back-trajectories and surface footprints are used to explain features in the aircraft data (on 1/17/17) and TRAX data (on 1/31/17) related to interbasin exchange from the Utah Valley to the Salt Lake Valley. As explained further in Lin et al. [118] the footprint information can be combined with gridded emission inventory data to estimate, at any particular time and receptor, the relative amount of a tracer's concentration from each surface source.

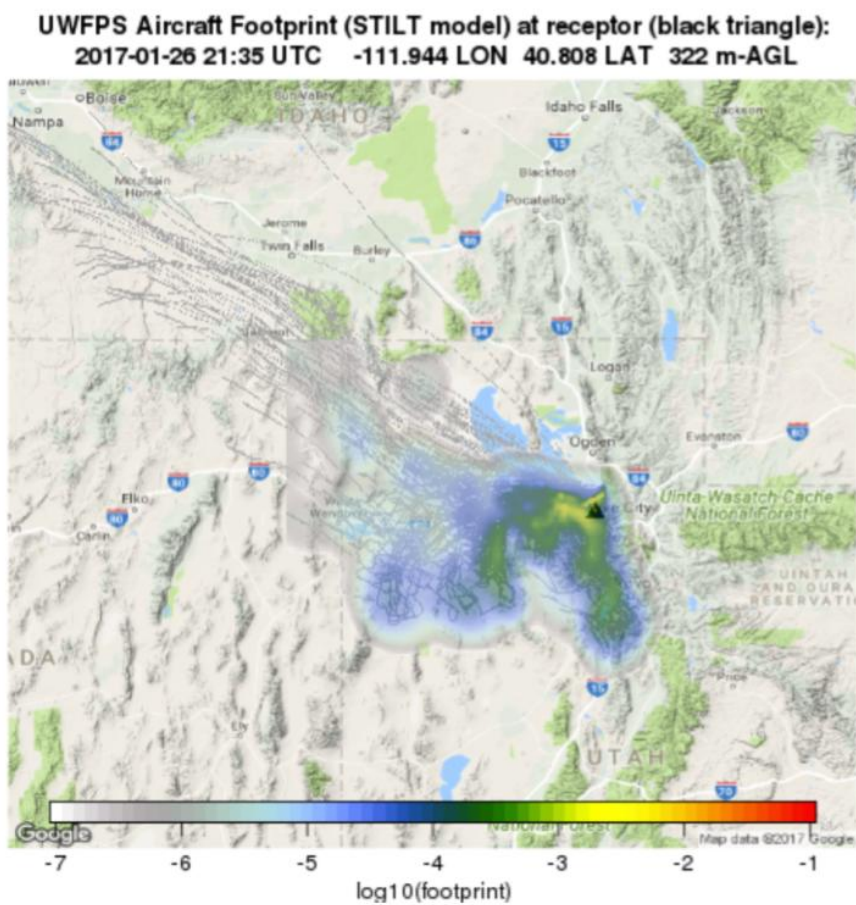


Figure 7.9 An example of footprint graphics provided for the aircraft data of 1/26/17, available on the University of Utah website.

## 8 Implications Control Strategy Development

This section provides a summary of major findings relevant to development of control strategies for winter PM<sub>2.5</sub> in Utah.

### 8.1 Limiting Reagent in Ammonium Nitrate Formation

Section 4 described excess and limiting reagents in the formation of ammonium nitrate, NH<sub>4</sub>NO<sub>3</sub>, the principal component of aerosol mass during winter pollution episodes in northern Utah. Total reduced nitrogen, NH<sub>x</sub>, is the sum of gas phase ammonia, NH<sub>3</sub>, and particulate phase ammonium, NH<sub>4</sub><sup>+</sup>, NH<sub>x</sub> = NH<sub>3</sub>(g) + NH<sub>4</sub><sup>+</sup>(p), and is derived from direct emissions of NH<sub>3</sub>(g). Total nitrate is the sum of gas phase nitric acid, HNO<sub>3</sub>, and particle phase nitrate, NO<sub>3</sub><sup>-</sup>, HNO<sub>3</sub>(g) + NO<sub>3</sub><sup>-</sup>(p), derived from the emission and subsequent oxidation of nitrogen oxides (NO<sub>x</sub> = NO + NO<sub>2</sub>). Section 4 describes two methods for determination of which reagent family limits NH<sub>4</sub>NO<sub>3</sub> formation.

Method #1 examines the ratio of the total nitrate to total reduced nitrogen (Section 4.1, equation 1). Ratios greater than unity indicate a reduced nitrogen limitation, while ratios less than unity indicate nitrate limitation. Twin Otter measurements in the three major air basins (Cache, Utah and eastern Salt Lake Valleys) indicate that across northern Utah the system is most commonly nitrate limited during UWFPS. This finding is consistent with recent analyses of ground based measurements in northern Utah, which generally conclude that the system is nitrate limited (e.g., [10]). UWFPS 2017 was the first study to address the question of reagent limitation in Utah Valley. The aircraft data show some data points in Utah Valley and SLV that lie either at the transition point between oxidized and reduced nitrogen, or that lie slightly within the NH<sub>x</sub> limited regime. This transition, or reduced nitrogen limitation, occurred exclusively during later stages of the more persistent pollution episodes, but was not observed at the UU or Logan ground sites or from the aircraft during clean or short-lived pollution episodes. Thus, it is possible that as pollution episodes proceed, the system moves from a more nitrate to a less nitrate limited regime, and there may be an altitude dependence associated with this change. Validation of this finding will require additional analyses as well as a greater sample size across a larger number of pollution episodes and ground site locations (particularly in Utah Valley) than those sampled during UWFPS 2017.

The aircraft measurements provide spatially resolved data for the ratio of nitrate to reduced nitrogen across the region and as a function of height above ground. Of the three major valleys, the Cache Valley was most clearly in the nitrate limited regime, with only a small number of data points approaching equivalence and no data points showing reduced nitrogen limitation. The Salt Lake Valley was the least nitrate limited during pollution episodes, with the generally largest ratio of total nitrate to reduced nitrogen. The Utah Valley was more similar to the Salt Lake Valley than to Cache Valley, but exhibited slightly lower ratios of nitrate to reduced nitrogen compared to Salt Lake. None of the valleys exhibited a clear dependence of the ratio as a function of either height above ground or time of day.

A second method for examining nitrate vs.  $\text{NH}_x$  limitations is thermodynamic modeling using the ISORROPIA model constrained by observations of gas phase  $\text{HNO}_3$ ,  $\text{NH}_3$  and  $\text{HCl}$  together with particle composition. The model predicts the observed partitioning between gas and aerosol phase nitrate and  $\text{NH}_x$  reasonably well, but fails to predict partitioning of chloride, a smaller component of the aerosol. The model response to two-fold reductions in either total nitrate or  $\text{NH}_x$  provides an assessment of the effect of reductions in either species in the three major valleys. The Cache Valley model shows a proportional response of reduction in  $\text{NH}_4\text{NO}_3$  to reduction in total nitrate, but a less than proportional response to reduction in  $\text{NH}_x$ , providing clear evidence for nitrate limitation there. This result is consistent with the analysis of method #1. The Salt Lake and Utah Valleys show more complicated responses to two-fold reductions in either reagent, consistent with a system that is closer to the equivalence point in these valleys. The result is again broadly consistent with method #1, and may indicate that 50% reductions in either reagent would be effective in reducing  $\text{NH}_4\text{NO}_3$  aerosol in Salt Lake and Utah Valleys, even if the system is generally nitrate limited there.

## 8.2 Emissions of $\text{NH}_3$ and $\text{NO}_x$

Assessment of the emissions of  $\text{NO}_x$  and  $\text{NH}_3$  is in a preliminary state as of the writing of this report. The NEI-2011 emissions inventory shows that on-road emissions are the largest single contribution to  $\text{NO}_x$  (59%), whereas area sources (agriculture) are by far the largest contribution to  $\text{NH}_3$  (86%) region wide.

Total emissions for  $\text{NO}_x$  and  $\text{NH}_3$  based on the UDAQ inventory are shown in Figure 8.1 for Northern Utah counties.  $\text{NO}_x$  emissions in densely populated areas (Salt Lake, Davis and Weber Counties) are significantly higher than in less populated areas, whereas  $\text{NH}_3$  emissions are more evenly distributed between county areas. For air quality purposes, the relative contribution of  $\text{NO}_x$  to  $\text{NH}_3$  emissions is of importance as these affect the limiting reagent for secondary particle formation (see Sect 8.1). The ratio of molar  $\text{NO}_x$  to  $\text{NH}_3$  emissions given in Figure 8.1 show that  $\text{NO}_x$  emissions greatly exceed those of  $\text{NH}_3$  in Salt Lake, Davis, Weber and Tooele Counties, emission of  $\text{NO}_x$  and  $\text{NH}_3$  are of similar magnitude in Box Elder County and Utah County, and  $\text{NH}_3$  emissions are higher than  $\text{NO}_x$  in Cache County. A more detailed map of  $\text{NO}_x$  to  $\text{NH}_3$  emissions is shown in Figure 8.2, illustrating the differences between densely populated areas and agricultural areas. As not all  $\text{NO}_x$  emitted will result in formation of fine particulate matter, the conversion rate of  $\text{NO}_x$  to nitrate has to be considered for air quality purposes. Measurements of both  $\text{NO}_x$  and nitrates from this report (Sections 3.2 and 3.3) suggest that about 5-30% of the emitted  $\text{NO}_x$  is oxidized to nitrate, which is then available for the formation of secondary aerosols. For that reason, only densely populated regions with high  $\text{NO}_x$  emissions (e.g. Salt Lake County and Davis County) or regions where  $\text{NH}_3$  emissions are very small (e.g. Wasatch Range) are likely to exhibit an  $\text{NH}_3$  limited regime.

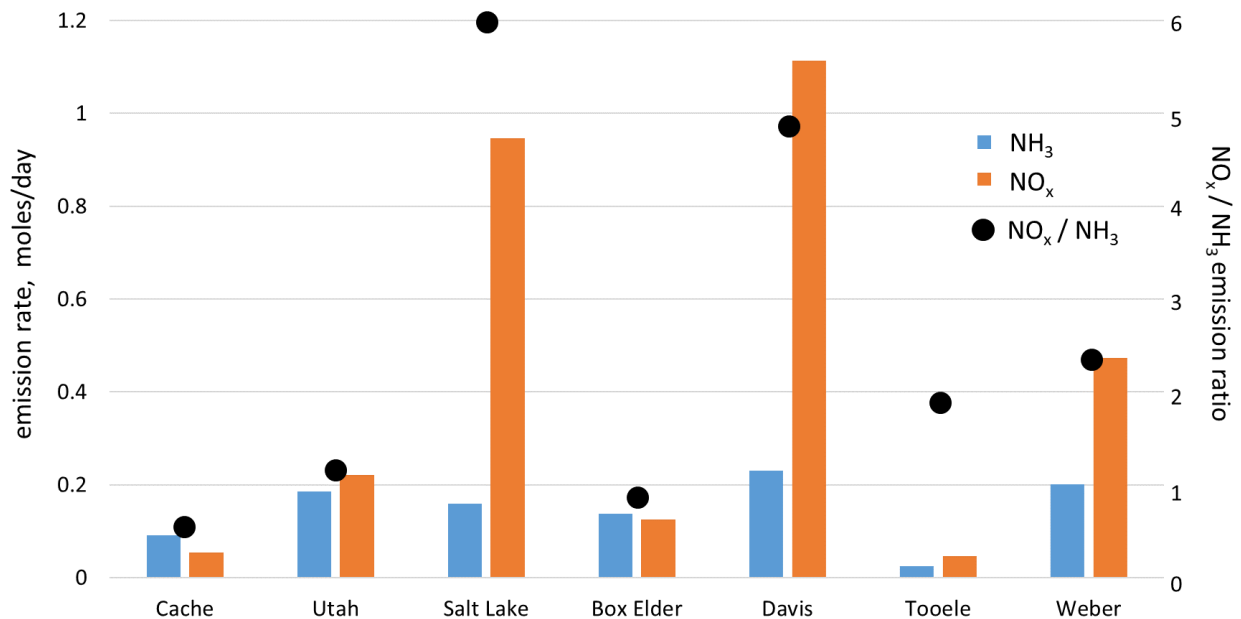


Figure 8.1 NH<sub>3</sub> and NO<sub>x</sub> emissions in Northern Utah counties retrieved from the UDAQ inventory. Shown are the total emissions per county for a day in February and the ratio of NO<sub>x</sub>/NH<sub>3</sub> emissions.

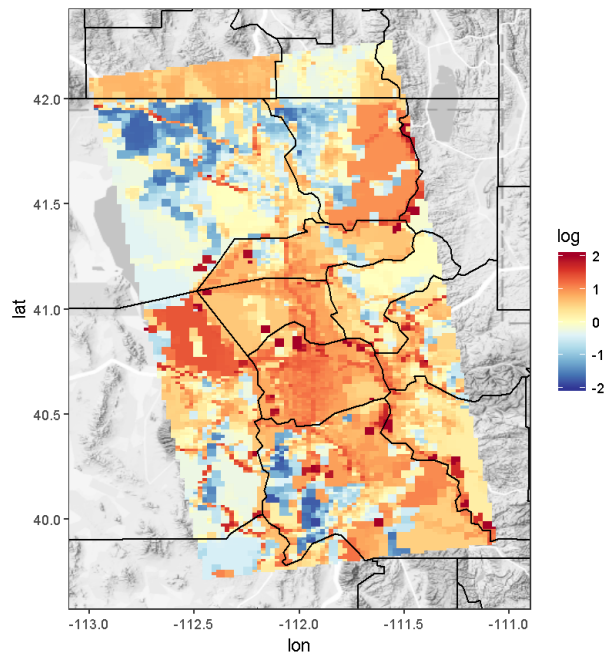


Figure 8.2 Ratio of NO<sub>x</sub>/NH<sub>3</sub> emissions retrieved from the UDAQ inventory for a day in February. Considering that only about 5-30 % of NO<sub>x</sub> are oxidized to nitrate, the orange colored areas (NO<sub>x</sub>/NH<sub>3</sub> ratio ~ 10) indicate regions where NH<sub>4</sub>NO<sub>3</sub> formation might be NH<sub>3</sub> limited assuming that local emissions represent the reagent limitation in a given area.

The interpretation of  $\text{NH}_3$  and  $\text{NO}_x$  emissions in Figures 8.1 and 8.2 relies on the reliability of emission estimates given in the inventories. Spatial distributions of  $\text{NH}_3$  and  $\text{NO}_x$  emissions from the inventory may be compared to measurements of total  $\text{NH}_x$  and either  $\text{NO}_x$  or  $\text{NO}_y$  (total oxidized nitrogen) from the aircraft. Figure 3.28 shows a comparison of the spatial distribution of Twin Otter  $\text{NO}_x$  during representative PCAP and non-PCAP flights in comparison to the distribution from the inventory. The observed spatial patterns are broadly consistent with those in the inventory, with large  $\text{NO}_x$  values over the major urban areas in the Salt Lake and Utah Valleys and the north metro area (Ogden), but smaller amounts in the Cache Valley. A similar comparison can be made between the  $\text{NH}_3$  inventory in Figure 6.2 and the observed  $\text{NH}_3$  distributions from the Twin Otter flights in Figure 3.38 and Figure 3.39. Whereas the inventory shows comparable  $\text{NH}_3$  emissions in the inventories for Cache, Utah and Salt Lake Counties, the aircraft data are consistent with  $\text{NH}_3$  hot spots in Utah and Cache Valleys relative to Salt Lake Valley. The contrast is especially true for Cache Valley, which consistently showed the largest  $\text{NH}_3$  mixing ratios. Our observations also indicate the importance of inter-basin exchange processes in transporting  $\text{PM}_{2.5}$ , oxidants and precursor species between the Salt Lake and Utah Valleys.

As discussed in Section 6.1, there is a discrepancy (at least a factor of 2) between current EPA inventory estimates and the bulk (median) observations from the Twin Otter in terms of the  $\text{NH}_x/(\text{NO}_x+\text{NO}_3^-(p))$  ratio. Ongoing and further analysis of Twin Otter measurements, which includes (1) comparison of  $\text{NO}_x$  and total  $\text{NH}_x$  measurements with estimates derived from emission footprints and inventory maps and (2) the assessment of observed ratios of  $\text{NH}_3$  and total  $\text{NH}_x$  to  $\text{NO}_x$  and total  $\text{NO}_y$ , will give a more detailed insight of the spatial consistency with the inventories. As outlined in Section 6, analysis of ground based data can further take advantage of  $\text{NH}_3$  and  $\text{NH}_x$  measurements relative to those of  $\text{CO}_2$ ,  $\text{CH}_4$  and  $\text{CO}$  for comparisons to previous literature and to the emissions inventory.

### 8.3 Residential Wood Combustion

Past ground-based work has shown varying contributions of wood smoke emissions to  $\text{PM}_{2.5}$  in the study region. Cropper et al. [99] reported that  $\text{PM}_{2.5}$  in the Utah Valley on BYU campus is 34% primary, dominated by wood smoke, suggesting the contribution from diesel and gasoline vehicles to the organic fraction of the aerosol mass is small at this site. However, according another analysis by Kelly et al. [9], diesel and gasoline contribute to roughly half of the primary  $\text{PM}_{2.5}$  at Lindon. Recent radiocarbon analysis from ground sites in the Salt Lake Valley at the University of Utah, Hawthorne, and Rose Park indicate that fossil fuels were the dominant sources of carbonaceous aerosol during winter, contributing to 88% (80-98%) of the black carbon in aerosols and 58% (48-69%) of the organic carbon in aerosols [101]. This implies that the contemporary biomass component including wood combustion contributed to less than half of the organic carbon in aerosols. Although the actual contribution is uncertain and may vary spatially, the radiocarbon data indicate that there is a non-negligible contribution from fossil fuels and other combustion sources in the wintertime.

During the UWFPS study, our combined data sets indicate that 20% of the PM<sub>2.5</sub> mass was organic material on average. The AMS marker for biomass burning aerosols ( $m/z$  60 from levoglucosan) was sometimes elevated above background levels at the Cache Valley ground site, whereas it was rarely elevated in the aircraft data. This is consistent with primary emissions of wood smoke contributing locally to ground-based measurements of PM<sub>2.5</sub>. The effect of wood combustion on the regional aerosol, however, is unclear because this AMS marker degrades as smoke ages in the atmosphere and secondary (aged) biomass burning aerosols could be a contributor to the observed organic mass in the aircraft data. Furthermore, a large contribution from fossil fuels to the organic carbon in the aircraft measurements cannot be precluded. Therefore, more work is needed to distinguish the sources of organic material in the regional PM<sub>2.5</sub> during PCAP episodes.

## 9 Recommendations for Further Research

This section describes a set of open research questions that could be more fully developed from the existing data collected during UWFPS 2017 or that could be addressed through the design of future field studies in northern Utah. The section identifies limitations and gaps in the UWFPS 2017 measurements. The questions and research needs are not listed in order of priority, nor is the list expected to be exhaustive. These questions may assist in the design of future air quality studies in northern Utah.

### ***Volatile organic compound (VOC) levels and emissions in northern Utah***

Measurements during UWFPS mainly targeted understanding of ammonium nitrate aerosol and its formation chemistry. The limited scientific payload of the Twin Otter aircraft did not allow for measurements of VOCs by standard methods such as whole air sampling (WAS) [119] or proton transfer reaction mass spectrometry (PTRMS) [120]. Similarly, ground site measurements included only limited VOC measurements, such as the twice daily samples from the Logan / Cache Valley site and the PTRMS measurements from the UU / Salt Lake Valley site. Speciated VOC measurements at higher frequency, incorporating a wider spectrum of compounds and with better spatial coverage of the region would significantly augment the analysis capabilities of future data sets. These measurements could be accomplished through better instrumentation at ground sites distributed throughout the region, a mobile laboratory (instrumented vehicle) capable of sampling from multiple locations or during drives, from the Twin Otter or equivalent aircraft, or all three. Such a data set would allow for significantly better attribution of emission sources and analysis of atmospheric chemical processes.

The real-time measurements from UU suggest oxygenated VOCs such as HCHO and CH<sub>3</sub>CHO are present during the pollution episodes at high concentrations and can significantly influence the atmospheric chemistry that occur within the PCAPs, by acting as a radical source. Measurements of fully speciated VOC composition and photolysis parameters in the three valleys will be essential to identify the most important VOCs for O<sub>3</sub> formation and characterize their sources, hence will be critical to improve air quality both in summer and winter months.

Recent analysis of volatile organic compound data from California suggests that a class of compounds emitted from personal care products, solvents, paints and other sources is now a large or even dominant urban VOC source relative to more conventional emissions from sources such as motor vehicles [121]. If so, such emissions may be an especially important contribution during the winter season, when biogenic emissions are much weaker. Future winter air quality studies would benefit from a detailed investigation of the contribution from Volatile Chemical Products (VCPs) in northern Utah.

### ***Chemical mechanism for ammonium nitrate and odd oxygen formation***

Conversion of  $\text{NO}_x$  to soluble nitrate ( $\text{NO}_3^-$ ) occurs through oxidation processes that take place during both daytime and nighttime. Data collected during UWFPS will be useful in this regard, but future studies could be designed to answer this question more completely. More complete measurements of speciated VOCs referred to above would greatly assist in understanding rates of wintertime photochemical processes. Measurements of solar radiation and actinic flux to accurately characterize photochemical rates are also needed, either from aircraft or ground sites. Measurements of atmospheric radicals, such as hydroxyl (OH), hydroperoxy ( $\text{HO}_2$ ) and organic peroxy ( $\text{RO}_2$ ) radicals (e.g. [122, 123]), as well as nitrate radicals ( $\text{NO}_3$ ) (e.g. [124]) would allow for better understanding of both daytime and nighttime atmospheric chemistry.

### ***Quantifying contributions from exchange between the PCAP and the free troposphere***

The source of oxidants to convert  $\text{NO}_x$  to  $\text{NO}_3^-$  depends on understanding both the atmospheric chemistry described above and the exchange processes that bring  $\text{O}_3$  from the overlying free troposphere into the cold air pools in the major valleys. Twin Otter measurements from UWFPS have characterized vertical profiles in ozone and odd oxygen with greater detail than previous studies in the region. Understanding the balance between exchange processes and photochemistry will be an important constraint for atmospheric chemical models of ammonium nitrate in the region. Section 5 outlines a measurement methodology for quantification of the relevant transport processes. Future analysis can take advantage of the extensive existing data set for understanding  $\text{O}_3$  exchange, and future measurements can be designed with quantification of this process as an important goal.

### ***Apparent shift towards less nitrate limitation during pollution episodes***

Section 4 examined the question of nitrate and reduced nitrogen limitations during pollution episodes in northern Utah. Both the Salt Lake and Utah Valleys appear to be less nitrate limited during episodes than more moderately polluted periods, and may even tend towards equivalence or slight reduced nitrogen limitations. The time dependence of this limiting reagent warrants further investigation, either using existing data sets, including UWFPS 2017, or through design of future studies.

### ***Uncertainty in $\text{NH}_3$ sources along the Wasatch Front and quantifying contributions from inter-basin exchange***

Since the Wasatch Front appears to be less nitrate limited than previous assessment may have indicated, better characterization of  $\text{NH}_3$  sources in this region will be critical. During the UWFPS, high time resolution real-time  $\text{NH}_3$  measurements were conducted aboard the Twin Otter and in Logan in Cache Valley. However, continuous  $\text{NH}_3$  measurements along the Wasatch Front were

limited. Hourly  $\text{NH}_3$  measurements were conducted at UU by AIM-IC and temporally integrated ambient  $\text{NH}_3$  concentrations were obtained for both the Cache Valley and Wasatch Front, with fewer sampling sites along the Wasatch Front for three separate, 7-day sampling periods. Our observations indicate that  $\text{NH}_3$  in Utah valley is on average higher than the SLV and shows more variability with lower mixing ratios above Utah Lake (flight 13) and hotspots near Spanish Fork and Lindon. In contrast,  $\text{NH}_3$  levels are lower and more homogeneous in the SLV. Section 5 also highlights importance of inter-basin exchange processes that can potentially transport  $\text{NH}_3$  from Utah Valley to Salt Lake Valley. It is not certain what is the contribution of the inter-basin transport of  $\text{NH}_3$  from Utah Valley to  $\text{NH}_3$  in the SLV. If it is a significant contributor, a reduction of  $\text{NH}_3$  in Utah Valley before the onset of pollution episodes can effectively lead to the reductions in  $\text{NH}_4\text{NO}_3$  in the SLV and eventually in Utah Valley during pollution episodes. As a result,  $\text{NH}_3$  sources along the Wasatch Front warrants future investigation.

### ***Understanding the chemical and meteorological impact of the Great Salt Lake on $\text{PM}_{2.5}$ concentrations in the SLV***

Lake breezes and synoptically-forced air mass exchanges with the Great Salt Lake (GSL) are clearly affecting  $\text{PM}_{2.5}$  concentrations on the ground in the northern part of the Salt Lake Valley (SLV). The chemical differences in these air masses were not adequately characterized during the UWFPS study with the individual, well-instrumented SLV ground site at UU and the limited time-duration of the Twin Otter measurements. In the future, there should be more ground-site measurements looking at the chemical and meteorological impact of the GSL on the ground site measurements of  $\text{PM}_{2.5}$ . Such a network should include chemical aerosol speciation (including refractory species) on an hourly (or faster) time basis along with relevant gas phase species and essential meteorological measurements at several strategic locations within the SLV and perhaps on Antelope Island.

### ***Uncertainty in the wood smoke contribution to $\text{PM}_{2.5}$ mass during pollution episodes***

Section 6.2 and section 8.3 have described the issues with respect to residential wood combustion and its contribution to particulate matter during pollution episodes. Measurements during UWFPS could partially but not fully quantify this contribution. Future studies that include speciated VOCs, more complete measurements of organic aerosol with higher resolution mass spectrometry techniques, additional tracers of wood combustion (carbon monoxide, black carbon and brown carbon, etc.) together with both regional (multiple ground sites, mobile laboratory) and vertical (aircraft) data for these species would allow for a more readily quantified assessment of the contribution of wood smoke to winter aerosol in northern Utah. Similar approaches have been employed in mountainous European cities to evaluate the spatial distribution of wood burning in residential areas and its contribution to regional  $\text{PM}_{2.5}$  [125].

### ***Uncertainty in the role of coarse mode aerosol and other salt surfaces as area sources of halogens and sinks of nitrogen oxides***

The aerosol composition data from the University of Utah ground site indicates that there are minor contributions of alkali and alkaline metals (sodium, calcium, and magnesium) to PM<sub>2.5</sub> mass during PCAP episodes. These species are likely to dominate the mineral/coarse mode aerosol. Known chemical reactions on the surfaces of dust, road salt, and lake salt aerosols could provide area sources of halogens and sinks of nitrogen oxides. However, the role that these aerosols play in the atmospheric chemistry of the region is not well-understood and should be examined in future studies.

### ***Thermodynamic models of the aerosol system and potential kinetic limitations to aerosol growth***

The investigation of thermodynamic models presented in this report indicates potential issues with partitioning of chloride between the gas phase (as hydrochloric acid) and particulate phase (as ammonium chloride), where the models consistently predict a higher fraction in the aerosol phase than observed. Furthermore, high PM<sub>2.5</sub> mass concentrations occurred during times when the ambient conditions were below the ice frost point and the products of the gas phase concentrations of ammonia and nitric acid were much greater than expected by extrapolating the equilibrium partitioning constant to these temperatures. This indicates either that the vapor pressures of these gases cannot be extrapolated below the frost point or that the system was out of equilibrium and aerosol growth was kinetically limited. Hence, the thermodynamic models of this aerosol system need further evaluation and the possibility of kinetic limitations to aerosol growth needs to be explored.

### ***Reactive species in agricultural emissions***

Emission inventories for northern Utah suggest that a large source of ammonia that participates in ammonium nitrate formation is agricultural. However, agricultural emissions may be a source for other compounds important to the atmospheric chemical system in the region. A focus of the Smithfield site in the Cache Valley was to better understand such emission sources, and further analysis of these data may provide new insights into the role of these compounds. Recent research in the Colorado Front Range, an area also subject to large agricultural emissions in close proximity to an urban area, have identified a number of compounds, including alcohols, carboxylic acids, carbonyls, phenolic species and nitrogen and sulfur containing species [126]. Measurements from the Smithfield site have identified compounds such as dimethyl sulfide, DMS, present in large concentrations, and have provided initial quantification of speciated organic amines. A more complete accounting of these compounds would help to better understand the impacts of agricultural emissions on northern Utah air quality as part of a future study.

### ***Emissions controls on diesel and other vehicle types during winter and the importance of cold starts***

Recently, aircraft-measurement based studies have reported significant uncertainties in NO<sub>x</sub> emissions from transportation over cities [127, 128]. While these studies were performed in summertime, less is known about uncertainties of NO<sub>x</sub> emissions during wintertime. A major gap is the influence of high emissions that occur from cold-starting engines [129-131], especially the effectiveness of selective catalytic reduction (SCR) systems installed in 2010 and later model year diesel trucks. SCR systems are not required to operate below a specified operating temperature [132], and therefore there may be excess diesel NO<sub>x</sub> emissions that occur under real-world driving and weather conditions [133, 134]. Catalytic technologies also emit NH<sub>3</sub> [135], which can be a significant source in urban areas [136]. Roadside measurements could help to better constrain uncertainties in transportation NO<sub>x</sub> and NH<sub>3</sub> emissions [132, 137, 138], including examples of past roadside measurements that have occurred in Utah [139].

### ***Uncertainties in PCAP meteorology that affects modeling***

Crosman and Horel [31] provide a detailed summary of deficiencies seen in mesoscale meteorological models of the Wasatch region during cold-pool outbreaks. Limitations imposed by local topography, Salt Lake water temperature specification, land-use characterization including snow and urban effects, parameterized boundary layer physics, and current computational constraints can all prevent adequate simulations of cold-pool development and evolution. A determination of the best WRF model settings for model domains having 1.3 to 4km horizontal resolution is critical to UDAQ and NOAA/CSD photochemical modeling efforts. The impact of differing meteorological formulations on gas-phase and aerosol simulations also needs more thorough evaluation. The WRF/Chem analysis done in Section 7.2 showed a very significant effect on regional predictions of NO<sub>y</sub> during the main UWFPS PCAP by simply modifying the default horizontal diffusion settings within the WRF formulation.

As computer power increases, the variety of modeling needs and capabilities of coupled meteorological and air chemistry models in the Salt Lake Valley will continue to increase [31, 32]. If a number of challenges with respect to modeling the complex wintertime pollution episodes can be addressed, understanding of the complex meteorology and chemistry would likely significantly benefit. Additional research is needed to improve the meteorological models, including the following:

- Careful time-varying treatment of the snow cover, land surface state, Great Salt Lake temperature.
- Investigating using satellite remote sensing nudging to improve forecasts of cloud cover within simulations.
- Investigating the impact of very high resolution of cold-air pool simulations, particularly with respect to canyon and gap flows, where the resolution for current simulations,  $\Delta X$ ,

of 1-3 km is too coarse to resolve flows from the deeply grooved canyons along the Wasatch Front.

- Coupling the aerosol and pollution feedbacks on cloud cover occurrence and radiative fluxes.
- Determining how to best improve models of top-down turbulent erosion, which frequently prematurely mixes out cold-air pools in current numerical weather prediction models.

## 10 References

1. Whiteman, C.D., S.W. Hoch, J.D. Horel, and A. Charland, *Relationship between particulate air pollution and meteorological variables in Utah's Salt Lake Valley*. Atmospheric Environment, 2014. **94**: p. 742-753.
2. Green, M.C., J.C. Chow, J.G. Watson, K. Dick, and D. Inouye, *Effects of snow cover and atmospheric stability on winter PM<sub>2.5</sub> concentrations in western U.S. valleys*. J. Applied Meteorology and Climatology, 2015. **54**: p. 1191-1201.
3. Silcox, G.D., K.E. Kelly, E.T. Crosman, C.D. Whiteman, and B.L. Allen, *Wintertime PM<sub>2.5</sub> concentrations during persistent, multi-day cold-air pools in a mountain valley*. Atmospheric Environment, 2012. **46**: p. 17-24.
4. Malek, E., T. Davis, R.S. Martin, and P.J. Silva, *Meteorological and environmental aspects of one of the worst national air pollution episodes (January, 2004) in Logan, Cache Valley, Utah, USA*. Atmospheric Research, 2006. **79**(2): p. 108-122.
5. Beard, J.D., C. Beck, R.A. Graham, S.C. Packham, M. Traphagan, R.T. Giles, and J.G. Morgan, *Winter temperature inversions and emergency department visits for asthma in Salt Lake County, Utah, 2003-2008*. Environn. Health Perspect., 2012. **120**: p. 1385-1390.
6. Pope, C.A., J.B. Muhlestein, H.T. May, D.G. Renlund, J.L. Anderson, and B.D. Horne, *Ischemic heart disease events triggered by short-term exposure to fine particulate air pollution*. Circulation, 2006. **114**: p. 2443-2448.
7. UDAQ, *Salt Lake City, UT PM<sub>2.5</sub> Nonattainment SIP*, UDAQ: <https://deq.utah.gov/Pollutants/P/pm/pm25/moderate-area-state-implementation-plans.htm>.
8. Hansen, J.C., W.R. Woolwine, B.L. Bates, J.M. Clark, R.Y. Kuprov, P. Mukherjee, J.A. Murray, M.A. Simmons, M.F. Waite, N.L. Eatough, D.J. Eatough, R. Long, and B.D. Grover, *Semicontinuous PM<sub>2.5</sub> and PM<sub>10</sub> Mass and Composition Measurements in Lindon, Utah, during Winter 2007*. Journal of the Air & Waste Management Association, 2010. **60**(3): p. 346-355.
9. Kelly, K.E., R. Kotchenruther, R. Kuprov, and G.D. Silcox, *Receptor model source attributions for Utah's Salt Lake City airshed and the impacts of wintertime secondary ammonium nitrate and ammonium chloride aerosol*. Journal of the Air & Waste Management Association, 2013. **63**(5): p. 575-590.
10. Kuprov, R., D.J. Eatough, T. Cruickshank, N. Olson, P.M. Cropper, and J.C. Hansen, *Composition and secondary formation of fine particulate matter in the Salt Lake Valley: Winter 2009*. Journal of the Air & Waste Management Association, 2014. **64**(8): p. 957-969.
11. Mangelson, N.F., L. Lewis, J.M. Joseph, W. Cui, J. Machir, D.J. Eatough, L.B. Rees, T. Wilkerson, and D.T. Jensen, *The Contribution of Sulfate and Nitrate to Atmospheric Fine Particles During Winter Inversion Fogs in Cache Valley, Utah*. Journal of the Air & Waste Management Association, 1997. **47**(2): p. 167-175.
12. Long, R.W., N.L. Eatough, D.J. Eatough, M.B. Meyer, and W.E. Wilson, *Continuous Determination of Fine Particulate Matter Mass in the Salt Lake City Environmental Monitoring Project: A Comparison of Real-Time and Conventional TEOM Monitor Results*. Journal of the Air & Waste Management Association, 2005. **55**(12): p. 1782-1796.
13. Long, R.W., N.L. Eatough, N.F. Mangelson, W. Thompson, K. Fiet, S. Smith, R. Smith, D.J. Eatough, C.A. Pope, and W.E. Wilson, *The measurement of PM<sub>2.5</sub>, including semi-volatile components, in the EMPACT program: results from the Salt Lake City Study*. Atmospheric Environment, 2003. **37**(31): p. 4407-4417.

14. Long, R.W., W.K. Modey, P.S. Smith, R. Smith, C. Merrill, J. Pratt, A. Stubbs, N.L. Eatough, D.J. Eatough, W.C. Malm, and W.E. Wilson, *One and three hour PM<sub>2.5</sub> characterization, speciation, and source apportionment using continuous and integrated samplers*. *Aerosol Sci. and Tech.*, 2005. **39**(3): p. 238-248.
15. Baasandorj, M., S.W. Hoch, R. Bares, J.C. Lin, S.S. Brown, D.B. Millet, R. Martin, K. Kelly, K.J. Zarzana, C.D. Whiteman, W.P. Dube, G. Tonnesen, I.C. Jaramillo, and J. Sohl, *Coupling between Chemical and Meteorological Processes under Persistent Cold-Air Pool Conditions: Evolution of Wintertime PM<sub>2.5</sub> Pollution Events and N<sub>2</sub>O<sub>5</sub> Observations in Utah's Salt Lake Valley*. *Environmental Science & Technology*, 2017. **51**(11): p. 5941-5950.
16. Brown, S.G., N.P. Hyslop, P.T. Roberts, M.C. McCarthy, and F.W. Lurmann, *Wintertime Vertical Variations in Particulate Matter (PM) and Precursor Concentrations in the San Joaquin Valley during the California Regional Coarse PM/Fine PM Air Quality Study*. *Journal of the Air & Waste Management Association*, 2006. **56**(9): p. 1267-1277.
17. Chow, J.C., L.W.A. Chen, J.G. Watson, D.H. Lowenthal, K.A. Magliano, K. Turkiewicz, and D.E. Lehrman, *PM<sub>2.5</sub> chemical composition and spatiotemporal variability during the California Regional PM<sub>10</sub>/PM<sub>2.5</sub> Air Quality Study (CRPAQS)*. *Journal of Geophysical Research: Atmospheres*, 2006. **111**(D10): p. n/a-n/a.
18. Lurmann, F.W., S.G. Brown, M.C. McCarthy, and P.T. Roberts, *Processes Influencing Secondary Aerosol Formation in the San Joaquin Valley during Winter*. *Journal of the Air & Waste Management Association*, 2006. **56**(12): p. 1679-1693.
19. Prabhakar, G., C. Parworth, X. Zhang, H. Kim, D. Young, A.J. Beyersdorf, L.D. Ziemba, J.B. Nowak, T.H. Bertram, I.C. Faloona, Q. Zhang, and C.D. Cappa, *Observational assessment of the role of nocturnal residual-layer chemistry in determining daytime surface particulate nitrate concentrations*. *Atmos. Chem. Phys. Discuss.*, 2017. **2017**: p. 1-58.
20. Pusede, S.E., K.C. Duffey, A.A. Shusterman, A. Saleh, J.L. Laughner, P.J. Wooldridge, Q. Zhang, C.L. Parworth, H. Kim, S.L. Capps, L.C. Valin, C.D. Cappa, A. Fried, J. Walega, J.B. Nowak, A.J. Weinheimer, R.M. Hoff, T.A. Berkoff, A.J. Beyersdorf, J. Olson, J.H. Crawford, and R.C. Cohen, *On the effectiveness of nitrogen oxide reductions as a control over ammonium nitrate aerosol*. *Atmos. Chem. Phys.*, 2016. **16**(4): p. 2575-2596.
21. Watson, J.G. and J.C. Chow, *A wintertime PM<sub>2.5</sub> episode at the Fresno, CA, supersite*. *Atmospheric Environment*, 2002. **36**(3): p. 465-475.
22. Osthoff, H.D., J.M. Roberts, A.R. Ravishankara, E.J. Williams, B.M. Lerner, R. Sommariva, T.S. Bates, D. Coffman, P.K. Quinn, J.E. Dibb, H. Stark, J.B. Burkholder, R.K. Talukdar, J.F. Meagher, F.C. Fehsenfeld, and S.S. Brown, *High levels of nitryl chloride in the polluted subtropical marine boundary layer*. *Nature Geosciences*, 2008. **1**: p. 324-328.
23. Thornton, J.A., J.P. Kercher, T.P. Riedel, N.L. Wagner, J. Cozic, J.S. Holloway, W.P. Dubé, G.M. Wolfe, P.K. Quinn, A.M. Middlebrook, B. Alexander, and S.S. Brown, *A large atomic chlorine source inferred from mid-continental reactive nitrogen chemistry*. *Nature*, 2010. **464**: p. 271-274.
24. Lareau, N.P., E. Crosman, C.D. Whiteman, J.D. Horel, S.W. Hoch, W.O.J. Brown, and T.W. Horst, *The Persistent Cold-Air Pool Study*. *Bulletin of the American Meteorological Society*, 2013. **94**(1): p. 51-63.
25. Crosman, E.T. and J.D. Horel, *Winter Lake Breezes near the Great Salt Lake*. *Boundary-Layer Meteorology*, 2016. **159**(2): p. 439-464.
26. Whiteman, C.D., *Winter visibility study*. *J. Appl. Meteor.*, 1999. **38**(8): p. 1029-1029.

27. Whiteman, C.D. and S.W. Hoch, *Pseudovertical Temperature Profiles in a Broad Valley from Lines of Temperature Sensors on Sidewalls*. Journal of Applied Meteorology and Climatology, 2014. **53**(11): p. 2430-2437.
28. Young, J.S. and C.D. Whiteman, *Laser Ceilometer Investigation of Persistent Wintertime Cold-Air Pools in Utah's Salt Lake Valley*. Journal of Applied Meteorology and Climatology, 2015. **54**(4): p. 752-765.
29. Lareau, N.P. and J.D. Horel, *Turbulent Erosion of Persistent Cold-Air Pools: Numerical Simulations*. Journal of the Atmospheric Sciences, 2014. **72**(4): p. 1409-1427.
30. Lareau, N.P. and J.D. Horel, *Dynamically Induced Displacements of a Persistent Cold-Air Pool*. Boundary-Layer Meteorology, 2015. **154**(2): p. 291-316.
31. Crosman, E.T. and J.D. Horel, *Large-eddy simulations of a Salt Lake Valley cold-air pool*. Atmospheric Research, 2017. **193**: p. 10-25.
32. Foster, C.S., E.T. Crosman, and J.D. Horel, *Simulations of a Cold-Air Pool in Utah's Salt Lake Valley: Sensitivity to Land Use and Snow Cover*. Boundary-Layer Meteorology, 2017. **164**(1): p. 63-87.
33. Lu, W. and S. Zhong, *A numerical study of a persistent cold air pool episode in the Salt Lake Valley, Utah*. Journal of Geophysical Research: Atmospheres, 2014. **119**(4): p. 1733-1752.
34. Zardi, D. and C.D. Whiteman, in *Mountain Weather Research and Forecasting*, F. Chow and S. De Wekker, Editors. 2013, Springer: Dordrecht.
35. Schnell, R.C., S.J. Oltmans, R.R. Neely, M.S. Endres, J.V. Molenaar, and A.B. White, *Rapid photochemical production of ozone at high concentrations in a rural site during winter*. Nature Geosciences, 2009. **2**: p. 120-122.
36. Perring, A.E., J.P. Schwarz, R.S. Gao, A.J. Heymsfield, C.G. Schmitt, M. Schnaiter, and D.W. Fahey, *Evaluation of a Perpendicular Inlet for Airborne Sampling of Interstitial Submicron Black-Carbon Aerosol*. Aerosol Science and Technology, 2013. **47**(10): p. 1066-1072.
37. Canagaratna, M.R., J.T. Jayne, J.L. Jimenez, J.D. Allan, M.R. Alfarra, Q. Zhang, T.B. Onasch, F. Drewnick, H. Coe, A. Middlebrook, A. Delia, L.R. Williams, A.M. Trimborn, M.J. Northway, P.F. DeCarlo, C.E. Kolb, P. Davidovits, and D.R. Worsnop, *Chemical and microphysical characterization of ambient aerosols with the aerodyne aerosol mass spectrometer*. Mass Spectrometry Reviews, 2007. **26**(2): p. 185-222.
38. Drewnick, F., S.S. Hings, P. DeCarlo, J.T. Jayne, M. Gonin, K. Fuhrer, S. Weimer, J.L. Jimenez, K.L. Demerjian, S. Borrmann, and D.R. Worsnop, *A New Time-of-Flight Aerosol Mass Spectrometer (TOF-AMS)—Instrument Description and First Field Deployment*. Aerosol Science and Technology, 2005. **39**(7): p. 637-658.
39. Jayne, J.T., D.C. Leard, X. Zhang, P. Davidovits, K.A. Smith, C.E. Kolb, and D.R. Worsnop, *Development of an aerosol mass spectrometer for size and composition analysis of submicron particles*. Aerosol Sci. Technol., 2000. **33**: p. 49-70.
40. Bahreini, R., E.J. Dunlea, B.M. Matthew, C. Simons, K.S. Docherty, P.F. DeCarlo, J.L. Jimenez, C.A. Brock, and A.M. Middlebrook, *Design and operation of a pressure-controlled inlet for airborne sampling with an aerodynamic aerosol lens*. Aerosol Sci. and Technol., 2008. **42**(6): p. 465-471.
41. Liao, J., C.A. Brock, D.M. Murphy, D.T. Sueper, A. Welti, and A.M. Middlebrook, *Single particle measurements of bouncing particles and in-situ collection efficiency from an airborne aerosol mass spectrometer (AMS) with light scattering detection*. Atmos. Meas. Tech., 2017. **in press**.
42. Bahreini, R., B. Ervens, A.M. Middlebrook, C. Warneke, J.A. de Gouw, P.F. DeCarlo, J.L. Jimenez, C.A. Brock, J.A. Neuman, T.B. Ryerson, H. Stark, E. Atlas, J. Brioude, A. Fried,

- J.S. Holloway, J. Peischl, D. Richter, J. Walega, P. Weibring, A.G. Wollny, and F.C. Fehsenfeld, *Organic aerosol formation in urban and industrial plumes near Houston and Dallas, Texas*. J. Geophys. Res., 2009. **114**: p. D00F16.
43. Cai, Y., D.C. Montague, W. Mooiweer-Bryan, and T. Deshler, *Performance characteristics of the ultra high sensitivity aerosol spectrometer for particles between 55 and 800nm: Laboratory and field studies*. Journal of Aerosol Science, 2008. **39**(9): p. 759-769.
  44. Brock, C.A., J. Cozic, R. Bahreini, K.D. Froyd, A.M. Middlebrook, A. McComiskey, J. Brioude, O.R. Cooper, A. Stohl, K.C. Aikin, J.A. de Gouw, D.W. Fahey, R.A. Ferrare, R.S. Gao, W. Gore, J.S. Holloway, G. Hübner, A. Jefferson, D.A. Lack, S. Lance, R.H. Moore, D.M. Murphy, A. Nenes, P.C. Novelli, J.B. Nowak, J.A. Ogren, J. Peischl, R.B. Pierce, P. Pilewskie, P.K. Quinn, T.B. Ryerson, K.S. Schmidt, J.P. Schwarz, H. Sodemann, J.R. Spackman, H. Stark, D.S. Thomson, T. Thornberry, P. Veres, L.A. Watts, C. Warneke, and A.G. Wollny, *Characteristics, sources, and transport of aerosols measured in spring 2008 during the aerosol, radiation, and cloud processes affecting Arctic Climate (ARCPAC) Project*. Atmos. Chem. Phys., 2011. **11**(6): p. 2423-2453.
  45. Lee, B.H., F.D. Lopez-Hilfiker, C. Mohr, T. Kurtén, D.R. Worsnop, and J.A. Thornton, *An Iodide-Adduct High-Resolution Time-of-Flight Chemical-Ionization Mass Spectrometer: Application to Atmospheric Inorganic and Organic Compounds*. Environmental Science & Technology, 2014. **48**(11): p. 6309-6317.
  46. Lee, B.H., F.D. Lopez-Hilfiker, P.R. Veres, E.E. McDuffie, D.L. Fibiger, T.L. Sparks, C.J. Ebben, J.R. Green, J.C. Schroder, P. Campuzano-Jost, S. Iyer, E.L. D'Ambro, S. Schobesberger, S.S. Brown, P.J. Wooldridge, R.C. Cohen, S. Bililign, J.L. Jimenez, T. Kurtén, A.J. Weinheimer, L. Jaegle, and J.A. Thornton, *Flight deployment of a high-resolution time-of-flight chemical ionization mass spectrometer: observations of reactive halogen and nitrogen oxide species*. J. Geophys. Res., 2017. **in preparation**.
  47. Fuchs, H., W.P. Dubé, B.M. Lerner, N.L. Wagner, E.J. Williams, and S.S. Brown, *A sensitive and versatile detector for atmospheric NO<sub>2</sub> and NO<sub>x</sub> based on blue diode laser cavity ring-down spectroscopy*. Environ. Sci. Technol., 2009. **43**: p. 7831-7836.
  48. Washenfelder, R.A., W.P. Dubé, N.L. Wagner, and S.S. Brown, *Measurement of atmospheric ozone by cavity ring-down spectroscopy*. Environ. Sci. Technol., 2011. **45**: p. 2938-2944.
  49. Wild, R.J., P.M. Edwards, W.P. Dubé, K. Baumann, E.S. Edgerton, P.K. Quinn, J.M. Roberts, A.W. Rollins, P.R. Veres, C. Warneke, E.J. Williams, B. Yuan, and S.S. Brown, *A Measurement of Total Reactive Nitrogen, NO<sub>y</sub>, together with NO<sub>2</sub>, NO and O<sub>3</sub> via Cavity Ring-Down Spectroscopy*. Environ. Sci. Technol., 2014. **48**: p. 9609-9615.
  50. Ellis, R.A., J.G. Murphy, E. Pattey, R. van Haarlem, J.M. O'Brien, and S.C. Herndon, *Characterizing a Quantum Cascade Tunable Infrared Laser Differential Absorption Spectrometer (QC-TILDAS) for measurements of atmospheric ammonia*. Atmos. Meas. Tech., 2010. **3**(2): p. 397-406.
  51. Middlebrook, A.M., R. Bahreini, J.L. Jimenez, and M.R. Canagaratna, *Evaluation of Composition-Dependent Collection Efficiencies for the Aerodyne Aerosol Mass Spectrometer using Field Data*. Aerosol Science and Technology, 2012. **46**(3): p. 258-271.
  52. Crosman, E.T., A.A. Jacques, and J.D. Horel, *A novel approach for monitoring vertical profiles of boundary-layer pollutants: Utilizing routine news helicopter flights*. Atmospheric Pollution Research, 2017. **8**(5): p. 828-835.
  53. Markovic, M.Z., T.C. Vandenboer, and J.G. Murphy, *Characterization and optimization of an online system for the simultaneous measurement of atmospheric water-soluble constituents in the gas and particle phases*. J. Environ. Monit., 2012. **14**(7): p. 1872-1884.

54. EPA, *Technical Assistance Document (TAD) For Precursor Gas Measurements in the NCore Multi-Pollutant Monitoring Network*, 2005, United States Environmental Protection Agency.
55. Roadman, M.J., J.R. Scudlark, J.J. Meisinger, and W.J. Ullman, *Validation of Ogawa passive samplers for the determination of gaseous ammonia concentrations in agricultural settings*. *Atmospheric Environment*, 2003. **37**(17): p. 2317-2325.
56. Farmer, D.K., A. Matsunaga, K.S. Docherty, J.D. Surratt, J.H. Seinfeld, P.J. Ziemann, and J.L. Jimenez, *Response of the Aerosol Mass Spectrometer to organonitrates and organosulfates and implications for field studies*. *PNAS*, 2010. **107**: p. 6670-6675.
57. Mitchell, L., E. Crosman, A. Jacques, B. Fasoli, L. Leclair-Marzolf, J. Horel, D. Bowling, J. Ehleringer, and J. Lin, *Monitoring of trace gases and pollutants across an urban area using a light-rail public transit platform*. *Atmospheric Environment*, 2018. **submitted**.
58. von Schneidemesser, E., P.S. Monks, J.D. Allan, L. Bruhwiler, P. Forster, D. Fowler, A. Lauer, W.T. Morgan, P. Paasonen, M. Righi, K. Sindelarova, and M.A. Sutton, *Chemistry and the Linkages between Air Quality and Climate Change*. *Chemical Reviews*, 2015. **115**(10): p. 3856-3897.
59. Zhang, R., G. Wang, S. Guo, M.L. Zamora, Q. Ying, Y. Lin, W. Wang, M. Hu, and Y. Wang, *Formation of Urban Fine Particulate Matter*. *Chemical Reviews*, 2015. **115**(10): p. 3803-3855.
60. Brown, S.S., J.A. Neuman, T.B. Ryerson, M. Trainer, W.P. Dubé, J.S. Holloway, C. Warneke, J.A. de Gouw, S.G. Donnelly, E. Atlas, B. Matthew, A.M. Middlebrook, R. Peltier, R.J. Weber, A. Stohl, J.F. Meagher, F.C. Fehsenfeld, and A.R. Ravishankara, *Nocturnal odd-oxygen budget and its implications for ozone loss in the lower troposphere*. *Geophys. Res. Lett.*, 2006. **33**: p. L08801.
61. Kim, S., T.C. VandenBoer, C.J. Young, T.P. Riedel, J.A. Thornton, R. Swarthout, B. Sive, B.M. Lerner, J.B. Gilman, C. Warneke, J.M. Roberts, A. Guenther, N.L. Wagner, W.P. Dubé, E.J. Williams, and S.S. Brown, *The primary and recycling sources of OH during the NACHTT-2011 campaign*. *J. Geophys. Res.*, 2014. **119**: p. 6886-6896.
62. Fahey, D.W., G. Hübler, D.D. Parrish, E.J. Williams, R.B. Norton, B.A. Ridley, H.B. Singh, S.C. Liu, and F.C. Fehsenfeld, *Reactive nitrogen species in the troposphere: Measurements of NO, NO<sub>2</sub>, HNO<sub>3</sub>, particulate nitrate, peroxyacetyl nitrate (PAN), O<sub>3</sub>, and total reactive odd nitrogen (NO<sub>y</sub>) at Niwot Ridge, Colorado*. *Journal of Geophysical Research: Atmospheres*, 1986. **91**(D9): p. 9781-9793.
63. Sillman, S., *The relation between ozone, NO<sub>x</sub> and hydrocarbons in urban and polluted rural environments*. *Atmos. Environ.*, 1999. **33**: p. 1821-1845.
64. Winer, A.M., J.W. Peters, J.P. Smith, and J.N. Pitts, *Response of commercial chemiluminescent nitric oxide-nitrogen dioxide analyzers to other nitrogen-containing compounds*. *Environmental Science & Technology*, 1974. **8**(13): p. 1118-1121.
65. *National Atmospheric Deposition Program Ammonia Monitoring Network (NADP AMoN)*, 2017: <http://nadp.sws.uiuc.edu/data/sites/list/?net=AMoN>,.
66. Atkins, D.H.F. and D.S. Lee, *Indoor concentrations of ammonia and the potential contribution of humans to atmospheric budgets*. *Atmospheric Environment. Part A. General Topics*, 1993. **27**(1): p. 1-7.
67. *Utah Division of Air Quality, 2017, Air Monitoring Program, Data Archive, Particulate PM 2.5*, 2017: <http://www.airmonitoring.utah.gov/dataarchive/archpm25.htm>.
68. Foster, K.L., R.A. Plastridge, J.W. Bottenheim, P.B. Shepson, B.J. Finlayson-Pitts, and C.W. Spicer, *The Role of Br<sub>2</sub> and BrCl in Surface Ozone Destruction at Polar Sunrise*. *Science*, 2001. **291**(5503): p. 471-474.

69. Sander, R. and P.J. Crutzen, *Model study indicating halogen activation and ozone destruction in polluted air masses transported to the sea*. J. Geophys. Res., 1996. **101**(D4): p. 9121-9138.
70. Kercher, J.P., T.P. Riedel, and J.A. Thornton, *Chlorine activation by N<sub>2</sub>O<sub>5</sub>: simultaneous, in-situ detection of ClNO<sub>2</sub> and N<sub>2</sub>O<sub>5</sub> by chemical ionization mass spectrometry*. Atmos. Meas. Tech., 2009. **2**: p. 193-204.
71. Riedel, T.P., T.H. Bertram, T.A. Crisp, E.J. Williams, B.M. Lerner, A. Vlasenko, S.-M. Li, J.B. Gilman, J. de Gouw, D.M. Bon, N.L. Wagner, S.S. Brown, and J.A. Thornton, *Nitryl chloride and molecular chlorine in the coastal marine boundary layer*. Environ. Sci. Technol., 2012. **46**: p. 10463-10470.
72. Stutz, J., B. Alicke, R. Ackermann, A. Geyer, A.B. White, and E. Williams, *Vertical profiles of NO<sub>3</sub>, N<sub>2</sub>O<sub>5</sub>, O<sub>3</sub>, and NO<sub>x</sub> in the nocturnal boundary layer: 1. Observations during the Texas Air Quality Study 2000*. J. Geophys. Res., 2004. **109**(D12): p. D12306.
73. Bares, R., J.C. Lin, S.W. Hoch, D. Mendoza, M. Baasandorj, B. Fasoli, and L.E. Mitchell, *The wintertime co-variation of CO<sub>2</sub> and criteria pollutants in an urban valley of the Western U.S.* 2017. **In Preparation**.
74. Lin, J.C., M. L., C. E., M. D., B. M., B. R., F. B., B. D., P. D., C. D., S. C., G. K., P. R., B. M., J. A., H.S. W., and E. J., *CO<sub>2</sub> and carbon emissions from cities: linkages to air quality, socioeconomic activity and stakeholders in the Salt Lake City urban area*. Bulletin of the American Meteorological Society, 2017.
75. Pataki, D.E., B.J. Tyler, R.E. Peterson, A.P. Nair, W.J. Steenburgh, and E.R. Pardyjak, *Can carbon dioxide be used as a tracer of urban atmospheric transport?* Journal of Geophysical Research D: Atmospheres, 2005. **110**(15): p. 1-8.
76. Ahmadov, R., S. McKeen, M. Trainer, R. Banta, A. Brewer, S.S. Brown, P.M. Edwards, J.A. de Gouw, G.J. Frost, J. Gilman, D. Helmig, B. Johnson, A. Karion, A. Koss, A. Langford, B. Lerner, J. Olson, S. Oltmans, J. Peischl, G. Pétron, Y. Pichugina, J.M. Roberts, T. Ryerson, R. Schnell, C. Senff, C. Sweeney, C. Thompson, P.R. Veres, C. Warneke, R. Wild, E.J. Williams, B. Yuan, and R. Zamora, *Understanding high wintertime ozone pollution events in an oil- and natural gas-producing region of the western US*. Atmos. Chem. Phys., 2015. **15**(1): p. 411-429.
77. Turnbull, J.C., C. Sweeney, A. Karion, T. Newberger, S.J. Lehman, M.O. Cambaliza, P.B. Shepson, K. Gurney, R. Patarasuk, and I. Razlivanov, *Toward quantification and source sector identification of fossil fuel CO<sub>2</sub> emissions from an urban area: Results from the INFLUX experiment*. Journal of Geophysical Research : Atmospheres, 2014: p. 292-312.
78. Wilkey, J., K. Kelly, I.C. Jaramillo, J. Spinti, M. Hogue, D. Pasqualini, J. Wilkey, K. Kelly, I.C. Jaramillo, and J. Spinti, *Predicting emissions from oil and gas operations in the Uinta Basin , Utah*. Journal of the Air & Waste Management Association, 2016. **66**(5): p. 528-545.
79. Keppel-Aleks, G., P.O. Wennberg, R.A. Washenfelder, D. Wunch, T. Schneider, G.C. Toon, R.J. Andres, J.F. Blavier, B. Connor, K.J. Davis, A.R. Desai, J. Messerschmidt, J. Notholt, C.M. Roehl, V. Sherlock, B.B. Stephens, S.A. Vay, and S.C. Wofsy, *The imprint of surface fluxes and transport on variations in total column carbon dioxide*. Biogeosciences, 2012. **9**(3): p. 875-891.
80. Wang, J.W., A.S. Denning, L. Lu, I.T. Baker, K.D. Corbin, and K.J. Davis, *Observations and simulations of synoptic, regional, and local variations in atmospheric CO<sub>2</sub>*. Journal of Geophysical Research Atmospheres, 2007. **112**(4).
81. Xueref, I., C. Gerbig, A. Fridlind, J.C. Lin, S.C. Wofsy, B.C. Daube, A.S. Ackerman, J.E. Smith, D. Sayres, J. Vellovic, D.G. Baumgardner, D. Wang, E. Weinstock, A.E. Andrews, E.W. Gottlieb, and J.G. Anderson, *Combining a receptor-oriented framework for tracer*

- distributions with a cloud-resolving model to study transport in deep convective clouds: Application to the NASA CRYSTAL-FACE campaign. *Geophysical Research Letters*, 2004. **31**(14): p. 1-5.
82. Borsari, V., J. Vicente, and D. Assunção, *Ammonia emissions from a light-duty vehicle*. Transportation Research Part D, 2017. **51**: p. 53-61.
  83. Perrino, C., M. Catrambone, A.D. Menno, D. Bucchianico, and I. Allegrini, *Gaseous ammonia in the urban area of Rome, Italy and its relationship with traffic emissions*. *Atmospheric Environment*, 2010. **36**(2002): p. 5385-5394.
  84. Bares, R., J. Lin, D. Mendoza, M. Baasandorj, W. Sebastian, B. Fasoli, and L. Mitchell, *Excess carbon dioxide as a tracer for air pollution in the Salt Lake Valley during winter time and slope validation of modeled CO<sub>2</sub>: CO<sub>2</sub> emission signatures*, 2016.
  85. Kuprov, R., P. Barickman, M. Baasandorj, N. Daher, K. Kelley, and S. Packham, *2015 Special Toxids Study Report*, 2016, Utah Division of Air quality.
  86. Baasandorj, M., J. Hansen, R. Kuprove, D.J. Eatough, P.M. Cropper, D.K. Orsen, J.H. Lin, and D. Millet, *West Valley High Time REsolution Air Toxics Monitoring Campaign Report*, 2017, U.S. EPA and Utah Division of Air Quality.
  87. de Gouw, J.A., D. Welsh-Bon, C. Warneke, W.C. Kuster, L. Alexander, A.K. Baker, A.J. Beyersdorf, D.R. Blake, M. Canagaratna, A.T. Celada, L.G. Huey, W. Junkermann, T.B. Onasch, A. Salcido, S.J. Sjostedt, A.P. Sullivan, D.J. Tanner, O. Vargas, R.J. Weber, D.R. Worsnop, X.Y. Yu, and R. Zaveri, *Emission and chemistry of organic carbon in the gas and aerosol phase at a sub-urban site near Mexico City in March 2006 during the MILAGRO study*. *Atmos. Chem. Phys.*, 2009. **9**(10): p. 3425-3442.
  88. Chang, S. and D.T. Allen, *Atmospheric Chlorine Chemistry in Southeast Texas: Impacts on Ozone Formation and Control*. *Environ. Sci. Technol.*, 2006. **40**(1): p. 251-262.
  89. Nowak, J.B., J.A. Neuman, R. Bahreini, A.M. Middlebrook, J.S. Holloway, S.A. McKeen, D.D. Parrish, T.B. Ryerson, and M. Trainer, *Ammonia sources in the California South Coast Air Basin and their impact on ammonium nitrate formation*. *Geophysical Research Letters*, 2012. **39**(7): p. L07804.
  90. UDAQ, Logan, UT-ID PM2.5 Nonattainment SIP, UDAQ: <https://deq.utah.gov/Pollutants/P/pm/pm25/moderate-area-state-implementation-plans.htm>.
  91. UDAQ, Provo, UT PM2.5 Nonattainment SIP, UDAQ: <https://deq.utah.gov/Pollutants/P/pm/pm25/moderate-area-state-implementation-plans.htm>.
  92. Martin, R., Cache Valley Air Quality Studies, 2006: <http://citeseerx.ist.psu.edu/viewdoc/download?doi=10.1.1.127.8179&rep=rep1&type=pdf>.
  93. Fountoukis, C. and A. Nenes, *ISORROPIA II: a computationally efficient thermodynamic equilibrium model for K<sup>+</sup>-Ca<sup>2+</sup>-Mg<sup>2+</sup>-NH<sub>4</sub><sup>+</sup>-Na<sup>+</sup>-SO<sub>4</sub><sup>2-</sup>-NO<sub>3</sub><sup>-</sup>-Cl-H<sub>2</sub>O aerosols*. *Atmos. Chem. Phys.*, 2007. **7**(17): p. 4639-4659.
  94. Nenes, A., S.N. Pandis, and C. Pilinis, *ISORROPIA: A new thermodynamic equilibrium model for multiphase multicomponent inorganic aerosols*. *Aquat. Geoch.*, 1998. **4**: p. 123-152.
  95. Horel, J., M. Splitt, L. Dunn, J. Pechmann, B. White, C. Ciliberti, S. Lazarus, J. Slemmer, D. Zaff, and J. Burks, *Mesowest: Cooperative Mesonets in the Western United States*. *Bulletin of the American Meteorological Society*, 2002. **83**(2): p. 211-225.
  96. Sun, K., L. Tao, D.J. Miller, D. Pan, L.M. Golston, M.A. Zondlo, R.J. Griffin, H.W. Wallace, Y.J. Leong, M.M. Yang, Y. Zhang, D.L. Mauzerall, and T. Zhu, *Vehicle Emissions as an*

- Important Urban Ammonia Source in the United States and China*. Environmental science & technology, 2017. **51**(4) p. 2472-2481.
97. Suarez-Bertoa, R., P. Mendoza-Villafuerte, P. Bonnel, V. Lilova, L. Hill, A. Perujo, and C. Astorga, *On-road measurement of NH<sub>3</sub> and N<sub>2</sub>O emissions from a Euro V heavy-duty vehicle*. Atmospheric Environment, 2016. **139**: p. 167-175.
  98. Eilerman, S.J., J. Peischl, J.A. Neuman, T.B. Ryerson, K.C. Aikin, M.W. Holloway, M.A. Zondlo, L.M. Golston, D. Pan, C. Floerchinger, and S. Herndon, *Characterization of Ammonia, Methane, and Nitrous Oxide Emissions from Concentrated Animal Feeding Operations in Northeastern Colorado*. Environmental Science & Technology, 2016. **50**(20): p. 10885-10893.
  99. Cropper, P.M., D.J. Eatough, D.K. Overson, J.C. Hansen, F. Caka, and R.A. Cary, *Use of a GC-MS Organic Aerosol Monitor for In-Field Detection of Fine Particulate Organic Compounds in Source Apportionment*. Journal of the Air & Waste Management Association, 2017. **submitted**: p. null-null.
  100. Kotchenruther, R.A., *Source apportionment of PM<sub>2.5</sub> at multiple Northwest U.S. sites: Assessing regional winter wood smoke impacts from residential wood combustion*. Atmospheric Environment, 2016. **142**(Supplement C): p. 210-219.
  101. Mouteva, G.O., J.T. Randerson, S.M. Fahmi, S.E. Bush, J.R. Ehleringer, X. Xu, G.M. Santos, R. Kuprov, B.A. Schichtel, and C.I. Czimczik, *Using radiocarbon to constrain black and organic carbon aerosol sources in Salt Lake City*. Journal of Geophysical Research: Atmospheres, 2017. **in press**: p. n/a-n/a.
  102. Daher, N., *Positive Matrix Factorization Modeling To Consider The Impact Of Emissions From Solid Fuel Burning Devices*, 2017, Utah DAQ.
  103. Cubison, M.J., A.M. Ortega, P.L. Hayes, D.K. Farmer, D. Day, M.J. Lechner, W.H. Brune, E. Apel, G.S. Diskin, J.A. Fisher, H.E. Fuelberg, A. Hecobian, D.J. Knapp, T. Mikoviny, D. Riemer, G.W. Sachse, W. Sessions, R.J. Weber, A.J. Weinheimer, A. Wisthaler, and J.L. Jimenez, *Effects of aging on organic aerosol from open biomass burning smoke in aircraft and laboratory studies*. Atmos. Chem. Phys., 2011. **11**(23): p. 12049-12064.
  104. Hennigan, C.J., M.A. Miracolo, G.J. Engelhart, A.A. May, A.A. Presto, T. Lee, A.P. Sullivan, G.R. McMeeking, H. Coe, C.E. Wold, W.M. Hao, J.B. Gilman, W.C. Kuster, J. de Gouw, B.A. Schichtel, J.L. Collett Jr, S.M. Kreidenweis, and A.L. Robinson, *Chemical and physical transformations of organic aerosol from the photo-oxidation of open biomass burning emissions in an environmental chamber*. Atmos. Chem. Phys., 2011. **11**(15): p. 7669-7686.
  105. <http://www.camx.com/>.
  106. Rodriguez, M.A., M.G. Barna, K.A. Gebhart, J.L. Hand, Z.E. Adelman, B.A. Schichtel, J.L. Collett, and W.C. Malm, *Modeling the fate of atmospheric reduced nitrogen during the Rocky Mountain Atmospheric Nitrogen and Sulfur Study (RoMANS): Performance evaluation and diagnosis using integrated processes rate analysis*. Atmospheric Environment, 2011. **45**(1): p. 223-234.
  107. Ahmadov, R., S.A. Mckeen, A.L. Robinson, R. Bahreini, A.M. Middlebrook, J.A. de Gouw, J. Meagher, E.Y. Hsie, E. Edgerton, S. Shaw, and M. Trainer, *A volatility basis set model for summertime secondary organic aerosol over the eastern United States in 2006*. J. Geophys. Res., 2012. **117**: p. D06301.
  108. EPA, <https://www.epa.gov/air-emissions-inventories/2011-national-emissions-inventory-nei-documentation>. 2017.
  109. [ftp://aftp.fsl.noaa.gov/divisions/taq/emissions\\_data\\_2011/](ftp://aftp.fsl.noaa.gov/divisions/taq/emissions_data_2011/).
  110. Hall, S.J., G. Maurer, S.W. Hoch, R. Taylor, and D.R. Bowling, *Impacts of anthropogenic emissions and cold air pools on urban to montane gradients of snowpack ion*

- concentrations in the Wasatch Mountains, Utah*. Atmospheric Environment, 2014. **98**: p. 231-241.
111. [http://www.inscc.utah.edu/~hoch/AIRQUAL\\_2016-2017/ValleyHeatDeficit\\_UWFPS.csv](http://www.inscc.utah.edu/~hoch/AIRQUAL_2016-2017/ValleyHeatDeficit_UWFPS.csv).
  112. McDonald, B.C., T.R. Dallmann, E.W. Martin, and R.A. Harley, *Long-term trends in nitrogen oxide emissions from motor vehicles at national, state, and air basin scales*. J. Geophys. Res., 2012. **117**: p. D00V18.
  113. Young, C.J., R.A. Washenfelder, L.H. Mielke, H.D. Osthoff, P. Veres, A.K. Cochran, T.C. VandenBoer, H. Stark, J. Flynn, N. Grossberg, C.L. Haman, B. Lefer, J.B. Gilman, W.C. Kuster, C. Tsai, O. Pikelnaya, J. Stutz, J.M. Roberts, and S.S. Brown, *Vertically resolved measurements of nighttime radical reservoirs in Los Angeles and their contribution to the urban radical budget*. Environ. Sci. Technol., 2012. **46**: p. 10965-10973.
  114. Rappenglück, B., G. Lubertino, S. Alvarez, J. Golovko, B. Czader, and L. Ackermann, *Radical precursors and related species from traffic as observed and modeled at an urban highway junction*. Journal of the Air & Waste Management Association, 2013. **63**(11): p. 1270-1286.
  115. Brown, S.S., T.B. Ryerson, A.G. Wollny, C.A. Brock, R. Peltier, A.P. Sullivan, R.J. Weber, W.P. Dubé, M. Trainer, J.F. Meagher, F.C. Fehsenfeld, and A.R. Ravishankara, *Variability in nocturnal nitrogen oxide processing and its role in regional air quality*. Science, 2006. **311**: p. 67-70.
  116. Finlayson-Pitts, B.J., L.M. Wingen, A.L. Sumner, D. Syomin, and K.A. Ramazan, *The heterogeneous hydrolysis of NO<sub>2</sub> in laboratory systems and in outdoor and indoor atmospheres: An integrated mechanism*. Phys. Chem. Chem. Phys., 2003. **5**(2): p. 223-242.
  117. Pusede, S.E., T.C. VandenBoer, J.G. Murphy, M.Z. Markovic, C.J. Young, P.R. Veres, J.M. Roberts, R.A. Washenfelder, S.S. Brown, X. Ren, C. Tsai, J. Stutz, W.H. Brune, E.C. Browne, P.J. Wooldridge, A.R. Graham, R. Weber, A.H. Goldstein, S. Dusanter, S.M. Griffith, P.S. Stevens, B.L. Lefer, and R.C. Cohen, *An Atmospheric Constraint on the NO<sub>2</sub> Dependence of Daytime Near-Surface Nitrous Acid (HONO)*. Environmental Science & Technology, 2015. **49**(21): p. 12774-12781.
  118. Lin, J.C., C. Gerbig, S.C. Wofsy, A.E. Andrews, B.C. Daube, K.J. Davis, and C.A. Grainger, *A near-field tool for simulating the upstream influence of atmospheric observations: The Stochastic Time-Inverted Lagrangian Transport (STILT) model*. Journal of Geophysical Research: Atmospheres, 2003. **108**(D16): p. n/a-n/a.
  119. Lerner, B.M., J.B. Gilman, K.C. Aikin, E.L. Atlas, P.D. Goldan, M. Graus, R. Hendershot, G.A. Isaacman-VanWertz, A. Koss, W.C. Kuster, R.A. Lueb, R.J. McLaughlin, J. Peischl, D. Sueper, T.B. Ryerson, T.W. Tokarek, C. Warneke, B. Yuan, and J.A. de Gouw, *An improved, automated whole air sampler and gas chromatography mass spectrometry analysis system for volatile organic compounds in the atmosphere*. Atmos. Meas. Tech., 2017. **10**(1): p. 291-313.
  120. Yuan, B., A. Koss, C. Warneke, J.B. Gilman, B.M. Lerner, H. Stark, and J.A. de Gouw, *A high-resolution time-of-flight chemical ionization mass spectrometer utilizing hydronium ions (H<sub>3</sub>O<sup>+</sup> ToF-CIMS) for measurements of volatile organic compounds in the atmosphere*. Atmos. Meas. Tech., 2016. **9**(6): p. 2735-2752.
  121. McDonald, B.C., J.A. de Gouw, J.B. Gilman, S.H. Jathar, A. Akherati, C.D. Cappa, J.L. Jimenez, J. Lee-Taylor, P.L. Hayes, S.A. McKeen, Y.Y. Cui, S.-W. Kim, D.R. Gentner, G. Isaacman-VanWertz, A.H. Goldstein, R.A. Harley, G.J. Frost, J.M. Roberts, T.B. Ryerson, and M. Trainer, *Volatile chemical products emerging as largest petrochemical source of urban organic emissions*. Science, 2018. **359**(6377): p. 760.

122. Faloon, I.C., D. Tan, R.L. Lesher, N.L. Hazen, C.L. Frame, J.B. Simpas, H. Harder, M. Martinez, P. Di Carlo, X. Ren, and W.H. Brune, *A Laser-induced Fluorescence Instrument for Detecting Tropospheric OH and HO<sub>2</sub>: Characteristics and Calibration*. *J. Atmos. Chem.*, 2004. **47**: p. 139-167.
123. Fuchs, H., B. Bohn, A. Hofzumahaus, F. Holland, K.D. Lu, S. Nehr, F. Rohrer, and A. Wahner, *Detection of HO<sub>2</sub> by laser-induced fluorescence: calibration and interferences from RO<sub>2</sub> radicals*. *Atmos. Meas. Tech.*, 2011. **4**(6): p. 1209-1225.
124. Brown, S.S., H. Stark, S.J. Ciciora, R.J. McLaughlin, and A.R. Ravishankara, *Simultaneous in-situ detection of atmospheric NO<sub>3</sub> and N<sub>2</sub>O<sub>5</sub> via cavity ring-down spectroscopy*. *Rev. Sci. Instr.*, 2002. **73**(9): p. 3291-3301.
125. Elser, M., C. Bozzetti, I. El-Haddad, M. Maasikmets, E. Teinmaa, R. Richter, R. Wolf, J.G. Slowik, U. Baltensperger, and A.S.H. Prévôt, *Urban increments of gaseous and aerosol pollutants and their sources using mobile aerosol mass spectrometry measurements*. *Atmos. Chem. Phys.*, 2016. **16**(11): p. 7117-7134.
126. Yuan, B., M.M. Coggon, A.R. Koss, C. Warneke, S. Eilerman, J. Peischl, K.C. Aikin, T.B. Ryerson, and J.A. de Gouw, *Emissions of volatile organic compounds (VOCs) from concentrated animal feeding operations (CAFOs): chemical compositions and separation of sources*. *Atmos. Chem. Phys.*, 2017. **17**(8): p. 4945-4956.
127. Anderson, D.C., C.P. Loughner, G. Diskin, A. Weinheimer, T.P. Canty, R.J. Salawitch, H.M. Worden, A. Fried, T. Mikoviny, A. Wisthaler, and R.R. Dickerson, *Measured and modeled CO and NO<sub>y</sub> in DISCOVER-AQ: An evaluation of emissions and chemistry over the eastern US*. *Atmospheric Environment*, 2014. **96**(Supplement C): p. 78-87.
128. Travis, K.R., D.J. Jacob, J.A. Fisher, P.S. Kim, E.A. Marais, L. Zhu, K. Yu, C.C. Miller, R.M. Yantosca, M.P. Sulprizio, A.M. Thompson, P.O. Wennberg, J.D. Crouse, J.M. St. Clair, R.C. Cohen, J.L. Laughner, J.E. Dibb, S.R. Hall, K. Ullmann, G.M. Wolfe, I.B. Pollack, J. Peischl, J.A. Neuman, and X. Zhou, *Why do models overestimate surface ozone in the Southeast United States?* *Atmos. Chem. Phys.*, 2016. **16**(21): p. 13561-13577.
129. Drozd, G.T., Y. Zhao, G. Saliba, B. Frodin, C. Maddox, R.J. Weber, M.C.O. Chang, H. Maldonado, S. Sardar, A.L. Robinson, and A.H. Goldstein, *Time Resolved Measurements of Speciated Tailpipe Emissions from Motor Vehicles: Trends with Emission Control Technology, Cold Start Effects, and Speciation*. *Environmental Science & Technology*, 2016. **50**(24): p. 13592-13599.
130. May, A.A., N.T. Nguyen, A.A. Presto, T.D. Gordon, E.M. Lipsky, M. Karve, A. Gutierrez, W.H. Robertson, M. Zhang, C. Brandow, O. Chang, S. Chen, P. Cicero-Fernandez, L. Dinkins, M. Fuentes, S.-M. Huang, R. Ling, J. Long, C. Maddox, J. Massetti, E. McCauley, A. Miguel, K. Na, R. Ong, Y. Pang, P. Rieger, T. Sax, T. Truong, T. Vo, S. Chattopadhyay, H. Maldonado, M.M. Maricq, and A.L. Robinson, *Gas- and particle-phase primary emissions from in-use, on-road gasoline and diesel vehicles*. *Atmospheric Environment*, 2014. **88**(Supplement C): p. 247-260.
131. Weilenmann, M., J.-Y. Favez, and R. Alvarez, *Cold-start emissions of modern passenger cars at different low ambient temperatures and their evolution over vehicle legislation categories*. *Atmospheric Environment*, 2009. **43**(15): p. 2419-2429.
132. Bishop, G.A., B.G. Schuchmann, and D.H. Stedman, *Heavy-Duty Truck Emissions in the South Coast Air Basin of California*. *Environmental Science & Technology*, 2013. **47**(16): p. 9523-9529.
133. Anenberg, S.C., J. Miller, R. Minjares, L. Du, D.K. Henze, F. Lacey, C.S. Malley, L. Emberson, V. Franco, Z. Klimont, and C. Heyes, *Impacts and mitigation of excess diesel-related NO<sub>x</sub> emissions in 11 major vehicle markets*. *Nature*, 2017. **545**(7655): p. 467-471.

134. Misra, C., J.F. Collins, J.D. Hermer, T. Sax, M. Krishnamurthy, W. Sobieralski, M. Burntizki, and D. Chernich, *In-Use NOx Emissions from Model Year 2010 and 2011 Heavy-Duty Diesel Engines Equipped with Aftertreatment Devices*. Environmental Science & Technology, 2013. **47**(14): p. 7892-7898.
135. Bishop, G.A. and D.H. Stedman, *Reactive Nitrogen Species Emission Trends in Three Light-/Medium-Duty United States Fleets*. Environmental Science & Technology, 2015. **49**(18): p. 11234-11240.
136. Sun, K., L. Tao, D.J. Miller, D. Pan, L.M. Golston, M.A. Zondlo, R.J. Griffin, H.W. Wallace, Y.J. Leong, M.M. Yang, Y. Zhang, D.L. Mauzerall, and T. Zhu, *Vehicle Emissions as an Important Urban Ammonia Source in the United States and China*. Environmental Science & Technology, 2017. **51**(4): p. 2472-2481.
137. Bishop, G.A., A.M. Peddle, D.H. Stedman, and T. Zhan, *On-Road Emission Measurements of Reactive Nitrogen Compounds from Three California Cities*. Environ. Sci. Technol., 2010. **44**(9): p. 3616-3620.
138. Dallmann, T.R., R.A. Harley, and T.W. Kirchstetter, *Effects of Diesel Particle Filter Retrofits and Accelerated Fleet Turnover on Drayage Truck Emissions at the Port of Oakland*. Environmental Science & Technology, 2011. **45**(24): p. 10773-10779.
139. Bishop, G.A., D.H. Stedman, J.E. Peterson, T.J. Hosick, and P.L. Guenther, *A Cost-Effectiveness Study of Carbon Monoxide Emissions Reduction Utilizing Remote Sensing*. Air & Waste, 1993. **43**(7): p. 978-988.